Polarization of Heavy Quarkonium Production in the Color Evaporation Model

By

VINCENT CHEUNG
DISSERTATION

Submitted in partial satisfaction of the requirements for the degree of

DOCTOR OF PHILOSOPHY

in

Physics

in the

OFFICE OF GRADUATE STUDIES

of the

UNIVERSITY OF CALIFORNIA

DAVIS

Approved:

Ramona Vogt, Chair

Manuel Calderón De La Barca Sánchez

Hsin-Chia Cheng

Committee in Charge

2020

Contents

List of Figures

List of Tables

Abstract

Polarization of Heavy Quarkonium Production in the Color Evaporation Model

A series of quarkonium production and polarization calculations are presented. All calculations are based upon the color evaporation model (CEM) as well as the newly-developed improved CEM (ICEM). We employ these models to consider the polarized production of quarkonium by restricting the final state quark-antiquark pair to be in the desired spin state. The first calculation separates the polarized yield from the total yield according to the J_z of the quark-antiquark pair. The second calculation separates the polarized yield from the total yield according to the J and J_z of the quark-antiquark pair, while also considering the feed down production from higher energy bound states. The third and fourth calculations consider the p_T-dependence of the polarization and production, by considering off-shell initial state gluons using the k_T-factorization approach for prompt J/ψ and prompt $\Upsilon(n\mathrm{S})$. The last calculation computes the p_T-dependence of the polarization and production using the collinear factorization approach for direct J/ψ. As our calculations become successively more complex, we find that our polarization predictions using the CEM are in better agreement with experimental data without losing the ability to describe the production yield.

Acknowledgments

I would like to thank my parents for their continued support that allows me to chase my dream over the past ten years. Mom and Dad, I am sorry that I have left you and can't take care of you for so long. I thank my brother, Michael, for his emotional support on my studies as well as for taking care of my parents while I am away. My warm thanks to the love of my life, Agatha, for being with me and supporting me at all times. I love you.

I would like to thank my adviser, Ramona Vogt, for her patience and caring communication. It has been my pleasure and honor to work with you. I sincerely thank you from the bottom of my heart for taking care of me both professionally and emotionally. Thank you Daniel Cebra, for connecting me with Ramona. I would like to thank the Nuclear Physics Group at UCD for financially supporting my travel, facilitating my office space on campus, and giving me the best education and exposure to the science community. My deep thanks to Feng Yuan for all the valuable discussions and Bernd Kniehl for the initiation of and encouragement throughout this project. My work wouldn't be achievable without you.

I would like to express my deep appreciation to the staff and faculty members at UCD, especially Rena Zieve, Rajiv Singh, Dina Zhabinskaya, and Angela Sharma for always working in favor of my teaching preferences. Thank you for approving me to conduct the entire instruction of PHY 1 and 7, allowing me to build teaching experiences here. As a student relying heavily on teaching assistantship, your help should not be left unmentioned.

Special acknowledgments go to Manuel Calderón De La Barca Sánchez, Hsin-Chia Cheng, John Terning, Jack Gunion, colleagues at the Nuclear Physics Group at UCD, the Nuclear Theory Group at Lawrence Berkeley National Laboratory, and friends in the High Energy Theory Group at UCD. Every advice you gave has been an important part of my intellectual growth.

Chapter 1

Introduction

1.1 The Standard Model

The Standard Model of particle physics [1–3] describes three fundamental interactions in the universe and classifies elementary particles into three categories: leptons, quarks, and gauge bosons. It also contains a scalar boson, the Higgs boson. All the elementary particles are shown in Fig. 1.1. It is based on the gauge group SU$(3)_C\times$ SU$(2)_L\times$ U$(1)_Y$ where the SU$(3)_C$ subgroup refers to the quantum chromodynamics (QCD) sector and the SU$(2)_W\times$ U$(1)_Y$ subgroup refers to the unbroken electroweak sector. The symmetry of the electroweak subgroup is broken via the Higgs mechanisms [5–9] leaving the symmetry of the electromagnetic subgroup, U$(1)_{\mathrm{QED}}$, preserved in the electroweak symmetry breaking. The QCD sector describes the strong interactions of quarks (denoted as q in general) and gluons (g). The Standard Model is well established and can explain a wide variety of experimental phenomena in particle physics.

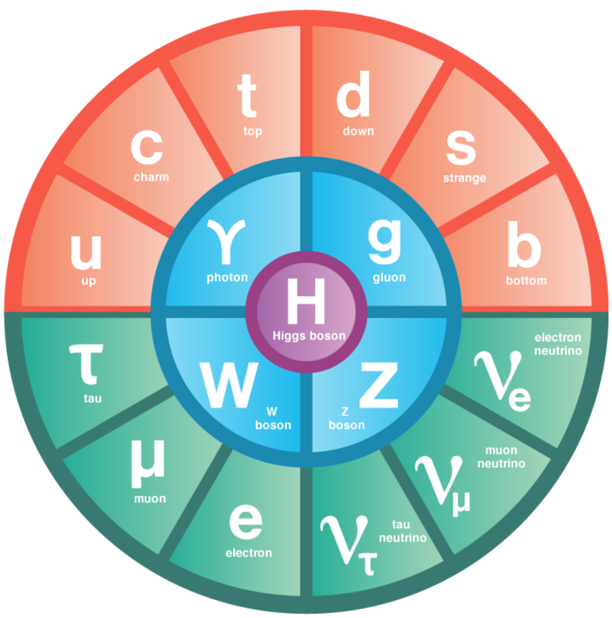

Figure 1.1. (Taken from Ref. [4]). Elementary particles in the Standard Model of particle physics. Particles are either quarks (redorange), leptons (emerald), gauge bosons (cyan), or the Higgs boson (purple).

1.2 Quarks and gluons

Quarks are elementary particles of the QCD sector in the Standard Model. They are fermions with spin 1/2 ($\hbar = 1$). A quark carries one of the three color charges: red, green, and blue which form the fundamental representation of $\mathrm{SU}(3)_C$. There are six types of quarks: d (down), u (up), s (strange), c (charm), b (bottom), and t (top), and they are accompanied by their anti-particles, anti-quarks (denoted as $\bar{q}$ in general): $\bar{d}$ (anti-down), $\bar{u}$ (anti-up), $\bar{s}$ (anti-strange), $\bar{c}$ (anti-charm), $\bar{b}$ (anti-bottom), $\bar{t}$ (anti-top). Anti-quarks have the same masses and spins, but with opposite color and electric charges: anti-red, anti-green, and anti-blue. Gluons are the gauge bosons of the QCD $\mathrm{SU}(3)_C$ non-Abelian theory. They are massless spin-1 particles and carry colors in the adjoint representation of the $\mathrm{SU}(3)_C$ symmetry. In the parameterization of SU(3) rotations, there are $3^2 - 1 = 8$ degrees of freedom, and so there are eight kinds of gluons. Since gluons carry both color charges and anti-color charges, they are responsible for mediating the strong interaction between quarks and anti-quarks.

Quarks are separated into three generations because the charged weak coupling is significantly stronger for quarks within the same generation. Each generation has similar properties but the mass is significantly heavier from one generation to another. Also, the difference in quark mass within a generation becomes larger across generations. The first generation contains the lightest two quarks, the down quark and the up quark. They are responsible for the net electric charges of protons and neutrons. A proton is a bound state of two up quarks and a down quark (uud). A neutron is a bound state of an up quark and two down quarks (udd). Since a proton carries $+1$ electric charge (relative to the absolute charge of an electron) and a neutron carries 0 electric charges, up and down quarks must carry fractional charges. A down quark carries $-1/3$ electric charge and an up quark carries $2/3$ electric charge. Although the down and up quarks account for the electric charges of protons and neutrons, the majority of the proton mass comes from the interactions of quarks and gluons inside the proton.

The second generation contains two heavier quarks, the strange quark and the charm quark. They have the same properties as the down and up quarks respectively except their masses are higher. The third generation contains two even heavier quarks, the bottom and the top quarks. Similarly, they have the same properties as the strange and charm quarks respectively but their masses are much higher. Because of the significant mass difference, the up, down, and strange quarks are referred to as the light quarks while the charm, bottom, and top quarks are referred to as the heavy quarks. Often, a light quark is denoted as q and a heavy quark is denoted as Q. The quark flavors with masses and electric charges are listed in Table 1.1.

Table 1.1. The quark flavors q, their current bare mass m_q, and their electric charge relative to the electron charge e_q. Antiquarks have the same masses but oppotite electric charges.

quark flavor (q)	m_q	e_q
up (u)	$2.2^{+0.5}_{-0.4}$ MeV	$\frac{2}{3}$
down (u)	$4.7^{+0.5}_{-0.3}$ MeV	$-\frac{1}{3}$
strange (s)	95^{+9}_{-3} MeV	$-\frac{1}{3}$
charm (s)	$1.275^{+0.025}_{-0.035}$ GeV	$\frac{2}{3}$
bottom (s)	$4.18^{+0.04}_{-0.03}$ GeV	$-\frac{1}{3}$
top (t)	173.0 ± 0.04 GeV	$\frac{2}{3}$

1.3 The strong interaction

The QCD Lagrangian is given by

$$\mathcal{L}_{\rm QCD} = \sum_q \bar{\psi}_{q,a}(i\gamma^\mu\partial_\mu\delta_{ab} - g_s\gamma^\mu t^C_{ab}\mathcal{A}^C_\mu - m_q\delta_{ab})\psi_{q,b} - \frac{1}{4}F^A_{\mu\nu}F^{A,\mu\nu} , \qquad (1.1)$$

where repeated indices (μ, ν, a, b, A, and C) are summed over. Here, μ and ν are Lorentz indices which run from 1 to 4 (space-time symmetry), a and b are color indices which run from 1 to 3 (three colors of quarks), and A and C are the adjoint color indices which run from 1 to 8 (8 kinds of gluons). The quark spinors and gluon fields are denoted as $\psi_{q,a}$ and $\mathcal{A}^C_\mu$ respectively. The generators of the SU(3)$_C$ group are denoted as t^C_{ab}. The γ^μ are the Dirac matrices. The quantity g_s is the QCD coupling constant and is the only input parameter of QCD. It is related to the strong coupling constant, α_s, by

$$g_s^2 = 4\pi\alpha_s . \qquad (1.2)$$

Finally, F, the field strength tensor and is given by

$$F^A_{\mu\nu} = \partial_\mu\mathcal{A}^A_\nu - \partial_\nu\mathcal{A}^A_\mu - g_s f_{ABC}\mathcal{A}^B_\mu\mathcal{A}^C_\nu , \qquad (1.3)$$

where

$$[t^A, t^B] = i f_{ABC} t^C \ , \tag{1.4}$$

are the structure constans of the SU(3)$_C$ group.

The strong coupling constant, α_s, describes the strength of the strong interaction in vacuum. However, the effective strength of the strong interaction is not a constant. Since QCD is renormalizable, this coupling constant can be expressed in terms of an unphysical renormalization scale, μ_R, by the renormalization group equation,

$$\mu_R^2 \frac{d\alpha_s}{d\mu_R^2} \ = \ \beta(\alpha_s) = -(b_0\alpha_s^2 + b_1\alpha_s^3 + b_2\alpha_s^4 + \mathcal{O}(\alpha_s^5)) \ , \tag{1.5}$$

where $b_0 = (33 - 2n_f)/(12\pi)$, $b_1 = (159 - 19n_f)/(24\pi^2)$, and $b_2 = (2857 - 5033n_f/9 + 325n_f^2/27)/(128\pi^3)$ for SU(3). Here, n_f is the number of "light" quark flavors defined compared to the renormalization scale as $m_q \ll \mu_R$. Truncating the sum at $\mathcal{O}(\alpha_s^2)$ (also called as 1-loop) and solving for α_s as a function of μ_R gives

$$\alpha_s(\mu_R^2) \ = \ \frac{12\pi}{(33 - 2n_f)\ln\frac{\mu_R^2}{\Lambda_{\mathrm{QCD}}^2}} \ , \tag{1.6}$$

where $\Lambda_{\mathrm{QCD}} \approx 200$ MeV is the QCD scale defined where α_s diverges. When μ_R is brought near the scale of the momentum transfer, Q_T, in a given process, $\alpha_s(\mu_R^2 \simeq Q^2)$ is then an indicative measure of the effective strength of the strong interaction. For example, the strong coupling constant, when Q is taken at the mass of the Z boson measured by experiments averages to a value of $\alpha_s = 0.1187 \pm 0.0052$ [10].

One can observe that the effective strong coupling constant in Eq. (1.6) gets smaller as a function of Q. This traces back to the minus sign in Eq. (1.5). This is the origin of asymptotic freedom, which leads to a decreasing strong coupling for increasing energy scale or decreasing length scale. On the other hand, the strong force gets stronger when the energy scale decreases or when the length scale increases. This is known as color confinement and is the reason why free quarks and gluons do not exist in nature.

Asymptotic freedom allows the use of perturbative Feynman calculus in QCD to calculate scattering amplitudes. This is because the scattering amplitude in a given QCD process is a sum of the allowed interactions embedded in the Lagrangian in Eq. (1.1). When g_s is in the limit $g_s \ll 1$, the scattering amplitudes are perturbatively calculable. Since the masses of the charm and bottom quarks are much heavier than the QCD scale, the effective coupling is small enough so that perturbative QCD can be employed to calculate scattering amplitudes involving heavy quark production.

1.4 The parton model

Quarks and gluons are also called partons because they are found inside the proton in deep-inelastic scattering (DIS) experiments where an electron of momentum k scatters off a proton of momentum p by emitting a highly off-shell photon of momentum q, represented by $e^- p \to e^- X$. The virtual photon is then able to interact with the parton inside the proton electromagnetically. Deep in DIS refers to the limit where the photon virtuality, defined as $Q_T^2 = -q_T^2$, much greater than the squared proton mass, but below the squared Z boson mass. Inelastic in DIS refers to the limit where the invariant mass of the unobserved final state hadronic system is greater than the proton mass. The differential cross section for this process in this limit is

$$\frac{d^2\sigma}{dx dQ_T^2} = \frac{4\pi\alpha^2}{Q_T^4}\left[(1-y)\frac{F_2(x,Q_T^2)}{x} + y^2 F_1(x,Q_T^2)\right], \tag{1.7}$$

where α is the electromagnetic coupling, $F_1(x,Q_T^2)$ and $F_2(x,Q_T^2)$ are proton structure functions, x is the fraction of the total momentum carried by the parton struck by the virtual photon given by $x = Q_T^2/(2p \cdot q)$, and y is defined as $(q \cdot p)/(k \cdot p)$ and known as the inelasticity of the collision.

In the parton model, the underlying ineraction in DIS is the QED elastic scattering of $e^- q \to e^- q$, where the differential cross section can be written as

$$\frac{d\sigma}{dQ_T^2} = \frac{4\pi\alpha^2 e_q^2}{Q_T^4}\left[(1-y) + \frac{y^2}{2}\right], \tag{1.8}$$

where e_q is the electric charge of the quark, q. Although the down and up quarks are responsible for the electric charge of a proton, the interaction between the quarks and gluons within the proton will give rise to pair production of $q\bar{q}$ such as $u\bar{u}$ and $d\bar{d}$ at smaller distance scale or probing at a high-energy scale. The down and up quarks that make up the proton are then called the valence quarks and the pair-produced quarks are called sea quarks. Both valence and sea quarks interact with the electron according to Eq. (1.8). Even though we expect the valence quarks to carry approximately 1/3 of the proton momentum, because quarks and gluons are constantly interacting with each other, the momentum of the quarks within the proton is distributed over all fractional momenta. We denote the probability density function of finding a parton of flavor i with momentum fraction x of the proton's momentum as $f_i(x)$. This function is also called the parton distribution function (PDF). Therefore, the cross section in Eq. 1.8 contributed by a particular quark flavor, q_i of electric charge e_{q_i} can be written as

$$\frac{d\sigma_i}{dQ_T^2} = \frac{4\pi\alpha^2}{Q^4}\left[(1-y)+\frac{y^2}{2}\right]e_{q_i}^2 f_{q_i}(x)dx \;, \tag{1.9}$$

where $f_{q_i}(x)dx$ is the number of quarks with momentum fraction between x and $x+dx$. Summing over all quark flavors gives

$$\frac{d^2\sigma}{dx dQ_T^2} = \sum_i \frac{4\pi\alpha^2 e_{q_i}^2}{Q_T^4}\left[(1-y)+\frac{y^2}{2}\right]f_{q_i}(x) \;, \tag{1.10}$$

which allows comparison with the DIS cross section in Eq. 1.7,

$$F_2(x, Q_T^2) = x\sum_i e_{q_i}^2 f_{q_i}(x) \tag{1.11}$$

$$F_2(x, Q_T^2) = 2xF_1(x, Q_T^2) \;. \tag{1.12}$$

1.4.1 Cross Sections

Since partonic interactions are the underlying processes, and the partons distributions are described by the PDFs, the cross section of any given final state is thus a convolution of the parton densities of the collision partners with the partonic cross section. In a hadronic collision, the cross section is

$$\sigma = f_1 \otimes f_2 \otimes \hat{\sigma} \;, \tag{1.13}$$

where f_1 and f_2 are the PDFs of the hadrons, and $\hat{\sigma}$ is the partonic cross section. Note that this equation is valid only if both collision partners are hadrons. PDFs are non-perturbative in QCD and are obtained by fitting the experimental data. In perturbative QCD (pQCD), a factorization approach is used to calculate the cross section of a process by separating the perturbative short-distance partonic cross section from the non-perturbative long-distance PDFs. In the collinear factorization approach, the parton momentum is collinear with the proton momentum. At leading order, the cross section for any given final state in $p+p$ collisions can be expressed as

$$\sigma \;=\; \sum_{i,j=q,\bar{q},g} \int dx_1 dx_2 \; f_{i/p}(x_1,\mu_F^2) f_{j/p}(x_2,\mu_F^2) \hat{\sigma}_{ij}(\mu_R) \;, \tag{1.14}$$

where i and j are summed over all partons, x_1 and x_2 are the longitudinal momentum fraction carried by the partons of the proton momenta, μ_F is the factorization scale, and $\hat{\sigma}_{ij}(\mu_R)$ is the partonic cross section calculable in pQCD at the renormalization scale, μ_R. The partonic cross section, in general, contains powers of the strong coupling constant, α_s, which depends on the renormalization scale. Naturally, both the renormalization scale and the factorization scale are taken to be of the same order as the scale of the interaction ($\mu_R \simeq \mu_F \simeq Q$). The factorization approach is assumed to hold as long as the interaction scale is much larger than the QCD scale ($Q \gg \Lambda_{\mathrm{QCD}}$). In analogy with strong coupling, the scale dependence of the PDFs has to follow the Dokshitzer-Gribov-Lipatov-Altarelli-Parisi (DGLAP) equations [11–14], which can be expressed as a convolution of the probability of obtaining such parton from all other partons via QCD interactions (P) and the PDFs of other partons

$$\frac{df}{d\ln Q} \;=\; P \otimes f \;. \tag{1.15}$$

The probabilities are also known as the splitting functions. When written explicitly in terms of individual splitting functions and PDFs, the DGLAP equation takes the form

$$Q^2 \frac{df_{i/p}(x,Q^2)}{dQ^2} \;=\; \sum_j \int_x^1 \frac{dy}{y} P_{i/j}\left(\frac{x}{y}, \alpha_s(Q^2)\right) f_{j/p}(y,Q^2) \tag{1.16}$$

where j is summed over all parton flavors and $P_{i/j}$ are the probabilities for obtaining parton i from the splitting of parton j. There are three splittings allowed by the QCD Lagrangian: $g \to q\bar{q}$, $q \to qg$, and $g \to gg$. Note that the first two splittings are also allowed by the QED Lagrangian but the third splitting is exclusive to QCD, which makes the strong coupling constant stronger at longer distance scales and leads to confinement. As we probe at shorter distance scales (same as increasing the factorization scale), we can see more deeply into the proton where there are more splittings and thus giving us access to smaller x. Thus, at higher Q^2, the PDFs reveal a higher density of low x partons, and due to momentum conservation, the density of high x partons is reduced shown in Fig. 1.2 using the CT14 PDFs [15]. Note that the density of gluons is at least an order of magnitude higher at low x ($x < 0.01$) than the light quark density. Therefore, objects that can be produced in gg interactions are going to have the largest contribution to the cross section from that channel, except at very low energies or very high x where the gluon density is low compared to the light quarks.

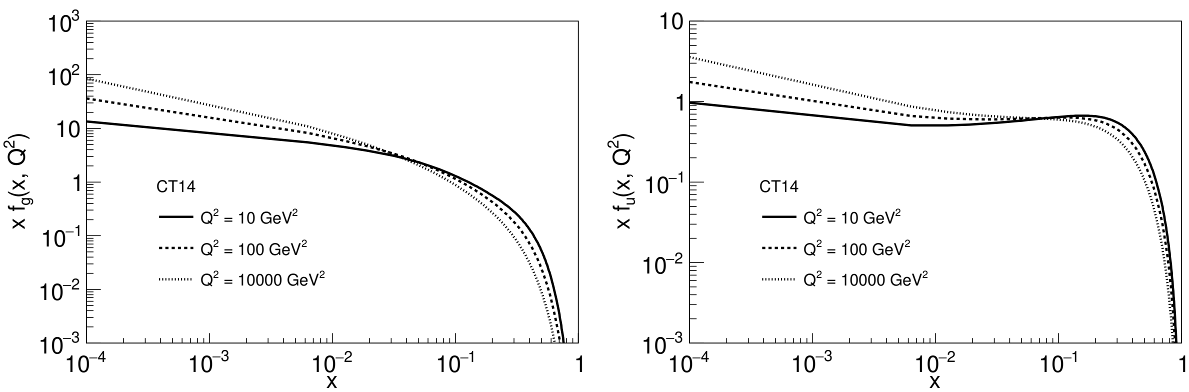

Figure 1.2. The momentum distribution, $xf(x, Q^2)$, of gluons (left) and the total (sum of valence and sea contributions) up quarks (right) as a function of x using the CT14 central set [15]. The interaction scale is set at $Q^2 = 10$ GeV^2 (solid), 100 GeV^2 (dashed), 10000 GeV^2 (dotted). As the interaction scale increases, the access to low x parton becomes more availale. The increase of the up quark density at lower x ($x < 0.01$) is from the rise of the sea contribution in $f_u = f_{u_V} + f_{u_s}$.

In the collinear factorization approach, the transverse momenta of the partons are neglected. However, the DGLAP equation fails at small values of x where the splitting functions diverge. This happens in high-energy collisions where the typical ratio $x \simeq Q^2/s$, (s is the center-of-mass energy squared) becomes very small. This results a large logarithmic contributions in the perturbation series in $\alpha_s \ln(1/x)$.

The BFKL approach [16–18] resums the leading $\ln(1/x)$ terms in the divergence based on gluon Reggeization that assumes the incoming gluons have a finite transverse momentun and are off mass shell. The approach describes the evolution of gluon transverse momentum distribution, $\Phi(x, k_T^2, Q^2)$, which is also known as transverse momentum distribution (TMD), as a convolution of the BFKL kernel ($\mathcal{K}$) and the TMD, analogous to Eq. 1.15

$$\frac{d\Phi}{d\ln(1/x)} = \mathcal{K} \otimes \Phi \ . \tag{1.17}$$

When both collision partners are being probed at x values that are sufficiently low to be in the regime where BFKL approach holds rather than collinear factorization, the cross section in $p+p$ collisions, is then a convolution of the TMD's and the partonic cross section

$$\sigma = \Phi_1 \otimes \Phi_2 \otimes \hat{\sigma} \ . \tag{1.18}$$

A hybrid approach where an unintegrated PDF for one collision partner and a collinear distribution for the other collision partner at higher x can also be used if the conditions are not matched. The BFKL approach is also known as the k_T-factorization approach. Note that the partonic cross section here equations is not the same as in the collinear factorization approach as gluons in the scattering matrix elements are off shell. At leading order, the cross section for any given final state in $p+p$ collisions in the k_T-factorization approach can be expressed as

$$\sigma = \sum_{i,j=q,\bar{q},g} \int \frac{dx_1}{x_1} \frac{dx_2}{x_2} dk_{1T}^2 k_{2T}^2 \frac{d\phi_1}{2\pi} \frac{d\phi_2}{2\pi} \ \Phi_{i/p}(x_1, k_{1T}^2, \mu_F^2) \Phi_{j/p}(x_2, k_{2T}^2, \mu_F^2) \hat{\sigma}_{ij} \ , \tag{1.19}$$

where $\phi_{1,2}$ are the azimuthal angles of the parton and $\Phi_{i/p}(x_1, k_{1T}^2, \mu_F^2)$ is the TMD. TMDs are also known as unintegrated PDFs (uPDFs) as they are related to the collinear PDFs by an integration over k_T^2

$$x f(x, Q^2) = \int_0^{\mu_F^2} dk_T^2 \Phi(x, k_T^2, Q^2) \ , \tag{1.20}$$

such that the normalization in Eqs. (1.14) and (1.19) agree. Note that the collinear factorization should be used for massive colliding objects unless the collision energy is very high such that x is very low. The x- and k_T-evolution of the unintegrated PDFs as a function of k_T are shown in Fig. 1.3 using the JH-2013 uPDFs [19].

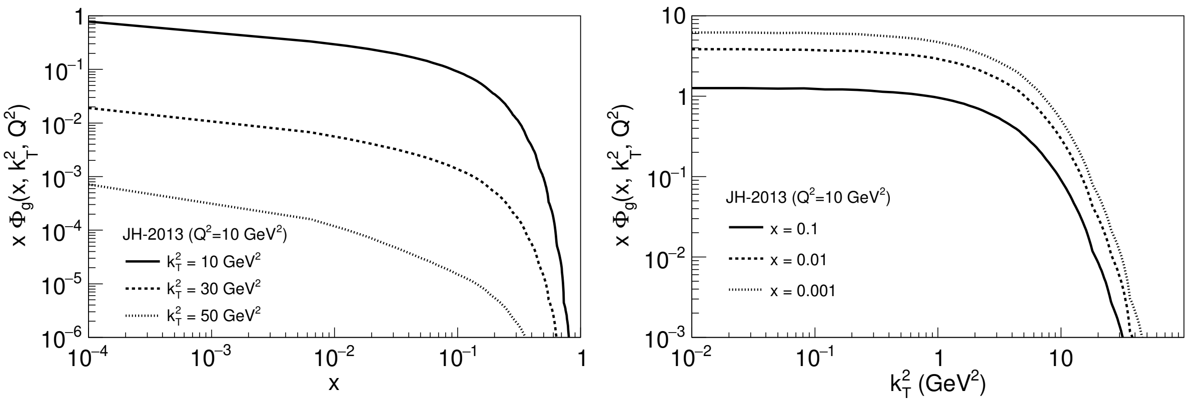

Figure 1.3. The momentum distribution, $x\Phi(x, k_T^2, Q^2)$, of gluons as a function of x (left) and k_T^2 (right) using the JH-2013 uPDF set 1 [19]. On the left plot, k_T^2 is set at 10 GeV^2 (solid), 30 GeV^2 (dashed), and 50 GeV^2 (dotted). On the right plot, x is set at 0.1 (solid), 0.01 (dashed), and 0.001 (dotted). On both plots, the interaction scale is set at $Q^2 = 10$ GeV^2.

1.4.2 Nuclear PDFs

The parton distributions of a bound nucleon inside a nucleus of mass number, A, is known as nuclear PDFs (nPDFs). In general, there are two ways to describe the mechanics of nPDFs. The first way is to write the nPDFs ($f_{i/A}(x, Q^2)$) as a product of the PDFs of a free proton (f_i^p) and the nuclear modification ($R_i(x, Q^2, A)$), presented in the form

$$f_{i/A}(x, Q^2, A) = R_i(x, Q^2, A) f_{i/p}(x, Q^2) \ . \tag{1.21}$$

Examples using this modification include the HKN [20], EPPS [21], and DSSZ [22] nuclear modifications. Another approach is to parameterize the nPDF as a function of A while using the free proton PDFs as a boundary condition:

$$f_{i/A}(x, Q^2) = f_{i/A}(x, Q^2, A) \ , \tag{1.22}$$

as used in the nCTEQ approach [23]. In either approach, the reason of using nPDFs for nuclear targets is that a bound proton inside a nucleus behaves different than a free proton. Thus, the nuclear modification, $R_i(x, Q^2, A)$, in either approach is not unity. Experimentally, this is measured by the ratio of the nuclear structure function to the deuteron structure function

$$R_i(x, Q^2, A) = \frac{F_{2A}(x, Q^2)/A}{F_{2d}(x, Q^2)/2} \ . \tag{1.23}$$

In the low x region ($x < 0.01$), the nuclear modification is less than 1. This is known as shadowing, mostly being interpreted as a result of combinations of partons from different nucleons when their momenta is small. At intermediate x values ($0.01 < x < 0.2$), there is an enhancement in the nPDFs, called antishadowing. At large$x$ values ($x > 0.2$), a depletion is a again observed. This region is also called the EMC region, first observed by the European Muon Collaboration [24]. As A increases, the nuclear modification becomes larger. The A dependence of the nuclear modification is shown in Fig. 1.4 using the central EPPS16 nuclear modification [21]. The nuclear modification for bound neutrons can be obtained using isospin symmetry. For example, the total up quark distribution per nucleon in a nucleus with mass and atomic number A and Z respectively is

$$\begin{aligned} f_{u/A}(x,Q^2) &= \frac{Z}{A}(R_{u_V}(x,Q^2,A)f_{u_V/p}(x,Q^2) + R_{u_s}(x,Q^2,A)f_{u_s/p}(x,Q^2)) \quad (1.24) \\ &+ \frac{A-Z}{A}(R_{d_V}(x,Q^2,A)f_{d_V/p}(x,Q^2) + R_{d_s}f_{d_s/p}(x,Q^2)) \quad (1.25) \end{aligned}$$

Using the nuclear modification, in a $p+A$ collision, the cross section of any given final state can be written as

$$\sigma = \sum_{i,j=q,\bar{q},g} \int dx_1 dx_2 \; f_{i/p}(x_1,\mu_F^2) f_{j/A}(x_2,\mu_F^2) \hat{\sigma}_{ij} \; . \quad (1.26)$$

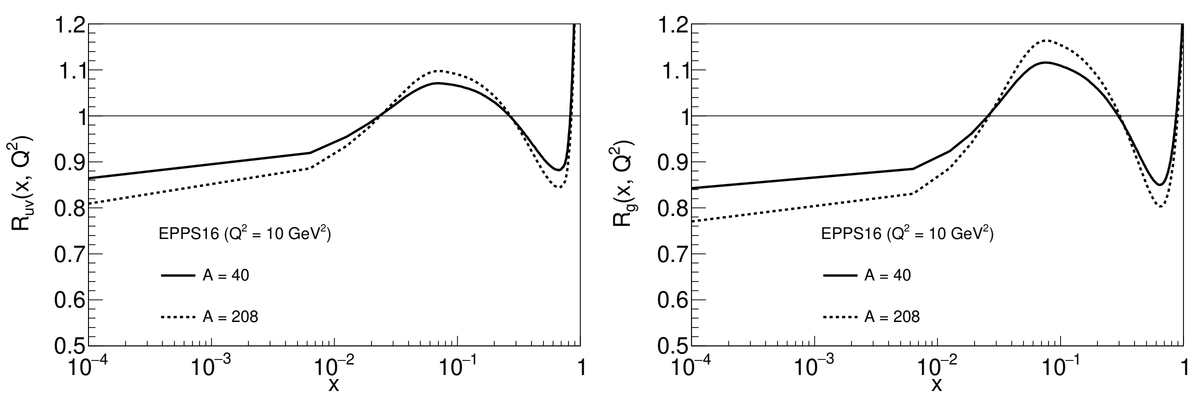

Figure 1.4. The nuclear modification, $R(x,Q^2,A)$, for valence up quarks (left) and gluons (right) for the central EPPS16 parameterization [21]. The modification is shown for $A = 40$ (solid) and $A = 208$ (dashed). The interaction scale is set at $Q^2 = 10$ GeV^2.

1.5 Hadrons

Since partons are subject to color confinement, they are not observed as free quarks, but rather as bound states, known as hadrons. Because the QCD scale, Λ_{QCD}, is about 200 MeV, this means partons must form hadrons on the confinement length scale of about 1 fm ($\hbar c \approx 197$ MeV fm). There are two types of hadrons: mesons and baryons. A meson is a bound state of a quark with an anti-quark. For example, a positively charged pion (π^+) is a bound state of an up quark (u) and an anti-down quark ($\bar{d}$). A baryon is a bound state of three quarks, and protons and neutrons are examples of baryons. The top quark, the most massive particle in the Standard Model, decays into W^+b. This is a fast process with a lifetime at the order of 10^{-25} s, which is much shorter than the strong interaction timescale. Thus, the top quark is the only quark that is too short-lived to form bound states. Quarks and anti-quarks exist inside hadrons because of the nature of the strong force. The strong force gets stronger when two colored objects are pulled apart. On the other hand, the strong force gets weaker when the length scale decreases. As a result, quarks and gluons are acting as free particles within the hadron. These behaviors are known as confinement and asymptotic freedom as the quarks and gluons are confined inside a hadron but are free within the hadron as the interaction gets asymptotically weaker with decreasing length scale.

1.6 Quarkonia

A meson consisting of a heavy quark and a heavy anti-quark is also known as a quarkonium ($\mathcal{Q}$). A quarkonium state consisting of a bound $c\bar{c}$ pair is known as charmonium, while one consisting of a bound $b\bar{b}$ pair is known as bottomonium. The second generation of quarks in the Standard Model was confirmed by the discovery of charmonium, bound by the inter-quark potential given as a function of inter-quark separation, r [25, 26]

$$V(r) \quad = \quad \sigma r - \frac{\alpha_c}{r} + V_{\mathrm{spin}} \, , \tag{1.27}$$

where the term linear in r refers to QCD confinement at long distance, the $1/r$ term refers to the Coulomb-like short distance behavior, and the third term is the spin-dependent potential including contributions from spin-orbit and spin-spin couplings. Bound state

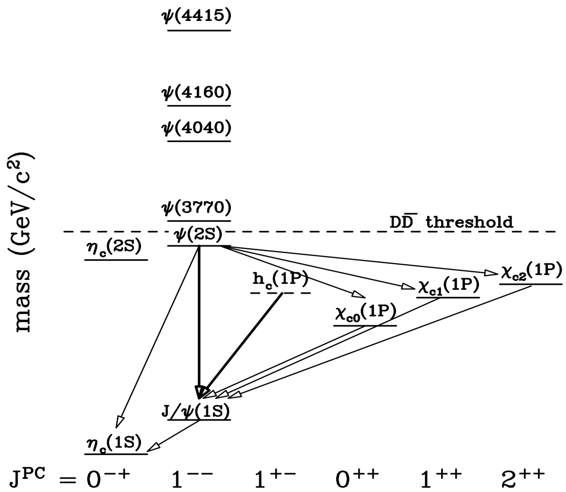

Figure 1.5. (Taken from Ref. [27]) The charmonium family. States are organized according to their spin states. From left to right: spin singlet with no orbital angular momentum (η), spin triplet with no orbital angular momentum (ψ), spin singlet with orbital angular momentum $1\hbar$ (h_c), and spin triplets with orbital angular momentum $1\hbar$ and a total angular momentum J (χ_{cJ}).

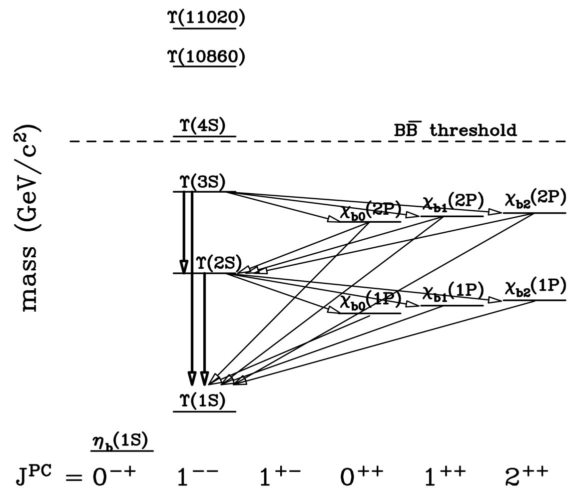

Figure 1.6. (Taken from Ref. [27]) The bottomonium family. States are organized according to their spin states. From left to right: spin singlet with no orbital angular momentum (η), spin triplet with no orbital angular momentum (Υ), and spin triplets with orbital angular momentum $1\hbar$ and a total angular momentum J (χ_{cJ}). The unconfirmed spin singlet with orbital angular momentum $1\hbar$ (h) states are not shown here.

solutions to the Schrödinger equation with the inter-quark potential in Eq. (1.27) are classified according to the quantum numbers such as spin (S) and orbital angular momentum (L). S is the vector sum of the spins of the quark and the antiquark. Since quarks and anti-quarks are spin $\frac{1}{2}$ particles, S can take either 0 or 1. L is the quantum number associated with the spatial symmetry of the angular distribution of the bound state wave function. It is common to sum these angular momenta to give the total angular momentum (J) so that each solution can be labeled in the spectroscopic notation, ${}^{2S+1}L_J$, which corresponds to an observable quarkonium state. Figures 1.5 and 1.6 shows the families of charmonium and bottomonium respectively.

A meson formed by a heavy quark (or anti-quark) and a light anti-quark (or quark), is commonly referred to as an open heavy flavor meson. A charm quark bound with a light anti-quark is referred to as a D meson while an anti-charm quark bound with a light quark is referred to as a $\overline{D}$ meson. Similarly, a bottom quark bound with a light anti-quark is

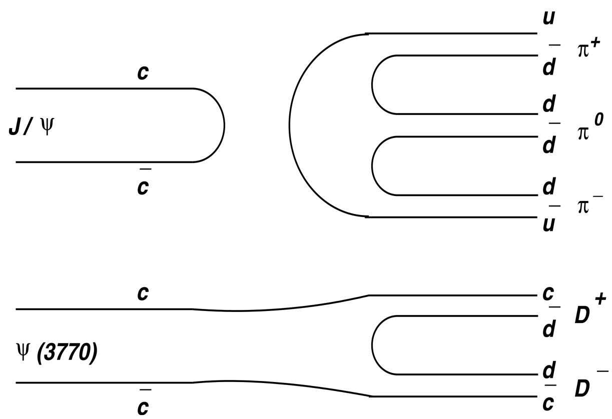

Figure 1.7. (Taken from Ref. [27]) Above: OZI suppressed hadronic decay of J/ψ into three pions. Below: OZI favored hadronic decay of $\psi(3770)$ into two D mesons.

referred to as a B meson and an anti-bottom quark bound with a light quark is called a $\overline{B}$ meson. The mass of a pair of open heavy flavor mesons, $2m_H$ (H=D, B), is known as the hadronic threshold. The mass of a D^0 meson with quark content $c\bar{u}$, has a mass of 1.86 GeV while the mass of a B^0 meson with quark content $\bar{b}d$, has a mass of 5.28 GeV. Thus, the hadronic threshold is $2m_D = 3.72$ GeV for charmonium and $2m_B = 10.56$ GeV for bottomonium.

Since the potential in Eq. (1.27) is infinite as $r \to \infty$, there are infinite number of quarkonium states. However, quarkonia whose masses are below the hadronic threshold decay electromagnetically and whose masses are above the hadronic threshold decay hadronically. This is because when the quarkonium mass is below this threshold, it is kinematically forbidden to decay hadronically into a pair of open heavy flavor mesons. In addition, three hard (high-energy) gluons have to be emitted for the quarkonium to decay hadronically to light mesons, and thus the decay is suppressed. On the other hand, when the quarkonium mass is above this threshold, it is kinematically allowed to decay hadronically into open charm mesons without annihilating the heavy flavor and thus the decay is favored. These phenomena were described by Okubo, Zweig, and Iizuka. Their observations are summarized by the OZI rule [28–30] , which states that in a decay if the quark lines are not connected between the initial states and the final states, it is suppressed. The inverse is also true; if the quark lines are connected between the initial states and the final states, the process is favored. The suppressed hadronic decay of J/ψ

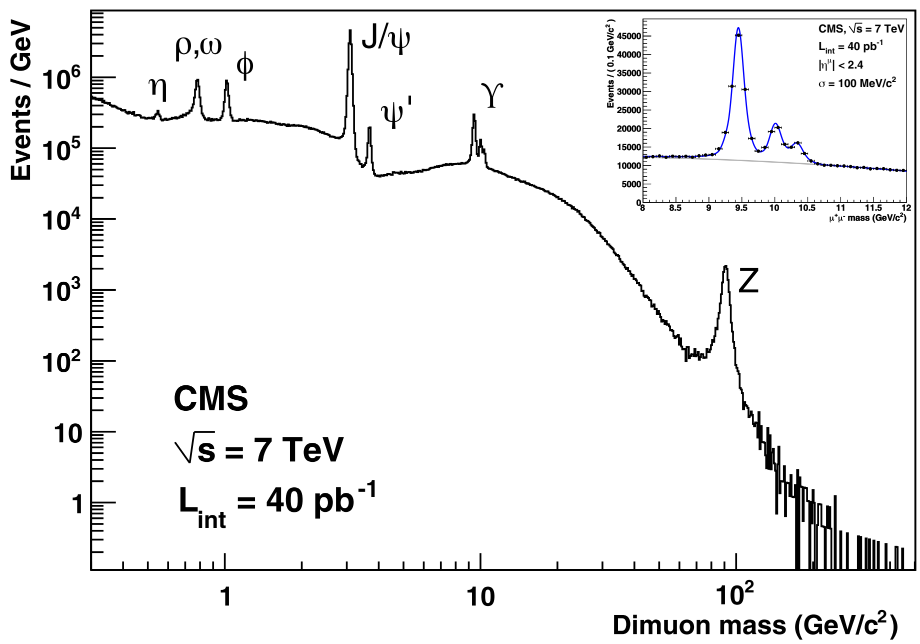

Figure 1.8. (Taken from Ref. [31]) : The invariant mass spectrum of dimuons measured at the CMS detector in $p + p$ collisions at $\sqrt{s} = 7$ TeV within the range $\eta \leq 1$. All neutral $J^{PC} = 1^{--}$ particles are shown as peaks in the spectrum. They include (from low mass to high mass): η, ρ and ω, ϕ, J/ψ, ψ', $\Upsilon(n\mathrm{S})$, and the Z boson. A zoom of the 8 to 12 GeV region showing the three $\Upsilon(n\mathrm{S})$ peaks is presented on the top right.

(with a mass of 3.10 GeV) into hadrons and the favored hadronic decay of $\psi(3770)$ are illustrated in Fig. 1.7.

Since the hadronic decay of quarkonia below the $H\overline{H}$ threshold is OZI suppressed, vector quarkonia (e.g. J/ψ) dominantly decay electromagnetically into $\ell^+\ell^-$ pairs. This gives a sharp peak in the dilepton mass spectrum when one reconstructs the pairs in any collider detector. For example, by reconstructing the $\mu^+\mu^-$ pairs, all neutral $J^{PC} = 1^{--}$ particles including the S state quarkonia are shown as peaks in the invariant mass spectrum of dimuons. The dimuon invariant mass spectrum obtained by the CMS Collaboration is shown in Fig. 1.8.

1.7 Quarkonium polarization

Since quarkonia may, in general, have a non-zero total angular momentum. If we consider a quarkonium having a total angular momeum of J, the angular momentum

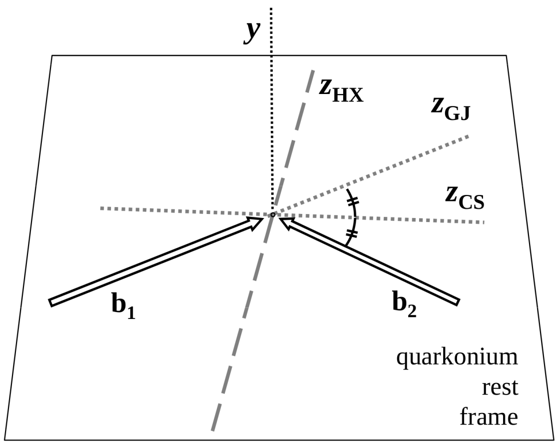

Figure 1.9. (Taken from Ref. [34]) The orientation of the polarization z-axis in the helicity (HX) frame, the Gottfried-Jackson (GJ) frame, and the Collins-Soper (CS) frame with respect to the directions of motion of the colliding beams (b_1, b_2). The quarkonium is produced in the same direction as the z_{HX}-axis.

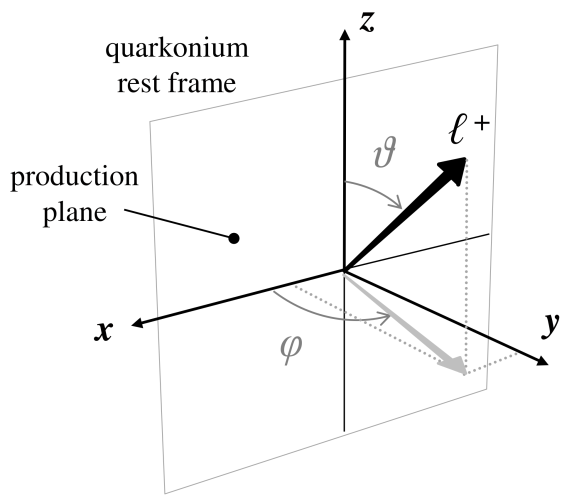

Figure 1.10. (Taken from Ref. [34]) The coordinate system used to measure the polarization experimentally. ϑ is measured from the polarization z-axis to the positively charged lepton from the decay. φ is measured from the polarization x-axis to the projection of the positively charged lepton onto the xy-plane.

state, when projected onto any z-axis, generally takes the form

$$|\psi\rangle \quad = \quad \sum_{J_z=-J}^{J} a_{J_z} \, |J, J_z\rangle \ , \tag{1.28}$$

where $a_{J_z} \in \mathbb{C}$ with $\sum_{J_z=-J}^{J} |a_{J_z}|^2 = 0$, and J_z is the z-component of the total angular momentum. The tendency of a quarkonium to be in a certain angular momentum projection state is known as the polarization. For example, an unpolarized $J = 1$ quarkonium production means an equal amount of $J_z = -1, 0, +1$ is produced and thus $|a_0|^2 = |a_{+1}|^2 = |a_{-1}|^2 = \frac{1}{3}$. There are commonly three choices (also known as frames) for the direction of the z-axis in the rest frame of the quarkonium. In the helicity (HX) frame, the z-axis is defined as the flight direction of the quarkonium itself. In the Gottfried-Jackson (GJ) frame [32], the z-axis is defined as the direction of the momentum of one of the two colliding beams. In the Collins-Soper (CS) frame [33], the z-axis is defined as the bisector of the angle between one beam and the opposite beam. The orientation of the three axes is shown in Fig. 1.9. Experimentally, the polarization of any S-state vector meson is obtained from its decay to l^+l^- pair by measuring the distribution of the angle between the z-axis and the direction the positively-charged lepton travels in the quarkonium rest frame. The angle is illustrated in Fig. 1.10. Conventionally, the y-axis is defined as the cross product of the colliding beam momenta, $\vec{P}_1$ and $\vec{P}_2$

$$\hat{y} = \frac{\vec{P}_1 \times \vec{P}_2}{|\vec{P}_1 \times \vec{P}_2|} . \tag{1.29}$$

The x-axis is then determined by the right-handed convention $\hat{x} = \hat{y} \times \hat{z}$.

Once a frame is chosen, the angular distribution of the production can be expanded in terms of the polarization parameters (λ_ϑ, λ_ϕ, and $\lambda_{\vartheta\phi}$) given by [34],

$$\frac{d\sigma}{d\Omega} \propto \frac{1}{3+\lambda_\vartheta}\left[1 + \lambda_\vartheta \cos^2\vartheta + \lambda_\varphi \sin^2\vartheta \cos(2\phi) + \lambda_{\vartheta\varphi} \sin(2\vartheta)\cos\phi\right] , \tag{1.30}$$

where ϑ and φ denote the angle polar and azimuthual angles respectively, λ_ϑ describes the polar anisotropy, λ_φ describes the azimuthual anisotropy, and $\lambda_{\vartheta\varphi}$ describes the polar-azimuthal correlation. The polarization parameters of the $J^{PC} = 1^{--}$ states (e.g J/ψ and $\Upsilon(n\mathrm{S})$) are related to the production polarized amplitudes a_{J_z} [34]

$$\lambda_\vartheta = \frac{1-3|a_0|^2}{1+a_0^2} , \tag{1.31}$$

$$\lambda_\varphi = \frac{2\,\mathrm{Re}[a_{+1}a_{-1}^*]}{1+a_0^2} , \tag{1.32}$$

$$\lambda_{\vartheta\varphi} = \frac{\sqrt{2}\,\mathrm{Re}[a_0^*(a_+ - a_-)]}{1+a_0^2} . \tag{1.33}$$

Therefore, when quarkonium production is equally distributed among $J_z = -1, 0, +1$ projection states, $\lambda_\vartheta = 0$ and thus the production is polarly symmetric. When the production only yields $J_z = \pm 1$, the production is said to be completely transverse, and $\lambda_\vartheta = +1$. When the production only yields $J_z = 0$, the production is said to be completely longitudinal, and $\lambda_\vartheta = -1$. In a single elementary process, there is no combination of a_{J_z}'s such that all polarization parameters are zero. Intrinsic isotropic production, where $\lambda_\vartheta = \lambda_\phi = \lambda_{\vartheta\phi} = 0$, either has to come from a mixture of subprocesses or randomization effects through modeling.

However, since the mixing of a_{J_z}'s changes upon any rotation, λ_ϑ in one frame can only describe such mixing in that particular frame. This means intrinsic transverse production,

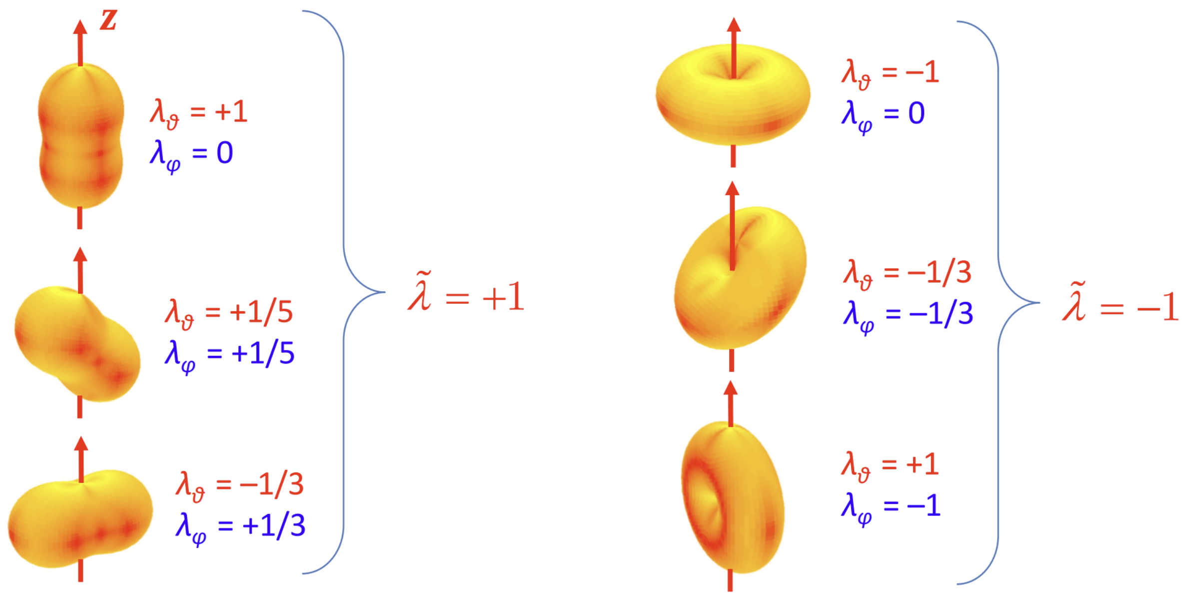

Figure 1.11. (Taken from Ref. [34]) Completely transverse angular distribution (left) and completely longitudinal angular distribution (right). The polarization axis is chosen to be the symmetry axis where there the distributions are azimuthally isotropic (top). The distributions are rotated such that azimuthal anisotropies are introduced (center). The distributions are rotated by 90° where more azimuthal anisotropies are introduced (bottom). Since the angular distributions are rotationally invariant, the invariant polarization parameter $\tilde{\lambda}$ reflects λ_ϑ in the frame where there is no azimuthal anisotropy.

when measured in a frame where the polarization axis is not perfectly aligned with the symmetry axis with no azimuthal anisotropy, will give λ_ϑ different than +1. Similarly, intrinsic longitudinal production in one frame, when measured in another frame, will give a non-zero λ_ϑ. These scenarios are illustrated in Fig. 1.11. However, the angular distribution itself is rotationally invariant. One of the combinations to form a rotationally invariant polarization parameter ($\tilde{\lambda}$) is [34]

$$\tilde{\lambda} = \frac{\lambda_\vartheta + 3\lambda_\varphi}{1 - \lambda_\varphi} . \tag{1.34}$$

Although there are more ways to construct rotationally invariant polarization parameters, the choice of $\tilde{\lambda}$ here will be the same as the polar anisotropy parameter (λ_ϑ) in a frame where the distribution is azimuthally isotropic ($\lambda_{\vartheta\phi} = 0$). Thus, considering also the frame-invariant polarization parameter, $\tilde{\lambda}$, can remove frame-induced kinematic dependencies when comparing theoretical predictions to data.

Measuring and predicting the polarization is important to understand the collider detector acceptance. This is because the kinematic acceptance of the detector for measuring quarkonium production depends on the quarkonium polarization [35]. As shown in Fig 1.12, the experimental acceptance in ATLAS varies if the J/ψ polarization is changed. Understanding the acceptance is important for correctly measuring the production cross section. When the polarization is unknown, one either has to assume the production is unpolarized or report the cross section for each polarization assumption. The former option is mostly adopted but the uncertainty in the acceptance will contribute to the systematic uncertainty of the measurement. Therefore, understanding the polarization can reduce the uncertainty in yield measurements.

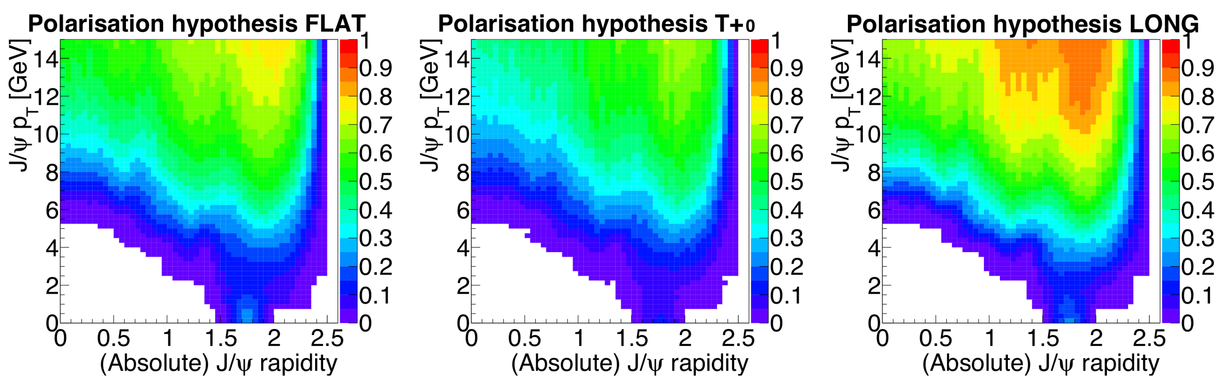

Figure 1.12. (Taken from Ref. [35]) The experimental acceptance assuming the J/ψ polarization is unpolarized (left), totally transverse (middle), and totally longitudinal (right).

1.8 Quarkonium production

The J/ψ was the first hadron containing charm quarks to be discovered. Before the discovery of J/ψ in 1974, the early version of the quark model only had three quarks, the down, up, and strange quarks. They were thought to be part of an SU(3) symmetry. Having 3 quarks in the model seemed promising as it neatly explained the multiplets of baryons and mesons formed by these quarks and their anti-quarks. Earlier in 1964, Bjorken and Glashow [36] suggested a fourth quark in the quark model to make it an SU(4) theory, which was later supported by Glashow, Iliopoulos, and Maiani [37]. This is because at that time, four leptons (e, ν_e, μ, and ν_μ) were discovered and the weak interaction between leptons and quarks would clearly require a fourth quark in the quark model to explain the absence of flavor-changing neutral currents. In November 1974, the J/ψ was discovered simultaneously at Brookhaven National Laboratory by a group led by Samuel Ting and at SLAC by Burton Richter's group [38, 39]. Richter and Ting were awarded the Nobel Prize in Physics in the same year.

In 1975, a new lepton, the tau lepton was discovered by Martin Perl [40]. The tau lepton also has its neutrino (ν_τ). These discoveries, again, made an imbalance between the number of leptons (six) and the number of quarks (four at that time). Soon in 1977, a meson with a mass of 9.5 GeV was discovered [41] and was quickly recognized as the bound state of the fifth quark, the bottom quark, and its anti-quark. The meson was named Υ.

1.8.1 Production channels

Quarkonia can be produced in many collision systems. Hadronic collisions, where hadrons collide with other hadrons, can be achieved at hadronic colliders such as $p+p$, $p+A$, $d+A$, and $A+A$ at the Relativistic Heavy-Ion Collider (RHIC), $p+\bar{p}$ at the Tevatron collider, and $p+p$, $p+A$, and $A+A$ at the Large Hadron Collider (LHC). Other collision systems include two-photon scattering achievable at the Large Electron-Positron Collider (LEP), hadron-electron (e^-A) collisions at HERA, and electron-positron (e^+e^-) collisions at KEKB.

Quarkonium production can be divided between prompt and non-prompt production. Take J/ψ production as an example, prompt production includes the direct production of the final quarkonium state (J/ψ) as well as feed-down from decays of higher quarkonium states (ψ(2S), χ_{c1}(1P), and χ_{c2}(2P)). Non-prompt production refers to the production of the final quarkonium state from decays of comparatively longer-lived B hadrons. Prompt and non-prompt production can be separated by reconstructing the decay products to the vertices of production. Non-prompt quarkonia are indicated by their displaced vertices because of the lifetime of B-hadrons. Since there is no top hadron, bottomonia are produced in prompt production only. The total cross section, obtained by summing the prompt and non-prompt cross sections, is also known as the inclusive cross section.

1.8.2 Production models

Although both J/ψ and Υ were discovered more than 40 years ago, the production mechanism is still not well understood. Specifically, how a heavy quark-antiquark pair hadronizes into a quarkonium state has not been figured out. Several models, including the color singlet model (CSM) [42, 43], nonrelativistic QCD (NRQCD) [44] and the color evaporation model (CEM) [45–48], have been proposed to predict the total yield, the transverse momentum (p_T) and the rapidity (y) distributions, and the polarization of quarkonium production in different particle collider machines. A brief timeline of quarkonia discoveries and the production models is shown in Fig. 1.13.

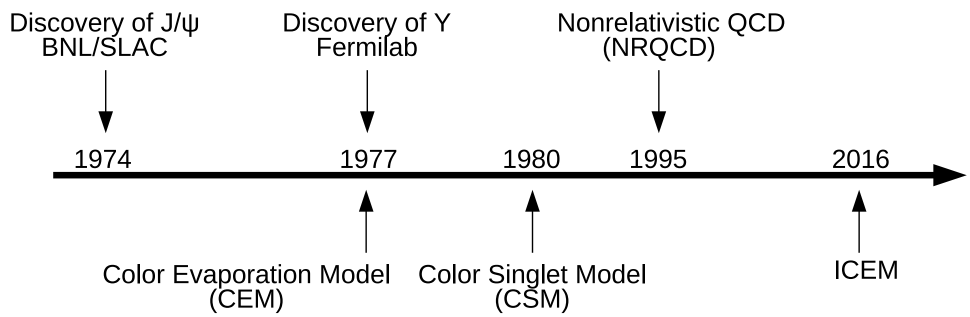

Figure 1.13. The timeline of quarkonia discoveries and the production models.

As quarkonia are bound states of $Q\overline{Q}$, they can either be produced in the color singlet state or one of the color octet states. Because of confinement, all observable hadrons are color singlets, even though they may have initially been produced as colored objects. Thus, the CSM considers the production of heavy quark-antiquark pairs in the color singlet state in the limit the heavy quark relative velocity is zero ($v \to 0$). It assumes the quantum state of the pair remains the same between production and its hadronization. In the CSM, the production cross section of an S state quarkonium, $\mathcal{Q}$, in hadronic collisions takes the form

$$\begin{aligned} d\sigma[\mathcal{Q}+X] &= \sum_{i,j}\int dx_i dx_j f_i(x_1,\mu_F) f_j(x_2,\mu_F) d\hat{\sigma}_{i+j\to(Q\overline{Q})+X}(\mu_R) \\ &\times \ |R(0)|^2 \,, \end{aligned} \tag{1.35}$$

where $f_i(x,\mu_F)$ is the parton distribution function (PDF) of the proton as a function of the fraction of momentum carried by the colliding hadron x at factorization scale μ_F and

$\hat{\sigma}_{i+j\to(Q\overline{Q})+X}(\mu_R)$ is the partonic cross section evaluated at the renormalization scale μ_R. The cross section is normalized by the squared wave function at the origin $|R(0)|^2$ for S states, and is normalized by the squared of the derivative $|R'(0)|^2$ for P states. However, the cross section in the CSM calculated at leading order ($\mathcal{O}(\alpha_s^3)$) underestimated the data at the Tevatron by more than an order of magnitude especially, at high p_T. Even calculations to next-to-leading order ($\mathcal{O}(\alpha_s^4)$) still underestimate the data by a factor of ten. The evaluation of the real correction at $\mathcal{O}(\alpha_s^5)$ (also known as NNLO*) [50] is shown to be able to fill most of the gap between the NLO calculation and the experimental results. These results are shown in Fig. 1.14.

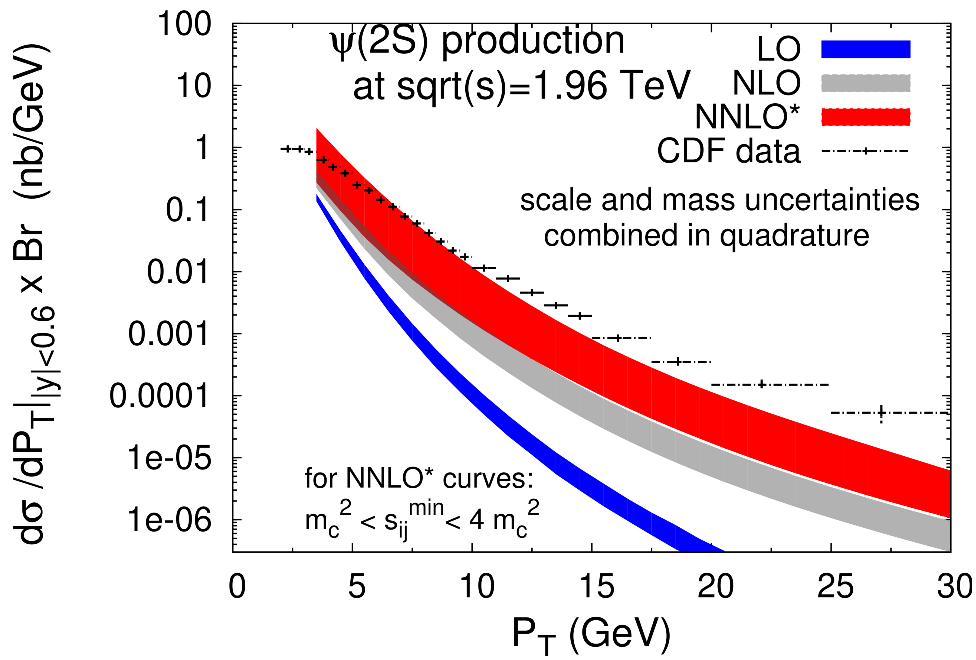

Figure 1.14. (Taken from Ref. [49]) The p_T-distributions of ψ(2S) in the CSM calculated at leading order (blue), next-to-leading order (gray), and partial next-to-next-leading order (red) compared to the data measured at CDF at $\sqrt{s} = 1.96$ TeV. The calculation in the CSM converges to the data as the significant contribution at NNLO* fills most of the gap between the data and the NLO results. See Ref. [50] for details.

Most recent studies of quarkonium production employ NRQCD which, in addition to the color singlet contribution of the CSM, includes the contribution from color octet states. NRQCD is an effective field theory where production is described as an expansion in powers of α_s and the heavy quark velocity, v. It separates the quarkonium production cross section into different color and spin states and further factorizes the short distance coefficients from the long distance matrix elements (LDMEs). In the NRQCD approach, the J/ψ production cross section is given by

$$\sigma_{J/\psi} = \sum_n \sigma_{c\bar{c}[n]} \langle \mathcal{O}^{J/\psi}[n] \rangle \; , \tag{1.36}$$

where $\sigma_{c\bar{c}[n]}$ are the cross sections in a particular color and spin state n calculated in perturbative QCD, $\langle \mathcal{O}^{J/\psi}[n] \rangle$ are the non-perturbative LDMEs that describe the conversion of $c\bar{c}[n]$ states into the final state J/ψ. The leading term in the sum in the limit $v \to 0$ is $n = {}^3S_1^{[1]}$, which corresponds to the contribution from the color singlet. Truncating the sum at this point reduces NRQCD to the CSM. The subleading terms are the corrections from the color octet states (${}^3P_J^{[8]}$,${}^3S_1^{[8]}$ and ${}^1S_0^{[8]}$), of relative order $\mathcal{O}(v^4)$. The LDMEs have to be obtained by fitting theoretical predictions to data, usually p_T distributions above some p_T cut. At each order of α_s, there will be four LDMEs in total, one for CS and three for CO contributions.

The universality of the mixing of LDMEs is tested in the first and only global analysis of NLO J/ψ production by photoproduction, two-photon scattering, and hadroproduction [51]. The analysis compares all available J/ψ data with a p_T cut of 1 GeV for photoproduction and two-photon scattering, and 3 GeV for hadroproduction. It shows that NRQCD is capable of describing most of the production data with a goodness of fit of $\chi^2_{\mathrm{d.o.f}} = 4.42$. A comparison to data of the NLO NRQCD global fit is shown in Fig. 1.15, where the gap between the data and the CSM results is filled by the contribution from CO states. However, using the same set of LDMEs from the global fit, NRQCD predicts a strong transverse polarization of the J/ψ [52], which differs significantly from the measured data shown in Fig. 1.16.

The production yields are not the only measurements that can test quarkonium production models. Spin-related measurements like the polarization are strong tests of production models; in this respect, the NRQCD LDMEs fail to describe both the yields and polarization simultaneously for p_T cuts less than twice the mass of the J/ψ. [53]. If one chooses a low p_T cut (3 GeV) to fit the LDMEs to the global yields, including those from $e^+ + e^-$ at HERA, $e + p$ at HERA, $p + p$ at ATLAS and $p + \bar{p}$ at CDF, NRQCD will

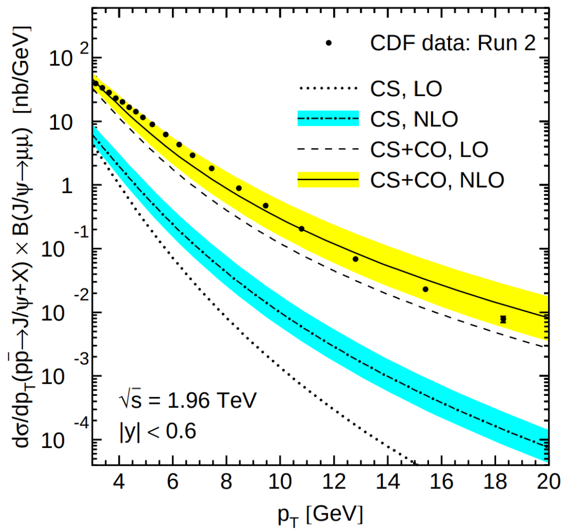

Figure 1.15. (Taken from Ref. [51]) The J/ψ cross section measured at $\sqrt{s}$ = 1.96 TeV at CDF compared to the NLO NRQCD global fit results. The contributions from LO CSM (dotted), NLO CSM (cyan, dot-dashed), LO NRQCD (dashed), and NLO NRQCD (yellow, solid) are shown.

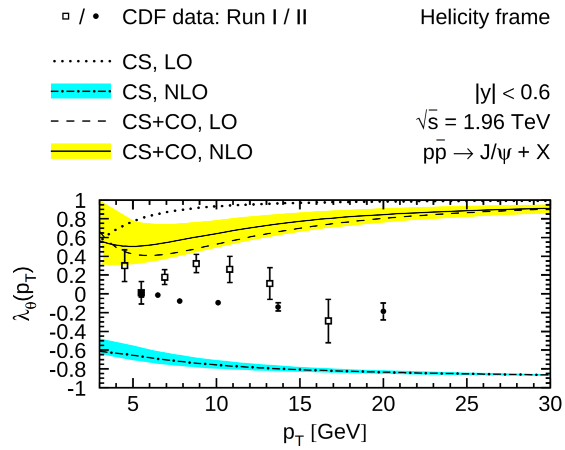

Figure 1.16. (Taken from Ref. [52]) The polarization parameter, λ_ϑ, measured at $\sqrt{s}$ = 1.96 TeV compared to the NLO NRQCD global fit results. Both Run I (empty boxes) and Run II (solid circles) are shown. The calculated results from LO CSM (dotted), NLO CSM (cyan, dot-dashed), LO NRQCD (dashed), and NLO NRQCD (yellow, solid) are shown.

completely disagree with the polarization data observed in the $p + \bar{p}$ collisions at CDF. If the LDMEs are only fitted to data from the hadronic production with a higher p_T cut (5 GeV), NRQCD can describe the polarization better at the expense of overshooting production data from other experiments. If the LDMEs are also fitted with the polarization data with an even higher p_T cut (7 GeV), NRQCD will overshoot the production data elsewhere even more. These NRQCD predictions to the J/ψ production and polarization are shown in Fig. 1.17.

The CEM, which considers all heavy quark-antiquark pair production, regardless of the quarks' color, spin, and momentum, is also able to predict the total yields and the distributions. The CEM restricts the invariant mass of the heavy quark-antiquark pair to be less than twice the mass of the lowest mass meson that can be formed with the heavy quark as a constituent. Since the color is averaged over, there are fewer parameters to be fitted to the data than NRQCD. The CEM has so far only been used to predict spin-averaged quarkonium production: the polarization was not considered before.

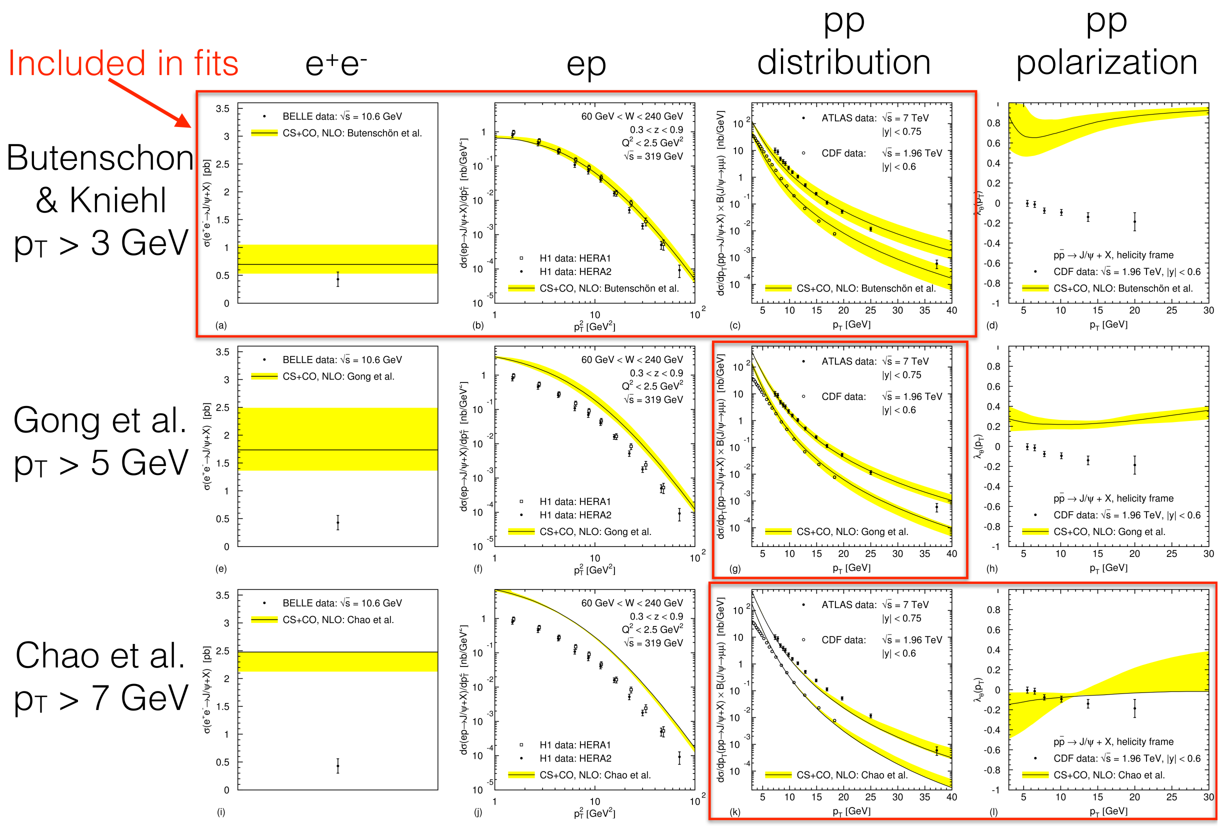

Figure 1.17. (Modified from Ref. [53]) (From left to right) NRQCD predictions of the total J/ψ cross section compared to data measured at BELLE at $\sqrt{s}$ = 10.6 GeV, the transverse momentum distribution in photoproduction compared to data measured at H1 at $\sqrt{s}$ = 319 GeV, and in hadroproduction compared to data measured at CDF and ATLAS at $\sqrt{s}$ = 1.96 and 7 TeV respectively, and the polarization parameter compared to data measured at CDF in Tevatron Run II. (From top to bottom) The predictions of NRQCD in a global fit [51], a hadroproduction-only fit [54], and a fit including polarization [55].

In a $p+p$ collision, at leading order, the production cross section for a quarkonium state $\mathcal{Q}$ in the CEM is given by

$$\sigma \;=\; F_{\mathcal{Q}} \sum_{i,j} \int_{4m_{\mathcal{Q}}^2}^{4m_H^2} d\hat{s} \int dx_1 dx_2 f_{i/p}(x_1,\mu^2) f_{j/p}(x_2,\mu^2) \hat{\sigma}_{ij}(\hat{s}) \delta(\hat{s} - x_1 x_2 s) \;, \quad (1.37)$$

where i and j are q, $\overline{q}$ and g such that $ij = q\overline{q}$ or gg. The square of the heavy quark pair invariant mass is $\hat{s}$ while the square of the center-of-mass energy in the $p+p$ collision is s. Here, $F_{\mathcal{Q}}$ is a universal factor for the quarkonium state and is independent of the projectile, target, and energy. $F_{\mathcal{Q}}$ is fixed by comparison of the next-leading-order (NLO) calcultion of $\sigma_{\mathcal{Q}}^{\rm CEM}$ to J/ψ and Υ.

In the traditional CEM, the relative production of one state to the other is a constant. For example, the relative production of $\psi(2\mathrm{S})$ to J/ψ. In attempt to describe the relative production, an improved version of the CEM, the improved CEM (ICEM) [56] was developed. In the ICEM, the lower limit is changed from the production threshold to the mass of the quarkonia. A distinction is also made between the momentum of the $c\bar{c}$ pair and that of charmonium so that the p_T spectra will be softer and thus may explain the high p_T data better. The production cross section in the ICEM is given by

$$\sigma = F_{\mathcal{Q}} \sum_{i,j} \int_{M_\psi}^{2m_H} dM \int dx_i dx_j f_i(x_i, \mu_F) f_j(x_j, \mu_F) d\hat{\sigma}_{ij \to c\bar{c}+X}(p_{c\bar{c}}, \mu_R)|_{p_{c\bar{c}}=\frac{m}{M_\psi}p_\psi} \quad (1.38)$$

With these changes, the ICEM is then able to describe the production cross section ratio of $\psi(2\mathrm{S})$ to J/ψ as a function of p_T, whereas, in the traditional CEM, the fraction is a constant.

Since quarkonium polarization is a relative measure, in the ICEM, the polarization is inherently independent of $F_{\mathcal{Q}}$. We take full advantage of this fact since the CEM is already shown to be able to describe the production yields and distributions. The goal of this study is to describe the polarization using the ICEM.

1.9 Organization

The remainder of this dissertation is composed of published papers in Physical Review D and a manuscript to be submitted. It is organized as follows:

Chapter 2 presents published results [57] from the first spin-dependent calculation in the CEM using the leading order matrix elements in the collinear factorization approach. It includes all the partonic subprocesses at $\mathcal{O}(\alpha_s^2)$ to calculate the relative production $\sigma^{J_z=0}/\sigma^{\mathrm{tot.}}$. This is a proof of concept that the CEM can be used to calculate spin-dependent observables.

Chapter 3 [58] is a continuation of the previous calculation by further extracting the $J = 1$ (for S and χ_1 P states) and the $J = 2$ (for χ_2 P states) components from the total production cross section. The ICEM is used to distinguish one state from another. Feed-down production is also included so that the polarization of the directly produced as well as the promptly produced states can be calculated.

Chapter 4 presents published results [59] from the first p_T-dependent J/ψ polarization calculation in the ICEM using the k_T-factorization approach. Bringing p_T dependence to the calculation allows us to compare to all of the polarization data in hadronic production. We demonstrate that the ICEM can describe the p_T-distributions and the rapidity distributions of the production, and the relative production of χ_{c1} and χ_{c2} along with the polarization.

Chapter 5 [60] is a direct application of the previous calculation to bottomonium. We again show the polarization, the p_T-distributions and the rapidity distributions, and the relative production of χ_{b1} and χ_{b2}. We find the polarization of $\Upsilon(n\mathrm{S})$ in the ICEM agrees with the unpolarized measurements.

Chapter 6 is a manuscript to be submitted. This is the first p_T-dependent J/ψ polarization calculation in the ICEM using the collinear factorization approach. It presents the polarization of direct J/ψ calculated at $\mathcal{O}(\alpha_s^3)$ including all anisotropy parameters of the production as well as the frame-invariant polarization parameter, $\tilde{\lambda}$. We find the invariant polarization of direct J/ψ agrees with the experimental results.

Chapter 7 contains brief closing remarks regarding future prospects with the ICEM.

Chapter 2

Polarized Heavy Quarkonium Production in the Color Evaporation Model

Polarized Heavy Quarkonium Production in the Color Evaporation Model

V. Cheung[a] and R. Vogt[a,b,1]

[a]Department of Physics

University of California, Davis

Davis, CA 95616, USA

and

[b]Nuclear and Chemical Sciences Division

Lawrence Livermore National Laboratory

Livermore, CA 94551, USA

ABSTRACT

We explore polarized heavy quarkonium production using the color evaporation model at leading order. We present the polarized to total yield ratio as a function of center of mass energy and rapidity in $p+p$ collisions. At energies far above the $Q\overline{Q}$ production threshold, we find charmonium and bottomonium production to be longitudinally polarized ($J_z = 0$). The quarkonium states are also longitudinally polarized at central rapidity, becoming transversely polarized ($J_z = \pm 1$) at the most forward rapidities.

[1]This work was performed under the auspices of the U.S. Department of Energy by Lawrence Livermore National Laboratory under Contract DE-AC52-07NA27344 and supported by the U.S. Department of Energy, Office of Science, Office of Nuclear Physics (Nuclear Theory) under contract number DE-SC-0004014.

2.1 Introduction

Even more than 40 years after the discovery of J/ψ, the production mechanism of quarkonium is still not well understood. Most recent studies of quarkonium production employ nonrelativistic QCD (NRQCD) [61], which is based on an expansion of the cross section in the strong coupling constant and the $Q\overline{Q}$ velocity [44]. The cross section is factorized into hard and soft contributions and divided into different color and spin states. Each color state carries a weight, the long distance matrix elements (LDMEs) that are typically adjusted to the data above some minimum transverse momentum, p_T, value. The NRQCD cross section has been calculated up to next-to-leading order (NLO). The LDMEs, conjectured to be universal, fail to describe both the yields and polarization simultaneously for p_T cuts less than twice the mass of the quarkonium state. The polarization is sensitive to the p_T cut: the cut $p_T > 10$ GeV was chosen to describe both the yield and polarization in Ref. [62] while $p_T > 3m$ was chosen for the excited states $\psi(2S)$ and $\Upsilon(3S)$ in Ref. [63] to fit the polarization. The universality of the LDMEs can be tested by using those obtained at high p_T to calculate the p_T-integrated cross section. In Ref. [64], the p_T-integrated NRQCD cross section is calculated with LDMEs obtained with p_T cuts in the range $3 < p_T < 10$ GeV. The resulting midrapidity cross sections, $d\sigma/dy|_{y=0}$, systematically overshoot the J/ψ data. The lowest p_T cut is most compatible with $d\sigma/dy|_{y=0}$ while calculations based on higher p_T cuts can be up to an order of magnitude away from the data [64]. More recent analysis has shown that the η_c p_T distributions calculated with LDMEs obtained from J/ψ yields using heavy quark spin symmetry [65–67], overshoots the high p_T LHCb η_c results [68].

The Color Evaporation Model (CEM) [56, 69–71], which considers all $Q\overline{Q}$ ($Q = c$, b) production regardless of the quarks' color, spin, and momentum, is able to predict both the total yields and the rapidity distributions with only a single normalization parameter [72]. The CEM has so far only been used to predict spin-averaged quarkonium production: the polarization was not considered before. This paper presents a leading order (LO) calculation of quarkonium polarization in the CEM, a p_T-integrated result. Currently, there are no exclusive NLO polarized $Q\overline{Q}$ calculations on which to impose the $H\overline{H}$ (H

$= D$, B) mass threshold. Our calculation is a first step toward a full CEM polarization result that provides a general idea of whether there is any appreciable LO polarization that might carry through to the next order even though the kinematics are different. We will begin to address the p_T dependence in a further publication.

In the CEM, all quarkonium states are treated the same as $Q\overline{Q}$ below the $H\overline{H}$ threshold where the invariant mass of the heavy quark pair is restricted to be less than twice the mass of the lowest mass meson that can be formed with the heavy quark as a constituent. The distributions for all quarkonium family members are assumed to be identical. (See Ref. [56] for a new treatment of the CEM p_T distributions based on mass-dependent thresholds.) In a $p + p$ collision, the production cross section for a quarkonium state is given by

$$\sigma = F_Q \sum_{i,j} \int_{4m_Q^2}^{4m_H^2} d\hat{s} \int dx_1 dx_2 f_{i/p}(x_1, \mu^2) f_{j/p}(x_2, \mu^2) \hat{\sigma}_{ij}(\hat{s}) \delta(\hat{s} - x_1 x_2 s) \ , \quad (2.1)$$

where i and j are q, $\overline{q}$ and g such that $ij = q\overline{q}$ or gg. The square of the heavy quark pair invariant mass is $\hat{s}$ while the square of the center-of-mass energy in the $p+p$ collision is s. Here $f_{i/p}(x, \mu^2)$ is the parton distribution function (PDF) of the proton as a function of the fraction of momentum carried by the colliding parton x at factorization scale μ and $\hat{\sigma}_{ij}$ is the parton-level cross section. Finally, F_Q is a universal factor for the quarkonium state and is independent of the projectile, target, and energy. At leading order, the rapidity distribution, $d\sigma/dy$, is

$$\begin{aligned} \frac{d\sigma}{dy} = {} & F_Q \int_{4m_Q^2}^{4m_H^2} \frac{d\hat{s}}{s} \Big\{ f_{g/p}(x_1, \mu^2) f_{g/p}(x_2, \mu^2) \hat{\sigma}_{gg}(\hat{s}) + \sum_{q=u,d,s} [f_{q/p}(x_1, \mu^2) f_{\overline{q}/p}(x_2, \mu^2) \\ & + f_{\overline{q}/p}(x_1, \mu^2) f_{q/p}(x_2, \mu^2)] \hat{\sigma}_{q\overline{q}}(\hat{s}) \Big\} \ , \end{aligned} \quad (2.2)$$

where $x_{1,2} = (\sqrt{\hat{s}/s}) \exp(\pm y)$. We take the square of the factorization and renormalization scales to be $\mu^2 = \hat{s}$.

2.2 Polarized $Q\overline{Q}$ production at the parton level

At the parton level, the leading order calculation forces the final state $Q\overline{Q}$ pair to be produced back-to-back with zero total transverse momentum. We define the polarization

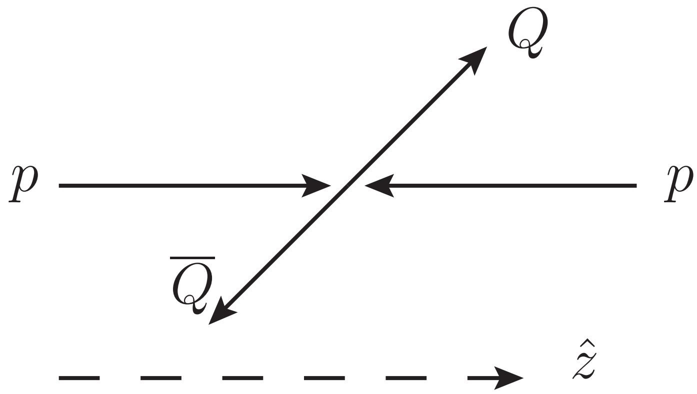

Figure 2.1. Orientation of z-axis indicated by the dashed arrowed line. Two proton arrows indicate the incoming beam directions. If the final state heavy quark-antiquark pair have the same helicity, then the total angular momentum along the z-axis, J_z, is 0 while if they have opposite helicity, then $J_z = \pm 1$.

of the $Q\overline{Q}$ pair to be either transversely polarized ($J_z = \pm 1$) or longitudinally polarized ($J_z = 0$) in the helicity frame where the z axis is pointing from $\overline{Q}$ to Q along the beam axis as shown in Fig. 2.1. Note that we are not distinguishing the $S = 1$ triplet state from the $S = 0$ singlet state. This will be addressed in a future publication, together with the separation into orbital angular momentum, L, states.

At leading order, there are four Feynman diagrams to consider, one for $q\overline{q}$ annihilation and three for gg fusion. Each diagram includes a color factor C and a scattering amplitude $\mathcal{A}$. The generic matrix element for each process is [73]

$$\mathcal{M}_{qq} = C_{qq}\mathcal{A}_{qq} , \tag{2.3}$$

$$\mathcal{M}_{gg} = C_{gg,\hat{s}}\mathcal{A}_{gg,\hat{s}} + C_{gg,\hat{t}}\mathcal{A}_{gg,\hat{t}} + C_{gg,\hat{u}}\mathcal{A}_{gg,\hat{u}} . \tag{2.4}$$

As previously mentioned, there is one diagram only for $q\overline{q} \to Q\overline{Q}$, thus a single amplitude, $\mathcal{A}_{qq}$. However, there are three diagrams for $gg \to Q\overline{Q}$ at leading order, the $\hat{s}$,

$\hat{t}$ and $\hat{u}$ channels. In terms of the Dirac spinors u and v, the individual amplitudes are

$$\mathcal{A}_{qq} = \frac{g_s^2}{\hat{s}}[\overline{u}(p')\gamma_\mu v(p)][\overline{v}(k)\gamma^\mu u(k')] \ , \tag{2.5}$$

$$\begin{aligned}\mathcal{A}_{gg,\hat{s}} &= -\frac{g_s^2}{\hat{s}}\Big\{ - 2k'\cdot\epsilon(k)[\overline{u}(p')\not{\epsilon}(k')v(p)] \\ &+ 2k\cdot\epsilon(k')[\overline{u}(p')\not{\epsilon}(k)v(p)] + \epsilon(k)\cdot\epsilon(k')[\overline{u}(p')(\not{k}' - \not{k})v(p)]\Big\} \ ,\end{aligned} \tag{2.6}$$

$$\mathcal{A}_{gg,\hat{t}} = -\frac{g_s^2}{\hat{t} - M^2}\overline{u}(p')\not{\epsilon}(k')(\not{k} - \not{p} + M)\not{\epsilon}(k)v(p) \ , \tag{2.7}$$

$$\mathcal{A}_{gg,\hat{u}} = -\frac{g_s^2}{\hat{u} - M^2}\overline{u}(p')\not{\epsilon}(k)(\not{k}' - \not{p} + M)\not{\epsilon}(k')v(p) \ . \tag{2.8}$$

Here g_s is the gauge coupling, M is the mass of heavy quark (m_c for charm and m_b for bottom), ϵ represents the gluon polarization vectors, γ^μ are the gamma matrices, k' (k) is the momentum of initial state light quark (antiquark) or gluon, and p' (p) is the momentum of final sate heavy quark (antiquark).

The amplitudes are separated according to the J_z of the final state, $J_z = 0$ or $J_z = \pm 1$. The total amplitudes are calculated for each final state J_z while averaging over the polarization of the initial gluons or the spin of the light quarks, depending on the process, in the spirit of the CEM.

The squared matrix elements, $|\mathcal{M}|^2$, are calculated for each J_z. The color factors, C, are calculated from the SU(3) color algebra and are independent of the polarization [73]. They are

$$\begin{aligned}|C_{qq}|^2 &= 2 \ , \\ |C_{gg,\hat{s}}|^2 &= 12 \ , \\ |C_{gg,\hat{t}}|^2 &= \frac{16}{3} \ , \\ |C_{gg,\hat{u}}|^2 &= \frac{16}{3} \ , \\ C^*_{gg,\hat{s}}C_{gg,\hat{t}} &= +6 \ , \\ C^*_{gg,\hat{s}}C_{gg,\hat{u}} &= -6 \ , \\ C^*_{gg,\hat{t}}C_{gg,\hat{u}} &= -\frac{2}{3} \ .\end{aligned} \tag{2.9}$$

The total squared amplitudes for a given J_z state,

$$|\mathcal{M}^{J_z}_{qq}|^2 = |C_{qq}|^2|\mathcal{A}_{qq}|^2 , \tag{2.10}$$

$$\begin{aligned} |\mathcal{M}^{J_z}_{gg}|^2 &= |C_{gg,\hat{s}}|^2|\mathcal{A}_{gg,\hat{s}}|^2 + |C_{gg,\hat{t}}|^2|\mathcal{A}_{gg,\hat{t}}|^2 + |C_{gg,\hat{u}}|^2|\mathcal{A}_{gg,\hat{u}}|^2 + 2C^*_{gg,\hat{s}}C_{gg,\hat{t}}\mathcal{A}^*_{gg,\hat{s}}\mathcal{A}_{gg,\hat{t}} \\ &+ 2C^*_{gg,\hat{s}}C_{gg,\hat{u}}\mathcal{A}^*_{gg,\hat{s}}\mathcal{A}_{gg,\hat{u}} + 2C^*_{gg,\hat{t}}C_{gg,\hat{u}}\mathcal{A}^*_{gg,\hat{t}}\mathcal{A}_{gg,\hat{u}} , \end{aligned} \tag{2.11}$$

are then used to obtain the partonic cross sections by integrating over solid angle:

$$\hat{\sigma}^{J_z}_{ij} = \int d\Omega \Big(\frac{1}{8\pi}\Big)^2 \frac{|\mathcal{M}^{J_z}_{ij}|^2}{\hat{s}} \sqrt{1 - \frac{4M^2}{\hat{s}}} . \tag{2.12}$$

The individual partonic cross sections for the longintudinal and transverse polarizations are

$$\hat{\sigma}^{J_z=0}_{q\overline{q}}(\hat{s}) = \frac{16\pi\alpha_s^2}{27\hat{s}^2} M^2\chi , \tag{2.13}$$

$$\hat{\sigma}^{J_z=\pm1}_{q\overline{q}}(\hat{s}) = \frac{4\pi\alpha_s^2}{27\hat{s}^2} \hat{s}\chi , \tag{2.14}$$

$$\begin{aligned} \hat{\sigma}^{J_z=0}_{gg}(\hat{s}) &= \frac{\pi\alpha_s^2}{12\hat{s}} \Big[\Big(4 - \frac{31M^2}{\hat{s}} + \frac{33M^2}{\hat{s}-4M^2}\Big)\chi \\ &+ \Big(\frac{4M^4}{\hat{s}^2} + \frac{31M^2}{2\hat{s}} - \frac{33M^2}{2(\hat{s}-4M^2)}\Big) \ln\frac{1+\chi}{1-\chi}\Big] , \end{aligned} \tag{2.15}$$

$$\begin{aligned} \hat{\sigma}^{J_z=\pm1}_{gg}(\hat{s}) &= \frac{\pi\alpha_s^2}{24\hat{s}} \Big[-11\Big(1 + \frac{3M^2}{\hat{s}-4M^2}\Big)\chi \\ &+ \Big(4 + \frac{M^2}{2\hat{s}} + 33\frac{M^2}{2(\hat{s}-4M^2)}\Big) \ln\frac{1+\chi}{1-\chi}\Big] , \end{aligned} \tag{2.16}$$

where $\chi = \sqrt{1 - 4M^2/\hat{s}}$. The sum of these results, $\hat{\sigma}^{J_z=0}_{ij} + \hat{\sigma}^{J_z=+1}_{ij} + \hat{\sigma}^{J_z=-1}_{ij}$, is equal to the total partonic cross section [74]:

$$\hat{\sigma}^{\text{tot.}}_{q\overline{q}}(\hat{s}) = \frac{8\pi\alpha_s^2}{27\hat{s}^2}(\hat{s} + 2M^2)\chi , \tag{2.17}$$

$$\hat{\sigma}^{\text{tot.}}_{gg}(\hat{s}) = \frac{\pi\alpha_s^2}{3\hat{s}} \Big[-\Big(7 + \frac{31M^2}{\hat{s}}\Big)\frac{1}{4}\chi + \Big(1 + \frac{4M^2}{\hat{s}} + \frac{M^4}{\hat{s}^2}\Big) \ln\frac{1+\chi}{1-\chi}\Big] . \tag{2.18}$$

Having computed the polarized $Q\overline{Q}$ production cross section at the parton level, we then convolute the partonic cross sections with the parton distribution functions (PDFs) to obtain the hadron-level cross section σ as a function of $\sqrt{s}$ using Eq. (2.1), and the rapidity distribution, $d\sigma/dy$, using Eq. (2.2). We employ the CTEQ6L1 [75] PDFs in this calculation and the running coupling constant $\alpha_s = g_s^2/(4\pi)$ is calculated at the one-loop level appropriate for the PDFs. We assume that the polarization is unchanged by the transition from the parton level to the hadron level, consistent with the CEM that the linear momentum is unchanged by hadronization. This is similar to the assumption made in NRQCD that once a $c\bar{c}$ is produced in a given spin state, it retains that spin state when it becomes a J/ψ.

2.3 Results

Since this is a LO calculation, we can only calculate the CEM polarization as a function of $\sqrt{s}$ and y but not p_T which will require us to go to NLO. However, the charm rapidity distribution at LO is similar to that at NLO [76]. The same is true for J/ψ production in the CEM. The only difference would be a rescaling of the parameter F_Q based on the ratio NLO/LO using the NLO scale determined in Nelson *et al.* [72]. The CEM results are in rather good agreement with the data from $p + p$ collisions [72].

We present the results as ratios of the cross section with $J_z = 0$ to the total cross section. Taking the ratio has the benefit of being independent of F_Q. In the remainder of this section, we discuss the energy dependence of the total cross section ratios for both charmonium and bottomonium (in the general sense as being in the mass range below the $H\overline{H}$ threshold) as well as for $c\bar{c}$ and $b\bar{b}$, integrated over all invariant mass. We show the ratios for charmonium and bottomonium production as a function of rapidity for selected energies. Finally, we discuss the sensitivity of our results to the choice of proton parton densities.

2.3.1 Energy dependence of the longitudinal polarization fraction

In this section, we compare the energy dependence of the fraction $\sigma^{J_z=0}/\sigma^{\text{tot.}}$ as a function of center of mass energy in $p + p$ collisions in Figs. 2.2 and 2.3. In the case of quarkonium, the integration in Eq. (2.1) is from twice the quark mass to twice the mass of the lowest lying open heavy flavor hadron. For open heavy flavor, the upper limit of the integral is extended to $\sqrt{s}$.

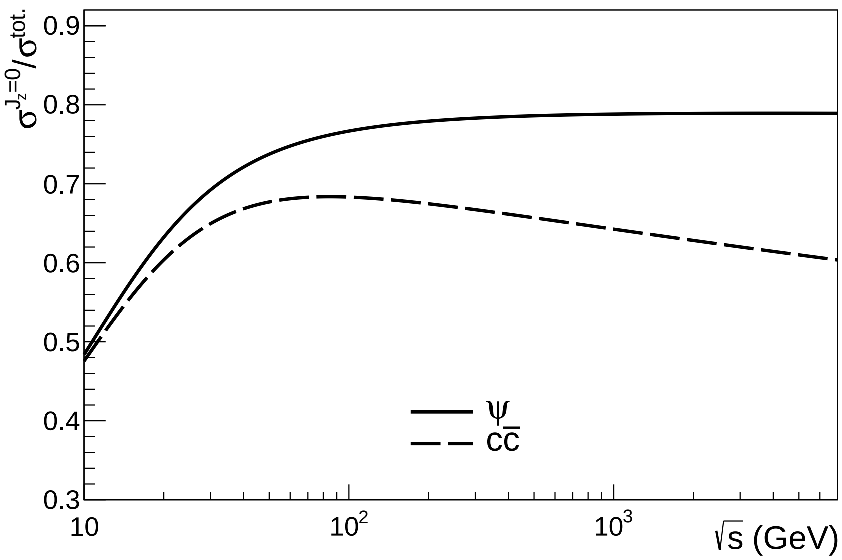

Figure 2.2. The energy dependence of the longitudinal fraction for production of charmonium (solid) and $c\bar{c}$ (dashed).

2.3.1.1 Charmonium and $c\bar{c}$

In Fig. 2.2 the charmonium production cross section is calculated by integrating the invariant mass of the $c\bar{c}$ pair from $2m_c$ ($m_c = 1.27$ GeV) to $2m_{D^0}$ ($m_{D^0} = 1.86$ GeV) in Eq. (2.1). We see that ψ production (solid curve in Fig. 2.2) is more than 50% longitudinally polarized for $\sqrt{s} > 10$ GeV. At $\sqrt{s} > 100$ GeV, the production ratio saturates at a longitudinal polarization fraction of 0.80.

The behavior of the total $c\bar{c}$ production fraction (dashed curve in Fig. 2.2) is quite different. Instead of saturating, like the charmonium ratio, it reaches a peak of 0.68 at $\sqrt{s} = 84$ GeV and then begins decreasing. This is because of the approximate helicity conservation at the parton level for $M/\sqrt{\hat{s}} \ll 1$. The narrow integration range of charmonium production assures that charmonium production never enters this region, keeping charmonium longitudinally polarized.

2.3.1.2 Bottomonium and $b\bar{b}$

The results for bottomonium and $b\bar{b}$ production are shown in Fig. 2.3. Here, the integral over the pair invariant mass is assumed to be from $2m_b$ ($m_b = 4.75$ GeV) to $2m_{B^0}$ ($m_{B^0} = 5.28$ GeV). For the more massive bottom quarks, the pairs start out transversely polarized for $\sqrt{s} < 40$ GeV. Bottomonium production becomes dominated by longitudinal

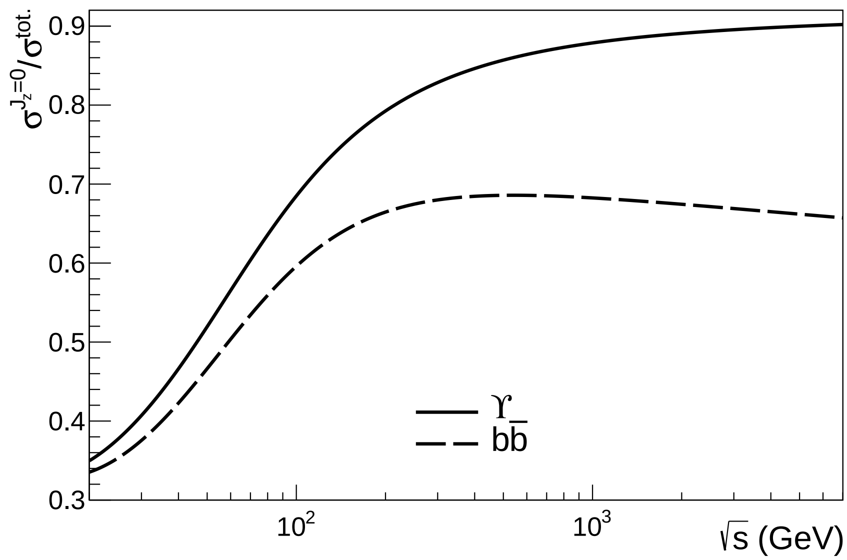

Figure 2.3. The energy dependence of the longitudinal fraction for production of bottomonium (solid) and $b\bar{b}$ (dashed). The result is shown above 20 GeV to be above the $B\overline{B}$ threshold.

polarization but the ratio saturates at 0.90 for $\sqrt{s}$ of $\sim$1 TeV, higher than the charmonium ratio at the same energy. The smaller longitudinal fraction at lower $\sqrt{s}$ for bottomonium is because of $q\overline{q}$ dominance of the total cross section at these energies. As the gg contribution rises, the longitudinal fraction increases.

We note that the point at which the bottomonium fraction is $\sim$0.50, $\sqrt{s} = 46.3$ GeV, is similar to the lowest energy at which Υ polarization has been measured, $\sqrt{s_{NN}} =$ 38.8 GeV. The E866/NuSea Collaboration measured the polarization of bottomonium production in p+Cu and found no polarization at low p_T in the Collins-Soper frame [77]. This result is compatible with our own because at leading order, the polarization axes in the helicity frame, the Collins-Soper frame, and the Gottfried-Jackson frame frame are coincident [34].

Likewise, the turnover in the $c\overline{c}$ polarization is also observed for $b\overline{b}$ but at a much higher energy, $\sqrt{s} = 550$ GeV. Although the energy scale is higher, the peak in the $b\overline{b}$ polarization ratio is almost the same as that for $c\overline{c}$, 0.69.

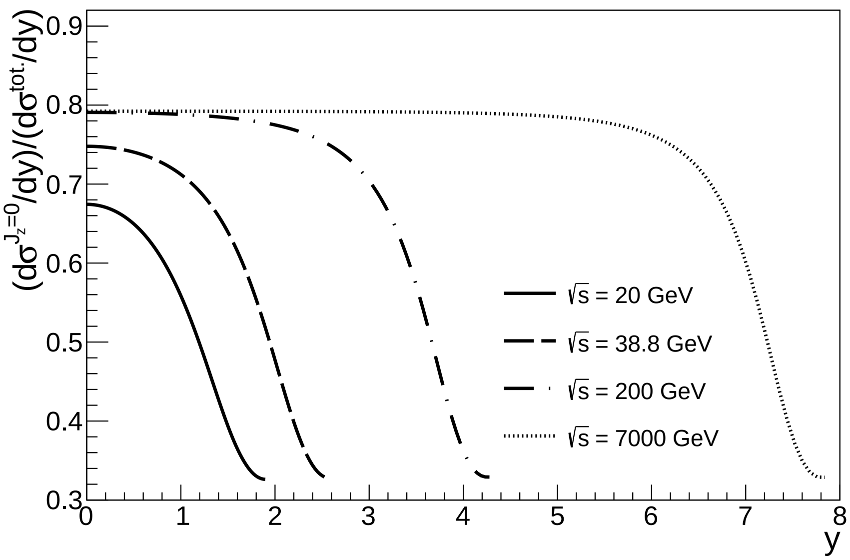

Figure 2.4. The rapidity dependence of the longitudinal fraction for production of charmonium at $\sqrt{s} = 20$ GeV (solid), 38.8 GeV (dashed), 200 GeV (dot-dashed), and 7000 GeV (dotted). The distributions are symmetric around $y = 0$.

2.3.2 Rapidity dependence of the longitudinal polarization fraction

We now turn to the rapidity dependence of our result, shown in Figs. 2.4 and 2.5. Four representative energies are chosen to illustrate. The lowest values, $\sqrt{s} = 20$ and 38.8 GeV were the highest available fixed-target energies at the CERN SPS for ion beams and the FNAL Tevatron for proton beams. The higher energies, $\sqrt{s} = 0.2$ and 7 TeV are energies available at the BNL RHIC and CERN LHC facilities. The results are presented for positive rapidity only because the rapidity distributions are symmetric around $y = 0$ in $p + p$ collisions.

2.3.2.1 Charmonium

The rapidity dependence for the charmonium longitudinal polarization fraction is shown in Fig. 2.4. The results are given up to the kinematic limits of production. The longitudinal fraction is greatest at $y = 0$ and decreases as $|y|$ increases. For the highest energies, where the longitudinal polarization has saturated in Fig. 2.2, the ratio is flat over a wide range of rapidity. The ratio remains greater than 0.50 as long as the gg contribution, with a significant $J_z = 0$ polarization, dominates production. As the phase space

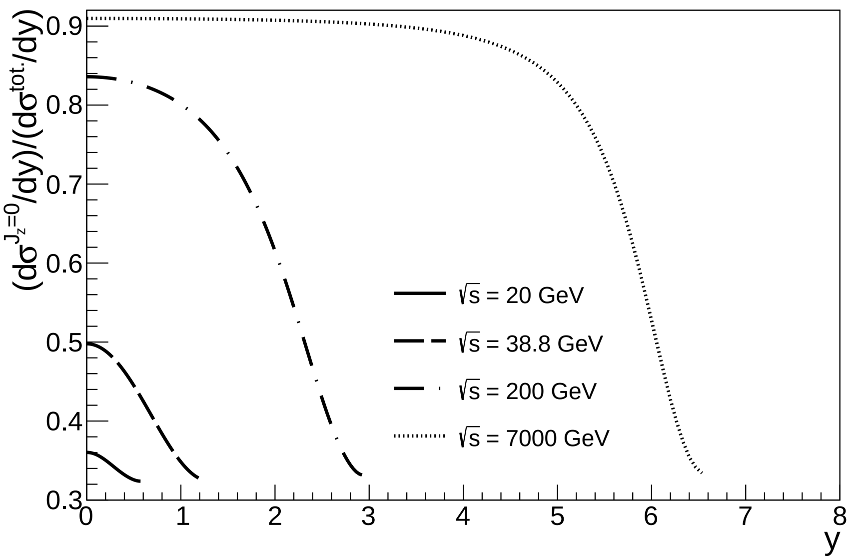

Figure 2.5. The rapidity dependence of the longitudinal fraction for production of bottomonium at $\sqrt{s} = 20$ GeV (solid), $\sqrt{s} = 38.8$ GeV (dashed), 200 GeV (dot-dashed), and 7000 GeV (dotted). The distributions are symmetric around $y = 0$.

for charmonium production is approached, the $q\overline{q}$ channel, predominantly transversely polarized, begins to dominate, causing the ratio to drop to a minimum of $\sim$0.30.

2.3.2.2 Bottomonium

The behavior of the bottomonium ratio as a function of rapidity, shown in Fig. 2.5, is similar to that of charmonium. The higher mass scale, however, reduces the kinematic range of the calculation. It also results in near transverse ($J_z = \pm 1$) polarization of bottomonium at fixed-target energies. The calculation at $\sqrt{s} = 38.8$ GeV shows that, at $y = 0$, the bottomonium ratio is consistent with no polarization, as measured by E866/NuSea [77]. At $\sqrt{s} = 20$ GeV, not far from production threshold, bottomonium is transversely polarized in the narrow rapidity range of production.

2.3.3 Sensitivity to the proton PDFs

We have tested the sensitivity of our results to the choice of PDFs used in the calculation. Since not many new LO proton PDFs are currently being made available, we compare our CTEQ6L1 results with calculations using the older GRV98 LO [78] set. We can expect the ratio to be the most sensitive to the choice of proton PDF because the PDFs can change the balance of gg to $q\overline{q}$ production, especially at lower $\sqrt{s}$ where the

x values probed by the calculations are large, $x \sim 0.1$. In particular, bottomonium production at $\sqrt{s} = 20$ GeV is most likely to be sensitive to the choice of PDF since the $q\overline{q}$ contribution is large at this energy. The results should, on the other hand, be relatively insensitive to the chosen mass and scale values since these do not strongly affect the relative contributions of gg and $q\overline{q}$.

This is indeed the case, for bottomonium production at $\sqrt{s} = 20$ GeV, close to the production threshold, the largest difference in the longitudinal ratio for the two PDF sets is 36% at $y = 0$. The sensitivity arises because the gg contribution is predominantly produced with $J_z = 0$ while the $q\overline{q}$ contribution is primarily produced with $J_z = \pm 1$. By $\sqrt{s} = 38.8$ GeV, the difference in the results is reduced to 20%. At collider energies, the difference is negligible. Since the gg contribution is dominant for charmonium already at $\sqrt{s} = 20$ GeV, the charmonium production ratio is essentially independent of the choice of proton PDF. Thus, away from production threshold, the results are robust with respect to the choice of PDF.

2.4 Conclusion

We have presented the energy and rapidity dependence of the polarization of heavy quarkonium production in $p + p$ collisions in the Color Evaporation Model. We find the quarkonium polarization to be longitudinal at most energies and around central rapidity while the polarization becomes transverse as the kinematic limits of the calculation, where $q\overline{q}$ production is dominant, are approached.

We note that the partonic cross sections, sorted by J_z in this calculation, are still mixtures of total angular momentum J and orbital angular momentum L states. So there is no immediate connection between these ratios and the lambda parameter of the data. In future work, we will extract the $S = 1$, $L = 0$ contribution from the partonic cross sections to narrow down into three distinct angular momentum states of $J = 1$ in order to give predictions for the polarization parameter λ_θ [34].

Because we have performed a leading order calculation, we cannot yet speak to the p_T dependence of the quarkonium polarization. We will address the p_T dependence in a separate publication.

Chapter 3

Polarization of Prompt J/ψ and Υ(1S) Production in the Color Evaporation Model

Polarization of Prompt J/ψ and Υ(1S) Production in the Color Evaporation Model

V. Cheung[a] and R. Vogt[a,b,1]

[a]Department of Physics
University of California, Davis
Davis, CA 95616, USA
and
[b]Nuclear and Chemical Sciences Division
Lawrence Livermore National Laboratory
Livermore, CA 94551, USA

ABSTRACT

We calculate the polarization of prompt J/ψ and Υ(1S) production using the color evaporation model at leading order. We present the polarization parameter λ_ϑ as a function of center-of-mass energy and rapidity in $p+p$ collisions. We also compare the x_F dependence to experimental results in p+Cu and π+W collisions, and predict the x_F dependence in p+Pb collisions at fixed-target energies. At energies far above the $Q\overline{Q}$ production threshold, we find the prompt J/ψ and Υ(1S) production to be longitudinally polarized with $\lambda_\vartheta^{J/\psi} = -0.51^{+0.05}_{-0.16}$ and $\lambda_\vartheta^{\Upsilon(1\mathrm{S})} = -0.69^{+0.03}_{-0.02}$. Both prompt J/ψ and prompt Υ(1S) are also longitudinally polarized at central rapidity, becoming transversely polarized at the most forward rapidities.

[1]This work was performed under the auspices of the U.S. Department of Energy by Lawrence Livermore National Laboratory under Contract DE-AC52-07NA27344 and supported by the U.S. Department of Energy, Office of Science, Office of Nuclear Physics (Nuclear Theory) under contract number DE-SC-0004014.

3.1 Introduction

One of the best ways to understand hadronization in QCD is to study the production of quarkonium. However, the production mechanism of quarkonium is still uncertain. Nonrelativistic QCD (NRQCD) [61], the most widely used model for quarkonium production encounters serious challenges in both the universality of the long distance matrix elements (LDMEs) and prediction of quarkonium polarization. The production cross sections in NRQCD, based on an expansion in the strong coupling constant and the $Q\overline{Q}$ velocity [44], is factorized into hard and soft contributions and divided into different color and spin states. The LDMEs, which weight the contributions from each color and spin state, are fit to the data above some minimum transverse momentum, p_T. These LDMEs, which are conjectured to be universal, fail to describe the yields and polarization simultaneously for p_T cuts less than twice the mass of the quarkonium state [62, 63]. They also depend on the collision system [54, 79–81]. Moreover, the polarization predicted by NRQCD is sensitive to the p_T cut. Thus the LDMEs are not universal as conjectured. The η_c p_T distributions calculated with LDMEs obtained from J/ψ yields using heavy quark spin symmetry [65–67], overshot the high p_T LHCb η_c results [68] in a recent analysis. The color evaporation model (CEM) and NRQCD can describe production yields rather well but spin-related measurements like the polarization are strong tests of production models. Quarkonium polarization is not the only test of the CEM. The CEM was also used recently to calculate transverse single spin asymmetries in J/ψ production [82, 83].

The CEM [56, 69–71], which considers all $Q\overline{Q}$ ($Q = c$, b) production regardless of the quark color, spin, and momentum, is able to predict both the total yields and the rapidity distributions with only a single normalization parameter [72]. We have previously presented the first polarization results in the CEM [57], which only considered charmonium and bottomonium production in general. This paper serves as a continuation of the previous work by presenting a leading order (LO) CEM calculation of the polarization in prompt J/ψ and $\Upsilon(1S)$ production. It is still a p_T-independent result because there are no exclusive next-to-leading order (NLO) polarized $Q\overline{Q}$ calculations on which to impose the $H\overline{H}$ ($H = D$, B) mass threshold. Our calculation is another step toward a full CEM polarization result that provides a general idea of whether there is any appreciable LO polarization that might carry through to the next order even though the kinematics are different. We will begin to address the p_T dependence in a subsequent publication.

In the traditional CEM, all quarkonium states are treated the same as $Q\overline{Q}$ below the $H\overline{H}$ threshold where the invariant mass of the heavy quark-antiquark pair is restricted to be less than twice the mass of the lowest mass meson that can be formed with the heavy quark as a constituent. The distributions for all quarkonium family members are assumed to be identical. In this paper, we use an improved CEM (ICEM) [56] where the invariant mass of the intermediate heavy quark-antiquark pair is constrained to be larger than the mass of produced quarkonium state, M_Q, instead of using the same lower limit of integration in the traditional CEM, $2m_Q$, as in our previous work and in Ref. [69]. The improved CEM describes the charmonium yields as well as the ratio of ψ' over J/ψ better than the traditional CEM. In a $p+p$ collision, the production cross section for a quarkonium state is then

$$\sigma = F_Q \sum_{i,j} \int_{M_Q^2}^{4m_H^2} d\hat{s} \int dx_1 dx_2 f_{i/p}(x_1,\mu^2) f_{j/p}(x_2,\mu^2) \hat{\sigma}_{ij}(\hat{s}) \delta(\hat{s} - x_1 x_2 s) \ , \tag{3.1}$$

where i and j are q, $\overline{q}$ and g such that $ij = q\overline{q}$ or gg. The square of the heavy quark pair invariant mass is $\hat{s}$ while the square of the center-of-mass energy in the $p+p$ collision is s. Here $f_{i/p}(x,\mu^2)$ is the parton distribution function (PDF) of the proton as a function of the fraction of momentum carried by the colliding parton x at factorization scale μ and $\hat{\sigma}_{ij}$ is the parton-level cross section. Finally, F_Q is a universal factor for the quarkonium state and is independent of the projectile, target, and energy. At leading order, the rapidity distribution, $d\sigma/dy$, in the ICEM is

$$\frac{d\sigma}{dy} = F_Q \sum_{i,j} \int_{M_Q^2}^{4m_H^2} \frac{d\hat{s}}{s} f_{i/p}(x_1,\mu^2) f_{\overline{q}/p}(x_2,\mu^2) \hat{\sigma}_{ij}(\hat{s}) \ , \tag{3.2}$$

where $x_{1,2} = (\sqrt{\hat{s}/s}) \exp(\pm y)$. The longitudinal momentum fraction distribution, $d\sigma/dx_F$, in the ICEM is

$$\frac{d\sigma}{dx_F} = F_Q \sum_{i,j} \int_{M_Q}^{2m_H} \frac{d\sqrt{\hat{s}}}{s} \frac{2\sqrt{\hat{s}}}{\sqrt{x_F^2 + 4\hat{s}/s}} f_{i/p}(x_1,\mu^2) f_{j/p}(x_2,\mu^2) \hat{\sigma}_{ij}(\hat{s}) \ , \tag{3.3}$$

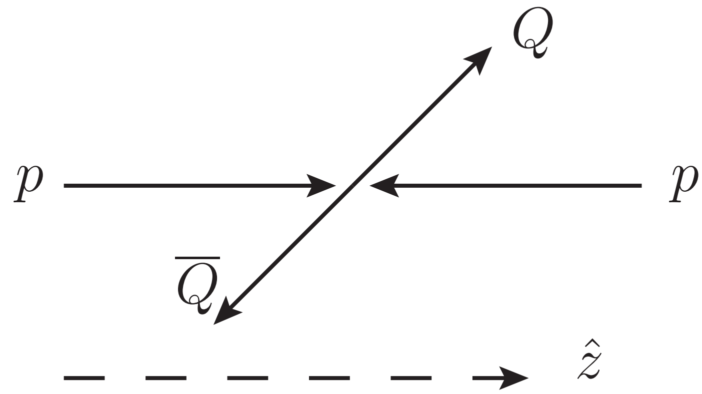

Figure 3.1. The orientation of the z axis is indicated by the dashed arrowed line. Two proton arrows indicate the incoming beam directions. If the quarks in the final state heavy quark-antiquark pair have the same helicity, then the total angular momentum along the z axis, J_z, is zero while if they have opposite helicity, then $J_z = \pm 1$.

where $x_{1,2} = (\pm x_F + \sqrt{x_F^2 + 4\hat{s}/s})/2$. We take the square of the factorization and renormalization scales to be $\mu^2 = \hat{s}$.

3.2 Polarization of directly produced $Q\overline{Q}$

At leading order in α_s, the final state $Q\overline{Q}$ pair is produced with zero total transverse momentum. We define the polarization axis (z axis) in the helicity frame pointing from $\overline{Q}$ to Q along the beam axis as shown in Fig. 3.1.

There are four $\mathcal{O}(\alpha_s^2)$ Feynman diagrams to consider, one for $q\overline{q} \to Q\overline{Q}$ and three for $gg \to Q\overline{Q}$. Each diagram includes a color factor C and a scattering amplitude $\mathcal{A}$. The generic matrix element for each process can be written as [73]

$$\mathcal{M}_{qq} = C_{qq}\mathcal{A}_{qq} \ , \tag{3.4}$$

$$\mathcal{M}_{gg} = C_{gg,\hat{s}}\mathcal{A}_{gg,\hat{s}} + C_{gg,\hat{t}}\mathcal{A}_{gg,\hat{t}} + C_{gg,\hat{u}}\mathcal{A}_{gg,\hat{u}} \ . \tag{3.5}$$

As previously mentioned, there is one diagram only for $q\overline{q} \to Q\overline{Q}$, thus a single amplitude, $\mathcal{A}_{qq}$. However, there are three diagrams for $gg \to Q\overline{Q}$ at leading order, the $\hat{s}$, $\hat{t}$ and $\hat{u}$

channels. In terms of the Dirac spinors u and v, the individual amplitudes are

$$\mathcal{A}_{qq} = \frac{g_s^2}{\hat{s}}[\overline{u}(p')\gamma_\mu v(p)][\overline{v}(k)\gamma^\mu u(k')] \,, \tag{3.6}$$

$$\begin{aligned}\mathcal{A}_{gg,\hat{s}} &= -\frac{g_s^2}{\hat{s}}\Big\{-2k'\cdot\epsilon(k)[\overline{u}(p')\not{\epsilon}(k')v(p)] + 2k\cdot\epsilon(k')[\overline{u}(p')\not{\epsilon}(k)v(p)] \\ &+ \epsilon(k)\cdot\epsilon(k')[\overline{u}(p')(\not{k}' - \not{k})v(p)]\Big\} \,, \end{aligned} \tag{3.7}$$

$$\mathcal{A}_{gg,\hat{t}} = -\frac{g_s^2}{\hat{t}-M^2}\overline{u}(p')\not{\epsilon}(k')(\not{k} - \not{p} + M)\not{\epsilon}(k)v(p) \,, \tag{3.8}$$

$$\mathcal{A}_{gg,\hat{u}} = -\frac{g_s^2}{\hat{u}-M^2}\overline{u}(p')\not{\epsilon}(k)(\not{k}' - \not{p} + M)\not{\epsilon}(k')v(p) \,. \tag{3.9}$$

Here g_s is the gauge coupling, M is the mass of heavy quark (m_c for charm and m_b for bottom), ϵ represents the gluon polarization vectors, γ^μ are the gamma matrices, k' (k) is the momentum of the initial state light quark (antiquark) or gluon, and p' (p) is the momentum of final sate heavy quark (antiquark).

At leading order, the final state $Q\overline{Q}$ is produced with no dependence on the azimuthal angle and thus $L_z = 0$. To extract the projection on a state with orbital-angular-momentum quantum number L, we find the corresponding Legendre component $\mathcal{A}_L$ in the amplitudes by

$$\mathcal{A}_{L=0} = \frac{1}{2}\int_{-1}^{1} dx\mathcal{A}(x=\cos\theta) \,, \tag{3.10}$$

$$\mathcal{A}_{L=1} = \frac{3}{2}\int_{-1}^{1} dx\; x\mathcal{A}(x=\cos\theta) \,. \tag{3.11}$$

The final state total spin is determined by the helicities of the heavy quarks. Two helicity combinations that result in $S_z = 0$ are added and normalized to give contribution to the spin triplet state ($S = 1$). Having the amplitudes for $S = 1$ with $S_z = 0, \pm 1$, and $L = 0, 1$ with $L_z = 0$, we calculate the amplitudes for $J = 0, 1, 2$. First, the amplitudes for $J = 1$, obtained by adding $S = 1$ and $L = 0$, are simply

$$\mathcal{A}_{J=1,J_z=\pm 1} = \mathcal{A}_{L=0,L_z=0;S=1,S_z=\pm 1} \,, \tag{3.12}$$

$$\mathcal{A}_{J=1,J_z=0} = \mathcal{A}_{L=0,L_z=0;S=1,S_z=0} \,. \tag{3.13}$$

Then, using angular momentum algebra, the amplitudes for $J = 0, 1, 2$, found by adding

$S = 1$ and $L = 1$, are:

$$\begin{aligned}
\mathcal{A}_{J=0,J_z=0} &= -\sqrt{\frac{1}{3}}\mathcal{A}_{L=1,L_z=0;S=1,S_z=0} \ , & (3.14)\\
\mathcal{A}_{J=1,J_z=\pm1} &= \mp\frac{1}{\sqrt{2}}\mathcal{A}_{L=1,L_z=0;S=1,S_z=\pm1} \ , & (3.15)\\
\mathcal{A}_{J=1,J_z=0} &= 0 \ , & (3.16)\\
\mathcal{A}_{J=2,J_z=\pm2} &= 0 \ , & (3.17)\\
\mathcal{A}_{J=2,J_z=\pm1} &= \frac{1}{\sqrt{2}}\mathcal{A}_{L=1,L_z=0;S=1,S_z=\pm1} \ , & (3.18)\\
\mathcal{A}_{J=2,J_z=0} &= \sqrt{\frac{2}{3}}\mathcal{A}_{L=1,L_z=0;S=1,S_z=0} \ . & (3.19)
\end{aligned}$$

Here, we have dropped terms that contain amplitudes of nonzero L_z. The amplitudes sorted by final state J and J_z are then squared while averaging over the polarization of the initial gluons or the spin of the light quarks, depending on the process, in the spirit of the CEM.

The squared matrix elements, $|\mathcal{M}|^2$, are calculated for each J, J_z state. The color factors, C, are calculated from the SU(3) color algebra and are independent of final state angular momentum [73]. They are

$$\begin{aligned}
|C_{qq}|^2 &= 2 \ ,\\
|C_{gg,\hat{s}}|^2 &= 12 \ ,\\
|C_{gg,\hat{t}}|^2 &= \frac{16}{3} \ ,\\
|C_{gg,\hat{u}}|^2 &= \frac{16}{3} \ ,\\
C^*_{gg,\hat{s}}C_{gg,\hat{t}} &= +6 \ ,\\
C^*_{gg,\hat{s}}C_{gg,\hat{u}} &= -6 \ ,\\
C^*_{gg,\hat{t}}C_{gg,\hat{u}} &= -\frac{2}{3} \ . \qquad (3.20)
\end{aligned}$$

Finally, the total squared amplitudes for a given J, J_z state,

$$\begin{aligned}
|\mathcal{M}^{J,J_z}_{qq}|^2 &= |C_{qq}|^2|\mathcal{A}_{qq}|^2 \ , & (3.21)\\
|\mathcal{M}^{J,J_z}_{gg}|^2 &= |C_{gg,\hat{s}}|^2|\mathcal{A}_{gg,\hat{s}}|^2 + |C_{gg,\hat{t}}|^2|\mathcal{A}_{gg,\hat{t}}|^2 + |C_{gg,\hat{u}}|^2|\mathcal{A}_{gg,\hat{u}}|^2 + 2C^*_{gg,\hat{s}}C_{gg,\hat{t}}\mathcal{A}^*_{gg,\hat{s}}\mathcal{A}_{gg,\hat{t}} &\\
&+ 2C^*_{gg,\hat{s}}C_{gg,\hat{u}}\mathcal{A}^*_{gg,\hat{s}}\mathcal{A}_{gg,\hat{u}} + 2C^*_{gg,\hat{t}}C_{gg,\hat{u}}\mathcal{A}^*_{gg,\hat{t}}\mathcal{A}_{gg,\hat{u}} \ , & (3.22)
\end{aligned}$$

are then used to obtain the partonic cross sections by integrating over a solid angle:

$$\hat{\sigma}_{ij}^{J,J_z} = \int d\Omega \Big(\frac{1}{8\pi}\Big)^2 \frac{|\mathcal{M}_{ij}^{J,J_z}|^2}{\hat{s}} \sqrt{1 - \frac{4M^2}{\hat{s}}} \ . \tag{3.23}$$

The partonic cross sections for $J^P = 1^-$ with $J_z = 0, \pm 1$ are found by adding the $L = 0$ and $S = 1$ contributions:

$$\hat{\sigma}_{q\bar{q}}^{J_z=0}(\hat{s}) = 0 \ , \tag{3.24}$$

$$\hat{\sigma}_{q\bar{q}}^{J_z=\pm 1}(\hat{s}) = \frac{\pi \alpha_s^2}{9\hat{s}} \chi \ , \tag{3.25}$$

$$\hat{\sigma}_{gg}^{J_z=0}(\hat{s}) = \frac{7\pi\alpha_s^2}{48\hat{s}} \frac{M^2}{\hat{s}\chi} \Big(\ln \frac{1+\chi}{1-\chi}\Big)^2 \ , \tag{3.26}$$

$$\hat{\sigma}_{gg}^{J_z=\pm 1}(\hat{s}) = \frac{\pi^3 \alpha_s^2}{1536\hat{s}} \chi \frac{(\sqrt{\hat{s}} - 2M)(37\sqrt{\hat{s}} + 38M)}{(2M + \sqrt{\hat{s}})^2} \ . \tag{3.27}$$

Here and in the following, $\chi = \sqrt{1 - 4M^2/\hat{s}}$.

The partonic cross sections for $J^P = 0^+$, obtained by adding the $L = 1$ and $S = 1$ states, are

$$\hat{\sigma}_{q\bar{q}}^{J_z=0}(\hat{s}) = 0 \ , \tag{3.28}$$

$$\hat{\sigma}_{gg}^{J_z=0}(\hat{s}) = \frac{9\pi\alpha_s^2}{16\hat{s}} \frac{M^2}{\hat{s}\chi^3} \Big(2\chi - \ln \frac{1+\chi}{1-\chi}\Big)^2 \ . \tag{3.29}$$

The individual partonic cross section for $J^P = 1^+$ with $J_z = 0, \pm 1$, found by adding the contributions from $L = 1$ and $S = 1$, are

$$\hat{\sigma}_{q\bar{q}}^{J_z=0}(\hat{s}) = 0 \ , \tag{3.30}$$

$$\hat{\sigma}_{q\bar{q}}^{J_z=\pm 1}(\hat{s}) = \frac{\pi \alpha_s^2}{18\hat{s}} \chi \ , \tag{3.31}$$

$$\hat{\sigma}_{gg}^{J_z=0}(\hat{s}) = 0 \ , \tag{3.32}$$

$$\hat{\sigma}_{gg}^{J_z=\pm 1}(\hat{s}) = \frac{3\pi^3 \alpha_s^2}{256\hat{s}} \chi \frac{(\sqrt{\hat{s}} - 2M)(4\hat{s} - 9M^2)}{(2M + \sqrt{\hat{s}})^3} \ . \tag{3.33}$$

The partonic cross sections for $J^P = 2^+$ with $J_z = 0, \pm 1$, obtained by adding the

$L = 1$ and $S = 1$ states, are

$$\hat{\sigma}_{q\bar{q}}^{J_z=0}(\hat{s}) = 0 \,, \tag{3.34}$$

$$\hat{\sigma}_{q\bar{q}}^{J_z=\pm 1}(\hat{s}) = \frac{\pi\alpha_s^2}{18\hat{s}}\chi \,, \tag{3.35}$$

$$\hat{\sigma}_{gg}^{J_z=0}(\hat{s}) = \frac{9\pi\alpha_s^2}{8\hat{s}}\frac{M^2}{\hat{s}\chi^3}\Big(2\chi - \ln\frac{1+\chi}{1-\chi}\Big)^2 \,, \tag{3.36}$$

$$\hat{\sigma}_{gg}^{J_z=\pm 1}(\hat{s}) = \frac{3\pi^3\alpha_s^2}{256\hat{s}}\chi\frac{(\sqrt{\hat{s}}-2M)(4\hat{s}-9M^2)}{(2M+\sqrt{s})^3} \,, \tag{3.37}$$

The sum of these results for each final state total angular momentum, $\sum_{J_z=-J}^{J_z=+J}\hat{\sigma}_{ij}^{J_z}$, is equal to the unpolarized partonic cross section $\hat{\sigma}_{ij}^{\rm unpol.}$.

Having computed the polarized $Q\overline{Q}$ production cross section at the parton level, we then convolute the partonic cross sections with the parton distribution functions (PDFs) to obtain the hadron-level cross section σ as a function of $\sqrt{s}$ using Eq. (3.1), and the rapidity distribution, $d\sigma/dy$, using Eq. (3.2). The quarkonium masses which appear as the lower limit of the $Q\overline{Q}$ invariant mass are listed in Table 3.1. We employ the CTEQ6L1 [75] PDFs in this calculation and the running coupling constant $\alpha_s = g_s^2/(4\pi)$ is calculated at the one-loop level appropriate for the PDFs.

3.3 Polarization of prompt J/ψ and Υ(1S)

We assume that the angular momentum of each directly produced quarkonium state is unchanged by the transition from the parton level to the hadron level, consistent with the CEM that the linear momentum is unchanged by hadronization. This is similar to the assumption made in NRQCD that once a $c\bar{c}$ is produced in a given spin state, it retains that spin state when it becomes a J/ψ.

We calculate the $J_z = 0, \pm 1$ to unpolarized ratios for each directly produced quarkonium state $\mathcal{Q}$ that has a contribution to the prompt production of J/ψ and Υ(1S): J/ψ, ψ(2S), χ_{c1}(1P), χ_{c2}(1P) and Υ(1S), Υ(2S), Υ(3S), χ_{b1}(1P), χ_{b2}(1P), χ_{b1}(2P), χ_{b2}(2P). These ratios, $R_{\mathcal{Q}}^{J_z}$, are then independent of $F_{\mathcal{Q}}$. We assume the feed-down production of J/ψ and Υ(1S) from the higher mass bound state follows the angular momentum algebra. Their contributions to the $J_z = 0$ to unpolarized ratios of prompt J/ψ and Υ(1S) are

Table 3.1. The mass M_Q, the feed-down contribution ratio c_Q, and the squared feed-down transition Clebsch-Gordan coefficients $S_Q^{J_z}$ for all quarkonium states contributing to the prompt production of J/ψ and Υ(1S). We assume the c_Q for χ_{b1}(1P) and χ_{b2}(1P) to be equal as well as that for χ_{b1}(2P) and χ_{b2}(2P).

Q	M_Q (GeV)	c_Q	$S_Q^{J_z=0}$	$S_Q^{J_z=\pm1}$
J/ψ	3.10	0.62	1	0
ψ(2S)	3.69	0.08	1	0
χ_{c1}(1P)	3.51	0.16	0	1/2
χ_{c2}(1P)	3.56	0.14	2/3	1/2
Υ(1S)	9.46	0.52	1	0
Υ(2S)	10.0	0.1	1	0
Υ(3S)	10.4	0.02	1	0
χ_{b1}(1P)	9.89	0.13	0	1/2
χ_{b2}(1P)	9.91	0.13	2/3	1/2
χ_{b1}(2P)	10.3	0.05	0	1/2
χ_{b2}(2P)	10.3	0.05	2/3	1/2

added and weighed by the feed-down contribution ratios c_ψ and c_Υ [84],

$$R_{J/\psi}^{J_z=0} = \sum_{\psi,J_z} c_\psi S_\psi^{J_z} R_\psi^{J_z} \ , \tag{3.38}$$

$$R_{\Upsilon(1S)}^{J_z=0} = \sum_{\Upsilon,J_z} c_\Upsilon S_\Upsilon^{J_z} R_\Upsilon^{J_z} \ , \tag{3.39}$$

where $S_Q^{J_z}$ is the transition probability from a given state Q produced in a given J_z state to J/ψ or Υ(1S) with $J_z = 0$ in a single decay. We assume two pions are emitted for an S state feed down, and a photon is emitted for a P state feed down. $S_Q^{J_z}$ is then 1 (if $J_z = 0$) or 0 (if $J_z = 1$) for $Q = \psi$(2S), Υ(2S), Υ(3S) since their transitions, $Q \to J/\psi+\pi\pi$ or $Q \to \Upsilon$(1S)$+\pi\pi$, do not change the angular momentum. For directly produced J/ψ and Υ(1S), $S_Q^{J_z}$ is then 1 for $J_z = 0$ and 0 for $J_z = 1$. $S_Q^{J_z}$ for χ states are the squares of the Clebsch-Gordan coefficients for the feed-down production from state χ to $J/\psi + \gamma$ or Υ(1S)$+\gamma$. The values of M_Q, c_Q, and $S_Q^{J_z}$ for all quarkonium states contributing to the prompt production of J/ψ and Υ(1S) are collected in Table 3.1. We further assume that the contributions from χ_{b1}(1P) and χ_{b2}(1P) are the same and also that the contributions from χ_{b1}(2P) and χ_{b2}(2P) are the same, similar to that in direct J/ψ production.

Finally, for each of the $J^P = 1^-$ S states, the $J_z = 0$ to the unpolarized ratio is then converted into the polarization parameter λ_ϑ by [34]

$$\lambda_\vartheta = \frac{1 - 3R^{J_z=0}}{1 + R^{J_z=0}} . \tag{3.40}$$

Consistent with our feed-down production treatment in Eqs. (3.38) and (3.39), for the $J^P = 1^+$ χ_1 P states, the $J_z = 0$ to unpolarized ratio is converted into the polarization parameter λ_ϑ by [85]

$$\lambda_\vartheta = \frac{-1 + 3R^{J_z=0}}{3 - R^{J_z=0}} . \tag{3.41}$$

We note that this is the polarization parameter of the prompt J/ψ or Υ(1S) state assuming the production comes purely from χ_{c1} or χ_{b1} feed down. For example, in the limit of $R^{J_z=0}_{\chi_1} \to 0$, our treatment in Eq. (3.38) gives $R^{J_z=0}_{J/\psi} = 0.5$ or $\lambda^{J/\psi}_\vartheta = -1/3$ by Eq. (3.40). Similarly, for each of the $J^P = 2^+$ χ_2 P states, the $J_z = 0$ to the unpolarized ratio is converted into the polarization parameter λ_ϑ by [85]

$$\lambda_\vartheta = \frac{-3 - 3R^{J_z=0}}{9 + R^{J_z=0}} . \tag{3.42}$$

Here we drop the terms with $J_z = \pm 2$ matrix elements since they are shown to be zero in Eq. (3.17). This is the polarization parameter of the prompt J/ψ or Υ(1S) state assuming the production comes purely from χ_{c2} or χ_{b2} feed down under our treatment in Eqs. (3.38) and (3.39).

3.4 Results

Since this calculation is LO in α_s, we can only calculate the polarization parameter λ_ϑ as a function of $\sqrt{s}$ and y (or x_F) but not p_T, which will require us to go to NLO, $\mathcal{O}(\alpha_s^3)$. However, the charm rapidity distribution at LO is similar to that at NLO [76]. The same is true for J/ψ production in the CEM. The only difference would be a rescaling of the parameter F_Q based on the ratio NLO/LO using the NLO scale determined in Ref. [72].

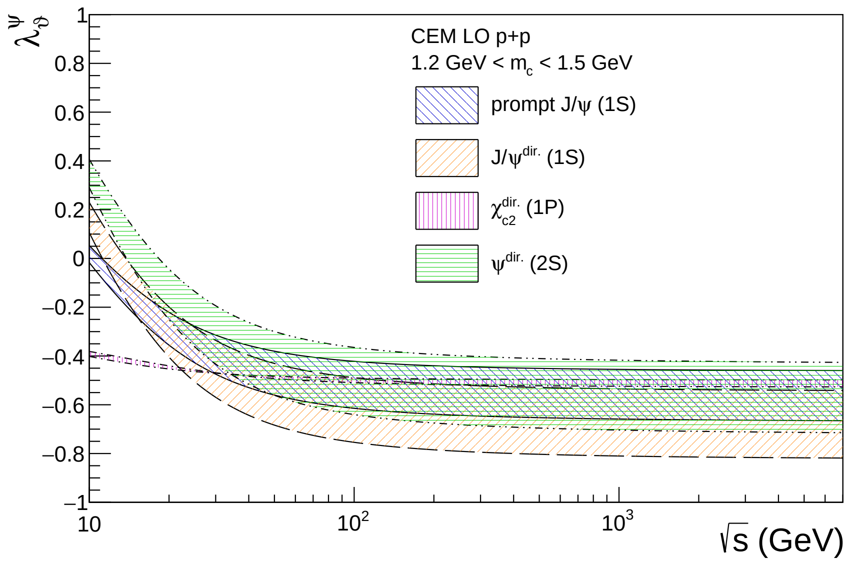

Figure 3.2. The energy dependence of the polarization parameter λ_ϑ for production of prompt J/ψ (solid), direct J/ψ (dashed), direct χ_{c2}(1P) (dot-dashed), and direct ψ(2S) (dot-dot-dashed).

The unpolarized CEM results are in rather good agreement with the data from $p+p$ collisions [72].

In the remainder of this section, we discuss the energy dependence of the polarization parameter λ_ϑ for the prompt production of J/ψ and Υ(1S), and direct production of quarkonium states that contribute to the feed-down production. We then show the polarization parameter for prompt J/ψ and Υ(1S) production as a function of rapidity for selected energies. We also compare our results as a function of the longitudinal momentum fraction to the polarization measured in fixed-target experiments as well as giving predictions for future fixed-target experiments. Finally, we discuss the sensitivity of our results to the choice of proton-parton density functions, the factorization scale, and the feed-down ratios considered.

3.4.1 Energy dependence of λ_ϑ

In this section, we compare the energy dependence of the polarization parameter λ_ϑ as a function of center-of-mass energy in $p+p$ collisions in Figs. 3.2 and 3.3. The integration in Eq. (3.1) for the direct production of each quarkonium state Q is from the mass of the quarkonium state M_Q to twice the mass of the lowest lying open heavy flavor hadron.

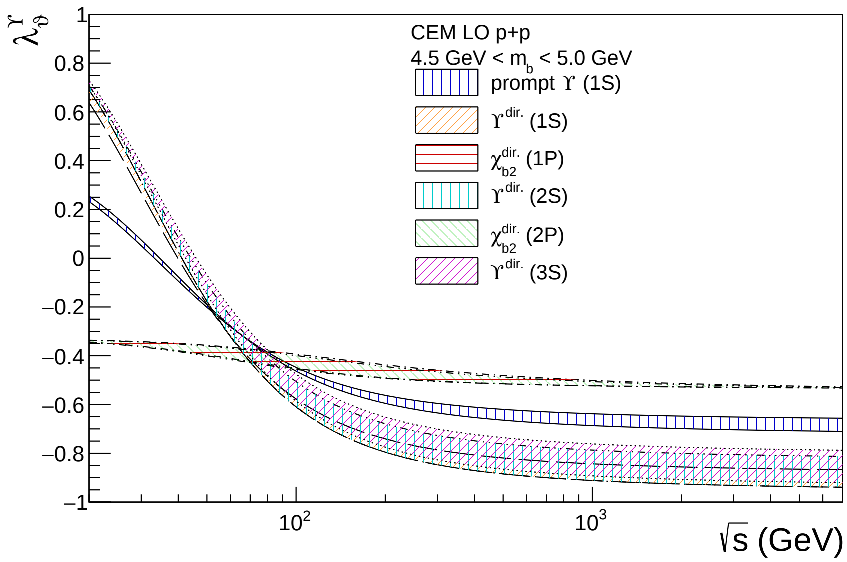

Figure 3.3. The energy dependence of the polarization parameter λ_ϑ for production of prompt Υ(1S) (solid), direct Υ(1S) (dashed), direct χ_{b2}(2P) (dot-dashed), direct Υ(2S) (dot-dot-dashed), direct χ_{b2}(2P) (dot-dot-dot-dashed), and direct Υ(3S) (dotted). The result is shown for $\sqrt{s} > 20$ GeV to be above the $B\overline{B}$ threshold.

The longitudinal to unpolarized ratios for the direct productions are then weighed to give the longitudinal to unpolarized ratio for the prompt production by Eqs. (3.38) and (3.39) using parameters listed in Table 3.1. The polarization parameters for prompt production and $J^P = 1^-$ (S states) are then calculated using Eq. (3.40). The polarization parameter for direct production of $J^P = 1^+(\chi_1$P states) and $2^+(\chi_2$P states) are calculated employing Eqs. (3.41) and (3.42) respectively. The mass of the charm quark m_c is varied around the base value 1.27 GeV from 1.2 to 1.5 GeV, while the mass of the bottom quark, m_b, is varied around the base value 4.75 GeV from 4.5 to 5.0 GeV to construct the uncertainty bands shown in the figures.

3.4.1.1 Direct production of J/ψ, ψ(2S), χ_{c2}(1P), and prompt production of J/ψ

In Fig. 3.2, the polarization paramters as a function of energy for direct production of the charmonium states below the hadron threshold and the prompt production of J/ψ are presented. The integral over the pair invariant mass is assumed to be from M_Q to $2m_{D^0}$ ($m_{D^0} = 1.86$ GeV). We see that all direct production of J/ψ, χ_{c2}(1P), and ψ(2S) is longitudinal for $\sqrt{s} > 20$ GeV. The prompt production of J/ψ (bounded by blue filled solid curves in Fig. 3.2) is longitudinally polarized for $\sqrt{s} > 10$ GeV. Both direct and prompt productions become more longitudinal as $\sqrt{s}$ increases. The polarization of direct $\psi(2S)$ is less longitudinal than that of direct J/ψ. This is because the improved CEM integrates from the mass of the quarkonium to the hadron threshold. Otherwise, the direct J/ψ and $\psi(2S)$ results would be equal since the traditional CEM uses $2m_c$ for the lower limit of integration for all states. The parton-level longitudinal to unpolarized fraction decreases as a function of $\sqrt{\hat{s}}$ for $J^P = 1^-$ production, so the hadron-level longitudinal to unpolarized fraction is smaller for direct $\psi(2S)$ due to its larger mass. Thus its polarization is less longitudinal. Prompt J/ψ production is dominated by the S states and thus is longitudinally polarized. At $\sqrt{s} > 100$ GeV, the polarization parameter for prompt J/ψ production saturates at $\lambda_\vartheta = -0.51^{+0.05}_{-0.16}$, while the polarization parameter for direct J/ψ saturates at $\lambda_\vartheta = -0.61^{+0.07}_{-0.21}$.

In the traditional color evaporation model, the polarization of direct J/ψ is slightly more longitudinal (an increase of $\sim$0.1 in $R^{J_z=0}_{J/\psi}$ in the energy interval presented).

The polarization parameter for direct χ_{c1} production is not shown in Fig. 3.2 because the direct production yields only $J_z = \pm 1$ by Eqs. (3.30) and (3.32), and thus Eq. (3.41) gives $\lambda_\vartheta = -1/3$.

3.4.1.2 Direct production of Υ(1S), Υ(2S), Υ(3S), χ_{c2}(1P), χ_{c2}(2P), and prompt production of Υ(1S)

The results for direct production of the bottomonium states and prompt production of $\Upsilon(1S)$ are shown in Fig. 3.3. Here, the integral over the pair invariant mass is assumed to be from M_Q to $2m_{B^0}$ ($m_{B^0} = 5.28$ GeV). For the more massive bottom quarks, direct production of $\Upsilon(1S)$, $\Upsilon(2S)$, and $\Upsilon(3S)$ starts out transversely polarized for $\sqrt{s} < 34$ GeV. This is because $q\overline{q} \to Q\overline{Q}$ dominates the total cross section at these energies. As the $gg \to Q\overline{Q}$ contribution rises, the longitudinal fraction R_Υ, increases and the direct production becomes longitudinal. As a result, the direct production of $\Upsilon(1S)$, $\Upsilon(2S)$, $\Upsilon(3S)$, $\chi_{c2}(1P)$, $\chi_{c2}(2P)$, and prompt production production of $\Upsilon(1S)$ becomes dominated by longitudinal polarization. Similar to charmonium production, the direct production of $\Upsilon(1S)$ is mostly longitudinally polarized at collider energies, followed by $\Upsilon(2S)$ and $\Upsilon(3S)$ due to the increase in the lower limit of integration. In the traditional color evaporation model, all directly produced S states have the same polarization. Note that the $\Upsilon(1S)$ polarization is the same in the improved and traditional color evaporation model since the mass of the $\Upsilon(1S)$ is less than $2m_b$. Compared to charmonium production, the longitudinal to unpolarized ratio at the parton level for bottomonium production decreases more slowly as a function of $\sqrt{\hat{s}}$ in the integration range. This makes the bottomomium polarization relatively less sensitive to the mass of the quark compared to charmonium polarization. The polarization parameter for prompt $\Upsilon(1S)$ saturates at $\lambda_\vartheta = -0.69^{+0.03}_{-0.02}$ while the polarization parameter for direct $\Upsilon(1S)$ saturates at $\lambda_\vartheta = -0.91^{+0.04}_{-0.03}$ for $\sqrt{s} \sim 1$ TeV. Note that the limit is lower for prompt $\Upsilon(1S)$ than for prompt J/ψ at the same energy.

Prompt production of $\Upsilon(1S)$ is unpolarized ($\lambda_\vartheta = 0$) for $\sqrt{s} = 34$ GeV. The polarization parameters for direct $\chi_{b1}(1P)$ and $\chi_{b1}(2P)$ production are not shown in Fig. 3.3 because direct production is only via $J_z = \pm 1$ according to Eqs. (3.30) and (3.32) and thus Eq. (3.41) gives $\lambda_\vartheta = -1/3$.

3.4.2 Rapidity dependence of λ_ϑ

We now turn to the rapidity dependence of our result, shown in Figs. 3.4 and 3.5. The direct production of each quarkonium state Q is obtained by integrating Eq. (3.2) from the mass of the quarkonium state M_Q to twice the mass of the lowest lying open heavy flavor hadron. The longitudinal to unpolarized ratios for the direct productions are then weighed to give the longitudinal to unpolarized ratio for the prompt production by Eqs. (3.38) and (3.39) using the c_Q values listed in Table 3.1. The polarization parameters for prompt production are then found by Eq. (3.40). Four representative energies are chosen for illustration. The lowest values, $\sqrt{s} = 20$ and 38.8 GeV, were the highest available fixed-target energies at the CERN Super Proton Synchrotron (SPS) for ion beams and the Fermi National Accelerator Laboratory (FNAL) Tevatron for proton beams. The higher energies, $\sqrt{s} = 0.2$ and 7 TeV are energies available at the Brookhaven National Laboratory (BNL) Relativistic Heavy Ion Collider and CERN LHC facilities. The results are presented for positive rapidity only because the rapidity distributions are symmetric around $y = 0$ in $p + p$ collisions. Again, the charm quark mass m_c is varied around

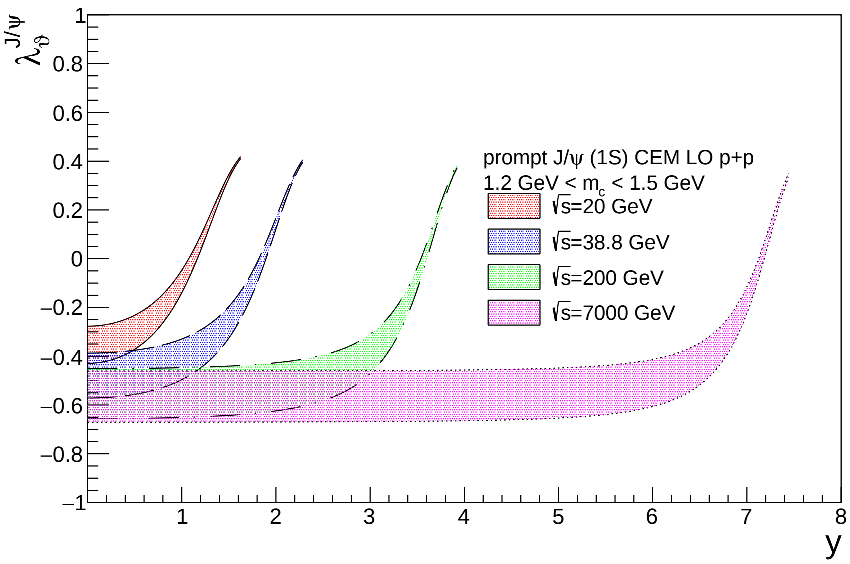

Figure 3.4. The rapidity dependence of the polarization parameter λ_ϑ for the production of prompt J/ψ at $\sqrt{s} = 20$ GeV (solid), 38.8 GeV (dashed), 200 GeV (dot-dashed), and 7000 GeV (dotted). The distributions are symmetric around $y = 0$.

1.27 GeV from 1.2 to 1.5 GeV, while the bottom quark mass m_b is varied around 4.75 GeV from 4.5 to 5.0 GeV to construct the uncertainty bands.

3.4.2.1 Direct production of J/ψ, ψ(2S), χ_{c2}(1P), and prompt production of J/ψ

The rapidity dependence of the polarization parameter for prompt J/ψ is shown in Fig. 3.4. The results are given up to the kinematic limits of production. The polarization parameter is negative with a minimum at $y = 0$ and increases as $|y|$ increases, becoming positive at the kinematic limit. For the highest energies, where the longitudinal polarization has saturated in Fig. 3.2, the polarization parameter is flat over a wide range of rapidity. The parameter remains negative as long as the $gg \to Q\overline{Q}$ contribution, with a significant longitudinal polarization, dominates production. As the phase space for charmonium production is approached, the $q\overline{q} \to Q\overline{Q}$ channel, predominantly transversely polarized, begins to dominate, causing the parameter to increase to a maximum of $\lambda_\vartheta \sim 0.4$.

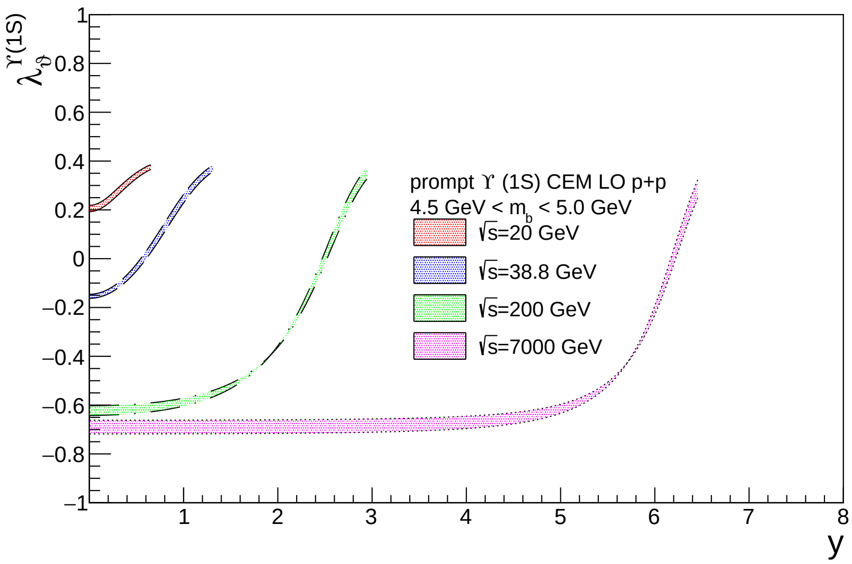

Figure 3.5. The rapidity dependence of the polarization parameter λ_ϑ for the production of prompt Υ(1S) at $\sqrt{s}$ = 20 GeV (solid), $\sqrt{s}$ = 38.8 GeV (dashed), 200 GeV (dot-dashed), and 7000 GeV (dotted). The distributions are symmetric around $y = 0$.

3.4.2.2 Direct production of Υ(1S), Υ(2S), Υ(3S), χ_{c2}(1P), χ_{c2}(2P), and prompt production of Υ(1S)

The behavior of the prompt Υ(1S) polarization parameter as a function of rapidity, shown in Fig. 3.5, is similar to that of prompt J/ψ. The higher mass scale, however, reduces the kinematic range of the calculation. It also results in an unpolarized to slightly transverse polarization of prompt Υ(1S) at fixed-target energies. At $\sqrt{s}$ = 20 GeV, not far from the production threshold, prompt Υ(1S) is transversely polarized in the narrow rapidity range of production.

3.4.3 Comparison to fixed-target data

In this section, we compare our results as a function of longitudinal momentum fraction x_F using Eq. (3.3) with the polarization parameters measured in fixed-target experiments. We compare our results to the results from the E866/NuSea Collaboration for the polarization of J/ψ [86, 87] and Υ(1S) [77] in p+Cu collisions at $\sqrt{s_{NN}}$ = 38.8 GeV as well as J/ψ in π+W at $\sqrt{s}$ = 22 GeV by the CIP Collaboration [88]. We multiply the CTEQ6L1 PDFs by the central EPS09 [89] nuclear modification to obtain the PDFs for

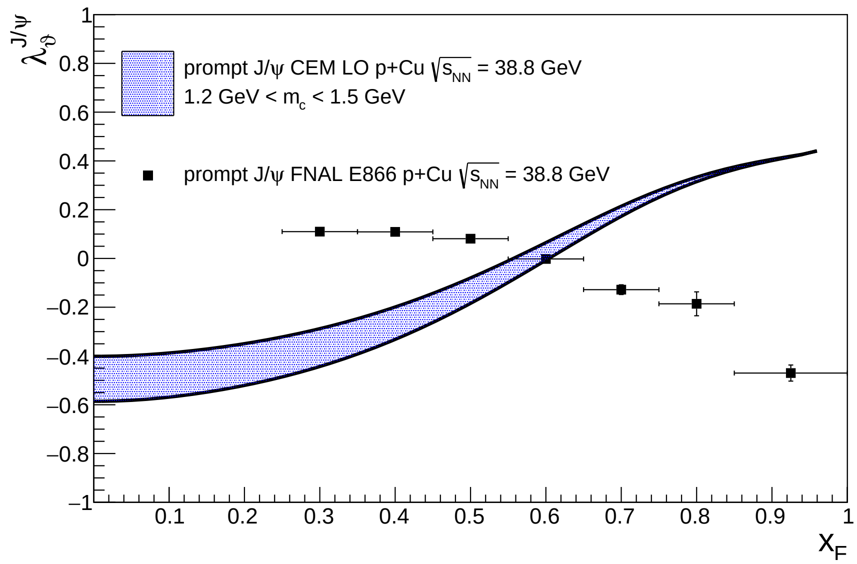

Figure 3.6. The x_F dependence of the polarization parameter λ_ϑ for prompt production of J/ψ in p+Cu collisions at $\sqrt{s_{NN}} = 38.8$ GeV is compared to the E866/NuSea data [86, 87]. The horizontal uncertainties are the experimental bin widths.

Cu and W. We employ the GRS99 [90] pion PDFs. The polarizations measured by the E866/Nusea Collaboration are made in the Collins-Soper frame and the polarization measured by the CIP Collaboration is measured in the Gottfried-Jackson frame. However, at leading order, the polarization axes in the helicity frame, the Collins-Soper frame, and the Gottfried-Jackson frame frame are coincident [34].

3.4.3.1 Prompt production of J/ψ in p+Cu collisions at $\sqrt{s_{NN}} = 38.8$ GeV

We compare our polarization predictions for prompt production of J/ψ in p+Cu collisions at $\sqrt{s} = 38.8$ GeV as a function of x_F on the results measured by the E866/NuSea Collaboration [86, 87] and is shown in Fig. 3.6. Since the x_F dependence is nearly symmetric around $x_F = 0$, the result is presented for positive x_F only. Both J/ψ and $\psi(2\mathrm{S})$ are included in the experimental results, but only about 1% of the contribution comes from the $\psi(2\mathrm{S})$. Our result is longitudinal at small values of x_F and becomes transverse at large x_F. The experimental results disagree with ours since the polarization parameter measured decreases as a function of x_F. Our x_F integrated prediction is $\lambda_\vartheta = -0.41^{+0.05}_{-0.13}$ while the experimental result reports $\lambda_\vartheta = 0.069 \pm 0.004$.

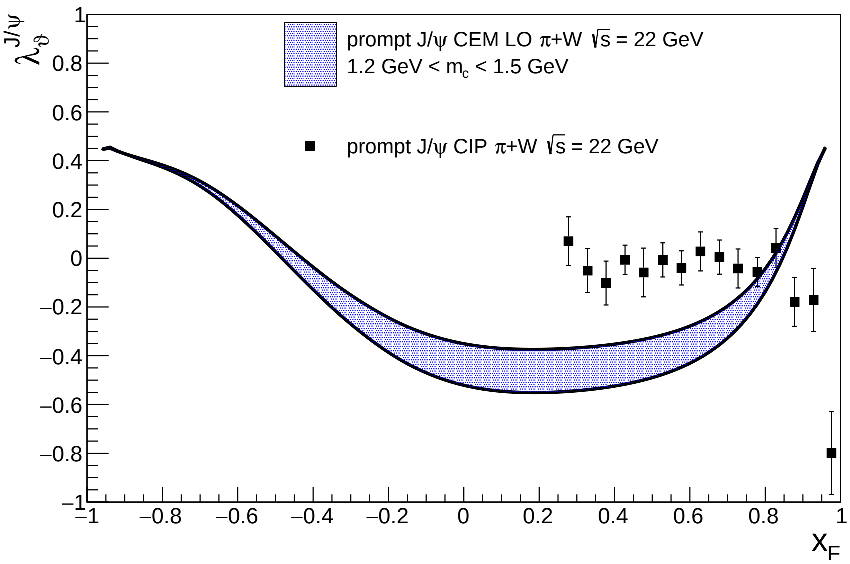

Figure 3.7. The x_F dependence of the polarization parameter λ_ϑ for prompt production of J/ψ in π+W collisions at $\sqrt{s} = 22$ GeV are compared to the CIP data [88].

3.4.3.2 Prompt production of J/ψ in π+W collisions at $\sqrt{s} = 20$ GeV

We compare our polarization predictions for prompt production of J/ψ in π+W collisions at $\sqrt{s} = 20$ GeV as a function of x_F to the measurement by the CIP Collaboration [88] in Fig. 3.7. The x_F dependence is not symmetric around $x_F = 0$ in this case due to the difference in the high x behavior of the pion PDFs relative to that of the proton PDFs. Therefore the result is shown over all x_F. We note that the polarization predictions differ slightly in π+W collisions at $\sqrt{s} = 20$ GeV compared to p+Cu collisions at $\sqrt{s_{NN}} = 38.8$ GeV. The polarization at $x_F = 0$ is less longitudinal in π+W collisions although the trend is similar: longitudinal polarization at small values of x_F and transverse at large x_F. The experimental results disagree with ours since the polarization parameter measured is near unpolarized as a function of x_F except for the last x_F bin. However, our prediction reaches a better agreement with data in π+W compared to p+Cu in terms of the behavior as a function of x_F. Our result predicts in the region of low to mid positive x_F, J/ψ is produced with a relatively constant moderate longitudinal polarization. Our x_F integrated prediction is $\lambda_\vartheta = -0.42^{+0.05}_{-0.13}$ while the experiment reports $\lambda_\vartheta = -0.02 \pm 0.06$.

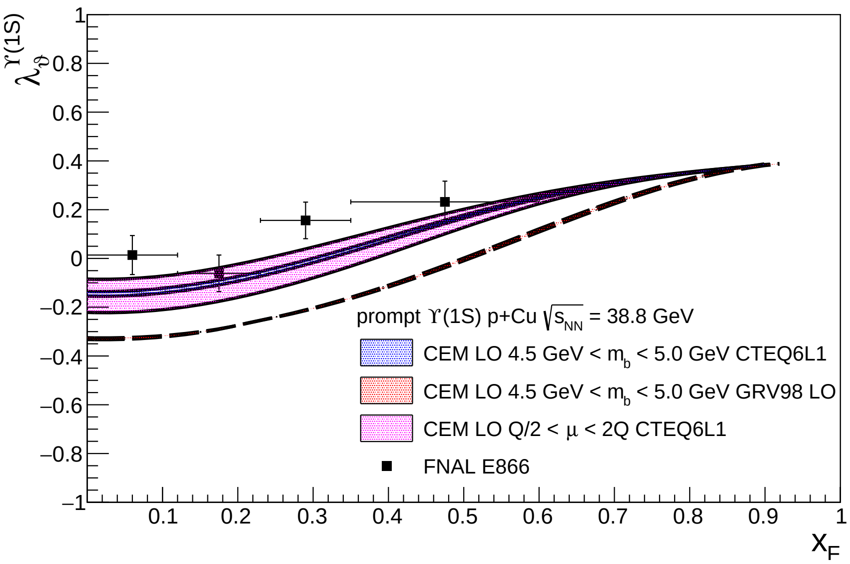

Figure 3.8. The x_F dependence of the polarization parameter λ_ϑ for prompt production of $\Upsilon(1S)$ in p+Cu collisions at $\sqrt{s}$ = 38.8 GeVusing CTEQ6L1 and varying m_b (blue solid), GRV98 LO and varying m_b (red dashed), CTEQ6L1 and varying Q (magenta solid), and the data (box). The horizontal uncertainties on the E866/NuSea data [77] are the bin widths.

3.4.3.3 Prompt production of $\Upsilon(1S)$ in p+Cu collisions at $\sqrt{s_{NN}} = 38.8$ GeV

We now turn to the x_F dependence of the polarization parameter in prompt $\Upsilon(1S)$ production. We compare our polarization predictions for prompt production of $\Upsilon(1S)$ in p+Cu collisions at $\sqrt{s} = 38.8$ GeV to the results measured by the E866/NuSea Collaboration [77] in Fig. 3.8. This is the lowest energy at which $\Upsilon(1S)$ polarization has been measured. Our results is slightly longitudinal at small values of x_F and becomes slightly transverse at large x_F. Our results are comparable to the data since both the predicted and measured polarization parameters increase as a function of x_F. Our result is consistent with the $\sim$0 polarization measured by the E866/NuSea Collaboration. The measured polarization for $\Upsilon(1S)$ independent of x_F is $\lambda_\vartheta = 0.07 \pm 0.04$ while our prediction is $\lambda_\vartheta = -0.06 \pm 0.01$.

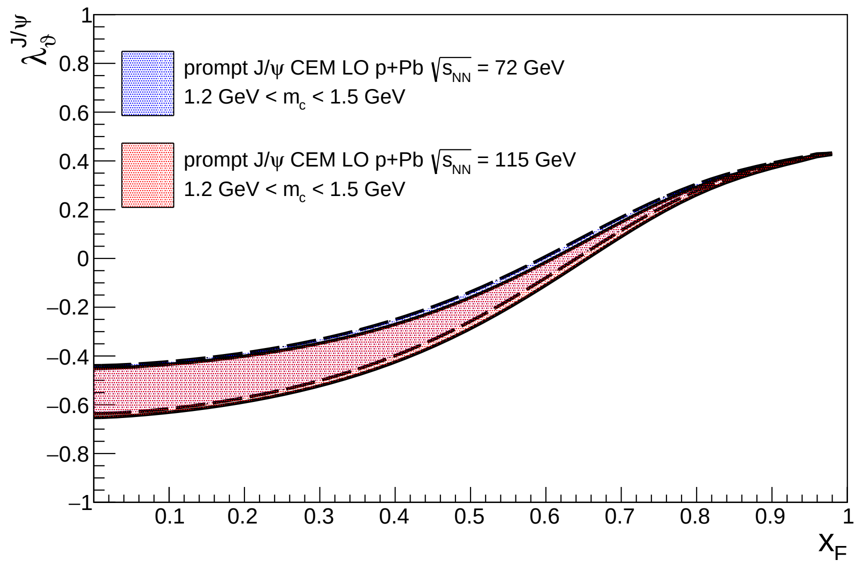

Figure 3.9. The x_F dependence of the polarization parameter λ_ϑ for production of J/ψ in p+Pb at $\sqrt{s_{NN}} = 72$ GeV (blue dashed) and 115 GeV (red solid).

3.4.4 Polarization predictions for prompt production of J/ψ and Υ(1S) in p+Pb collisions at fixed-target energies at the LHC

In this section, we present our polarization predictions for prompt production of J/ψ and Υ(1S) as a function of x_F using Eq. (3.3) for p+Pb fixed-target interactions at the LHC. The polarization predictions are presented for $\sqrt{s_{NN}} = 72$ and 115 GeV, the center-of-mass energies for a lead beam on a proton target and a proton beam on a lead target respectively. Since the x_F dependence is nearly symmetric around $x_F = 0$, the results are only presented for positive x_F. We again multiply the CTEQ6L1 PDFs by the central EPS09 nuclear modification to obtain the lead PDFs. Also, since our predictions are calculated at leading order, they are frame independent.

3.4.4.1 Prompt J/ψ production at the LHC

We present our polarization prediction for prompt J/ψ production in p+Pb interactions at $\sqrt{s_{NN}} = 72$ and 115 GeV as a function of x_F in Fig. 3.9. The longitudinal polarization already starts to saturate at these energies for prompt J/ψ production as presented in Fig. 3.2. Therefore, the polarization for prompt J/ψ production at these energies is very similar. The polarization is longitudinal at small x_F and becomes trans-

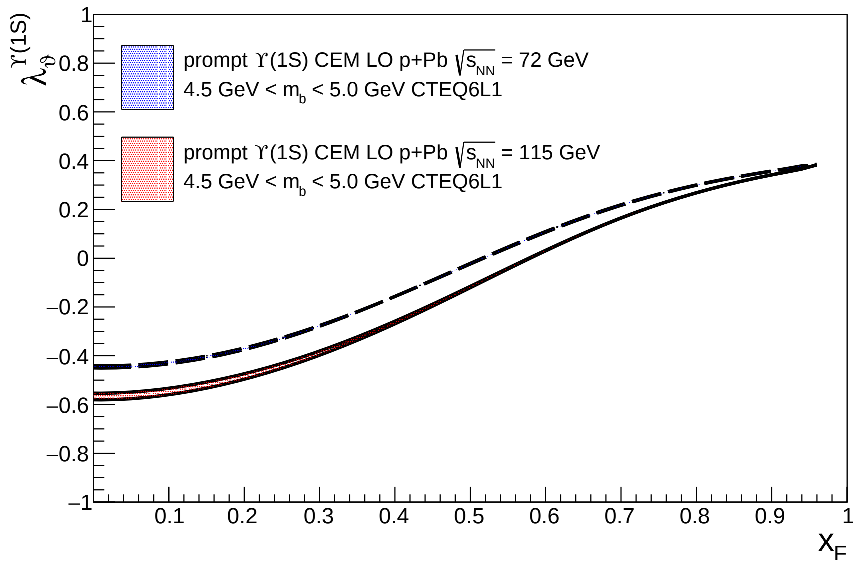

Figure 3.10. The x_F dependence of the polarization parameter λ_ϑ for production of Υ(1S) in p+Pb at $\sqrt{s_{NN}} = 72$ GeV (blue dashed) and 115 GeV (red solid).

verse at large x_F. Our x_F-integrated prediction is $\lambda_\vartheta = -0.46^{+0.04}_{-0.15}$ at $\sqrt{s_{NN}} = 72$ GeV and $\lambda_\vartheta = -0.46^{+0.03}_{-0.17}$ at $\sqrt{s_{NN}} = 115$ GeV.

3.4.4.2 Prompt Υ(1S) production at the LHC

The prediction for the polarization of prompt Υ(1S) production in p+Pb collisions at $\sqrt{s_{NN}} = 72$ and 115 GeV is given as a function of x_F in Fig. 3.10. Because of the higher mass scale, the longitudinal polarization is not saturated at these energies for prompt Υ(1S) production. Therefore, the polarization for prompt Υ(1S) production at these energies is different. The behavior of the polarization at both energies is similar. Prompt Υ(1S) is longitudinal at small x_F and becomes transverse at large x_F. However, the polarization at $\sqrt{s_{NN}} = 115$ GeV is more longitudinal. Our x_F integrated prediction is $\lambda_\vartheta = -0.367^{+0.002}_{-0.001}$ at $\sqrt{s_{NN}} = 72$ GeV and $\lambda_\vartheta = -0.51^{+0.01}_{-0.01}$ at $\sqrt{s_{NN}} = 115$ GeV.

3.4.5 Sensitivity to the proton PDFs

We have tested the sensitivity of our results to the choice of PDFs used in the calculation. Since few new LO proton PDFs are currently available, we compare our CTEQ6L1 results with calculations using the older GRV98 LO [78] set. We can expect the ratio to be the most sensitive to the choice of proton PDF because the PDFs can change the balance of gg to $q\overline{q}$ production, especially at lower $\sqrt{s}$ where the x values probed by the calculations are large, $x \sim 0.1$. In particular, the prompt production of $\Upsilon(1S)$ at $\sqrt{s} = 20$ GeV is most likely to be sensitive to the choice of PDF since the $q\overline{q}$ contribution is large at this energy. The results should, on the other hand, be relatively insensitive to the chosen mass and scale values since these do not strongly affect the relative contributions of gg and $q\overline{q}$.

This is indeed the case, for prompt $\Upsilon(1S)$ production at $\sqrt{s} = 20$ GeV, close to the production threshold, the largest difference in the longitudinal ratio for the two PDF sets is 15% at $y = 0$, making a difference in the polarization parameter, λ_ϑ of 0.35 around the unpolarized region. The sensitivity arises because the gg contributions in the prompt productions of the S states are predominantly produced with $J_z = 0$ while the $q\overline{q}$ contribution is primarily produced with $J_z = \pm 1$. By $\sqrt{s} = 38.8$ GeV, the difference in the results is reduced to 9%, making a difference in λ_ϑ of 0.18 around the slightly longitudinal region. The x_F dependence of prompt $\Upsilon(1S)$ polarization using GRV98 LO is also shown along with the prediction using CTEQ6L1 in Fig. 3.8. The prediction using GRV98 LO is more longitudinal compared to the prediction using CTEQ6L1. At collider energies, the difference is negligible. Since the gg contribution is dominant for J/ψ already at $\sqrt{s} = 20$ GeV, the prompt J/ψ production polarization is essentially independent of the choice of proton PDF. Thus, away from production threshold, the results are robust with respect to the choice of PDF.

3.4.6 Sensitivity to factorization scale

We have tested the sensitivity of our results to the factorization scale, μ. We varied the factorization scale for prompt J/ψ and $\Upsilon(1S)$ in the range: $Q/2 \leq \mu \leq 2Q$ while keeping the renormalization scale the same. We have found the longitudinal to unpolarized fractions $R^{J_z=0}_{J/\psi}$ and $R^{J_z=0}_{\Upsilon(1S)}$ are hardly changed in the range of μ varied at high energies where the polarization is saturated. The ratio for each directly produced charmonium $R^{J_z=0}_{\psi}$ is changed by $\sim$0.01 while $R^{J_z=0}_{\Upsilon}$ is changed by $\sim$0.001 for each directly produced bottomonium. We note that each individual polarized production cross section is affected by the variation in factorization scale. But at high energies, the production is dominated by the gluon fusion processes. Therefore, the polarization, which depends on the longitudinal to unpolarized ratio, is not sensitive to the factorization scale.

However, at fixed-target energies, where gluon fusion does not yet dominate production, the polarization is affected by the variation in the factorization scale. Indeed, the uncertainty bands for prompt Υ(1S) polarization due to varying the factorization scale is wider than that for varying the bottom quark mass at fixed-target energies. We also present the polarization of prompt Υ(1S) by varying the factorization scale at $\sqrt{s_{NN}} = 38.8$ GeV in Fig. 3.8. At $\sqrt{s_{NN}} = 38.8$ GeV, the uncertainty on the polarization of prompt Υ(1S) due to changing the factorization scale is $-0.05^{+0.05}_{-0.08}$, slightly closer to the measured polarization by the E866 Collaboration than that from varying the bottom quark mass. However, the uncertainty band due to factorization scale variation for prompt J/ψ is smaller than that due to changing m_c for all energies. This is because the polarization of prompt J/ψ saturates at a lower energy compared to prompt Υ(1S).

3.4.7 Sensitivity to feed-down ratios

We have tested the sensitivity of our results to the feed-down ratios we use in our calculations [84]. Since the prompt production of J/ψ and Υ(1S) is dominated by direct J/ψ and direct Υ(1S) respectively, we vary the feed-down ratio by changing the relative contribution by direct J/ψ and direct Υ(1S) to other states. That is, when $c_{J/\psi}$ increase, all other c_ψ decrease and vice versa, and similarly for $c_{\Upsilon(1S)}$ and other c_Υ. Using the base values of c_ψ and c_Υ in Table 3.1 and the reported uncertainty, we vary the feed-down ratios as given in Table 3.2. Considering only the variation of the feed-down ratios, the uncertainty on the polarization parameter for prompt J/ψ production at $\sqrt{s} = 7$ TeV is $\lambda_\vartheta = -0.51 \pm 0.01$. These uncertainties are much smaller than those due to the charm quark mass variation. The uncertainty on the polarization parameter for prompt Υ(1S) at $\sqrt{s} = 7$ TeV is $\lambda_\vartheta = -0.69^{+0.03}_{-0.04}$ due to changing c_Υ. These uncertainties are very similar to those due to varying m_b.

Table 3.2. Values of c_Q used to test the sensitivity of our results to the feed-down ratios. Based on the uncertainty in c_Q (third column), c'_Q (second column) is used assuming the promptly produced 1S states comprise less directly produced 1S states, and c''_Q (fourth column) is used assuming the promptly produced 1S states comprise more directly produced 1S states,

Q	c'_Q	c_Q	c''_Q
J/ψ	0.59	0.62±0.04	0.65
ψ(2S)	0.09	0.08±0.02	0.07
χ_{c1}(1P)	0.17	0.16±0.04	0.15
χ_{c2}(1P)	0.15	0.14±0.04	0.13
Υ(1S)	0.43	0.52±0.09	0.61
Υ(2S)	0.12	0.1±0.03	0.08
Υ(3S)	0.03	0.02±0.005	0.01
χ_{b1}(1P)	0.145	0.13±0.035	0.115
χ_{b2}(1P)	0.145	0.13±0.035	0.115
χ_{b1}(2P)	0.065	0.05±0.025	0.035
χ_{b2}(2P)	0.065	0.05±0.025	0.035

3.5 Conclusions

We have presented the energy and rapidity dependence of the polarization of prompt J/ψ and Υ(1S) production in $p+p$ collisions in the color evaporation model. We compare the x_F dependence to experimental results in p+Cu and π+W collisions at fixed-target energies. We also present our polarization predictions as a function of x_F for fixed-target experiments at the LHC. We find prompt J/ψ and Υ(1S) production to be longitudinally polarized, saturating at energies far above the $Q\overline{Q}$ production threshold, with $\lambda_\vartheta^{J/\psi} = -0.51^{+0.05}_{-0.16}$ and $\lambda_\vartheta^{\Upsilon(1S)} = -0.69^{+0.03}_{-0.02}$. We find the prompt J/ψ and Υ(1S) polarization to be longitudinal around central rapidity while the polarization becomes transverse as the kinematic limits of the calculation, where $q\overline{q}$ production is dominant, are approached.

Since our calculation is leading order, we cannot yet calculate the p_T dependence of quarkonium polarization. This will be addressed in a future publication. We will study the x_F dependence by integrating over a finite p_T range and whether it will improve the agreement with the data in Fig. 3.6.

Chapter 4

Production and Polarization of Prompt J/ψ in the Improved Color Evaporation Model using the k_T-factorization Approach

Production and Polarization of Prompt J/ψ in the Improved Color Evaporation Model using the k_T-factorization Approach

V. Cheung[a] and R. Vogt[a,b,1]

[a]Department of Physics
University of California, Davis
Davis, CA 95616, USA
and
[b]Nuclear and Chemical Sciences Division
Lawrence Livermore National Laboratory
Livermore, CA 94551, USA

ABSTRACT

We calculate the polarization of prompt J/ψ production in the improved color evaporation model at leading order employing the k_T-factorization approach. In this paper, we present the polarization parameter λ_ϑ of prompt J/ψ as a function of transverse momentum in $p+p$ and $p+A$ collisions to compare with data in the helicity, Collins-Soper and Gottfried-Jackson frames. We also present calculations of the charmonium production cross sections as a function of rapidity and transverse momentum. This is the first p_T-dependent calculation of charmonium polarization in the improved color evaporation model. We find agreement with both charmonium cross sections and polarization measurements.

[1]This work was performed under the auspices of the U.S. Department of Energy by Lawrence Livermore National Laboratory under Contract DE-AC52-07NA27344 and supported by the U.S. Department of Energy, Office of Science, Office of Nuclear Physics (Nuclear Theory) under contract number DE-SC-0004014.

4.1 Introduction

The production mechanism of quarkonium remains uncertain even more than 40 years after the discovery of the J/ψ. Nonrelativistic QCD (NRQCD) [61], the most widely employed model of quarkonium production encounters serious challenges in both the universality of the long distance matrix elements (LDMEs) and the prediction of quarkonium polarization [53]. The production cross sections in NRQCD, based on an expansion in the strong coupling constant and the $Q\overline{Q}$ velocity [44], is factorized into hard and soft contributions and divided into different color and spin states, including color octet contributions. The LDMEs, which weight the contributions from each color and spin state, are fit to the data above some minimum transverse momentum, p_T. These LDMEs, which are conjectured to be universal, fail to describe the yields and polarization simultaneously for p_T cuts less than twice the mass of the quarkonium state [62, 63]. They also depend on the collision system [54, 79–81]. Moreover, collinear factorization requires a p_T cut to fit the LDMEs to data above this cut. As a result, the polarization predicted by NRQCD is sensitive to the p_T cut [51, 54, 55] in the collinear factorization approach while in the k_T-factorization approach, J/ψ polarization can be calculated in NRQCD without p_T cut [91]. The η_c p_T distributions calculated with LDMEs obtained from J/ψ yields using heavy quark spin symmetry [65–67], can describe the LHCb η_c results [92, 93] but fails if a different p_T cut or feed-down treatment is used [68].

On the other hand, the color evaporation model (CEM) [56,69–71], which considers all $Q\overline{Q}$ ($Q = c, b$) production regardless of the quark color, spin, and momentum, is able to predict both the total yields and the rapidity distributions at hadron colliders with only a single normalization parameter per state [72]. However, the consistency between CEM and J/ψ electroproduction data at low $\sqrt{s}$ seen in Ref. [94] has not yet been addressed in our approach. Reference [95] derived a relationship between the traditional CEM and NRQCD assuming that NRQCD factorization holds to all orders and that the NRQCD sums over color and spin converge. It also assumed that no distinction is made between the spin states in the CEM. Both the CEM and NRQCD can describe production yields rather well but spin-related measurements such as the polarization are strong tests of production models. However, polarization is not the only test of models. The CEM was also used recently to calculate transverse single spin asymmetries in J/ψ production [82, 83].

We have previously presented the first polarization results in the CEM [57], which only considered charmonium and bottomonium production in general, followed by polarization results of the prompt J/ψ and $\Upsilon(1S)$ [58]. The later also took the feed-down production into account using the recently developed improved CEM (ICEM) [56]. However, those results were at leading order (LO) assuming collinear factorization and were thus p_T-independent. This paper serves as a continuation of the previous work by presenting a p_T-dependent LO ICEM calculation of the polarization in prompt J/ψ production using the k_T-factorization approach. This is a p_T-dependent result because the transverse momenta of the incoming gluons and their off-shell properties are not neglected in the k_T-factorization approach. Our calculation provides the first p_T-dependent ICEM polarization result and represents a step toward a full next-to-leading order (NLO) ICEM polarization result. We will begin to address the p_T dependence at NLO in a later publication.

In this paper, we present both the yields and the polarizations of charmonium as a function of p_T by formulating the ICEM in the k_T-factorization approach. In the high-energy limit, the contributions from t-channel gluon exchange can become dominant. The QCD evolution of the gluon distribution functions of the colliding partons is described by the Balitsky-Fadin-Kuraev-Lipatov (BKFL) evolution equation [96]. In this regime, the transverse momentum (k_T) of the incoming gluon can no longer be neglected. This phenomenological framework dealing with Reggeized t-channel gluons, is known as the k_T-factorization approach. We take the same effective Feynman rules for scattering processes involving incoming off-shell gluons [97] as in NRQCD [98]. Effectively, the momentum of the incoming Reggeon, k^μ, with transverse momentum k_T can be written in terms of the proton momentum p^μ and the fraction of longitudinal momentum x carried by the gluon as

$$k^\mu = xp^\mu + k_T^\mu \, . \tag{4.1}$$

The polarization 4-vector is

$$\epsilon^\mu(k_T) = \frac{k_T^\mu}{k_T} \, , \tag{4.2}$$

where $k_T^\mu = (0, \vec{k}_T, 0)$.

In the traditional CEM, all quarkonium states are treated the same as $Q\overline{Q}$ below the $H\overline{H}$ threshold. The invariant mass of the heavy quark-antiquark pair is restricted to be less than twice the mass of the lowest mass meson (H) that can be formed with the heavy quark as a constituent. The distributions for all quarkonium family members are assumed to be identical.

In the ICEM the invariant mass of the intermediate heavy quark-antiquark pair is constrained to be larger than the mass of produced quarkonium state, $M_\mathcal{Q}$, instead of twice the quark mass, $2m_q$, the lower limit in the traditional CEM [57, 69]. Because the charmonium momentum and integration range depend on the mass of the state, the kinematic distributions of the charmonium states are no longer identical in the ICEM and, for example the ψ' to J/ψ ratio depends on p_T. Using the k_T-factorization approach, in a $p+p$ collision, the ICEM production cross section for a directly produced quarkonium state $\mathcal{Q}$ is

$$\begin{aligned} \sigma &= F_\mathcal{Q} \int_{M_\mathcal{Q}^2}^{4m_H^2} d\hat{s} \int \frac{dx_1}{x_1} \int \frac{d\phi_1}{2\pi} \int dk_{1T}{}^2 \Phi_1(x_1, k_{1T}, \mu_{F1}^2) \\ &\times \int \frac{dx_2}{x_2} \int \frac{d\phi_2}{2\pi} \int dk_{2T}{}^2 \Phi_2(x_2, k_{2T}, \mu_{F2}^2) \hat{\sigma}(R + R \to Q\overline{Q}) \\ &\times \delta(\hat{s} - x_1 x_2 s + |\vec{k}_{1T} + \vec{k}_{2T}|^2) \, , \end{aligned} \tag{4.3}$$

where the square of the heavy quark pair invariant mass is $\hat{s}$ while the square of the center-of-mass energy in the $p+p$ collision is s. Here $\Phi(x, k_T, \mu_F^2)$ is the unintegrated parton distribution function (uPDF) for a parton with momentum fraction x and transverse momentum k_T interacting with factorization scale μ_F. The angles $\phi_{1,2}$ in Eq. (4.3) are between the $k_{T1,2}$ of the partons and the p_T of the final state quarkonium $\mathcal{Q}$. The parton-level cross section is $\sigma(R + R \to Q\overline{Q})$. Finally, $F_\mathcal{Q}$ is a universal factor for the directly produced quarkonium state $\mathcal{Q}$, and is independent of the projectile, target, and energy.

In this approach, the cross section is

$$
\begin{aligned}
\frac{d^4\sigma}{dp_T dy d\hat{s} d\phi} &= \sigma\delta(\hat{s} - x_1 x_2 s + p_T^2)\delta\Big(y - \frac{1}{2}\log\frac{x_1}{x_2}\Big)\delta\Big(p_T^2 - |\vec{k}_{1T}^2 + \vec{k}_{2T}^2|\Big)\delta(\phi - (\phi_1 - \phi_2)) \\
&= F_Q \int \frac{2}{\pi} k_{2T} dk_{2T} \sum_{k_{1T}} \Bigg[\frac{\Phi_1(k_{1T}, x_{10}, \mu_{F1}^2)}{x_{10}} \frac{\Phi_2(k_{2T}, x_{20}, \mu_{F2}^2)}{x_{20}} \\
&\times \; k_{1T} p_T \frac{\hat{\sigma}(R + R \to Q\overline{Q})}{s\sqrt{k_{2T}^2(\cos^2\phi - 1) + p_T^2}}\Bigg] , \qquad (4.4)
\end{aligned}
$$

where the sum k_{1T} is over the roots of $k_{1T}^2 + k_{2T}^2 + 2k_{1T}k_{2T}\cos\phi = p_T^2$, and $k_{1T,1}$ and $k_{1T,2}$ are

$$
\begin{aligned}
k_{1T,1} &= -k_{2T}\cos\phi + \sqrt{k_{2T}^2(\cos^2\phi - 1) + p_T^2} \qquad (4.5) \\
k_{1T,2} &= -k_{2T}\cos\phi - \sqrt{k_{2T}^2(\cos^2\phi - 1) + p_T^2} \, . \qquad (4.6)
\end{aligned}
$$

The momentum fractions x_{10} and x_{20} are

$$
\begin{aligned}
x_{10} &= \sqrt{\frac{\hat{s} + p_T^2}{s}} e^{+y} \, , \qquad (4.7) \\
x_{20} &= \sqrt{\frac{\hat{s} + p_T^2}{s}} e^{-y} \, . \qquad (4.8)
\end{aligned}
$$

Here, ϕ is the relative azimuthal angle between two incident Reggeons ($\phi = \phi_1 - \phi_2$) and p_T is the transverse momentum of the produced $Q\overline{Q}$.

The cross section may also be defined in terms of the total longitudinal momentum carried by the $Q\overline{Q}$ pair, x_F, instead of rapidity as

$$
\begin{aligned}
\frac{d^4\sigma}{dp_T dx_F d\hat{s} d\phi} &= \sigma\delta(\hat{s} - x_1 x_2 s + p_T^2)\delta(x_F - (x_1 - x_2))\delta\Big(p_T^2 - |\vec{k}_{1T}^2 + \vec{k}_{2T}^2|\Big) \\
&\times \; \delta(\phi - (\phi_1 - \phi_2)) \\
&= F_Q \int \frac{2}{\pi} k_{2T} dk_{2T} \sum_{k_{1T}} \Bigg[\frac{\Phi_1(k_{1T}, x_{10}, \mu_{F1}^2)}{x_{10}} \frac{\Phi_2(k_{2T}, x_{20}, \mu_{F2}^2)}{x_{20}} \\
&\times \; k_{1T} p_T \frac{\hat{\sigma}(R + R \to Q\overline{Q})}{\sqrt{x_F^2 s^2 + 4(\hat{s} + p_T^2)}\sqrt{k_{2T}^2(\cos^2\phi - 1) + p_T^2}}\Bigg] , \\
& \qquad (4.9)
\end{aligned}
$$

where x_{10} and x_{20} are now

$$x_{10} = \frac{1}{2}\left(x_F + \sqrt{x_F^2 + 4\frac{\hat{s}+p_T^2}{s}}\right) \tag{4.10}$$

$$x_{20} = \frac{1}{2}\left(-x_F + \sqrt{x_F^2 + 4\frac{\hat{s}+p_T^2}{s}}\right) . \tag{4.11}$$

Thus the transverse momentum distribution $d\sigma/dp_T$ in the ICEM is

$$\frac{d\sigma}{dp_T} = \int dy d\hat{s} d\phi \frac{d^4\sigma}{dp_T dy d\hat{s} d\phi} \tag{4.12}$$

$$= \int dx_F d\hat{s} d\phi \frac{d^4\sigma}{dp_T dx_F d\hat{s} d\phi} . \tag{4.13}$$

The two expressions are equivalent when calculating the transverse momentum without any longitudinal kinematic cuts. Equation (4.12) is used to compare to collider data with defined rapidity cuts while Eq. (4.13) is used to compare to fixed-target data with x_F cuts. Similarly, the rapidity distribution $d\sigma/dy$ in the ICEM is

$$\frac{d\sigma}{dy} = \int dp_T d\hat{s} d\phi \frac{d^4\sigma}{dp_T dy d\hat{s} d\phi} . \tag{4.14}$$

We take the renormalization and factorization scales to be $\mu_F = \mu_R = m_T$, where $m_T = \sqrt{\hat{s} + p_T^2}$ is the transverse mass of the $Q\overline{Q}$ pair. We will study the effect of varying these scales on the p_T distributions and the polarization.

4.2 Polarization of directly produced $Q\overline{Q}$

We define the polarization axis (z axis) in the helicity frame where z_{HX} is the flight direction of the quarkonium in the center of mass frame of the colliding beams, as shown in Fig. 4.1. In this section we outline the kinematics required to compute the polarized scattering cross sections in the helicity frame as well as the procedure to relate them to the polarized scattering cross sections in the Gottfried-Jackson frame [32] and the Collins-Soper frame [33].

In the lab frame, using Eqs. (4.1) and (4.2) the momenta of the initial state Reggeons can be written as

$$k_1^\mu = (x_1 s, k_{1T}\cos\phi_1, k_{1T}\sin\phi_1, x_1 s) \tag{4.15}$$

$$k_2^\mu = (x_2 s, k_{2T}\cos\phi_2, k_{2T}\sin\phi_2, -x_2 s) , \tag{4.16}$$

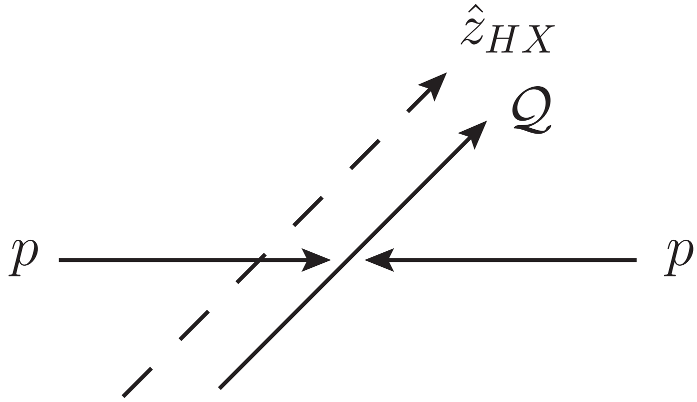

Figure 4.1. The orientation of polarization axis (z axis) in the helicity frame is indicated by the dashed arrow. The proton arrows indicate the incoming beam directions. The polarization axis is defined to be the direction of the produced ($\mathcal{Q}$) travels in the center-of-mass frame of the colliding beams. If the quarks in the $Q\overline{Q}$ pair with total angular momentum $J = 1$, they can either have the same angular momentum along the z axis, J_z, or opposite resulting in $J_z = 0$ (longitudinal) or $J_z = 1$ (transverse), respectively.

with polarization vectors

$$\epsilon_1^\mu = \left(0, \frac{\vec{k}_{1T}}{k_{1T}}, 0\right) = (0, \cos\phi_1, \sin\phi_1, 0) \tag{4.17}$$

$$\epsilon_2^\mu = \left(0, \frac{\vec{k}_{2T}}{k_{2T}}, 0\right) = (0, \cos\phi_2, \sin\phi_2, 0)\ . \tag{4.18}$$

We then boost the momenta along the beam direction to the frame where the total momentum of the Reggeons along the beam direction, $k_{1z} + k_{2z}$, is zero

$$k_1^\mu = \left(\frac{\sqrt{\hat{s} + p_T^2}}{2}, \vec{k}_{1T}, \frac{\sqrt{\hat{s} + p_T^2}}{2}\right)\ , \tag{4.19}$$

$$k_2^\mu = \left(\frac{\sqrt{\hat{s} + p_T^2}}{2}, \vec{k}_{2T}, -\frac{\sqrt{\hat{s} + p_T^2}}{2}\right)\ , \tag{4.20}$$

where $\hat{s} = x_1 x_2 s - |\vec{k}_{1T} + \vec{k}_{2T}|^2$ and $p_T^2 = |\vec{k}_{1T} + \vec{k}_{2T}|^2$. The polarization vectors are unchanged. We then apply a rotation such that the three momentum of the sum $k_1^\mu + k_2^\mu$ is aligned with a new z axis

$$k_1^\mu + k_2^\mu = \left(\sqrt{p_T^2 + \hat{s}}, \vec{0}, p_T\right)\ . \tag{4.21}$$

We then boost to the quarkonium rest frame where

$$k_1^\mu + k_2^\mu \;=\; \left(\sqrt{\hat{s}}, \vec{0}, 0\right) . \tag{4.22}$$

In this frame (helicity frame), the momenta of the initial state Reggeons are

$$k_1^\mu \;=\; \left(\frac{-\psi+\hat{s}}{2\sqrt{\hat{s}}}, \frac{\sqrt{\hat{s}}\lambda}{2}, \frac{k_{1T}k_{2T}\sin\phi}{p_T}, \frac{\psi\lambda}{2p_T}\right) , \tag{4.23}$$

$$k_2^\mu \;=\; \left(\frac{\psi+\hat{s}}{2\sqrt{\hat{s}}}, -\frac{\sqrt{\hat{s}}\lambda}{2}, -\frac{k_{1T}k_{2T}|\sin\phi}{p_T}, -\frac{\psi\lambda}{2p_T}\right) , \tag{4.24}$$

where $\psi = |\vec{k}_{1T}|^2 - |\vec{k}_{2T}|^2$, $\phi = \phi_1 - \phi_2$, and $\lambda = \sqrt{1 + p_T^2/\hat{s}}$. The polarization vectors are now

$$\epsilon_1^\mu \;=\; \left(-\frac{k_{1T}+k_{2T}\cos\phi}{\sqrt{\hat{s}}}, 0, \frac{k_{2T}\sin\phi}{p_T}, \frac{\lambda}{p_T}(k_{1T}+k_{2T}\cos\phi)\right) , \tag{4.25}$$

$$\epsilon_2^\mu \;=\; \left(-\frac{k_{2T}+k_{1T}\cos\phi}{\sqrt{\hat{s}}}, 0, -\frac{k_{1T}\sin\phi}{p_T}, \frac{\lambda}{p_T}(k_{2T}+k_{1T}\cos\phi)\right) . \tag{4.26}$$

The scattering amplitude of the process $R+R \to Q\overline{Q}$ is related to that of $g+g \to Q\overline{Q}$ by [97, 98]

$$\mathcal{A}(R+R \to Q+\overline{Q}) \;=\; \epsilon^\mu(k_1)\epsilon^\nu(k_2)\mathcal{A}_{\mu\nu}(g+g \to Q+\overline{Q}) , \tag{4.27}$$

where $\epsilon^\mu(k)$ is defined in Eq. (4.2). Evaluating $\mathcal{A}_{\mu\nu}(g+g \to Q+\overline{Q})$ using the conventional Feynman rules of QCD, there are three $gg \to Q\overline{Q}$ Feynman diagrams to consider at $\mathcal{O}(\alpha_s^2)$. The diagrams are labeled according to the squared mass of the propagator as $\hat{s}$, $\hat{t}$ and $\hat{u}$,

$$\hat{s} \;=\; (k_1+k_2)^2 , \tag{4.28}$$

$$\hat{t} \;=\; (k_1-p_2)^2 , \tag{4.29}$$

$$\hat{u} \;=\; (k_2-p_2)^2 , \tag{4.30}$$

where k_1 and k_2 are the momenta of the initial state Reggeons, and p_1 (p_2) is the momentum of the final state heavy quark (antiquark). Each diagram includes a color factor C and a scattering amplitude $\mathcal{A}$. The generic matrix element for the gluon fusion process can be written as [73]

$$\mathcal{M}_{gg} \;=\; C_{gg,\hat{s}}\mathcal{A}_{gg,\hat{s}} + C_{gg,\hat{t}}\mathcal{A}_{gg,\hat{t}} + C_{gg,\hat{u}}\mathcal{A}_{gg,\hat{u}} . \tag{4.31}$$

In terms of the Dirac spinors u and v, the individual amplitudes are

$$\begin{aligned}
\mathcal{A}_{gg,\hat{s}} &= -\frac{g_s^2}{\hat{s}}\Big\{ -(2k_2+k_1)\cdot\epsilon(k_1)[\bar{u}(p_1)\not{\epsilon}(k_2)v(p_2)] \\
&+ (2k_1+k_2)\cdot\epsilon(k_2)[\bar{u}(p_1)\not{\epsilon}(k_1)v(p_2)] \\
&+ \epsilon(k_1)\cdot\epsilon(k_2)[\bar{u}(p_1)(\not{k}_2-\not{k}_1)v(p_2)]\Big\}\ , && (4.32) \\
\mathcal{A}_{gg,\hat{t}} &= -\frac{g_s^2}{\hat{t}-m_c^2}\bar{u}(p_1)\not{\epsilon}(k_2)(\not{k}_1-\not{p}_2+m_c)\not{\epsilon}(k_1)v(p_2)\ , && (4.33) \\
\mathcal{A}_{gg,\hat{u}} &= -\frac{g_s^2}{\hat{u}-m_c^2}\bar{u}(p_1)\not{\epsilon}(k_1)(\not{k}_2-\not{p}_2+m_c)\not{\epsilon}(k_2)v(p_2)\ . && (4.34)
\end{aligned}$$

Here g_s is the gauge coupling, m_c is the charm quark mass, and ϵ represents the gluon polarization vectors.

In the process of evaluating the scattering amplitudes, we take advantage of the fact that at $\mathcal{O}(\alpha_s^2)$, the final state $Q\overline{Q}$ is produced with no dependence on the azimuthal angle ϕ' (and thus $L_{z'}=0$) in a rotated frame (primed frame) where the z' axis is defined as the direction of one of the incoming Reggeons. Since the Reggeons are head to head in this frame, the scattering amplitudes are independent of the azimuthal angle ϕ'. We first rotate the initial state momenta $\vec{p}$ from the helicity frame to the primed frame by an Euler rotation:

$$\vec{p'} = \mathcal{R}(0,\beta,\gamma)\vec{p}. \qquad (4.35)$$

The scattering amplitudes in the primed frame for $S=1$, sorted $S_{z'}$, are

$$\begin{aligned}
\mathcal{A}_{gg,\hat{s},S=1,S_{z'}=0} &= \frac{1}{\sqrt{2}}[(\mathcal{A}_{s1})+(\mathcal{A}_{s4})]\ , && (4.36) \\
\mathcal{A}_{gg,\hat{s},S=1,S_{z'}=\pm1} &= \mathcal{A}_{s2,3}\ , && (4.37) \\
\mathcal{A}_{gg,\hat{t},S=1,S_{z'}=0} &= \frac{1}{\sqrt{2}}[(\mathcal{A}_{t1})+(\mathcal{A}_{t4})]\ , && (4.38) \\
\mathcal{A}_{gg,\hat{t},S=1,S_{\prime}=\pm1} &= \mathcal{A}_{t2,3}\ , && (4.39) \\
\mathcal{A}_{gg,\hat{u},S=1,S_{z'}=0} &= \frac{1}{\sqrt{2}}[(\mathcal{A}_{u1})+(\mathcal{A}_{u4})]\ , && (4.40) \\
\mathcal{A}_{gg,\hat{u},S=1,S_{\prime}=\pm1} &= \mathcal{A}_{u2,3}\ , && (4.41)
\end{aligned}$$

where $\mathcal{A}_1$, $\mathcal{A}_2$, $\mathcal{A}_3$, and $\mathcal{A}_4$ refer to the amplitudes for the quark (antiquark) being projected to the positive (positive), positive (negative), negative (positive), and negative (negative) helicity states, respectively.

The $\hat{s}$-channel amplitudes are

$$\begin{aligned}
\mathcal{A}_{s1}\frac{\hat{s}}{g_s^2} &= \frac{m_c}{\sqrt{\hat{s}}}\Big[[(-\psi+3\hat{s})\epsilon_1^3\epsilon_2^0+(-\psi-3\hat{s})\epsilon_1^0\epsilon_2^3 \\
&+ (-2\epsilon_1^0\epsilon_2^0+2\epsilon_1^1\epsilon_2^1+2\epsilon_1^2\epsilon_2^2)\sqrt{(k_{1T}-k_{2T})^2+\hat{s})(k_{1T}+k_{2T})^2+\hat{s})}]\cos\theta' \\
&- [(\psi-3\hat{s})\epsilon_1^1\epsilon_2^0+(\psi+3\hat{s})\epsilon_1^0\epsilon_2^1 \\
&+ (\epsilon_1^3\epsilon_2^1+\epsilon_1^1\epsilon_2^3)\sqrt{(k_{1T}-k_{2T})^2+\hat{s})(k_{1T}+k_{2T})^2+\hat{s})}]\sin\theta'\Big]\ ,
\end{aligned} \tag{4.42}$$

$$\begin{aligned}
\mathcal{A}_{s2}\frac{\hat{s}}{g_s^2} &= \frac{i}{2}[(\psi-3\hat{s})\epsilon_1^2\epsilon_2^0+(\psi+3\hat{s})\epsilon_1^0\epsilon_2^2 \\
&+ (\epsilon_1^3\epsilon_2^2+\epsilon_1^2\epsilon_2^3)\sqrt{(k_{1T}-k_{2T})^2+\hat{s})(k_{1T}+k_{2T})^2+\hat{s})}] \\
&- \frac{1}{2}[(\psi-3\hat{s})\epsilon_1^1\epsilon_2^0+(\psi+3\hat{s})\epsilon_1^0\epsilon_2^1 \\
&+ (\epsilon_1^3\epsilon_2^1+\epsilon_1^1\epsilon_2^3)\sqrt{(k_{1T}-k_{2T})^2+\hat{s})(k_{1T}+k_{2T})^2+\hat{s})}]\cos\theta' \\
&+ \frac{1}{2}[(\psi-3\hat{s})\epsilon_1^3\epsilon_2^0+(\psi+3\hat{s})\epsilon_1^0\epsilon_2^3 \\
&+ (2\epsilon_1^0\epsilon_2^0-2\epsilon_1^1\epsilon_2^1-2\epsilon_1^2\epsilon_2^2)\sqrt{(k_{1T}-k_{2T})^2+\hat{s})(k_{1T}+k_{2T})^2+\hat{s})}]\sin\theta'\ ,
\end{aligned} \tag{4.43}$$

$$\begin{aligned}
\mathcal{A}_{s3}\frac{\hat{s}}{g_s^2} &= -\frac{i}{2}[(\psi-3\hat{s})\epsilon_1^2\epsilon_2^0+(\psi+3\hat{s})\epsilon_1^0\epsilon_2^2 \\
&+ (\epsilon_1^3\epsilon_2^2+\epsilon_1^2\epsilon_2^3)\sqrt{(k_{1T}-k_{2T})^2+\hat{s})(k_{1T}+k_{2T})^2+\hat{s})}] \\
&- \frac{1}{2}[(\psi-3\hat{s})\epsilon_1^1\epsilon_2^0+(\psi+3\hat{s})\epsilon_1^0\epsilon_2^1 \\
&+ (\epsilon_1^3\epsilon_2^1+\epsilon_1^1\epsilon_2^3)\sqrt{(k_{1T}-k_{2T})^2+\hat{s})(k_{1T}+k_{2T})^2+\hat{s})}]\cos\theta' \\
&+ \frac{1}{2}[(\psi-3\hat{s})\epsilon_1^3\epsilon_2^0+(\psi+3\hat{s})\epsilon_1^0\epsilon_2^3 \\
&+ (2\epsilon_1^0\epsilon_2^0-2\epsilon_1^1\epsilon_2^1-2\epsilon_1^2\epsilon_2^2)\sqrt{(k_{1T}-k_{2T})^2+\hat{s})(k_{1T}+k_{2T})^2+\hat{s})}]\sin\theta'\ ,
\end{aligned} \tag{4.44}$$

$$\begin{aligned}
\mathcal{A}_{s4}\frac{\hat{s}}{g_s^2} &= \frac{m_c}{\sqrt{\hat{s}}}\Big[[(\psi-3\hat{s})\epsilon_1^3\epsilon_2^0+(\psi+3\hat{s})\epsilon_1^0\epsilon_2^3 \\
&+ (2\epsilon_1^0\epsilon_2^0-2\epsilon_1^1\epsilon_2^1-2\epsilon_1^2\epsilon_2^2)\sqrt{(k_{1T}-k_{2T})^2+\hat{s})(k_{1T}+k_{2T})^2+\hat{s})}]\cos\theta' \\
&+ [(\psi-3\hat{s})\epsilon_1^1\epsilon_2^0+(\psi+3\hat{s})\epsilon_1^0\epsilon_2^1 \\
&+ (\epsilon_1^3\epsilon_2^1+\epsilon_1^1\epsilon_2^3)\sqrt{(k_{1T}-k_{2T})^2+\hat{s})(k_{1T}+k_{2T})^2+\hat{s})}]\sin\theta'\Big]\ .
\end{aligned} \tag{4.45}$$

The $\hat{t}$-channel amplitudes are

$$
\begin{aligned}
\mathcal{A}_{t1}\frac{\hat{t}-m_c^2}{g_s^2} &= -2\epsilon_1^1\epsilon_2^1 m_c\sqrt{\hat{s}}\chi + i\frac{(\epsilon_1^2\epsilon_2^1-\epsilon_1^1\epsilon_2^2)m_c\sqrt{(k_{1T}-k_{2T})^2+\hat{s})(k_{1T}+k_{2T})^2+\hat{s})}}{\sqrt{\hat{s}}} \\
&- \frac{m_c}{\sqrt{\hat{s}}}\Big[(\psi-\hat{s})\epsilon_1^3\epsilon_2^0+(\psi+\hat{s})\epsilon_1^0\epsilon_2^3 \\
&+ (\epsilon_1^0\epsilon_2^0-\epsilon_1^1\epsilon_2^1-\epsilon_1^2\epsilon_2^2+\epsilon_1^3\epsilon_2^3)\sqrt{(k_{1T}-k_{2T})^2+\hat{s})(k_{1T}+k_{2T})^2+\hat{s})}\Big]\cos\theta' \\
&+ 2m_c\sqrt{\hat{s}}\chi(\epsilon_1^1\epsilon_2^1-\epsilon_1^3\epsilon_2^3)\cos^2\theta' \\
&- \frac{m_c}{\sqrt{\hat{s}}}\Big[(\psi-\hat{s})\epsilon_1^1\epsilon_2^0+(\psi+\hat{s})\epsilon_1^0\epsilon_2^1 \\
&+ (\epsilon_1^3\epsilon_2^1+\epsilon_1^1\epsilon_2^3)\sqrt{(k_{1T}-k_{2T})^2+\hat{s})(k_{1T}+k_{2T})^2+\hat{s})}\Big]\sin\theta' \\
&- 2m_c\sqrt{\hat{s}}\chi(\epsilon_1^3\epsilon_2^1+\epsilon_1^1\epsilon_2^3)\sin\theta'\cos\theta'\ ,
\end{aligned}
\tag{4.46}
$$

$$
\begin{aligned}
\mathcal{A}_{t2}\frac{\hat{t}-m_c^2}{g_s^2} &= -\frac{1}{2}\Big[(\psi-\hat{s})\epsilon_1^3\epsilon_2^1-(\psi+\hat{s})\epsilon_1^1\epsilon_2^3 \\
&- (\epsilon_1^1\epsilon_2^0-\epsilon_1^0\epsilon_2^1)\sqrt{(k_{1T}-k_{2T})^2+\hat{s})(k_{1T}+k_{2T})^2+\hat{s})}\Big]\chi \\
&+ i\frac{1}{2}\Big[(\psi-\hat{s})\epsilon_1^2\epsilon_2^0+(\psi+\hat{s})\epsilon_1^0\epsilon_2^2 \\
&+ (\epsilon_1^3\epsilon_2^2+\epsilon_1^2\epsilon_2^3)\sqrt{(k_{1T}-k_{2T})^2+\hat{s})(k_{1T}+k_{2T})^2+\hat{s})}\Big] \\
&- \frac{1}{2}\Big[(\psi-\hat{s})\epsilon_1^1\epsilon_2^0+(\psi+\hat{s})\epsilon_1^0\epsilon_2^1 \\
&+ (\epsilon_1^3\epsilon_2^1+\epsilon_1^1\epsilon_2^3)\sqrt{(k_{1T}-k_{2T})^2+\hat{s})(k_{1T}+k_{2T})^2+\hat{s})}\Big]\cos\theta' \\
&- i\frac{1}{2}\Big[(\psi-\hat{s})\epsilon_1^2\epsilon_2^3-(\psi+\hat{s})\epsilon_1^3\epsilon_2^2 \\
&+ (\epsilon_1^2\epsilon_2^0-\epsilon_1^0\epsilon_2^2)\sqrt{(k_{1T}-k_{2T})^2+\hat{s})(k_{1T}+k_{2T})^2+\hat{s})}\Big]\chi\cos\theta' \\
&- (\epsilon_1^3\epsilon_2^1+\epsilon_1^1\epsilon_2^3)\hat{s}\chi\cos^2\theta' \\
&+ \frac{1}{2}\Big[(\psi-\hat{s})\epsilon_1^3\epsilon_2^0+(\psi+\hat{s})\epsilon_1^0\epsilon_2^3 \\
&+ (\epsilon_1^0\epsilon_2^0-\epsilon_1^1\epsilon_2^1-\epsilon_1^2\epsilon_2^2+\epsilon_1^3\epsilon_2^3)\sqrt{(k_{1T}-k_{2T})^2+\hat{s})(k_{1T}+k_{2T})^2+\hat{s})}\Big]\sin\theta' \\
&- i\frac{1}{2}\Big[(\psi-\hat{s})\epsilon_1^2\epsilon_2^1-(\psi+\hat{s})\epsilon_1^1\epsilon_2^2\Big]\chi\sin\theta' \\
&- (\epsilon_1^1\epsilon_2^1-\epsilon_1^3\epsilon_2^3)\hat{s}\chi\sin\theta'\cos\theta'\ ,
\end{aligned}
\tag{4.47}
$$

$$
\begin{aligned}
\mathcal{A}_{t3}\frac{\hat{t}-m_c^2}{g_s^2} &= -\frac{1}{2}\Big[(\psi-\hat{s})\epsilon_1^3\epsilon_2^1-(\psi+\hat{s})\epsilon_1^1\epsilon_2^3 \\
&- (\epsilon_1^1\epsilon_2^0-\epsilon_1^0\epsilon_2^1)\sqrt{(k_{1T}-k_{2T})^2+\hat{s})(k_{1T}+k_{2T})^2+\hat{s})}\Big]\chi \\
&- i\frac{1}{2}\Big[(\psi-\hat{s})\epsilon_1^2\epsilon_2^0+(\psi+\hat{s})\epsilon_1^0\epsilon_2^2 \\
&+ (\epsilon_1^3\epsilon_2^2+\epsilon_1^2\epsilon_2^3)\sqrt{(k_{1T}-k_{2T})^2+\hat{s})(k_{1T}+k_{2T})^2+\hat{s})}\Big] \\
&- \frac{1}{2}\Big[(\psi-\hat{s})\epsilon_1^1\epsilon_2^0+(\psi+\hat{s})\epsilon_1^0\epsilon_2^1 \\
&+ (\epsilon_1^3\epsilon_2^1+\epsilon_1^1\epsilon_2^3)\sqrt{(k_{1T}-k_{2T})^2+\hat{s})(k_{1T}+k_{2T})^2+\hat{s})}\Big]\cos\theta' \\
&+ i\frac{1}{2}\Big[(\psi-\hat{s})\epsilon_1^2\epsilon_2^3-(\psi+\hat{s})\epsilon_1^3\epsilon_2^2 \\
&+ (\epsilon_1^2\epsilon_2^0-\epsilon_1^0\epsilon_2^2)\sqrt{(k_{1T}-k_{2T})^2+\hat{s})(k_{1T}+k_{2T})^2+\hat{s})}\Big]\chi\cos\theta' \\
&- (\epsilon_1^3\epsilon_2^1+\epsilon_1^1\epsilon_2^3)\hat{s}\chi\cos^2\theta' \\
&+ \frac{1}{2}\Big[(\psi-\hat{s})\epsilon_1^3\epsilon_2^0+(\psi+\hat{s})\epsilon_1^0\epsilon_2^3 \\
&+ (\epsilon_1^0\epsilon_2^0-\epsilon_1^1\epsilon_2^1-\epsilon_1^2\epsilon_2^2+\epsilon_1^3\epsilon_2^3)\sqrt{(k_{1T}-k_{2T})^2+\hat{s})(k_{1T}+k_{2T})^2+\hat{s})}\Big]\sin\theta' \\
&+ i\frac{1}{2}\Big[(\psi-\hat{s})\epsilon_1^2\epsilon_2^1-(\psi+\hat{s})\epsilon_1^1\epsilon_2^2\Big]\chi\sin\theta' \\
&- (\epsilon_1^1\epsilon_2^1-\epsilon_1^3\epsilon_2^3)\hat{s}\chi\sin\theta'\cos\theta'\ ,
\end{aligned} \tag{4.48}
$$

$$
\begin{aligned}
\mathcal{A}_{t4}\frac{\hat{t}-m_c^2}{g_s^2} &= 2\epsilon_1^1\epsilon_2^1 m_c\sqrt{\hat{s}}\chi + i\frac{(\epsilon_1^2\epsilon_2^1-\epsilon_1^1\epsilon_2^2)m_c\sqrt{(k_{1T}-k_{2T})^2+\hat{s})(k_{1T}+k_{2T})^2+\hat{s})}}{\sqrt{\hat{s}}} \\
&+ \frac{m_c}{\sqrt{\hat{s}}}\Big[(\psi-\hat{s})\epsilon_1^3\epsilon_2^0+(\psi+\hat{s})\epsilon_1^0\epsilon_2^3 \\
&+ (\epsilon_1^0\epsilon_2^0-\epsilon_1^1\epsilon_2^1-\epsilon_1^2\epsilon_2^2+\epsilon_1^3\epsilon_2^3)\sqrt{(k_{1T}-k_{2T})^2+\hat{s})(k_{1T}+k_{2T})^2+\hat{s})}\Big]\cos\theta' \\
&- 2m_c\sqrt{\hat{s}}\chi(\epsilon_1^1\epsilon_2^1-\epsilon_1^3\epsilon_2^3)\cos^2\theta' \\
&+ \frac{m_c}{\sqrt{\hat{s}}}\Big[(\psi-\hat{s})\epsilon_1^1\epsilon_2^0+(\psi+\hat{s})\epsilon_1^0\epsilon_2^1 \\
&+ (\epsilon_1^3\epsilon_2^1+\epsilon_1^1\epsilon_2^3)\sqrt{(k_{1T}-k_{2T})^2+\hat{s})(k_{1T}+k_{2T})^2+\hat{s})}\Big]\sin\theta' \\
&+ 2m_c\sqrt{\hat{s}}\chi(\epsilon_1^3\epsilon_2^1+\epsilon_1^1\epsilon_2^3)\sin\theta'\cos\theta'\ .
\end{aligned} \tag{4.49}
$$

Finally, the $\hat{u}$-channel amplitudes are

$$
\begin{aligned}
\mathcal{A}_{u1}\frac{\hat{u}-m_c^2}{g_s^2} &= -2\epsilon_1^1\epsilon_2^1 m_c\sqrt{\hat{s}}\chi + i\frac{(\epsilon_1^2\epsilon_2^1-\epsilon_1^1\epsilon_2^2)M\sqrt{(k_{1T}-k_{2T})^2+\hat{s})(k_{1T}+k_{2T})^2+\hat{s})}}{\sqrt{\hat{s}}} \\
&+ \frac{m_c}{\sqrt{\hat{s}}}\Big[(\psi-\hat{s})\epsilon_1^3\epsilon_2^0+(\psi+\hat{s})\epsilon_1^0\epsilon_2^3 \\
&+ (\epsilon_1^0\epsilon_2^0-\epsilon_1^1\epsilon_2^1-\epsilon_1^2\epsilon_2^2+\epsilon_1^3\epsilon_2^3)\sqrt{(k_{1T}-k_{2T})^2+\hat{s})(k_{1T}+k_{2T})^2+\hat{s})}\Big]\cos\theta' \\
&+ 2m_c\sqrt{\hat{s}}\chi(\epsilon_1^1\epsilon_2^1-\epsilon_1^3\epsilon_2^3)\cos^2\theta' \\
&+ \frac{m_c}{\sqrt{\hat{s}}}\Big[(\psi-\hat{s})\epsilon_1^1\epsilon_2^0+(\psi+\hat{s})\epsilon_1^0\epsilon_2^1 \\
&+ (\epsilon_1^3\epsilon_2^1+\epsilon_1^1\epsilon_2^3)\sqrt{(k_{1T}-k_{2T})^2+\hat{s})(k_{1T}+k_{2T})^2+\hat{s})}\Big]\sin\theta' \\
&- 2m_c\sqrt{\hat{s}}\chi(\epsilon_1^3\epsilon_2^1+\epsilon_1^1\epsilon_2^3)\sin\theta'\cos\theta' \ ,
\end{aligned} \tag{4.50}
$$

$$
\begin{aligned}
\mathcal{A}_{u2}\frac{\hat{u}-m_c^2}{g_s^2} &= -\frac{1}{2}\Big[(\psi-\hat{s})\epsilon_1^3\epsilon_2^1-(\psi+\hat{s})\epsilon_1^1\epsilon_2^3 \\
&- (\epsilon_1^1\epsilon_2^0-\epsilon_1^0\epsilon_2^1)\sqrt{(k_{1T}-k_{2T})^2+\hat{s})(k_{1T}+k_{2T})^2+\hat{s})}\Big]\chi \\
&- i\frac{1}{2}\Big[(\psi-\hat{s})\epsilon_1^2\epsilon_2^0+(\psi+\hat{s})\epsilon_1^0\epsilon_2^2 \\
&+ (\epsilon_1^3\epsilon_2^2+\epsilon_1^2\epsilon_2^3)\sqrt{(k_{1T}-k_{2T})^2+\hat{s})(k_{1T}+k_{2T})^2+\hat{s})}\Big] \\
&+ \frac{1}{2}\Big[(\psi-\hat{s})\epsilon_1^1\epsilon_2^0+(\psi+\hat{s})\epsilon_1^0\epsilon_2^1 \\
&+ (\epsilon_1^3\epsilon_2^1+\epsilon_1^1\epsilon_2^3)\sqrt{(k_{1T}-k_{2T})^2+\hat{s})(k_{1T}+k_{2T})^2+\hat{s})}\Big]\cos\theta' \\
&- i\frac{1}{2}\Big[(\psi-\hat{s})\epsilon_1^2\epsilon_2^3-(\psi+\hat{s})\epsilon_1^3\epsilon_2^2 \\
&+ (\epsilon_1^2\epsilon_2^0-\epsilon_1^0\epsilon_2^2)\sqrt{(k_{1T}-k_{2T})^2+\hat{s})(k_{1T}+k_{2T})^2+\hat{s})}\Big]\chi\cos\theta' \\
&- (\epsilon_1^3\epsilon_2^1+\epsilon_1^1\epsilon_2^3)\hat{s}\chi\cos^2\theta' \\
&- \frac{1}{2}\Big[(\psi-\hat{s})\epsilon_1^3\epsilon_2^0+(\psi+\hat{s})\epsilon_1^0\epsilon_2^3 \\
&+ (\epsilon_1^0\epsilon_2^0-\epsilon_1^1\epsilon_2^1-\epsilon_1^2\epsilon_2^2+\epsilon_1^3\epsilon_2^3)\sqrt{(k_{1T}-k_{2T})^2+\hat{s})(k_{1T}+k_{2T})^2+\hat{s})}\Big]\sin\theta' \\
&- i\frac{1}{2}\Big[(\psi-\hat{s})\epsilon_1^2\epsilon_2^1-(\psi+\hat{s})\epsilon_1^1\epsilon_2^2\Big]\chi\sin\theta' \\
&- (\epsilon_1^1\epsilon_2^1-\epsilon_1^3\epsilon_2^3)\hat{s}\chi\sin\theta'\cos\theta' \ ,
\end{aligned} \tag{4.51}
$$

$$
\begin{aligned}
\mathcal{A}_{u3}\frac{\hat{u}-m_c^2}{g_s^2} &= -\frac{1}{2}\Big[(\psi-\hat{s})\epsilon_1^3\epsilon_2^1-(\psi+\hat{s})\epsilon_1^1\epsilon_2^3 \\
&- (\epsilon_1^1\epsilon_2^0-\epsilon_1^0\epsilon_2^1)\sqrt{(k_{1T}-k_{2T})^2+\hat{s})(k_{1T}+k_{2T})^2+\hat{s})}\Big]\chi \\
&+ i\frac{1}{2}\Big[(\psi-\hat{s})\epsilon_1^2\epsilon_2^0+(\psi+\hat{s})\epsilon_1^0\epsilon_2^2 \\
&+ (\epsilon_1^3\epsilon_2^2+\epsilon_1^2\epsilon_2^3)\sqrt{(k_{1T}-k_{2T})^2+\hat{s})(k_{1T}+k_{2T})^2+\hat{s})}\Big] \\
&+ \frac{1}{2}\Big[(\psi-\hat{s})\epsilon_1^1\epsilon_2^0+(\psi+\hat{s})\epsilon_1^0\epsilon_2^1 \\
&+ (\epsilon_1^3\epsilon_2^1+\epsilon_1^1\epsilon_2^3)\sqrt{(k_{1T}-k_{2T})^2+\hat{s})(k_{1T}+k_{2T})^2+\hat{s})}\Big]\cos\theta' \\
&+ i\frac{1}{2}\Big[(\psi-\hat{s})\epsilon_1^2\epsilon_2^3-(\psi+\hat{s})\epsilon_1^3\epsilon_2^2 \\
&+ (\epsilon_1^2\epsilon_2^0-\epsilon_1^0\epsilon_2^2)\sqrt{(k_{1T}-k_{2T})^2+\hat{s})(k_{1T}+k_{2T})^2+\hat{s})}\Big]\chi\cos\theta' \\
&- (\epsilon_1^3\epsilon_2^1+\epsilon_1^1\epsilon_2^3)\hat{s}\chi\cos^2\theta' \\
&- \frac{1}{2}\Big[(\psi-\hat{s})\epsilon_1^3\epsilon_2^0+(\psi+\hat{s})\epsilon_1^0\epsilon_2^3 \\
&+ (\epsilon_1^0\epsilon_2^0-\epsilon_1^1\epsilon_2^1-\epsilon_1^2\epsilon_2^2+\epsilon_1^3\epsilon_2^3)\sqrt{(k_{1T}-k_{2T})^2+\hat{s})(k_{1T}+k_{2T})^2+\hat{s})}\Big]\sin\theta' \\
&+ i\frac{1}{2}\Big[(\psi-\hat{s})\epsilon_1^2\epsilon_2^1-(\psi+\hat{s})\epsilon_1^1\epsilon_2^2\Big]\chi\sin\theta' \\
&- (\epsilon_1^1\epsilon_2^1-\epsilon_1^3\epsilon_2^3)\hat{s}\chi\sin\theta'\cos\theta'\ , \qquad (4.52)
\end{aligned}
$$

$$
\begin{aligned}
\mathcal{A}_{u4}\frac{\hat{u}-m_c^2}{g_s^2} &= 2\epsilon_1^1\epsilon_2^1 m_c\sqrt{\hat{s}}\chi + i\frac{(\epsilon_1^2\epsilon_2^1-\epsilon_1^1\epsilon_2^2)M\sqrt{(k_{1T}-k_{2T})^2+\hat{s})(k_{1T}+k_{2T})^2+\hat{s})}}{\sqrt{\hat{s}}} \\
&- \frac{m_c}{\sqrt{\hat{s}}}\Big[(\psi-\hat{s})\epsilon_1^3\epsilon_2^0+(\psi+\hat{s})\epsilon_1^0\epsilon_2^3 \\
&+ (\epsilon_1^0\epsilon_2^0-\epsilon_1^1\epsilon_2^1-\epsilon_1^2\epsilon_2^2+\epsilon_1^3\epsilon_2^3)\sqrt{(k_{1T}-k_{2T})^2+\hat{s})(k_{1T}+k_{2T})^2+\hat{s})}\Big]\cos\theta' \\
&- 2m_c\sqrt{\hat{s}}\chi(\epsilon_1^1\epsilon_2^1-\epsilon_1^3\epsilon_2^3)\cos^2\theta' \\
&- \frac{m_c}{\sqrt{\hat{s}}}\Big[(\psi-\hat{s})\epsilon_1^1\epsilon_2^0+(\psi+\hat{s})\epsilon_1^0\epsilon_2^1 \\
&+ (\epsilon_1^3\epsilon_2^1+\epsilon_1^1\epsilon_2^3)\sqrt{(k_{1T}-k_{2T})^2+\hat{s})(k_{1T}+k_{2T})^2+\hat{s})}\Big]\sin\theta' \\
&+ 2m_c\sqrt{\hat{s}}\chi(\epsilon_1^3\epsilon_2^1+\epsilon_1^1\epsilon_2^3)\sin\theta'\cos\theta'\ , \qquad (4.53)
\end{aligned}
$$

where $\chi=\sqrt{1-4m_c^2/\hat{s}}$. The calculation of $\mathcal{A}_{s1}\hat{s}/g_s^2$ is shown in the Appendix. The final state total spin is determined from the heavy quarks helicities. Two helicity combinations that result in $S_{z'}=0$ are added and normalized to give the contribution to the spin triplet state ($S=1$) in Eqs. (4.36), (4.38), and (4.40).

In this primed frame, to extract the projection on a state with orbital-angular-momentum quantum number L, we obtain the corresponding Legendre component $\mathcal{A}_L$ in the amplitudes by

$$\mathcal{A}_{L=0} = \frac{1}{2}\int_{-1}^{1} dx\mathcal{A}(x=\cos\theta')\ , \tag{4.54}$$

$$\mathcal{A}_{L=1} = \frac{3}{2}\int_{-1}^{1} dx\ x\mathcal{A}(x=\cos\theta')\ . \tag{4.55}$$

Having obtained the amplitudes for $S=1$ with $S_{z'}=0,\pm1$, and $L=0,1$ with $L_{z'}=0$, we calculate the amplitudes for $J=0,1,2$. The amplitudes for $J=1$, found by adding $S=1$ and $L=0$, are

$$\mathcal{A}_{J=1,J_{z'}=\pm1} = \mathcal{A}_{L=0,L_{z'}=0;S=1,S_{z'}=\pm1}\ , \tag{4.56}$$

$$\mathcal{A}_{J=1,J_{z'}=0} = \mathcal{A}_{L=0,L_{z'}=0;S=1,S_{z'}=0}\ . \tag{4.57}$$

Employing angular momentum algebra, the amplitudes for $J=0,1,2$, obtained by adding $S=1$ and $L=1$, are

$$\mathcal{A}_{J=0,J_{z'}=0} = -\sqrt{\frac{1}{3}}\mathcal{A}_{L=1,L_{z'}=0;S=1,S_{z'}=0}\ , \tag{4.58}$$

$$\mathcal{A}_{J=1,J_{z'}=\pm1} = \mp\frac{1}{\sqrt{2}}\mathcal{A}_{L=1,L_{z'}=0;S=1,S_{z'}=\pm1}\ , \tag{4.59}$$

$$\mathcal{A}_{J=1,J_{z'}=0} = 0\ , \tag{4.60}$$

$$\mathcal{A}_{J=2,J_{z'}=\pm2} = 0\ , \tag{4.61}$$

$$\mathcal{A}_{J=2,J_{z'}=\pm1} = \frac{1}{\sqrt{2}}\mathcal{A}_{L=1,L'_z=0;S=1,S_{z'}=\pm1}\ , \tag{4.62}$$

$$\mathcal{A}_{J=2,J_{z'}=0} = \sqrt{\frac{2}{3}}\mathcal{A}_{L=1,L_{z'}=0;S=1,S_{z'}=0}\ . \tag{4.63}$$

Using a Wigner representation of the inverse rotation defined in Eq. (4.35),

$$\mathcal{D}^J_{J_z,J_{z'}} = \langle J, J_z|\,\mathcal{R}(0,-\beta,-\gamma)\,|J, J_{z'}\rangle\ , \tag{4.64}$$

the amplitudes sorted by final state J and $J_{z'}$ are then rotated back into the helicity frame:

$$\mathcal{A}_{J,J_z} = \sum_{J'_z=-J}^{J} \mathcal{D}^J_{J_z,J_{z'}}\mathcal{A}_{J,J'_z}\ . \tag{4.65}$$

Next, the amplitudes sorted by final state J and J_z are squared for calculations in the helicity frame. For calculations in the other frames, the unsquared amplitudes can be further rotated to the Collins-Soper (CS) or the Gottfried-Jackson (GJ) frame. In the CS frame, the z axis is defined as the angle bisector of the angle between one proton beam and the opposite of the other proton beam. In the GJ frame, the z axis is defined as the direction of the momentum of one of the two colliding proton beams.

The squared matrix elements, $|\mathcal{M}|^2$, are calculated for each J, J_z combination. The color factors, C, are calculated from the SU(3) color algebra and are independent of final state angular momentum [73]. They are

$$
\begin{aligned}
|C_{gg,\hat{s}}|^2 &= 12 \, , \\
|C_{gg,\hat{t}}|^2 &= \frac{16}{3} \, , \\
|C_{gg,\hat{u}}|^2 &= \frac{16}{3} \, , \\
C^*_{gg,\hat{s}} C_{gg,\hat{t}} &= +6 \, , \\
C^*_{gg,\hat{s}} C_{gg,\hat{u}} &= -6 \, , \\
C^*_{gg,\hat{t}} C_{gg,\hat{u}} &= -\frac{2}{3} \, .
\end{aligned} \tag{4.66}
$$

Finally, the total squared amplitudes for a given J, J_z state,

$$
\begin{aligned}
|\mathcal{M}^{J,J_z}_{gg}|^2 &= |C_{gg,\hat{s}}|^2 |\mathcal{A}_{gg,\hat{s}}|^2 + |C_{gg,\hat{t}}|^2 |\mathcal{A}_{gg,\hat{t}}|^2 + |C_{gg,\hat{u}}|^2 |\mathcal{A}_{gg,\hat{u}}|^2 + 2C^*_{gg,\hat{s}} C_{gg,\hat{t}} \mathcal{A}^*_{gg,\hat{s}} \mathcal{A}_{gg,\hat{t}} \\
&+ 2C^*_{gg,\hat{s}} C_{gg,\hat{u}} \mathcal{A}^*_{gg,\hat{s}} \mathcal{A}_{gg,\hat{u}} + 2C^*_{gg,\hat{t}} C_{gg,\hat{u}} \mathcal{A}^*_{gg,\hat{t}} \mathcal{A}_{gg,\hat{u}} \, ,
\end{aligned} \tag{4.67}
$$

are then employed to calculate the partonic cross sections by integrating over solid angle

$$
\hat{\sigma}^{J,J_z} = \int d\Omega \left(\frac{1}{8\pi}\right)^2 |\mathcal{M}^{J,J_z}|^2 \frac{2\chi}{\sqrt{((k_{1T}-k_{2T})^2+\hat{s})((k_{1T}+k_{2T})^2+\hat{s})}} \, . \tag{4.68}
$$

The sum of the polarized partonic cross section results for each final state total angular momentum J, is equal to the unpolarized partonic cross section,

$$
\hat{\sigma}_{\text{unpol}} = \sum_{J_z=-J}^{J_z=+J} \hat{\sigma}^{J,J_z} \, . \tag{4.69}
$$

Having computed the polarized $Q\overline{Q}$ production cross section at the parton level, we then convolute the partonic cross sections with the uPDFs to obtain the hadron-level cross section σ as a function of p_T using Eq. (4.12) or (4.13) and as a function of y using Eq. (4.14). The quarkonium masses which appear as the lower limit of the $Q\overline{Q}$ invariant mass are listed in Table 4.1. We employ the ccfm-JH-2013-set1 [19] uPDFs in this calculation.

4.3 Polarization of prompt J/ψ

We assume that the angular momentum of each directly produced quarkonium state is unchanged by the transition from the parton level to the hadron level, consistent with the CEM expectation that the linear momentum is unchanged by hadronization [56]. This is similar to the assumption made in NRQCD that once a $c\bar{c}$ is produced in a given spin state, it retains that spin state when it becomes a J/ψ.

We calculate the $J_z = 0, \pm 1$ to unpolarized ratios for each directly produced quarkonium state $\mathcal{Q}$ that has a contribution to prompt J/ψ production: J/ψ, ψ(2S), χ_{c1}(1P) and χ_{c2}(1P). These ratios, $R_{\mathcal{Q}}^{J_z}$, are then independent of $F_{\mathcal{Q}}$. We assume the feed-down production of J/ψ from the higher mass bound states follows the angular momentum algebra. Their contributions to the $J_z = 0$ to unpolarized ratios of prompt J/ψ are added and weighed by the feed-down contribution ratios $c_{\mathcal{Q}}$ [84],

$$R_{J/\psi}^{J_z=0} \quad = \quad \sum_{\mathcal{Q},J_z} c_{\mathcal{Q}} S_{\mathcal{Q}}^{J_z} R_{\mathcal{Q}}^{J_z} \ , \tag{4.70}$$

where $S_{\mathcal{Q}}^{J_z}$ is the transition probability from a given state $\mathcal{Q}$ produced in a J_z state to a J/ψ with $J_z = 0$ in a single decay. We assume two pions are emitted for S state feed down, $\psi(2S) \to J/\psi\pi\pi$, and a photon is emitted for a P state feed down, $\chi_c \to J\psi\gamma$. $S_{\mathcal{Q}}^{J_z}$ is then 1 (if $J_z = 0$) or 0 (if $J_z = 1$) for $\mathcal{Q} = \psi(2S)$ since the transition, $\psi(2S) \to J/\psi\pi\pi$, does not change the angular momentum of the quarkonium state. For directly produced J/ψ, $S_{\mathcal{Q}}^{J_z}$ is 1 for $J_z = 0$ and 0 for $J_z = 1$. The $S_{\mathcal{Q}}^{J_z}$ for the χ states are the squares of the Clebsch-Gordan coefficients for the feed-down production via $\chi \to J/\psi + \gamma$. The values of $M_{\mathcal{Q}}$, $c_{\mathcal{Q}}$, and $S_{\mathcal{Q}}^{J_z}$ for all quarkonium states contributing to prompt J/ψ production are collected in Table 4.1.

Table 4.1. The mass $M_{\mathcal{Q}}$, the feed-down contribution ratio $c_{\mathcal{Q}}$, and the squared feed-down transition Clebsch-Gordan coefficients $S_{\mathcal{Q}}^{J_z}$ for all quarkonium states contributing to prompt J/ψ production.

$\mathcal{Q}$	$M_{\mathcal{Q}}$ (GeV)	$c_{\mathcal{Q}}$	$S_{\mathcal{Q}}^{J_z=0}$	$S_{\mathcal{Q}}^{J_z=\pm1}$
J/ψ	3.10	0.62	1	0
ψ(2S)	3.69	0.08	1	0
χ_{c1}(1P)	3.51	0.16	0	1/2
χ_{c2}(1P)	3.56	0.14	2/3	1/2

Finally, the $J_z = 0$ to the unpolarized ratio for prompt J/ψ is converted into the polarization parameter λ_ϑ [34],

$$\lambda_\vartheta = \frac{1 - 3R^{J_z=0}}{1 + R^{J_z=0}} , \tag{4.71}$$

where $-1 < \lambda_\vartheta < 1$. If $\lambda_\vartheta = -1$, J/ψ production is totally longitudinal, $\lambda_\vartheta = 0$ refers to unpolarized production, and for $\lambda_\vartheta = +1$, production is totally transverse.

4.4 Results

Although the matrix element in this calculation is LO in α_s, by convoluting the polarized partonic cross sections with the transverse momentum dependent uPDFs using the k_T-factorization approach, we can calculate the yield as well as the polarization parameter λ_ϑ as a function of p_T. The full NLO polarization including $q\bar{q}$ and $(q+\bar{q})g$ contributions, requiring us to go to $\mathcal{O}(\alpha_s^3)$, will be discussed in a future publication.

The traditional CEM can describe the unpolarized yield of charm and J/ψ production at both LO and NLO assuming collinear factorization [72,76]. The ICEM can also describe the ψ(2S) to J/ψ ratio at NLO while, in the traditional CEM, this ratio is independent of p_T [56]. Since this is the first calculation in the ICEM using the k_T-factorization approach, it is important to check if the unpolarized yield is also in agreement with the data.

In the remainder of this section, we first present how our approach describes the transverse momentum and rapidity distribution of the charmonium states in collider experiments. We then discuss the transverse momentum and rapidity dependence of the polarization parameter λ_ϑ for prompt J/ψ production and direct production of quarkonium states that contribute to the feed-down production. We compare our results to the polarization measured in fixed-target experiments as well as collider experiments in the helicity, Collins-Soper, and Gottfried-Jackson frames to discuss the frame dependence of the polarization parameter. Finally, we discuss the sensitivity of our results to the factorization and renormalization scales, the weight of each diagram, and the feed-down ratios considered. In our calculations, we construct the uncertainty bands by varying the charm quark mass, around its base value of 1.27 GeV in the interval $1.2 < m_c < 1.5$ GeV, and the renormalization scale around its base value of m_T in the interval $0.5 < \mu_R/m_T < 2$ while keeping the factorization scale fixed at $\mu_F = m_T$. The total uncertainty band is constructed by adding the two uncertainties in quadrature.

4.4.1 Unpolarized charmonium production

In this section, we present the p_T and rapidity distributions of charmonium states in our approach. In the spirit of the traditional CEM, $F_{\mathcal{Q}}$ in Eq. (4.3) has to be independent of the projectile, target, and energy for each quarkonium state $\mathcal{Q}$. Even though the focus of this paper is on polarization, which is $F_{\mathcal{Q}}$ independent, the unpolarized yield in the ICEM using the k_T-factorization approach was not considered before. Therefore, it is important to first confirm that this approach can indeed describe the charmonium yields as a function of p_T and rapidity before discussing polarization predictions. We first obtain $F_{J/\psi}$ and $F_{\psi(2S)}$ by comparing our results with the experimental data measured by the LHCb Collaboration and the CDF Collaboration respectively. Using the same $F_{J/\psi}$ and $F_{\psi(2S)}$, we compare our results with the experimental data measured at CDF and ALICE. We can only obtain $F_{\chi_{c1}}$ and $F_{\chi_{c2}}$ for the χ_c states by comparing the unpolarized yield with the data measured by the ATLAS Collaboration at $\sqrt{s} = 7$ TeV because these are the only measurements. We instead give predictions of χ_{c1} and χ_{c1} production at $\sqrt{s} = 13$ TeV. We also compare and predict the ratio of χ_{c2} to χ_{c1} at $\sqrt{s} = 7$ TeV and $\sqrt{s} = 13$ TeV. Note that we cannot expect our LO values of F_Q to be equal to those found for $J\psi$ and $\psi(2S)$ in Ref. [56]. Those calculations are NLO in the total cross section assuming collinear factorization, and include the $q\bar{q}$ and $(q + \bar{q})g$ channels where the contribution of the latter is non-negligible.

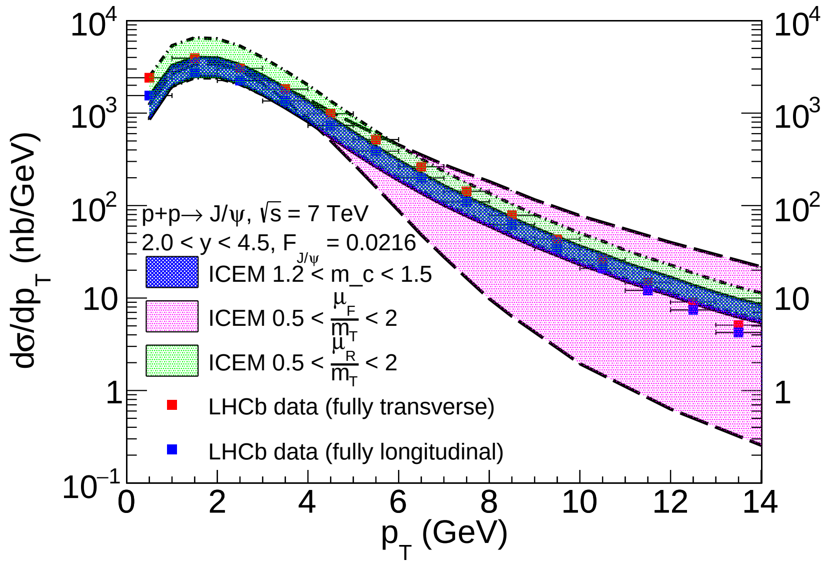

Figure 4.2. The p_T dependence of inclusive J/ψ production at $\sqrt{s} = 7$ TeV in the ICEM obtained by varying the renormalization scale (blue region), the factorization scale in the range $0.5 < \mu_F/m_T < 2$ (magenta region), and the renormalization scale in the range $0.5 < \mu_R/m_T < 2$ (green region). The LHCb data [99] assuming the J/ψ polarization is totally transverse, $\lambda_\vartheta = +1$ (red square), and totally longitudinal, $\lambda_\vartheta = -1$ (blue square), are shown. The LHCb data assuming $\lambda_\vartheta = 0$ lie between the red and blue points and are not shown.

4.4.1.1 J/ψ p_T distribution

We first discuss why we fix the factorization scale at $\mu_F = m_T$ instead of including a factor of 2 variation, as usual in most other approaches. In Fig. 4.2, we show the p_T distributions of inclusive J/ψ production at $\sqrt{s} = 7$ TeV found by fixing $m_c = 1.27$ GeV, and varying the factorization scale over the range $0.5 < \mu_F/m_T < 2$ and the renormalization scale over the range $0.5 < \mu_R/m_T < 2$ separately. We also fix $\mu_F/m_T = \mu_R/m_T = 1$ and vary the charm quark mass over the range $1.2 < m_c < 1.5$ GeV. The direct production cross section is calculated using Eq. (4.12) by integrating the pair invariant mass from $M_{J/\psi}$ to $2m_{D^0}$ ($m_{D^0} = 1.86$ GeV) over the rapidity range $2.0 < y < 4.5$. We assume the direct production is a constant fraction, 0.62 of the inclusive production [84]. We then are able to compare the inclusive p_T distribution in the ICEM with the LHCb data [99]. The result has a significant dependence on the factorization scale for $p_T > 5$ GeV. This is because the uPDFs have a sharp cutoff for $k_T > \mu_F$ and are thus very sensitive to the chosen factorization scale. The yield varies more as p_T approaches m_T at high p_T. At low p_T,

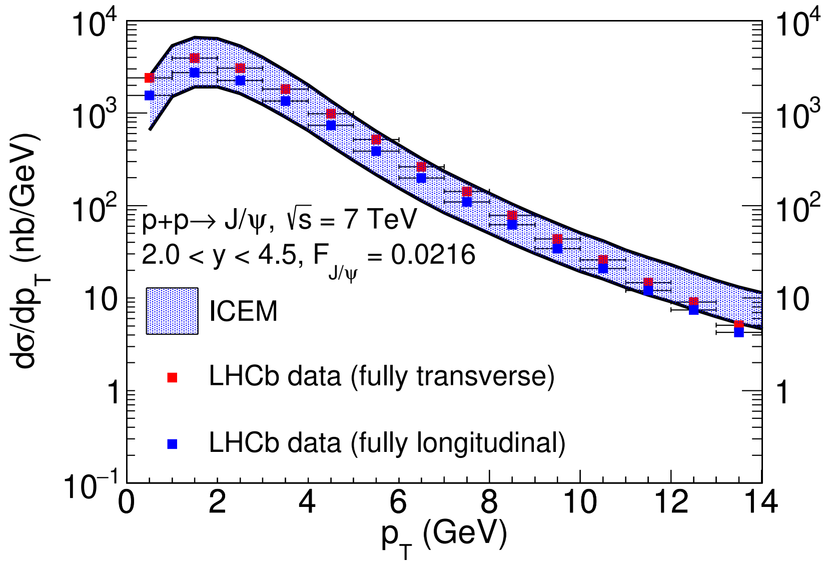

Figure 4.3. The p_T dependence of inclusive J/ψ production at $\sqrt{s} = 7$ TeV in the ICEM with combined mass and renormalization scale uncertainties. The LHCb data [99] are shown as in Fig. 4.2. The LHCb data assuming $\lambda_\vartheta = 0$ are not shown.

$m_T \sim M_Q$ and the cross section is independent of the factorization scale since $k_T \ll \mu_F$. At moderate p_T, the variation with μ_F is similar to or smaller than that due to the charm quark mass. At $p_T \sim 10$ GeV, $m_T \sim p_T$. Thus the lower limit on the factorization scale, $m_T/2$, is on the order of k_T and the yield drops off at this cutoff limit, while the upper limit on the factorization scale, $2m_T$, is still greater than k_T, enhancing the yield. Since at LO, only the $Q\overline{Q}$ pair carries the transverse momentum, the predictive power of the yield is limited by the uPDFs. Therefore, to construct a meaningful uncertainty band, we fix the factorization scale at $\mu_F = m_T$. As we push toward the limit of the k_T-factorization approach with uPDFs at high p_T at LO, we can only improve the high p_T limit by a full NLO calculation.

After fixing the factorization scale, the variation in renormalization scale then gives the largest uncertainty, followed by the variation in charm mass. When μ_R is reduced, the strong coupling constant is larger, increasing the yield. On the other hand, when m_c is reduced, the yield increases. In the remainder of this section, we present our results by adding the uncertainties due to variations of the charm mass and renormalization scale in quadrature.

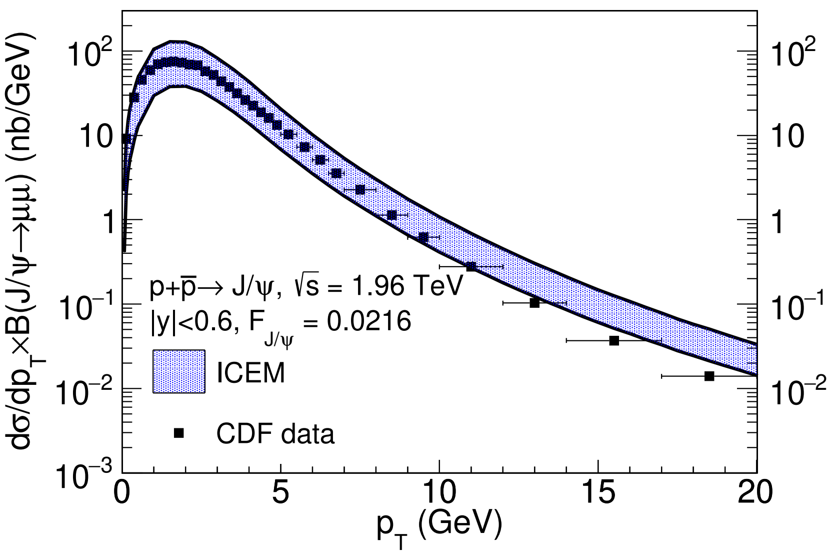

Figure 4.4. The p_T dependence of inclusive J/ψ production at $\sqrt{s} = 1.96$ TeV in the ICEM. The combined mass and renormalization scale uncertainties are shown in the band and compared to the CDF data [100].

The inclusive J/ψ p_T distribution at $\sqrt{s} = 7$ TeV with combined uncertainty is shown in Fig. 4.3. The ICEM result has a peak at $p_T \sim 2$ GeV, in agreement with the experimental results, but slightly overestimates the data at high p_T. The ICEM p_T distribution is within reasonable agreement with the data for all p_T. The experimental prompt production cross section depends on the polarization areof J/ψ since the polarization affects the acceptance and reconstruction efficiencies. LHCb checked the yields for the three polarization assumptions: $\lambda_\vartheta = -1, 0, +1$. The experimental p_T distribution for all polarization assumptions is within the uncertainty band constructed in the ICEM. By matching to the experimental unpolarized yield $\lambda_\vartheta = 0$, we find that the ICEM can describe the J/ψ p_T distribution with $F_{J/\psi} = 0.0216$. This is the fraction of $c\bar{c}$ pairs produced in the invariant mass range from $M_{J/\psi}$ to $2m_{D^0}$ that result in direct J/ψ, defined in Eq. (4.3).

We test the universality of $F_{J/\psi}$ by comparing the inclusive J/ψ p_T distribution in the ICEM at $\sqrt{s} = 1.96$ TeV and $|y| < 0.6$ with the CDF data [100] in Fig. 4.4. We again assume the direct production takes a constant fraction of 0.62 of the inclusive production [84] to obtain the inclusive J/ψ cross section. The ICEM results slightly overshoot the data at high p_T because both the direct and nonprompt contributions to

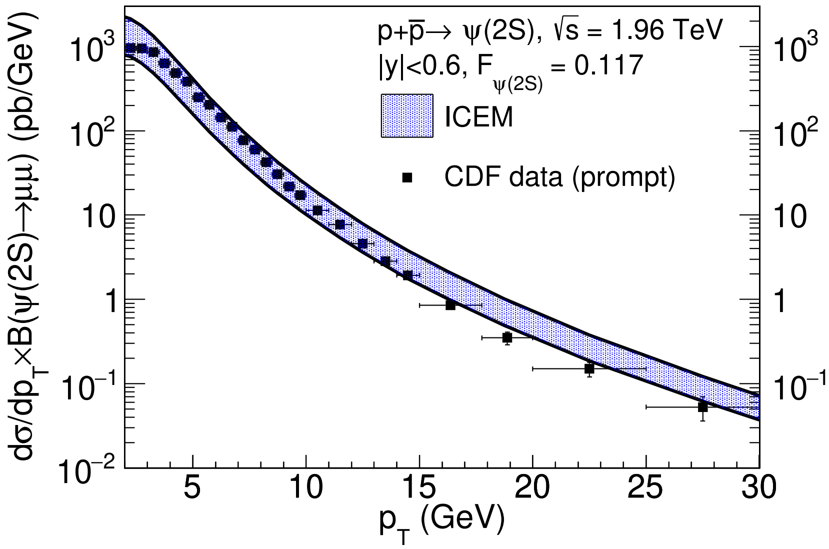

Figure 4.5. The p_T dependence of direct $\psi(2S)$ production at $\sqrt{s} = 1.96$ TeV in the ICEM. The combined mass and renormalization scale uncertainties are shown in the band and compared to the CDF data for prompt $\psi(2S)$ [102].

J/ψ production are p_T dependent [99, 101]. The direct-to-prompt J/ψ ratio decreases as p_T grows and the contribution from b decay to inclusive production is measured to be larger at high p_T than at low p_T. Combining the effects of both, using a constant direct-to-inclusive ratio of 0.62 gives an overestimate of the yields at high p_T. The calculated cross section differs from the measurements more as p_T increases. We note that if we fix $F_{J/\psi}$ from the CDF data alone, it agrees within 1.5% of that extracted from comparison to the LHCb data.

4.4.1.2 ψ(2S) p_T distribution

The inclusive $\psi(2S)$ p_T distribution at $\sqrt{s} = 1.96$ TeV is shown in Fig. 4.5. Here, the direct production cross section is calculated using Eq. (4.12) by integrating the pair invariant mass from $M_{\psi(2S)}$ to $2m_{D^0}$ over the rapidity range $|y| < 0.6$. We assume the direct production is the same as the prompt production as there are no quarkonium states that feed down to $\psi(2S)$ since its mass is just below $2m_{D^0}$. Therefore, we compare the p_T-integrated yield of direct $\psi(2S)$ with the CDF measurement [102]. We find $F_{\psi(2S)} = 0.117$. We note that $F_{\psi(2S)} > F_{J/\psi}$, primarily because the mass range is much smaller for $\psi(2S)$ than J/ψ. In the traditional CEM, $F_{\psi(2S)}$ is smaller than $F_{J/\psi}$ because the integration

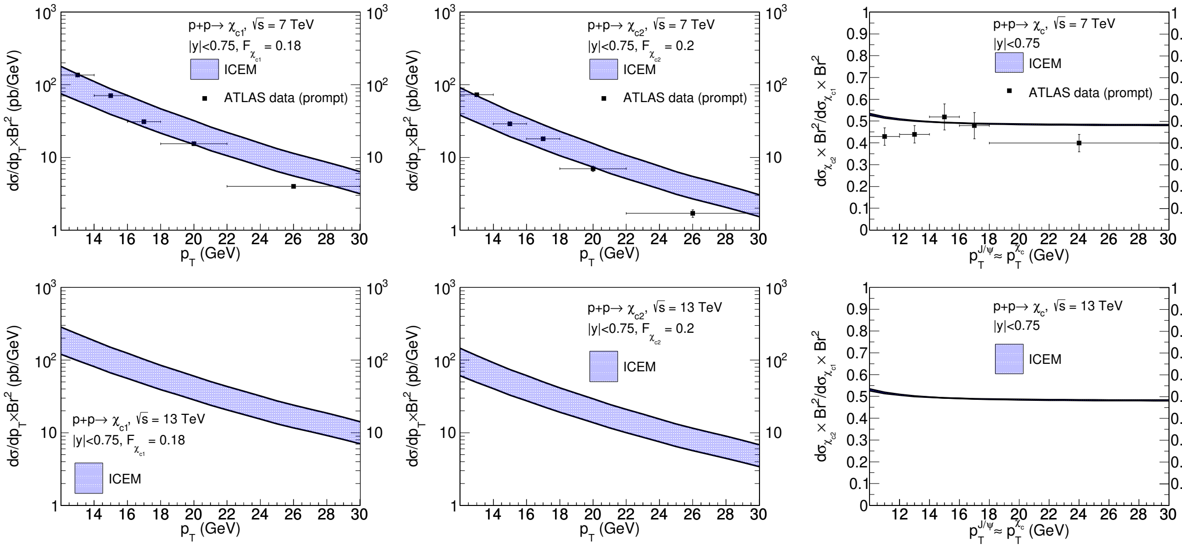

Figure 4.6. The direct χ_{c1} (left) and χ_{c2} (middle) p_T dependence multiplied by the branching ratios for $\chi_c \to J/\psi\gamma$ and for $J/\psi \to \mu^+\mu^-$, and the ratio of χ_{c2} to χ_{c1} (right) at $\sqrt{s} = 7$ TeV (top panels) and at $\sqrt{s} = 13$ TeV (bottom panels) in the ICEM with combined mass and renormalization scale uncertainties. The ATLAS data for prompt χ_c production are also shown [103].

over the pair invariant mass is the same for both J/ψ and ψ(2S). We add the contribution from nonprompt production reported by the CDF Collaboration to our prompt production yield to give the inclusive ψ(2S) yield shown in Fig. 4.5. We find agreement with the data within the combined uncertainty band constructed by varying the charm mass and the renormalization scale in the ICEM.

4.4.1.3 χ_{c1} and χ_{c2} p_T distribution

We now turn to the p_T dependence of χ_c production. The p_T distributions of direct χ_{c1}, direct χ_{c2}, and the ratio of χ_{c2} to χ_{c1} at $\sqrt{s} = 7$ TeV and 13 TeV are presented in Fig. 4.6. The direct production is calculated using Eq. (4.12) by integrating the pair invariant mass from M_{χ_c} to $2m_{D^0}$ ($m_{D^0} = 1.86$ GeV) over the rapidity range $|y| < 0.75$. We assume the prompt production of χ_c is approximately the same as the direct production. Thus, by comparing the direct χ_{c1} and χ_{c2} yields in the ICEM with the experimental yield of prompt χ_{c1} and χ_{c2} at $\sqrt{s} = 7$ TeV measured by the ATLAS Collaboration [103], we obtain $F_{\chi_{c1}} = 0.180$ and $F_{\chi_{c2}} = 0.20$. As is the case for $F_{\psi(2S)}$ and $F_{J/\psi}$, $F_{\chi_{c2}} > F_{\chi_{c1}}$ because the integration range over the pair invariant mass is smaller for χ_{c2} than for χ_{c1}.

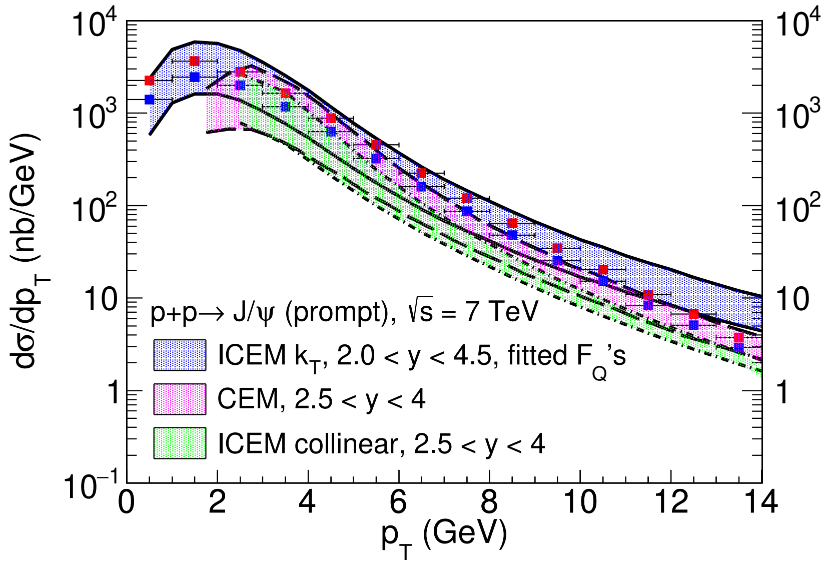

Figure 4.7. The p_T dependence of prompt J/ψ production at $\sqrt{s} = 7$ TeV in the ICEM using fitted F_Q's with combined mass and renormalization scale uncertainties (blue region), in the CEM [72] (magenta region), in the ICEM using collinear factorization approach [56] (green region). The LHCb data [99] assuming the J/ψ polarization is totally transverse, $\lambda_\vartheta = +1$ (red square), and totally longitudinal, $\lambda_\vartheta = -1$ (blue square), are shown. The LHCb data assuming $\lambda_\vartheta = 0$ lie between the red and blue points and are not shown.

In the traditional CEM, $F_{\chi_{c2}}$ is smaller than $F_{\chi_{c1}}$. The direct production in the ICEM describes prompt production of both χ_{c1} and χ_{c2} at $\sqrt{s} = 7$ TeV within the uncertainty bands constructed by varying the charm quark mass and renormalization scale. The ratio of the cross sections is also described by the ICEM. We calculate the χ_{c2} to χ_{c1} ratio to be ~ 0.5, almost independent of p_T. The ratios disagree with a recent NRQCD calculation [104], where the ratio decreases as p_T increases and is above the data. We assume that $p_{T\chi_c} \approx p_{TJ/\psi}$, not unreasonable since the mass difference is ~500 MeV and the decay photon is soft. We anticipate the direct χ_{c1} and χ_{c2} yields will be increased by 51% (at $p_T = 10$ GeV) to 120% (at $p_T = 30$ GeV) when $\sqrt{s}$ is increased from 7 TeV to 13 TeV. However, the ratio of χ_{c2} to χ_{c1} should remain approximately the same.

4.4.1.4 Prompt J/ψ p_T distribution

After fixing $F_{J/\psi}$, $F_{\psi(2S)}$, $F_{\chi_{c1}}$ and $F_{\chi c2}$, we calculate the prompt J/ψ p_T distribution at $\sqrt{s} = 7$ TeV in the rapidity range $2.0 < y < 4.5$ using the direct J/ψ, $\psi(2S)$, χ_{c1} and χ_{c2} yields and their branching ratios to J/ψ. The prompt J/ψ p_T distribution is shown

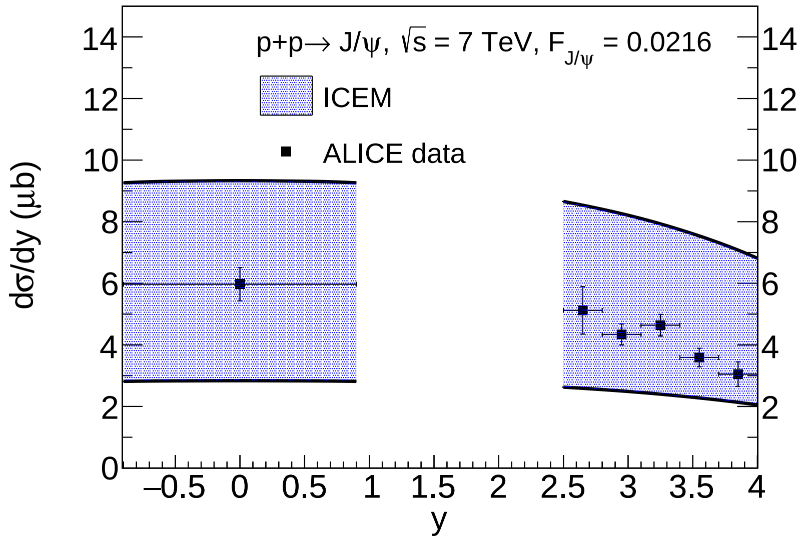

Figure 4.8. The rapidity dependence of inclusive J/ψ production at $\sqrt{s} = 7$ TeV in the ICEM. The combined mass and renormalization scale uncertainties are shown in the band and compared to the ALICE data [105].

in Fig. 4.7. The ICEM p_T distribution describes the data for most p_T but overshoots the data slightly at the highest p_T bin. The ICEM p_T distribution is within reasonable agreement with the data for all p_T. We extract the p_T dependent feed-down ratios c_ψ's by taking the direct to prompt ratio in this distribution. We find the feed-down ratios are very similar to those listed in Table 4.1. Additionally, we find $c_{J/\psi}$ decreases as p_T increases, in agreement with Ref. [101].

In the same figure, we compare the prompt J/ψ p_T distribution at $\sqrt{s} = 7$ TeV with that from the CEM [72] and ICEM [56] in the collinear factorization approach. Both uncertainty bands are constructed by varying the factorization scale in the interval $1.25 < \mu_F/m_T < 4.65$ and the renormalization scale in the interval $1.48 < \mu_F/m_T < 1.71$. Considering that those results are calculated in the ALICE muon arm acceptance $2.5 < y < 4$ other than that in the LHCb $2 < y < 4.5$, all distributions agree reasonably well with each other and the data.

4.4.1.5 J/ψ rapidity distribution

We now turn to the rapidity dependence of J/ψ production. The rapidity distribution of inclusive J/ψ at $\sqrt{s} = 7$ TeV is shown in Fig. 4.8. The direct production is calculated

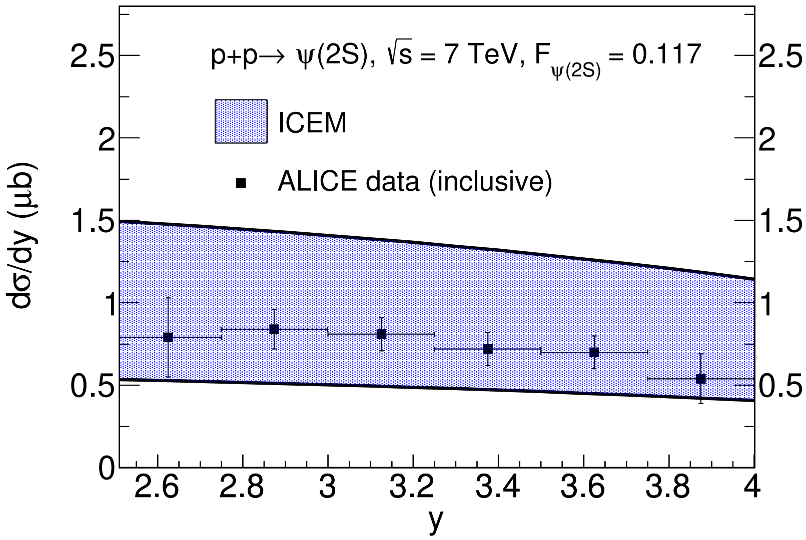

Figure 4.9. The rapidity dependence of direct ψ(2S) production at $\sqrt{s} = 7$ TeV in the ICEM. The combined mass and renormalization scale uncertainty are shown in the band and compared to the ALICE data for inclusive ψ(2S) [106].

using Eq. (4.14) by integrating over the p_T range $0 < p_T < 7$ GeV ($|y| < 0.9$) and $0 < p_T < 8$ GeV ($2.5 < y < 4$). We again assume the direct production is a constant 62% [84] of the inclusive production. We use the same $F_{J/\psi}$ again to compare the rapidity distribution in the ICEM with the measurement made by the ALICE Collaboration [105]. The difference in the integrated p_T range has a negligible effect on the rapidity distribution because the p_T dependence has already dropped by an order of magnitude by p_T ∼7-8 GeV. We find the ICEM can describe the ALICE rapidity distribution at $\sqrt{s} = 7$ TeV using the $F_{J/\psi}$ obtained at the same energy by LHCb in the forward rapidity region.

4.4.1.6 ψ(2S) rapidity distribution

The rapidity distribution of direct ψ(2S) at $\sqrt{s} = 7$ TeV is shown in Fig. 4.9. Here, the rapidity distribution is calculated in the interval $p_T < 12$ GeV at forward rapidity ($2.5 < y < 4$). We use the same $F_{\psi(2S)}$ to compare with inclusive ψ(2S) data from ALICE [106]. While the lower bound of our uncertainty band should still be lower than the data when the contribution from B decays are added, our baseline should slightly overshoot the inclusive ψ(2S) data. Our results also agree with the direct ψ(2S) rapidity distribution from a recent NRQCD calculation at LO using the k_T-factorization approach [104].

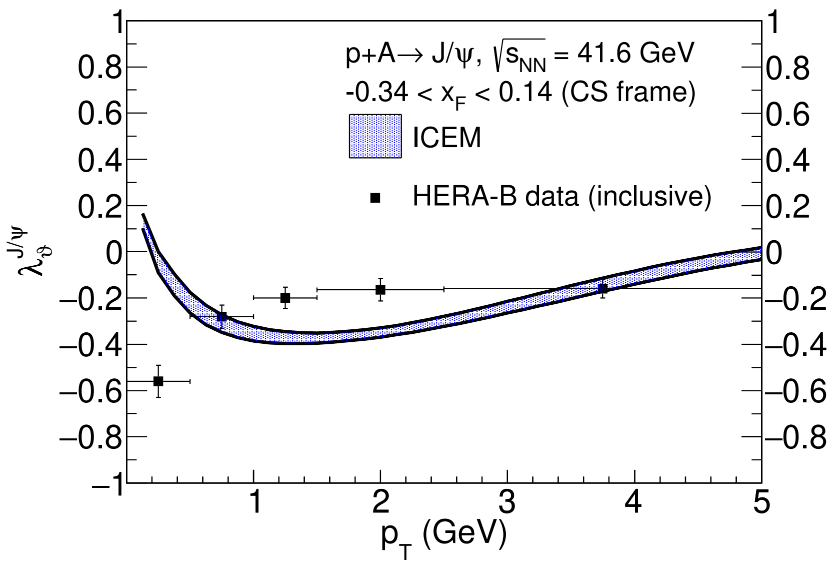

Figure 4.10. The p_T dependence of the polarization parameter λ_ϑ for prompt J/ψ production in the Collins-Soper frame at $\sqrt{s_{NN}} = 41.6$ GeV in the ICEM with mass uncertainties is compared to the HERA-B data for inclusive J/ψ [107].

4.4.2 p_T dependence of λ_ϑ

Here, we present the p_T dependence of the polarization parameter λ_ϑ in $p+p$ and $p+A$ collisions. Because the polarization parameter is defined as the ratio of polarized to unpolarized cross sections in Eq. (4.70) and these cross sections depend on μ_R and μ_F in the same way, the polarization parameter is independent of the scale choice. However, the amplitudes themselves are mass dependent so that the polarized to unpolarized ratio in λ_ϑ depends on the charm quark mass. Thus the only uncertainty on λ_ϑ in our calculation is due to the variation of m_c in the range $1.2 < m_c < 1.5$ GeV. We note that the polarization varies rather slowly because $m_T \sim p_T \gg m_{J/\psi}$ over most of the p_T range considered. In this section, the uncertainty band is only due to the mass variation and therefore the uncertainty is reduced relative to the yield calculations.

We also note that we find the feed-down contributions from each directly produced quarkonium state to prompt J/ψ polarization to be very similar. Therefore, the prompt j/ψ polarization has a weak dependence on the feed-down fractions. This behavior was also found in Ref. [58].

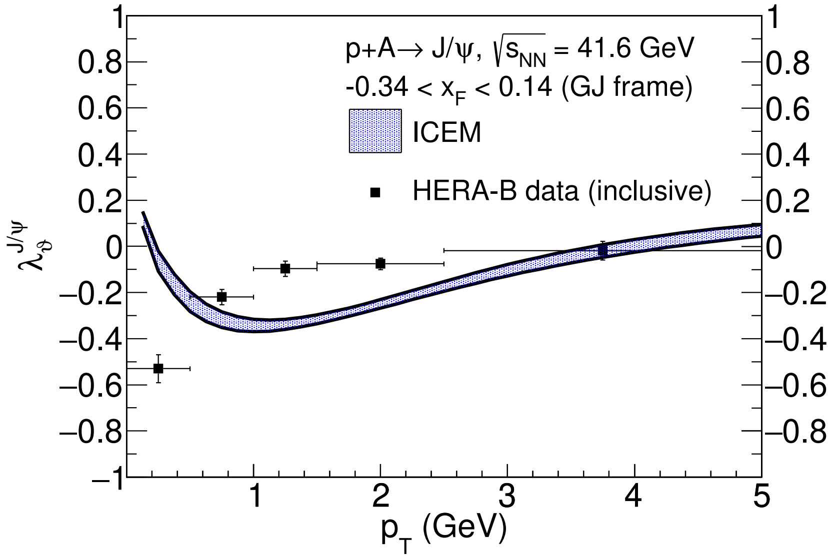

Figure 4.11. The p_T dependence of the polarization parameter λ_ϑ for prompt J/ψ production in the Gottfried-Jackson frame at $\sqrt{s_{NN}} = 41.6$ GeV in the ICEM with mass uncertainties is compared to the HERA-B data for inclusive J/ψ [107].

4.4.2.1 Charmonium polarization in $p+A$ collisions at fixed-target energies

The polarization results for prompt production of J/ψ at $\sqrt{s_{NN}} = 41.6$ GeV are shown in Figs. 4.10 and 4.11. Although the HERA-B data are taken on nuclear targets, C and W, and there are known nuclear modifications of the parton densities in the nucleus, λ_ϑ is independent of any modification. This is because the ratios of the polarized to unpolarized cross sections are in the same kinematic acceptance and any nuclear effects cancel in the ratio. Thus there is no difference in polarization between the two target nuclei. We compare our results with the C and W combined data measured by the HERA-B Collaboration in the region $-0.34 < x_F < 0.14$ [107].

Prompt J/ψ polarization in the ICEM is close to unpolarized in both the CS and GJ frames for $p_T < 5$ GeV. At $p_T = 0$, the two z axes, $z_{\rm CS}$ and $z_{\rm GJ}$, are in the same direction. Thus the polarization is the same in that limit. As p_T increases, the two axes depart from each other. Thus the polarization is slightly less longitudinal in the GJ frame than in the CS frame. This behavior is also consistent with the experimental data showing that the J/ψ polarization at very low p_T is not affected by switching from the CS frame to the GJ frame. At higher p_T the polarization is slightly less longitudinal in the GJ frame than in

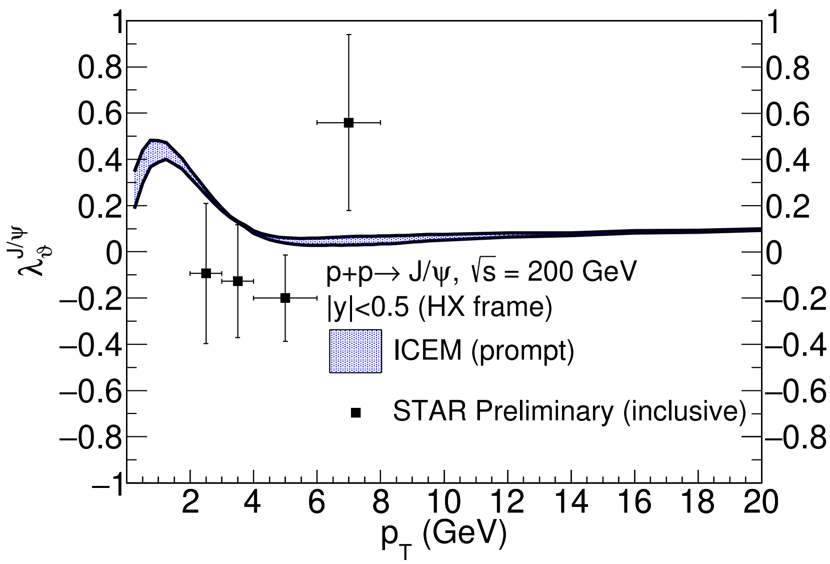

Figure 4.12. The p_T dependence of the polarization parameter λ_ϑ for prompt J/ψ production at $\sqrt{s} = 200$ GeV in the ICEM with mass uncertainty. The STAR data for inclusive J/ψ are also shown.

the CS frame. The ICEM results are in fair agreement with the experimental data except at the lowest p_T.

4.4.2.2 Charmonium polarization in $p+p(\bar{p})$ collisions

We present the polarization parameters for prompt J/ψ in $p+p$ collisions at $\sqrt{s} =$ 200 GeV in Fig. 4.12. We compare our results with the data from the STAR Collaboration in the region $|y| < 0.5$ [108] in the helicity frame. The ICEM polarization of prompt J/ψ in the helicity frame is slightly transverse at low p_T ($p_T < M_{J/\psi}$). The result becomes unpolarized at moderate p_T ($M_{J/\psi} < p_T < 2M_{J/\psi}$) before changing to slightly transverse at high p_T. The ICEM polarization agrees fairly well with the data at small and moderate p_T for inclusive J/ψ polarization at STAR.

We also compared the polarization parameters for prompt J/ψ in $p+\bar{p}$ collisions at $\sqrt{s} = 1.96$ TeV with the data measured by the CDF Collaboration in the region $|y| < 0.6$ [109] in the helicity frame, shown in Fig 4.13. The ICEM prompt J/ψ polarization does not depend strongly on $\sqrt{s}$ or whether the collision is $p+p$ or $p+\bar{p}$. We find the trend in the p_T dependence of the polarization is the same. At high p_T, the prompt J/ψ polarization measured by the CDF Collaboration is slightly longitudinal to unpolarized

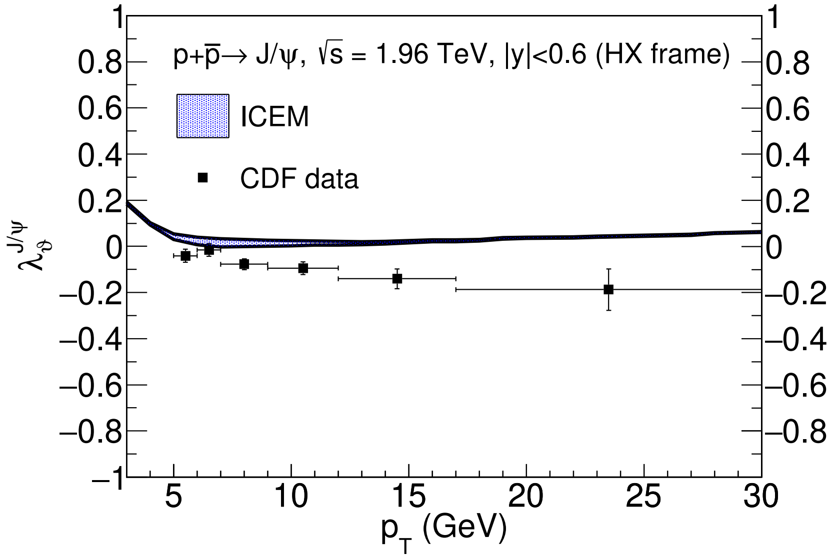

Figure 4.13. The p_T dependence of the polarization parameter λ_ϑ for prompt J/ψ production at $\sqrt{s} = 1.96$ TeV in the ICEM with mass uncertainty. The CDF data are also shown [109].

while the ICEM polarization is slightly transverse. The polarization predicted by NRQCD also shows a similar behavior at this energy [110]. However, NRQCD predicts a stronger transverse polarization ($\lambda_\vartheta \sim 0.6$) than ICEM in the high p_T limit.

4.4.3 Rapidity dependence of λ_ϑ

Next we turn to the rapidity dependence of λ_ϑ. We calculate the prompt J/ψ polarization in the helicity frame for $p + p$ collisions at $\sqrt{s} = 7$ TeV in two rapidity ranges, $|y| < 0.6$ and $0.6 < |y| < 1.2$, shown in Figs. 4.14 and 4.15 respectively. We compare our results to the experimental data from the CMS Collaboration [111]. There is no difference in the polarization of prompt J/ψ in these two rapidity regions in the ICEM. In the ICEM, the polarization parameter λ_ϑ of prompt J/ψ production increases very slowly in the high p_T limit and reaches $\lambda_\vartheta \sim 0.12$ at $p_T = 70$ GeV. The ICEM polarization agrees with the experimental results at central rapidity within uncertainty except the data in the $30 < p_T < 35$ bin. The experiment reports the polarization is less transverse in the forward rapidity region. Our results in the ICEM still agree with the data even though the calculated polarization does not depend on rapidity in this range at 7 TeV.

We also do not observe variations in the polarization parameter λ_ϑ at $\sqrt{s} = 7$ TeV

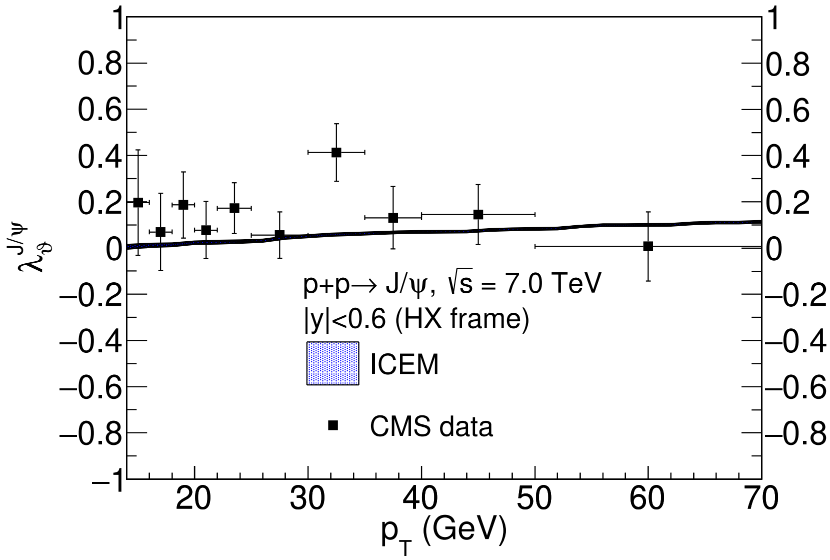

Figure 4.14. The p_T dependence of the polarization parameter λ_ϑ for prompt J/ψ production at $\sqrt{s} = 7$ TeV in the region $|y| < 0.6$ in the ICEM with mass uncertainty. The CMS data are also shown [111].

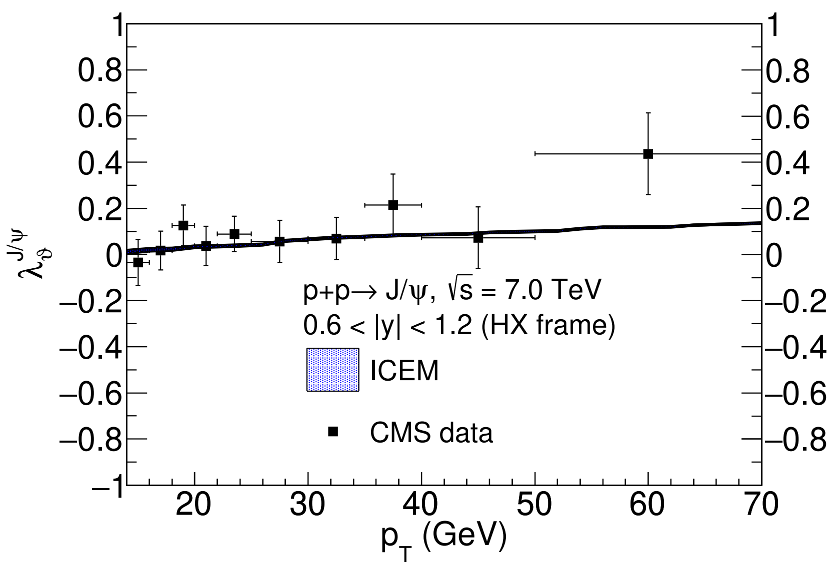

Figure 4.15. The p_T dependence of the polarization parameter λ_ϑ for prompt J/ψ production at $\sqrt{s} = 7$ TeV in the region $0.6 < |y| < 1.2$ in the ICEM with mass uncertainty. The CMS data are also shown [111].

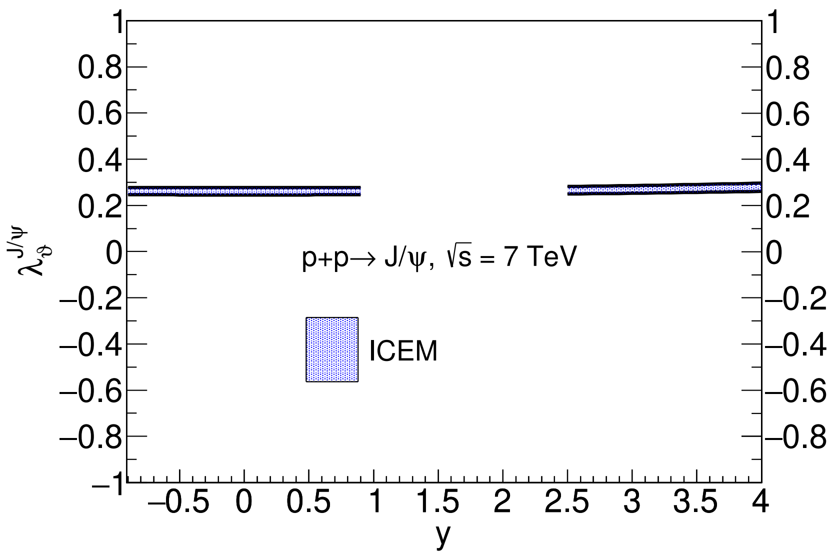

Figure 4.16. The p_T integrated rapidity dependence of λ_ϑ for prompt J/ψ production at $\sqrt{s} = 7$ TeV in the helicity frame in the ALICE acceptance. Note that we use the same kinematic cuts as on the yields in Fig. 4.8.

in the region of $y < 4$ using the same kinematics cut compared to the ALICE yield measurement in Fig. 4.8. We present the polarization as a function of rapidity in Fig. 4.16. The polarization parameter of prompt J/ψ for the p_T-integrated results is $\lambda_\vartheta = 0.26 \pm 0.02$.

4.4.4 Frame dependence of λ_ϑ

We now turn to the frame dependence of our 7 TeV results. We calculate the polarization parameter in $p+p$ collisions at $\sqrt{s} = 7$ TeV in both the helicity frame and the Collins-Soper frame, shown in Figs. 4.17 and 4.18 respectively. The polarization in the Collins-Soper frame is opposite to that in the helicity frame in the ICEM. We expect this because, in these kinematics, at order α_s^2, the polarization axis in the Collins-Soper frame is always perpendicular to that in the helicity frame. Therefore, at low p_T, where the J/ψ is predicted to be slightly transverse in the helicity frame, it is predicted to be slightly longitudinal in the Collins-Soper frame. Whereas, at moderate p_T, where the J/ψ is predicted to be unpolarized, it is also predicted to be unpolarized in the Collins-Soper frame. This behavior, however, is not measured experimentally. As we compare our results with the ALICE data [112], the ICEM polarization agrees with the data in the Collins-Soper frame but does not agree with the data in the helicity frame, especially at low p_T where

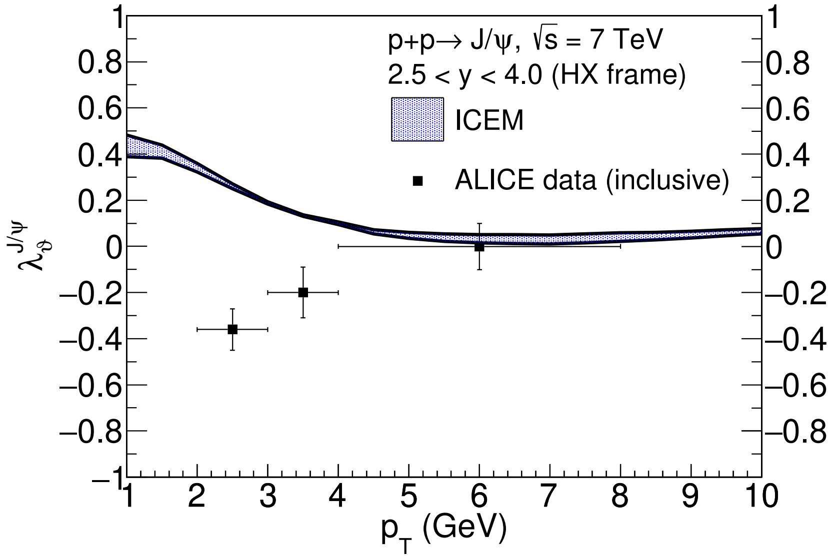

Figure 4.17. The p_T dependence of λ_ϑ for prompt J/ψ production at $\sqrt{s} = 7$ TeV in the helicity frame is compared with the ALICE inclusive J/ψ data [112].

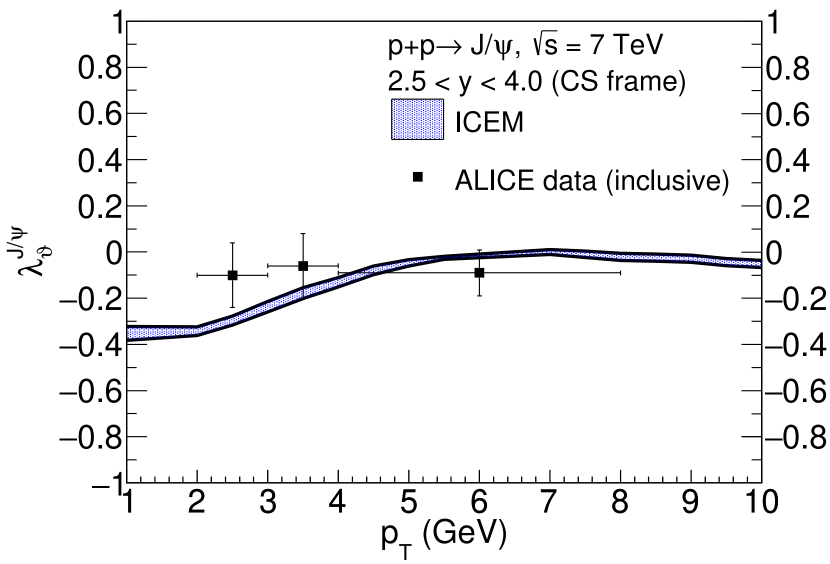

Figure 4.18. The p_T dependence of λ_ϑ for prompt J/ψ production at $\sqrt{s} = 7$ TeV in the Collins-Soper frame is compared with the ALICE inclusive J/ψ data [112].

the frame dependence is most significant.

We find similar results by comparing to the LHCb data in the Collins-Soper frame [113], shown in Figs. 4.19 and 4.20: the polarization in the ICEM agrees with the data in the Collins-Soper frame but not in the helicity frame. We expect that the difference in agreement of the calculations in different frames with the data may be resolved with a

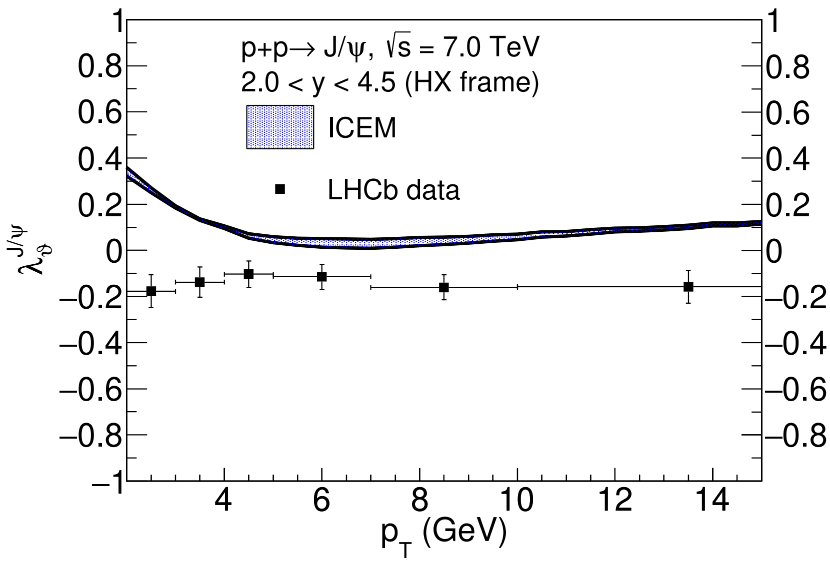

Figure 4.19. The p_T dependence of λ_ϑ for prompt J/ψ production at $\sqrt{s} = 7$ TeV in the helicity frame is compared with the LHCb data [113].

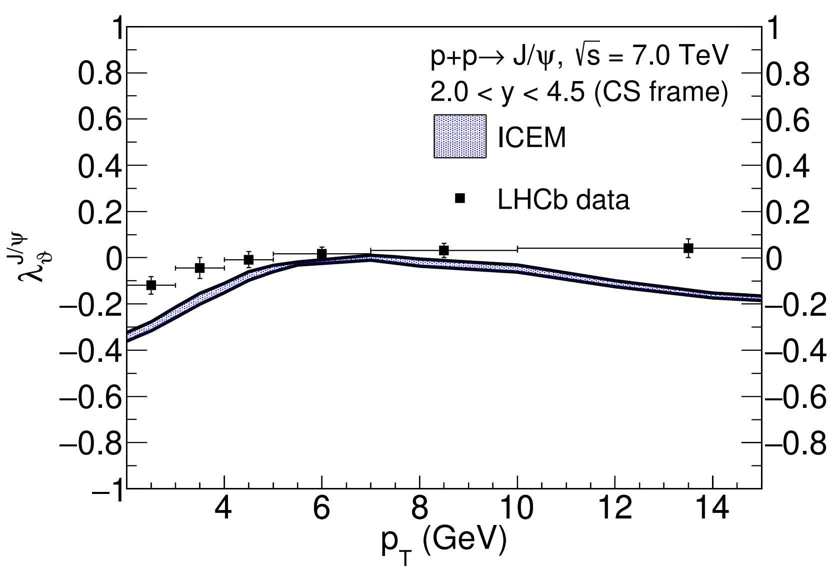

Figure 4.20. The p_T dependence of λ_ϑ for prompt J/ψ production at $\sqrt{s} = 7$ TeV in the Collins-Soper frame is compared with the LHCb data [113].

full α_s^3 calculation of the ICEM cross section.

Finally, we note that at low p_T the polarization in the Gottfried-Jackson frame is similar to that in the Collins-Soper frame, as shown in Figs. 4.10 and 4.11 for fixed-target energies. However at high p_T, the polarization in the Gottfried-Jackson frame is similar to that in the helicity frame. The differences are due to the definition of the polarization axes in the quarkonium rest frame. When $p_T \ll m_T$, the angle between the polarization axis in the Gottfried-Jackson frame and that in the Collins-Soper frame is small. As p_T increases, the polarization axis in the Gottfried-Jackson frame becomes collinear with that in the helicity frame. Therefore, the polarization calculated in the Gottfried-Jackson frame is opposite to that in the helicity frame at low p_T, and thus is similar to that in the Collins-Soper frame. But as p_T increases, the polarization in the Gottfried-Jackson frame should asymptotically approach the polarization in the helicity frame.

4.4.5 Sensitivity to scales and quark mass

We have already discussed the sensitivity of the charmonium yields to the factorization and the renormalization scales in Sec. 4.4.1.1. Here we note that the longitudinal to unpolarized fraction $R_{J/\psi}^{J_z=0}$ used in the calculation of λ_ϑ, is insensitive to scale variations because the longitudinal and transverse change similarly as the scales are varied. Therefore, the polarization parameter λ_ϑ for prompt J/ψ is independent of the scales for all energies considered. Similarly, while the unpolarized χ_{c1} and χ_{c2} cross sections vary appreciably with the scale choice, the χ_{c2} to χ_{c1} ratio is also independent of scales.

While the scale variations affect the polarized and unpolarized cross sections the same way, making λ_ϑ scale independently, the J_z components of the polarized cross section depend differently on quark mass. When $p_T \leq M_Q$, the longitudinally polarized partonic cross section decreases faster with increasing m_c than the transversely polarized partonic cross section in the helicity frame. Thus increasing the charm mass results in more transverse polarization. When $p_T > M_Q$, the longitudinally polarized partonic cross section decreases more slowly with increasing m_c than the transversely polarized partonic cross section, thus, here increasing the charm mass results in more longitudinal polarization. As $p_T \gg \hat{s}$, λ_ϑ becomes insensitive to m_c. Thus the uncertainty in λ_θ is narrower.

Table 4.2. Values of $c_{\mathcal{Q}}$ used to test the sensitivity of our results to the feed-down ratios. Based on the uncertainty in $c_{\mathcal{Q}}$ (third column), $c'_{\mathcal{Q}}$ (second column) is used assuming the promptly produced 1S states comprise less directly produced 1S states, and $c''_{\mathcal{Q}}$ (fourth column) is used assuming the promptly produced 1S states comprise more directly produced 1S states,

$\mathcal{Q}$	$c'_{\mathcal{Q}}$	$c_{\mathcal{Q}}$	$c''_{\mathcal{Q}}$
J/ψ	0.59	0.62±0.04	0.65
ψ(2S)	0.09	0.08±0.02	0.07
χ_{c1}(1P)	0.17	0.16±0.04	0.15
χ_{c2}(1P)	0.15	0.14±0.04	0.13

4.4.6 Sensitivity to feed-down ratios

We have tested the sensitivity of our results to the feed-down ratios used in our calculations [84]. Since prompt J/ψ production is dominated by direct J/ψ, we vary the feed-down ratio by changing the relative contribution of direct J/ψ and decays from excited states. Thus when the direct fraction, $c_{J/\psi}$, increases, all other c_ψ decrease and vice versa. Using the base values of c_ψ in Table 4.1 and the reported uncertainty, we vary the feed-down ratios as given in Table 4.2. Since the polarization of prompt J/ψ production does not vary at central rapidity, we study changes in the polarization by varying the feed-down ratios at $y = 0$. The p_T-integrated polarization parameter for prompt J/ψ production at $\sqrt{s} = 7$ TeV at $y = 0$ varies by 0.04 from 0.26 in the helicity frame. This variation is similar to that due to the charm quark mass variation.

4.4.7 Sensitivity to diagram weights

We have tested the sensitivity of our results to diagram weights. As shown in Ref. [98], the $\hat{s}$-channel diagram dominates color-octet production at high p_T. Turning off the contribution from this diagram by setting $\mathcal{A}_{gg,\hat{s}} = 0$ in Eq. (4.31) makes a significant difference in polarization as well as the uncertainty band in the high p_T limit. At 5 GeV, turning off the contribution from the $\hat{s}$-channel diagram reduces the cross section by 70%. The difference is larger at higher p_T. Thus the polarization is more sensitive to charm mass and gives a wider uncertainty band. The polarization parameter at $\sqrt{s} = 1.96$ TeV in the rapidity region $|y| < 0.6$ in the helicity frame in this case is shown in Fig. 4.21. The polar-

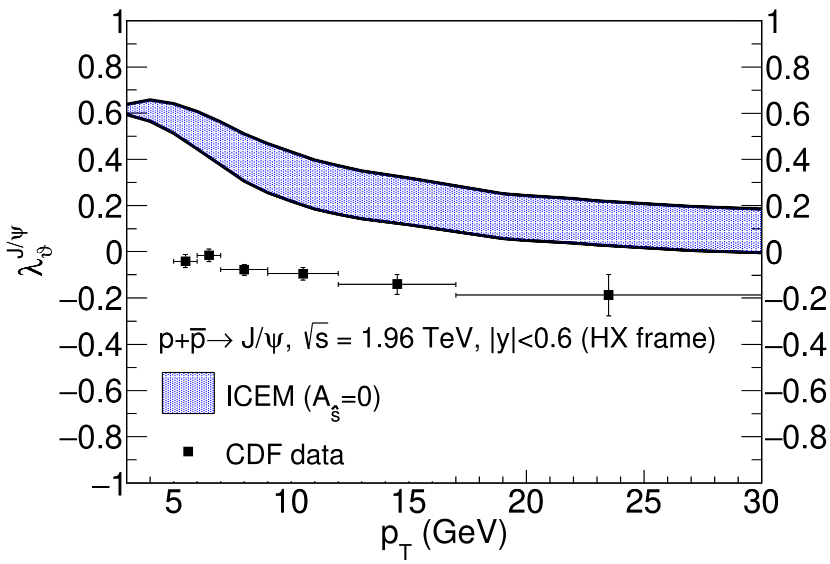

Figure 4.21. The p_T dependence of the polarization parameter λ_ϑ for prompt J/ψ production at $\sqrt{s} = 1.96$ TeV in the ICEM with mass uncertainty when the $\hat{s}$-channel contribution is excluded. The CDF data are also shown [109].

ization at low p_T is more transverse compared to Fig. 4.13. Instead of becoming slightly transverse at high p_T, prompt J/ψ production will remain approximately unpolarized with $\lambda_\vartheta = +0.14^{+0.04}_{-0.14}$ in the helicity frame when the $\hat{s}$-channel amplitude is completely turned off.

4.5 Conclusions

We have presented the transverse momentum and rapidity dependence of the charmonium cross section as well as the polarization of prompt J/ψ production in $p+p$ and $p+A$ collisions in the improved color evaporation model in the k_T-factorization approach. We compare the p_T dependence to data at both fixed-target energies and collider energies. We also present χ_c predictions as a function of p_T at $\sqrt{s} = 13$ TeV. We find prompt J/ψ production to be unpolarized at moderate p_T and slightly transverse in the high p_T limit in the helicity frame. We do not observe any rapidity dependence in the polarization in the ranges considered. We report the p_T-integrated polarization parameter for prompt J/ψ production at $\sqrt{s} = 7$ TeV to be $\lambda_\vartheta = 0.26 \pm 0.02$ at $y = 0$ in the helicity frame. We will study the p_T dependence of bottomonium states in this approach in a future publication.

Since our calculation of the matrix elements is leading order in α_s, the high p_T cross section varies strongly with the choice of factorization scale due to the limitations on the uPDFs as x increases. We expect improvements at high p_T when we calculate the cross section to $\mathcal{O}(\alpha_s^3)$ in a future publication.

4.6 Appendix: Calculation of $\mathcal{A}_{s1}\hat{s}/g_s^2$

The matrix elements used in this paper are obtained in the frame where the final state $Q\overline{Q}$ lies on the rotated z' axis. This requires the four momenta of the initial state Reggeons in the helicity frame represented in Eqs. (4.23) and (4.24) to be rotated such that they lie along the z' axis where the four momenta are

$$k_1^\mu = \Big(\frac{-\psi+\hat{s}}{2\sqrt{\hat{s}}}, 0, 0, \sqrt{k_{1T}^2 + \frac{(-\psi^2+\hat{s})^2}{4\hat{s}}}\Big) , \tag{4.72}$$

$$k_2^\mu = \Big(\frac{\psi+\hat{s}}{2\sqrt{\hat{s}}}, 0, 0, -\sqrt{k_{1T}^2 + \frac{(-\psi^2+\hat{s})^2}{4\hat{s}}}\Big) . \tag{4.73}$$

The final state momenta of the charm and anticharm quarks, p_1^μ and p_2^μ respectively, can be written as

$$p_1^\mu = \frac{\sqrt{\hat{s}}}{2}\Big(1, \chi\sin\theta', 0, \chi\cos\theta'\Big) , \tag{4.74}$$

$$p_2^\mu = \frac{\sqrt{\hat{s}}}{2}\Big(1, -\chi\sin\theta', 0, -\chi\cos\theta'\Big) , \tag{4.75}$$

with helicity spinors

$$\begin{aligned} u(p_1,\uparrow) &= \sqrt{E_1+m_c} \\ &\times \Big(c, s, \frac{p_1}{E_1+m_c}c, \frac{p_1}{E_1+m_c}s\Big) , \end{aligned} \tag{4.76}$$

$$\begin{aligned} u(p_1,\downarrow) &= \sqrt{E_1+m_c} \\ &\times \Big(-s, c, \frac{p_1}{E_1+m_c}s, -\frac{p_1}{E_1+m_c}c\Big) , \end{aligned} \tag{4.77}$$

$$\begin{aligned} v(p_2,\uparrow) &= \sqrt{E_2+m_c} \\ &\times \Big(\frac{p_2}{E_2+m_c}c, \frac{p_2}{E_2+m_c}s, -c, -s\Big) , \end{aligned} \tag{4.78}$$

$$\begin{aligned} v(p_1,\downarrow) &= \sqrt{E_2+m_c} \\ &\times \Big(\frac{p_2}{E_2+m_c}s, -\frac{p_2}{E_2+m_c}c, s, -c\Big) , \end{aligned} \tag{4.79}$$

where $E_{1,2} = p^0_{1,2}$ and $p_{1,2} = |\vec{p}_{1,2}|$, $s = \sin(\theta'/2)$ and $c = \cos(\theta'/2)$.

Then this amplitude can be found by

$$\mathcal{A}_{s1}\frac{\hat{s}}{g_s^2} = \bar{u}(p_1,\uparrow)[-(2k_2+k_1)\cdot\epsilon(k_1)\not{\epsilon}(k_2) \tag{4.80}$$

$$+ \quad (2k_1+k_2)\cdot\epsilon(k_2)\not{\epsilon}(k_1) \tag{4.81}$$

$$+ \quad (\epsilon(k_1)\cdot\epsilon(k_2)(\not{k}_2-\not{k}_1)]v(p_2,\uparrow)\ . \tag{4.82}$$

The result is simplified and expanded trigonometrically in Eq. (4.42). The rest of the amplitudes can be found by considering other combinations of charm and anticharm helicity states as well as going from the $\hat{s}$-channel diagram to $\hat{t}$- and $\hat{u}$-channel diagrams.

Chapter 5

Production and Polarization of Prompt $\Upsilon(n\mathbf{S})$ in the Improved Color Evaporation Model using the k_T-factorization Approach

Production and Polarization of Prompt $\Upsilon(n\mathrm{S})$ in the Improved Color Evaporation Model using the k_T-factorization Approach

V. Cheung[a] and R. Vogt[a,b,1]

[a]Department of Physics
University of California, Davis
Davis, CA 95616, USA
and
[b]Nuclear and Chemical Sciences Division
Lawrence Livermore National Laboratory
Livermore, CA 94551, USA

ABSTRACT

We calculate the polarization of prompt $\Upsilon(n\mathrm{S})$ production in the improved color evaporation model at leading order employing the k_T-factorization approach. We present the polarization parameter λ_ϑ of prompt $\Upsilon(n\mathrm{S})$ as a function of transverse momentum in $p+p$ and $p+\bar{p}$ collisions to compare with data in the helicity, Collins-Soper and Gottfried-Jackson frames. We also present calculations of the bottomonium production cross sections as a function of transverse momentum and rapidity. This is the first p_T-dependent calculation of bottomonium production and polarization in the improved color evaporation model. We find agreement with both bottomonium cross sections and polarization measurements.

[1]This work was performed under the auspices of the U.S. Department of Energy by Lawrence Livermore National Laboratory under Contract DE-AC52-07NA27344 and supported by the U.S. Department of Energy, Office of Science, Office of Nuclear Physics (Nuclear Theory) under contract number DE-SC-0004014.

5.1 Introduction

This paper is a continuation of our previous work [59] on quarkonium production and polarization in the improved color evaporation model using the k_T-factorization approach.

We first developed our LO calculation of quarkonium polarization in the ICEM [56] in Refs. [57, 58] employing collinear factorization. However, in this framework, we were unable to address the polarization as a function of p_T to compare with collider data. Therefore, we performed the first p_T-dependent polarization calculation in the ICEM [59] for prompt J/ψ production and polarization by employing the k_T-factorization approach. This paper is a continuation of that work where we now extend our p_T-dependent leading order (LO) ICEM calculation of quarkonium production and polarization in the k_T-factorization approach to prompt $\Upsilon(n\mathrm{S})$. We use the same scattering amplitudes as in Ref. [59]. This work also provides the first p_T-dependent ICEM $\Upsilon(n\mathrm{S})$ polarization result. We will begin to address the p_T dependence at NLO in a later publication.

We note that within the framework of nonrelativistic QCD (NRQCD) [61], the quarkonium polarization problem is less prominent in bottomonium than in charmonium. Fitting the long distance matrix elements to measurements of Υ yields and polarization for $p_T > 8$ GeV, NRQCD is able to provide a better description of bottomonium yields and polarization than for charmonium [54,114]. The heavier bottom quark mass allows better convergence of the double expansion in α_s and v. Reference [95] derived a relationship between the traditional CEM and NRQCD assuming that NRQCD factorization holds to all orders and that the NRQCD sums over color and spin converge. It also assumed that no distinction is made between the spin states in the CEM.

5.2 Production of polarized bottomonium in the k_T-factorization approach

In this paper, we present both the yields and polarizations of bottomonium as a function of p_T by formulating the ICEM in the k_T-factorization approach. We take the same effective Feynman rules for scattering processes involving incoming off-shell gluons [97] as in the NRQCD calculation of Ref. [98]. Effectively, the momentum of the incoming Reggeon, k^μ, with transverse momentum k_T can be written in terms of the proton momentum p^μ and the fraction of longitudinal momentum x carried by the gluon as

$$k^\mu = xp^\mu + k_T^\mu \ . \tag{5.1}$$

The polarization 4-vector is

$$\epsilon^\mu(k_T) = \frac{k_T^\mu}{k_T} \ , \tag{5.2}$$

where $k_T^\mu = (0, \vec{k}_T, 0)$.

In the traditional CEM, all bottomonium states are treated the same as $b\bar{b}$ below the $B\overline{B}$ threshold. The invariant mass of the heavy $b\bar{b}$ pair is restricted to be less than twice the mass of the lowest mass B meson. The distributions for all bottomonium family members are assumed to be identical. In the ICEM, the invariant mass of the intermediate $b\bar{b}$ pair is constrained to be larger than the mass of produced bottomonium state, $M_{\mathcal{Q}}$, instead of twice the bottom quark mass, $2m_b$, the lower limit in the traditional CEM [57, 69]. Because the bottomonium momentum and integration range now depend on the mass of the state, the kinematic distributions of the bottomonium states are no longer identical in the ICEM. Using the k_T-factorization approach, in a $p+p$ collision the ICEM production cross section for a directly-produced bottomonium state $\mathcal{Q}$ is

$$\begin{aligned} \sigma &= F_{\mathcal{Q}} \int_{M_{\mathcal{Q}}^2}^{4m_B^2} d\hat{s} \int \frac{dx_1}{x_1} \int \frac{d\phi_1}{2\pi} \int dk_{1T}{}^2 \Phi_1(x_1, k_{1T}, \mu_{F1}^2) \\ &\times \int \frac{dx_2}{x_2} \int \frac{d\phi_2}{2\pi} \int dk_{2T}{}^2 \Phi_2(x_2, k_{2T}, \mu_{F2}^2) \hat{\sigma}(R + R \to Q\overline{Q}) \\ &\times \delta(\hat{s} - x_1 x_2 s + |\vec{k}_{1T} + \vec{k}_{2T}|^2) \ , \end{aligned} \tag{5.3}$$

where the square of the heavy quark pair invariant mass is $\hat{s}$ while the square of the center-of-mass energy in the $p+p$ collision is s. Here $\Phi(x, k_T, \mu_F^2)$ is the unintegrated parton distribution function (uPDF) for a Reggeized gluon with a momentum fraction x and a transverse momentum k_T interacting with a factorization scale μ_F. The angles $\phi_{1,2}$ in Eq. (5.3) are between the $k_{T1,2}$ of the partons and the p_T of the final state bottomonium $\mathcal{Q}$. The parton-level cross section is $\sigma(R + R \to b\bar{b})$. Finally, $F_{\mathcal{Q}}$ is a universal factor for the directly-produced bottomonium state $\mathcal{Q}$, and is independent of the projectile, target, and energy. In this approach, the cross section is

$$\begin{aligned}
\frac{d^4\sigma}{dp_T dy d\hat{s} d\phi} &= \sigma\delta(\hat{s} - x_1 x_2 s + p_T^2)\delta\Big(y - \frac{1}{2}\log\frac{x_1}{x_2}\Big)\delta\Big(p_T^2 - |\vec{k}_{1T}^2 + \vec{k}_{2T}^2|\Big)\delta(\phi - (\phi_1 - \phi_2)) \\
&= F_{\mathcal{Q}} \int \frac{2}{\pi} k_{2T} dk_{2T} \sum_{k_{1T}} \Bigg[\frac{\Phi_1(k_{1T}, x_{10}, \mu_{F1}^2)}{x_{10}} \frac{\Phi_2(k_{2T}, x_{20}, \mu_{F2}^2)}{x_{20}} \\
&\times\ k_{1T} p_T \frac{\hat{\sigma}(R + R \to Q\overline{Q})}{s\sqrt{k_{2T}^2(\cos^2\phi - 1) + p_T^2}} \Bigg]
\end{aligned} \tag{5.4}$$

where the sum k_{1T} is over the roots of $k_{1T}^2 + k_{2T}^2 + 2k_{1T}k_{2T}\cos\phi = p_T^2$, and $k_{1T,1}$, $k_{1T,2}$ are

$$k_{1T,1} = -k_{2T}\cos\phi + \sqrt{k_{2T}^2(\cos^2\phi - 1) + p_T^2} \tag{5.5}$$

$$k_{1T,2} = -k_{2T}\cos\phi - \sqrt{k_{2T}^2(\cos^2\phi - 1) + p_T^2}\ . \tag{5.6}$$

The momentum fractions x_{10} and x_{20} are

$$x_{10} = \sqrt{\frac{\hat{s} + p_T^2}{s}} e^{+y}\ , \tag{5.7}$$

$$x_{20} = \sqrt{\frac{\hat{s} + p_T^2}{s}} e^{-y}\ . \tag{5.8}$$

Here, ϕ is the relative azimuthal angle between two incident Reggeons ($\phi = \phi_1 - \phi_2$) and p_T is the transverse momentum of the produced $b\bar{b}$.

Thus the transverse momentum distribution $d\sigma/dp_T$ in the ICEM is

$$\frac{d\sigma}{dp_T} = \int dy d\hat{s} d\phi \frac{d^4\sigma}{dp_T dy d\hat{s} d\phi}\ . \tag{5.9}$$

We integrate over rapidity to compare to collider data with defined rapidity cuts. Similarly, the rapidity distribution $d\sigma/dy$ in the ICEM is

$$\frac{d\sigma}{dy} = \int dp_T d\hat{s} d\phi \frac{d^4\sigma}{dp_T dy d\hat{s} d\phi}\ . \tag{5.10}$$

As our central result, we take the renormalization and factorization scales to be $\mu_F = \mu_R = m_T$, where m_T is the transverse mass of the $b\bar{b}$. We will study the effect of varying these scales on the p_T distributions and the polarization.

Table 5.1. The mass, $M_{\mathcal{Q}}$, and the squared feed-down transition Clebsch-Gordan coefficients, $S_{\mathcal{Q}}^{J_z}$, for all bottomonium states contributing to prompt $\Upsilon(n\mathrm{S})$ production.

$\mathcal{Q}$	$M_{\mathcal{Q}}$ (GeV)	$S_{\mathcal{Q}}^{J_z=0}$	$S_{\mathcal{Q}}^{J_z=\pm1}$
Υ(1S)	9.46	1	0
Υ(2S)	10.02	1	0
Υ(3S)	10.36	1	0
χ_{b1}(1P)	9.89	0	1/2
χ_{b2}(1P)	9.91	2/3	1/2
χ_{b1}(2P)	10.26	0	1/2
χ_{b2}(2P)	10.27	2/3	1/2
χ_{b1}(3P)	10.51	0	1/2
χ_{b2}(3P)	10.51	2/3	1/2

5.3 Polarization of prompt $\Upsilon(n\mathrm{S})$

We employ the scattering amplitudes calculated in Ref. [59] to compute the $b\bar{b}$ partonic production cross section $\hat{\sigma}^{J,J_z}$ according to the J^P of each directly produced bottomonium state below the $B\overline{B}$ threshold. We then convolute the polarized partonic cross sections with the uPDFs to obtain the hadron-level cross section, σ, as a function of p_T using Eq. (5.9). The bottomonium masses which appear as the lower limit of the $b\bar{b}$ invariant mass in the calculations of $\hat{\sigma}^{J,J_z}$ are listed in Table 5.1. We employ the ccfm-JH-2013-set1 [19] uPDFs in this calculation.

We assume that the angular momentum of each directly-produced bottomonium state is unchanged by the transition from the parton level to the hadron level, consistent with the CEM expectation that the linear momentum is unchanged by hadronization.

We calculate the ratio of the individual $J_z = 0, \pm1$ to the unpolarized partonic cross sections ratios for each directly-produced bottomonium state $\mathcal{Q}$ that has a contribution to prompt $\Upsilon(n\mathrm{S})$ production: Υ(1S), Υ(2S), Υ(3S), χ_{b1}(1P), χ_{b2}(1P), χ_{b1}(2P), χ_{b2}(3P), χ_{b1}(3P) and χ_{b2}(3P). These ratios, $R_{\mathcal{Q}}^{J_z}$, are then independent of $F_{\mathcal{Q}}$. We assume the feed-down production of $\Upsilon(n\mathrm{S})$ from the higher mass bound states follows the angular momentum algebra. Their contributions of these higher states to $R^{J_z=0}_{\Upsilon(n\mathrm{S})}$ for prompt $\Upsilon(n\mathrm{S})$ are added after weighting by the feed-down contribution ratios $c_{\mathcal{Q}}$ [101]:

$$R^{J_z=0}_{\Upsilon} = \sum_{\mathcal{Q},J_z} c_{\mathcal{Q}} S^{J_z}_{\mathcal{Q}} R^{J_z}_{\mathcal{Q}} \ . \tag{5.11}$$

Here $S^{J_z}_{\mathcal{Q}}$ is the transition probability from a given state $\mathcal{Q}$ produced in a J_z state to a $\Upsilon(n\mathrm{S})$ with $J_z = 0$ in a single decay. We assume two pions are emitted for S state feed down, $\Upsilon(2\mathrm{S}) \to \Upsilon(1\mathrm{S})\pi\pi$, and a photon is emitted for a P state feed down, $\chi_b(1\mathrm{P}) \to \Upsilon(1\mathrm{S})\gamma$. $S^{J_z}_{\mathcal{Q}}$ is then 1 (if $J_z = 0$) or 0 (if $J_z = 1$) for $\mathcal{Q} = \Upsilon(2\mathrm{S})$ since the transition, $\Upsilon(2\mathrm{S}) \to \Upsilon(1\mathrm{S})\pi\pi$, does not change the angular momentum of the quarkonium state. For directly produced $\Upsilon(n\mathrm{S})$, $S^{J_z}_{\mathcal{Q}}$ is 1 for $J_z = 0$ and 0 for $J_z = 1$. The $S^{J_z}_{\mathcal{Q}}$ for the χ states are the squares of the Clebsch-Gordan coefficients for the feed-down production via $\chi_b \to \Upsilon(n\mathrm{S})\gamma$. The bottomonium feed-down ratios are p_T-dependent [101]: the fraction of direct production is larger at low p_T than at high p_T. We consider two sets of feed-down ratios from Ref. [101]. These ratios are derived from LHC measurements [106, 115–122] assuming they vary with p_T but not rapidity [101]. The "low p_T" ratios are used to compare with LHCb data ($0 < p_T < 20$ GeV) where the "high p_T" ratios are employed to compare with CMS data ($10 < p_T < 50$ GeV). Here, we are assuming the feed-down contribution from $\chi_{b1}(n\mathrm{P})$ and $\chi_{b2}(n\mathrm{P})$ are the same as in our previous approach for the χ_c states [58]. A similar assumption is made for the other P states. The values of $M_{\mathcal{Q}}$ and $S^{J_z}_{\mathcal{Q}}$ for all bottomonium states contributing to prompt $\Upsilon(n\mathrm{S})$ production are collected in Table 5.1 and the values of $c_{\mathcal{Q}}$ in the two p_T regions are presented in Table 5.2.

Finally, the $J_z = 0$ to the unpolarized ratio for prompt $\Upsilon(n\mathrm{S})$ states are converted into the polarization parameter λ_ϑ [34],

$$\lambda_\vartheta = \frac{1 - 3R^{J_z=0}}{1 + R^{J_z=0}} \ , \tag{5.12}$$

where $-1 < \lambda_\vartheta < 1$. If $\lambda_\vartheta = -1$, $\Upsilon(n\mathrm{S})$ production is totally longitudinal, $\lambda_\vartheta = 0$ refers to unpolarized production, while production is totally transverse for $\lambda_\vartheta = +1$.

Table 5.2. The feed-down ratios, $c_{\mathcal{Q}}$, for prompt Υ(1S), Υ(2S), and Υ(3S) production from direct Υ(1S), Υ(2S), Υ(3S), $\chi_b(1P)$, $\chi_b(2P)$, and $\chi_b(3P)$ in the low p_T and high p_T regions [101]. We assume the feed-down contributions from $\chi_{b1}(n\mathrm{P})$ and $\chi_{b2}(n\mathrm{P})$ are the same as also done in Ref. [58].

	low p_T $c_{\mathcal{Q}}$ ($p_T \lesssim 20$ GeV)			high p_T $c_{\mathcal{Q}}$ ($p_T \gtrsim 20$ GeV)		
$\mathcal{Q}$ (direct \ prompt)	Υ(1S)	Υ(2S)	Υ(3S)	Υ(1S)	Υ(2S)	Υ(3S)
Υ(1S)	0.71	-	-	0.45	-	-
Υ(2S)	0.07	0.73	-	0.14	0.60	-
Υ(3S)	0.01	0.04	0.70	0.03	0.05	0.50
χ_{b1}(1P)	0.075	-	-	0.145	-	-
χ_{b2}(1P)	0.075	-	-	0.145	-	-
χ_{b1}(2P)	0.02	0.10	-	0.03	0.15	-
χ_{b2}(2P)	0.02	0.10	-	0.03	0.15	-
χ_{b1}(3P)	0.01	0.015	0.15	0.015	0.025	0.25
χ_{b2}(3P)	0.01	0.015	0.15	0.015	0.025	0.25

5.4 Results

Although the matrix elements in this calculation are LO in α_s, by convoluting the polarized partonic cross sections with the transverse momentum dependent uPDFs using the k_T-factorization approach, we can calculate the yield as well as the polarization parameter λ_ϑ as a function of p_T. The full NLO polarization, including $q\bar{q}$ and $(q+\bar{q})g$ contributions, will be discussed in a future publication.

The traditional CEM can describe the unpolarized yields of $\Upsilon(n\mathrm{S})$ production at NLO assuming collinear factorization [123]. In this calculation, we take advantage of the ICEM to calculate the direct production of the individual bottomonium states separately. Since this is the first bottomonium calculation in the ICEM using the k_T-factorization approach, it is important to check if our calculated unpolarized yields are also in agreement with the data.

We first check how our approach describes the transverse momentum and rapidity distribution of the bottomonium states at collider energies. We then discuss the transverse momentum dependence of the polarization parameter λ_ϑ for prompt $\Upsilon(n\mathrm{S})$ production. We compare our results to the polarization measured in collider experiments in the helicity (HX), Collins-Soper (CS) [33], and Gottfried-Jackson (GJ) [32] frames to discuss the frame dependence of λ_ϑ. W also discuss the sensitivity of our results to the bottom quark mass, the renormalization scale and the feed-down ratios. In our calculations, we construct the uncertainty bands by varying the bottom quark mass around its base value of 4.75 GeV, in the interval $4.5 < m_b < 5$ GeV, and the renormalization scale around its base value of m_T, in the interval $0.5 < \mu_R/m_T < 2$, while keeping the factorization scale fixed at $\mu_F = m_T$. The total uncertainty band is constructed by adding the mass and renormalization scale uncertainties in quadrature. We do not extend our calculation below $p+\bar{p}$ at Tevatron energies because at fixed-target energies and even at the RHIC collider the k_T-factorization approach with off-shell gluons is inappropriate for bottomonium.

5.4.1 Unpolarized bottomonium production

Here, we present the p_T and rapidity distributions of the $\Upsilon(n\mathrm{S})$ states as well as the ratio of $\chi_{b1}(1\mathrm{P})$ to $\chi_{b2}(1\mathrm{P})$ in our approach. In the spirit of the traditional CEM, $F_{\mathcal{Q}}$ in

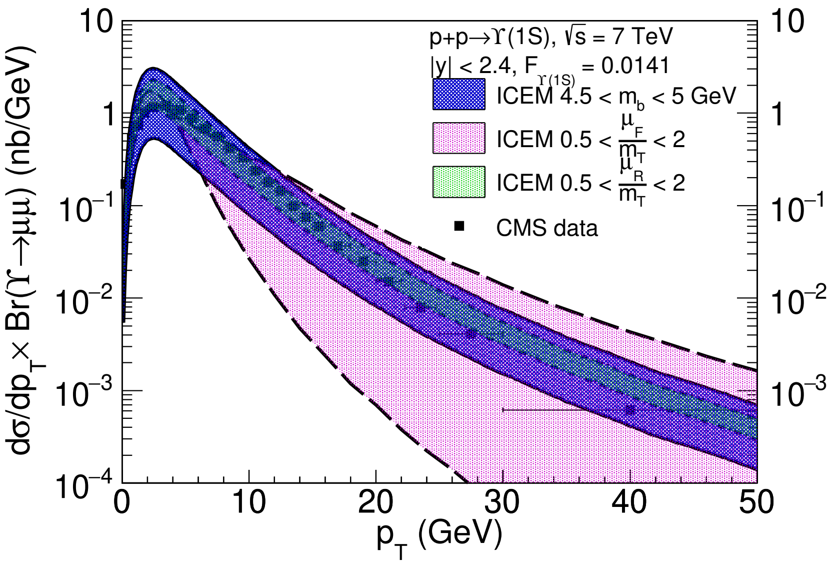

Figure 5.1. The p_T dependence of prompt Υ(1S) production at $\sqrt{s} = 7$ TeV in the ICEM obtained by varying the bottom quark mass (blue), the factorization scale in the range $0.5 < \mu_F/m_T < 2$ (magenta), and the renormalization scale in the range $0.5 < \mu_R/m_T < 2$ (green) is compared with the CMS midrapidity data [122].

Eq. (5.3) has to be independent of the projectile, target, and energy for each bottomonium state $\mathcal{Q}$. Even though the focus of this paper is on polarization, independent of $F_{\mathcal{Q}}$, the unpolarized bottomonium yields in the ICEM using the k_T-factorization approach were not calculated before. Therefore, it is important to first confirm that this approach can indeed describe the bottomonium yields as a function of p_T and rapidity before discussing polarization. The direct production cross section is calculated using Eq. (5.9) by integrating the pair invariant mass from $M_{\mathcal{Q}}$ to $2m_{B^0}$ ($m_{B^0} = 5.28$ GeV).

We first obtain $F_{\Upsilon(n\mathrm{S})}$ by comparing our results with the $\Upsilon(n\mathrm{S})$ yields measured by the CMS Collaboration at 7 TeV. Using the same $F_{\Upsilon(n\mathrm{S})}$, we compare our results with the $\Upsilon(n\mathrm{S})$ data measured at CDF and LHCb.

5.4.1.1 Υ(1S) p_T distribution

We found in our previous paper [59] that the charmonium p_T distribution has a significant dependence on the factorization scale for $p_T > 5$ GeV. In this paper, we also fix the factorization scale at $\mu_F = m_T$ instead of including a factor of two variation. In Fig. 5.1, we show the p_T distributions of prompt Υ(1S) production at $\sqrt{s} = 7$ TeV found by fixing

$m_b = 4.75$ GeV and varying the factorization scale over the range $0.5 < \mu_F/m_T < 2$ and the renormalization scale over the range $0.5 < \mu_R/m_T < 2$ separately. We also fix $\mu_F/m_T = \mu_R/m_T = 1$ and vary the bottom quark mass over the range $4.5 < m_b < 5$ GeV. The direct production cross section is calculated using Eq. (5.9) by integrating the pair invariant mass from $M_{\Upsilon(1S)}$ to $2m_{B^0}$ ($m_{D^0} = 5.28$ GeV) over the rapidity range $|y| < 2.4$. We assume that direct production is a constant fraction, 0.71 of the prompt production, according to the low p_T feed-down coefficients in Table 5.2, since the yield is dominated by production at low p_T. We then compare the prompt p_T distribution in the ICEM with the CMS data [122]. Similar to the charmonium p_T distribution, the result has a significant dependence on the factorization scale for $p_T > 5$ GeV. This is because the uPDFs have a sharp cutoff for $k_T > \mu_F$ and are thus very sensitive to the chosen factorization scale. The yield varies more as p_T approaches m_T at high p_T. At low p_T, $m_T \sim M_{\mathcal{Q}}$ and the cross section is independent of the factorization scale since $k_T \ll \mu_F$. At moderate p_T, the variation with μ_F is similar to or smaller than that due to the bottom quark mass. At $p_T \sim 10$ GeV, $m_T \sim p_T$. Thus the lower limit on the factorization scale, $m_T/2$, is on the order of k_T and the yield drops off at this cutoff limit of ~ 5 GeV, while the upper limit on the factorization scale, $2m_T$, is still greater than k_T, enhancing the yield. Since, at LO, only the $b\bar{b}$ pair carries the transverse momentum, the predictive power for the yields is limited by the uPDFs. Therefore, to construct a meaningful uncertainty band, we fix the factorization scale at $\mu_F = m_T$. As we push toward the limit of the k_T-factorization approach with uPDFs at high p_T at LO, we can only improve the high p_T limit by a full NLO calculation in the collinear factorization approach where there is no hard limit on μ_F as in k_T-factorization approach.

After fixing the factorization scale, the variation in bottom quark mass then gives the largest uncertainty, followed by the variation in renormalization scale. When μ_R is reduced, the strong coupling constant is larger, increasing the yield. On the other hand, when m_b is reduced, the yield increases. In the remainder of this section, we present our results by adding the uncertainties due to variations of the bottom mass and renormalization scale in quadrature.

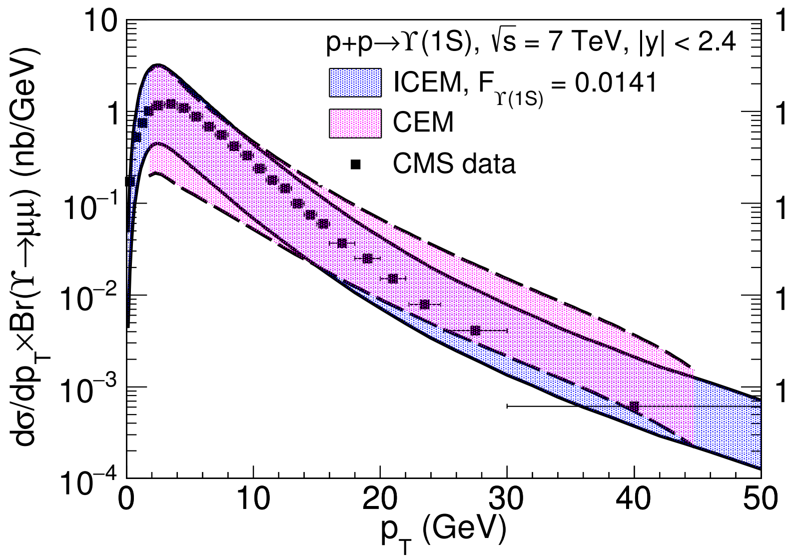

Figure 5.2. The p_T dependence of prompt Υ(1S) production at $\sqrt{s}$ = 7 TeV in the ICEM with combined mass and renormalization scale uncertainties (blue) and that in the CEM using collinear factorization approach (magenta). The CMS midrapidity data [122] from Fig. 5.1 are also shown.

The prompt Υ(1S) p_T distribution at $\sqrt{s} = 7$ TeV with combined uncertainty is shown in Fig. 5.2. The ICEM result has a peak at $p_T \sim 2.5$ GeV, in agreement with the data. By matching to the total experimental unpolarized yield in $|y| < 2.4$, we find that the ICEM can describe the Υ(1S) p_T distribution with $F_{\Upsilon(1S)} = 0.0141$. This is the fraction of $b\bar{b}$ pairs produced in the invariant mass range from $M_{\Upsilon(1S)}$ to $2m_{B^0}$, a difference of ∼1 GeV, that result in direct Υ(1S) production, defined in Eq. (5.3). In general, the ICEM p_T distribution agrees with the data for all p_T.

In the same figure, we compare the inclusive Υ(1S) p_T distributions with that from the CEM in the collinear factorization approach. The uncertainty band is constructed by combining the uncertainty by varying the bottom mass in the range $4.56 < m_b < 4.74$ GeV, the factorization scale in the range $0.91 < \mu_F/m_T < 2.17$, and the renormalization scale in the range $0.9 < \mu_R/m_T < 1.32$. We find two distributions agree reasonably well with each other and the data.

We test the universality of $F_{\Upsilon(1S)}$ by comparing the prompt Υ(1S) p_T distribution in the ICEM measured by LHCb [124] at $\sqrt{s} = 7$ TeV and $2 < y < 4.5$ in Fig. 5.3 and to the prompt Υ(1S) p_T distribution measured by D0 [125] at $\sqrt{s} = 1.8$ TeV and $|y| < 0.5$

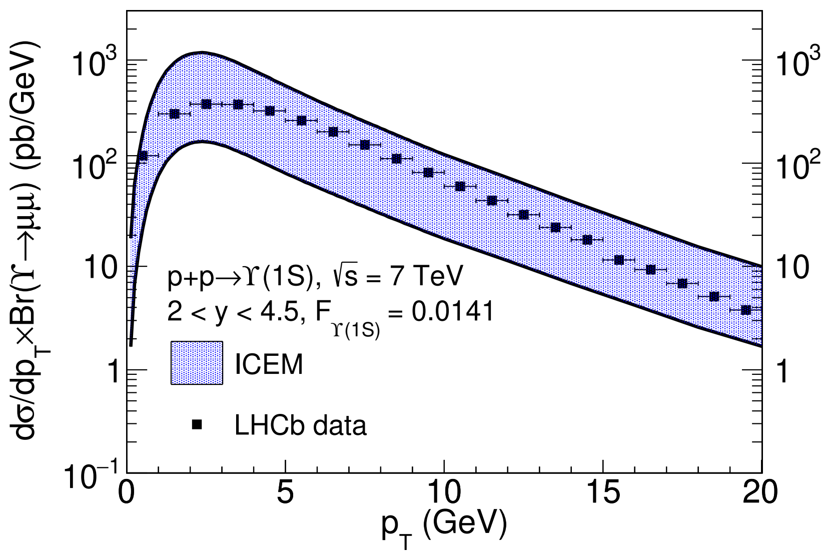

Figure 5.3. The p_T dependence of prompt Υ(1S) production at $\sqrt{s} = 7$ TeV and $2 < y < 4.5$ in the ICEM with combined mass and renormalization scale uncertainties is compared with the LHCb data [124].

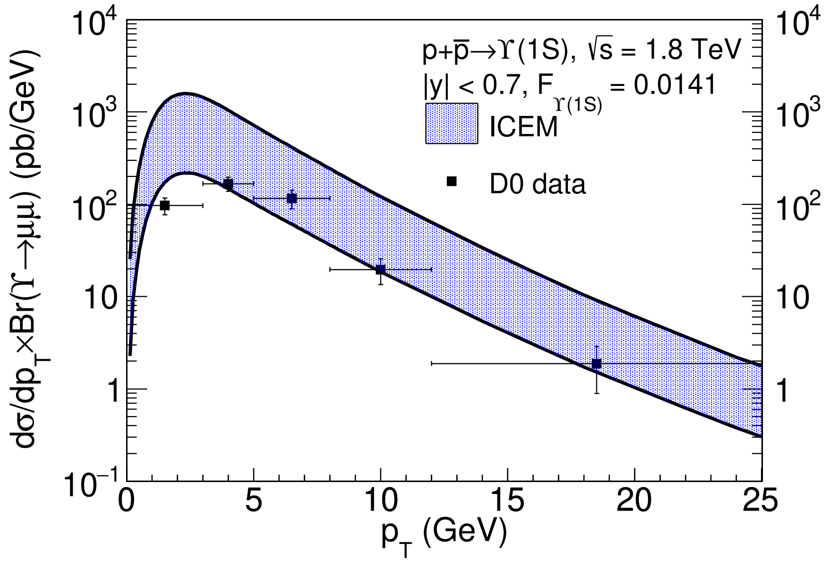

Figure 5.4. The p_T dependence of prompt Υ(1S) production at $\sqrt{s} = 7$ TeV and $|y| < 0.7$ in the ICEM with combined mass and renormalization scale uncertainties is compared with the D0 data [125].

in Fig. 5.4. We again assume the direct production is a constant fraction, 0.71, of the prompt production to obtain the prompt Υ(1S) cross section. We find the ICEM result agrees with the data for all p_T.

5.4.1.2 Υ(2S) p_T distribution

The prompt Υ(2S) p_T distribution at $\sqrt{s} = 7$ TeV is compared to the CMS measurement [122] over $|y| < 2.4$ in Fig. 5.5 and the LHCb data [124] in $2 < y < 4.5$ in Fig. 5.6. Here, the direct production cross section is calculated using Eq. (5.9) by integrating the pair invariant mass from $M_{\Upsilon(2S)}$ to $2m_{B^0}$ over the rapidity range $|y| < 2.4$. Similar to direct Υ(1S), we assume the direct production of Υ(2S) is a constant fraction, 0.73, of the prompt production. We then compare the p_T-integrated yield of prompt Υ(2S) with the CMS measurement [122]. By matching the p_T-integrated yield, we find $F_{\Upsilon(2S)} = 0.0144$. We note that $F_{\Upsilon(2S)} \gtrsim F_{\Upsilon(1S)}$, primarily because the integrated mass region is much narrower for Υ(2S) than Υ(1S), a difference of $\sim$0.5 GeV in this case. In the traditional CEM, $F_{\Upsilon(2S)}$ is smaller than $F_{\Upsilon(1S)}$ because the range of integration over the pair invariant mass is the same for all $\Upsilon(n\mathrm{S})$. We find agreement with the data within the combined uncertainty band constructed by varying the bottom quark mass and the renormalization scale in the ICEM. In both cases, the calculations, with their associated uncertainty bands, are in agreement with the data.

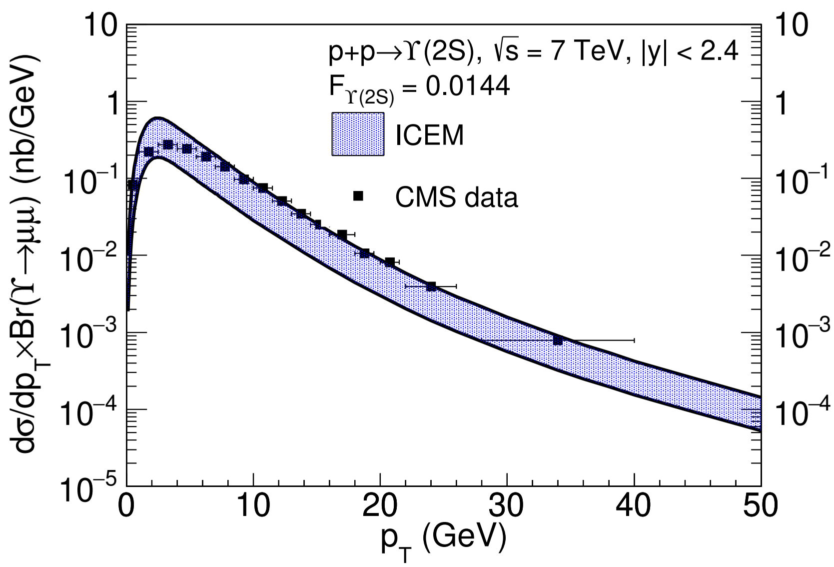

Figure 5.5. The p_T dependence of prompt Υ(2S) production at $\sqrt{s} = 7$ TeV and $2 < y < 4.5$ in the ICEM with combined mass and renormalization scale uncertainties is compared with the CMS midrapidity data [122].

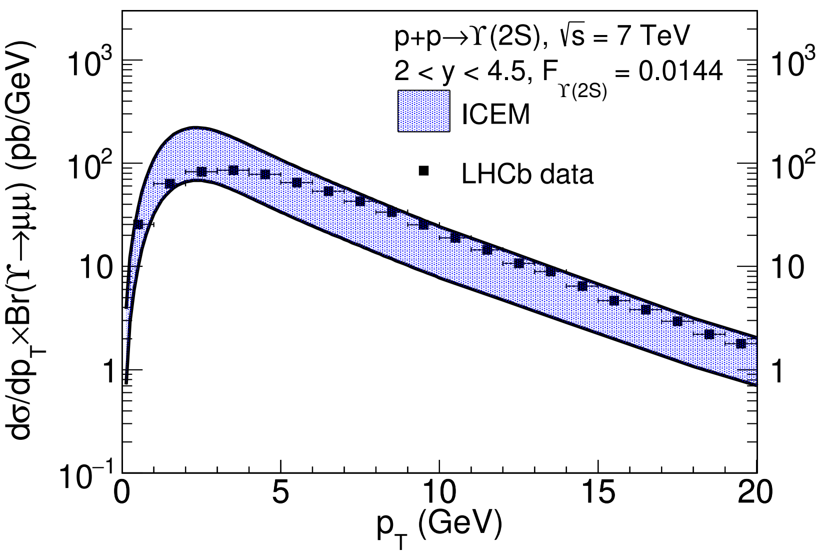

Figure 5.6. The p_T dependence of prompt Υ(2S) production at $\sqrt{s} = 7$ TeV and $2 < y < 4.5$ in the ICEM with combined mass and renormalization scale uncertainties is compared with the LHCb data [124].

5.4.1.3 Υ(3S) p_T distribution

The prompt Υ(3S) p_T distribution at $\sqrt{s} = 7$ TeV is compared to the CMS measurements [122] over $|y| < 2.4$ in Fig. 5.7 and the LHCb data [124] in $2 < y < 4.5$ in Fig. 5.8. Here, the direct production cross section is calculated using Eq. (5.9) by integrating the pair invariant mass from $M_{\Upsilon(3S)}$ to $2m_{B^0}$ over the rapidity range $|y| < 2.4$. Similar to direct Υ(1S), we assume the direct production of Υ(3S) is a constant fraction, 0.70, of the prompt production. Therefore, we compare the p_T-integrated yield of direct Υ(3S) with the CMS measurement [122]. We find $F_{\Upsilon(3S)} = 0.00229$. We note that also $F_{\Upsilon(3S)} \gtrsim F_{\Upsilon(1S)}$, because the mass range is still smaller for Υ(3S), a difference of only ~ 0.15 GeV. Again, in the traditional CEM, $F_{\Upsilon(3S)}$ is smaller than $F_{\Upsilon(1S)}$ and $F_{\Upsilon(2S)}$ because the range of integration over the pair invariant mass is also the same for both Υ(1S) and Υ(3S). There is fair agreement with the data within the combined uncertainty band constructed by varying the bottom quark mass and the renormalization scale in the ICEM. In both cases, the calculations, with their associated uncertainty bands, are in agreement with the data.

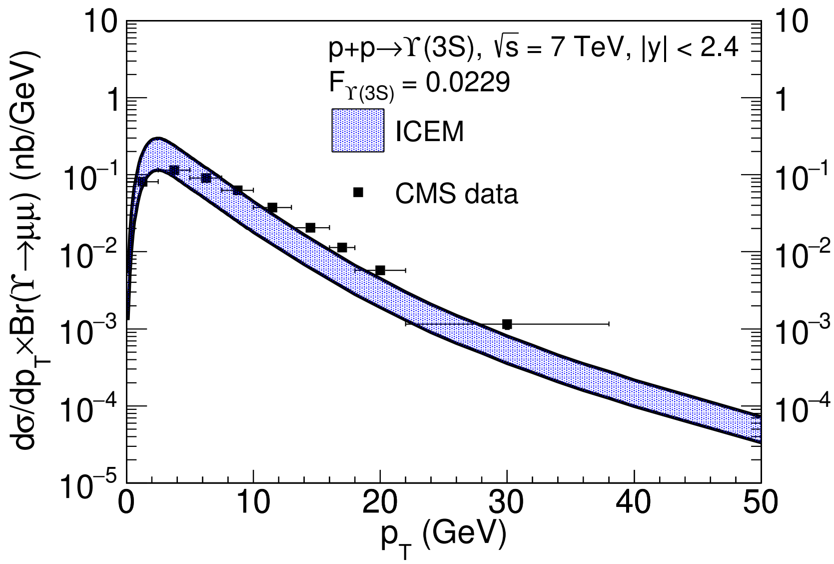

Figure 5.7. The p_T dependence of prompt Υ(3S) production at $\sqrt{s} = 7$ TeV in the ICEM with combined mass and renormalization scale uncertainties is compared with the CMS midrapidity data [122].

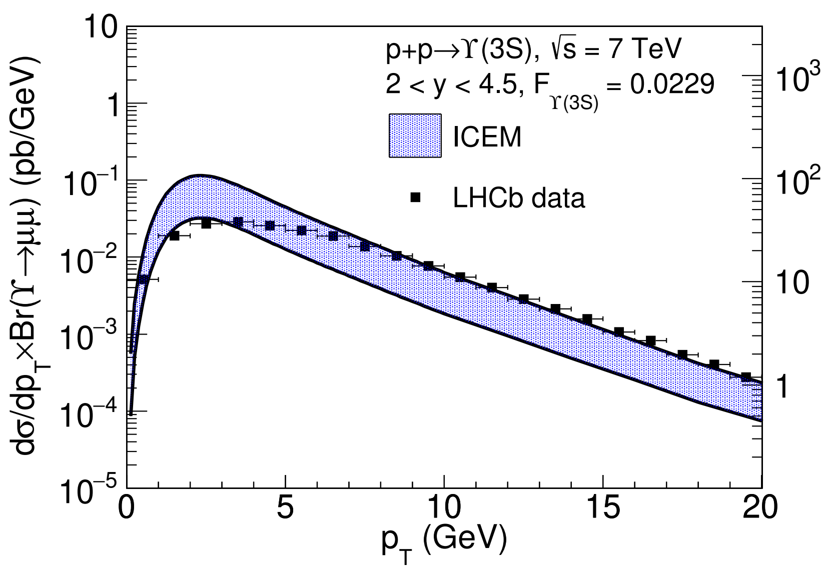

Figure 5.8. The p_T dependence of prompt Υ(2S) production at $\sqrt{s} = 7$ TeV and $2 < y < 4.5$ in the ICEM with combined mass and renormalization scale uncertainties is compared with the LHCb data [124].

5.4.1.4 Ratio of χ_{b2}(1P) to χ_{b1}(1P) production

We now turn to the p_T dependence of the ratio $\chi_{b2}(1\mathrm{P})/\chi_{b1}(1\mathrm{P})$ as a function of p_T. The ratios of direct χ_{b2}(1P) to direct χ_{b1}(1P) at $\sqrt{s} = 8$ TeV at central and forward

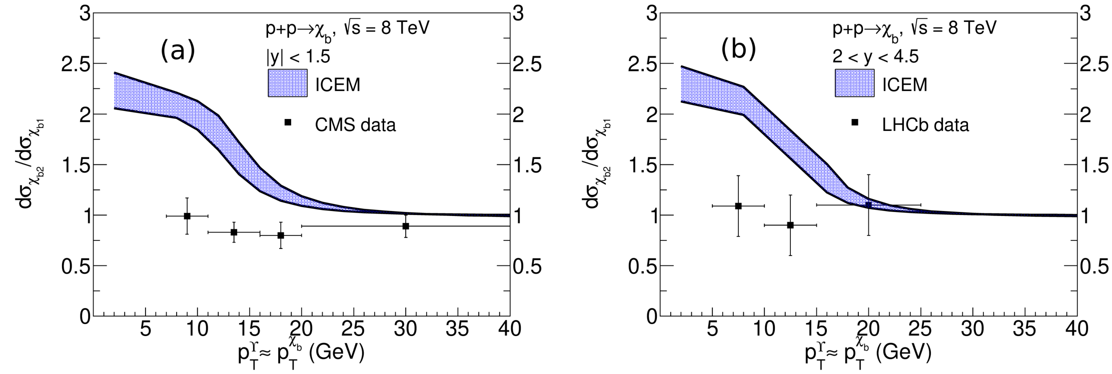

Figure 5.9. The ratio of $\chi_{b2}(1\text{P})$ to $\chi_{b1}(1\text{P})$ in the ICEM with combined mass and renormalization scale uncertainties at $\sqrt{s} = 8$ TeV at central rapidity $|y| < 1.5$ (a) and at forward rapidity $2 < y < 4.5$ (b) assuming $F_{\chi_{b1(1\text{P})}} = F_{\chi_{b2(1\text{P})}}$. The CMS data [126] and the LHCb data [127] are also shown in (a) and (b) respectively.

rapidities are presented in Fig. 5.9. Direct production is calculated using Eq. (5.9) by integrating the pair invariant mass from $M_{\chi_{b1,2}}(1\text{P})$ to $2m_{B^0}$ over two rapidity ranges, $|y| < 1.5$ and $2 < y < 4.5$ respectively, in order to compare with existing measurements [126, 127]. As there is not enough information on the feed-down production to χ_b, we assume the prompt production of $\chi_{b1,2}(1\text{P})$ is approximately the same as the direct production. Since there are no measurements of the absolute $\chi_{b1,2}(1\text{P})$ production cross sections, we cannot fix $F_{\chi_{b1,2}(1\text{P})}$. Furthermore, the data reports the ratio as a function of the p_T of $\Upsilon(1\text{S})$. To compare our results with the data, we then assume that $p_T^{\chi_b} \approx p_T^{\Upsilon(1\text{S})}$, not unreasonable since the mass difference between the states is ~ 500 MeV and the decay photon is soft. Thus the ICEM can only predict the trend of the relative production subject to an overall vertical shift. Similar to the χ_{c2} to χ_{c1} ratio in the ICEM [59], $\chi_{b2}(1\text{P})/\chi_{b1}(1\text{P})$ becomes constant for $p_T > 2M_{\chi_b}$. However, the relative production decreases with increasing p_T for $p_T < 2M_{\chi_b}$, independent of the rapidity range considered. Our ICEM results only agree with the data in the higher p_T range. This is because the difference between the amplitudes of χ_{b1} and χ_{b2} is most apparent at low p_T since the curvature of the distributions changes fastest near the peaks of the distributions. However, the measured relative production is approximately p_T independent at lower p_T. We note that the χ_{c2}/χ_{c1} ratios presented in Ref. [59] agreed with the data over the measured p_T range because, in that case, $p_T >> M_{\chi_c}$ over the range of the measurement. However, with the lower p_T range here

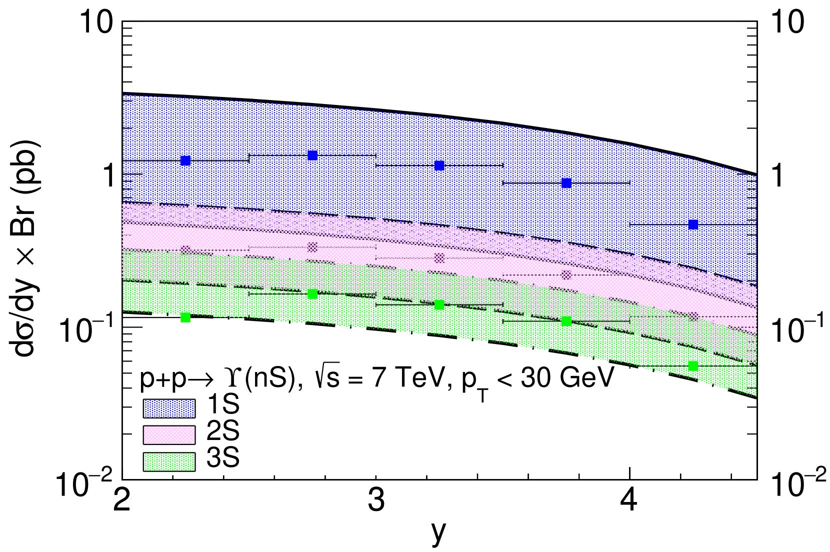

Figure 5.10. The rapidity dependence of prompt Υ(1S) (blue solid), Υ(2S) (magenta dashed), and Υ(3S) (green dot-dashed) production at $\sqrt{s} = 7$ TeV integrated over $p_T < 30$ GeV in the ICEM with combined mass and renormalization scale uncertainties are compared with the LHCb data [124].

this condition is not satisfied for χ_b.

5.4.1.5 $\Upsilon(n\mathrm{S})$ rapidity distribution

We now turn to the rapidity dependence of $\Upsilon(n\mathrm{S})$ production. The rapidity distribution of prompt of $\Upsilon(n\mathrm{S})$ at $\sqrt{s} = 7$ TeV is shown in Fig. 5.10. The direct production is calculated using Eq. (5.10) by integrating over the p_T range $0 < p_T < 30$ GeV. We again assume the direct production of Υ(1S, 2S, 3S) is a constant 71%, 73%, and 70% of prompt Υ(1S, 2S, 3S) production respectively. We use the same values of $F_{\Upsilon(n\mathrm{S})}$ determined for the p_T distributions to compare the rapidity distribution in the ICEM with the measurement made by the LHCb Collaboration [124]. We find the ICEM can describe the LHCb rapidity distribution at $\sqrt{s} = 7$ TeV using the $F_{\Upsilon(n\mathrm{S})}$ obtained at the same energy by CMS in the central rapidity region.

5.4.2 p_T dependence of λ_ϑ

Here, we present the p_T dependence of the polarization parameter λ_ϑ in $p + p$ and $p + \bar{p}$ collisions. Because the polarization parameter is defined as the ratio of polarized to unpolarized cross sections in Eq. (5.11) and these cross sections depend on μ_R in the same way, the polarization parameter is independent of the scale choice. Note that λ_ϑ is thus also independent of μ_F. However, the amplitudes themselves are mass dependent so that the polarized to unpolarized ratio in λ_ϑ depends on the bottom quark mass. Thus the only uncertainty on λ_ϑ in our calculation is due to the variation of m_b in the range $4.5 < m_b < 5$ GeV. Therefore, in this section, the uncertainty bands only include the mass variation and the uncertainty in the calculated polarization is reduced relative to those of the yield calculations.

We note that the J_z components of the polarized cross section depend differently on the bottom quark mass. When $p_T \leq M_\mathcal{Q}$, the longitudinally polarized partonic cross section decreases faster with increasing m_b than the transversely polarized partonic cross section in the helicity frame. Thus increasing the bottom quark mass results in more transverse polarization. When $p_T > M_\mathcal{Q}$, the longitudinally-polarized partonic cross section decreases more slowly with increasing m_b than the transversely-polarized partonic cross section. Thus, increasing the bottom quark mass results in more longitudinal polarization. As $p_T \gg \hat{s}$, λ_ϑ becomes insensitive to m_b. Thus the uncertainty in λ_θ is narrower at high p_T.

Our calculation also depends on the feed-down ratios presented in Table 5.2, taken from Ref. [101]. Here, "low p_T" refers to $p_T \lesssim 20$ GeV and "high p_T" refers to $p_T \gtrsim 20$ GeV. We use the "low p_T" ratios to compare our results with LHCb data ($0 < p_T < 20$ GeV) and the "high p_T" ratios to compare with the CMS data ($10 < p_T < 50$ GeV).

5.4.2.1 prompt $\Upsilon(n\mathrm{S})$ polarization in $p + p(\bar{p})$ collisions at low p_T

We present the polarization parameters for prompt $\Upsilon(1\mathrm{S})$ in $p + p$ collisions at $\sqrt{s} = 7$ TeV at forward rapidity ($2.2 < y < 3$) in the helicity frame (HX) in Fig. 5.11. We compare our results with data from the LHCb Collaboration in the forward rapidity region [128]. The ICEM polarization of prompt $\Upsilon(n\mathrm{S})$ in the helicity frame is slightly transverse at low p_T ($p_T < M_\Upsilon$). The result becomes unpolarized for $p_T > M_\Upsilon$. We do not find that the polarization has any significant rapidity dependence. The ICEM polarization agrees with the LHCb data for $p_T > M_\Upsilon$.

We also compare the polarization parameter for prompt $\Upsilon(1\mathrm{S})$ in $p+\bar{p}$ at $\sqrt{s} = 1.8$ TeV

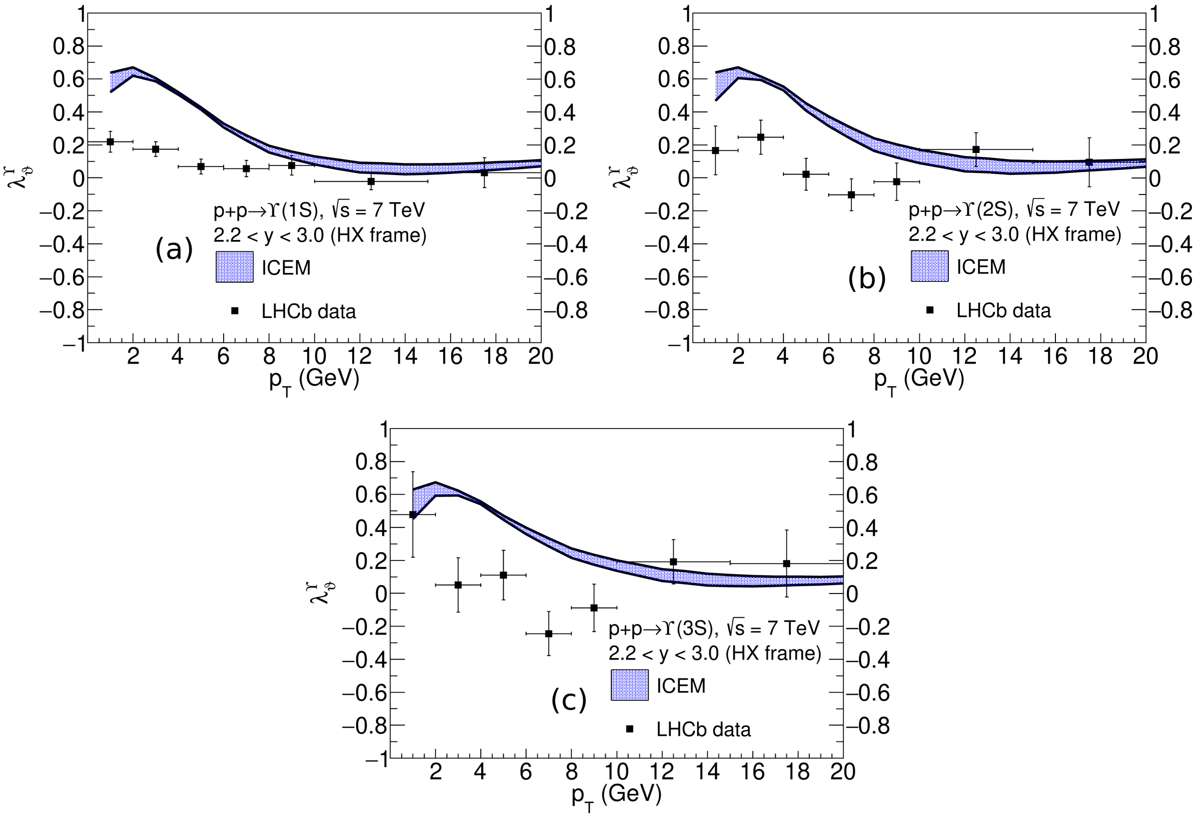

Figure 5.11. The p_T dependence of the polarization parameter λ_ϑ for prompt Υ(1S) (a), Υ(2S) (b), and Υ(3S) (c) production in the helicity frame at $\sqrt{s} = 7$ TeV in the ICEM using the "low p_T" c_Q's with mass uncertainties are compared to the LHCb data in the range $2.2 < y < 3$ [128].

with the data measured by the D0 Collaboration in the region $|y| < 0.4$ [129] in the helicity frame, shown in Fig. 5.12. We also do not find a strong dependence on $\sqrt{s}$ for the prompt Υ(1S) polarization in the ICEM. The trend in the p_T dependence of the polarization is the same. At the highest p_T bin, the prompt Υ(1S) polarization measured by the D0 Collaboration is slightly longitudinal while still agreeing with the ICEM calculation, which gives an unpolarized result.

We do not find significant differences in the polarizations among the $\Upsilon(n\text{S})$ states. This is because the calculations of the $\Upsilon(n\text{S})$ states differ from one another only by the integration limits of the ICEM. Furthermore, the polarization depends only on the ratio of polarized to unpolarized cross sections. Thus there is only a slight difference in polarization whether only direct production is included or if feed down also contributes.

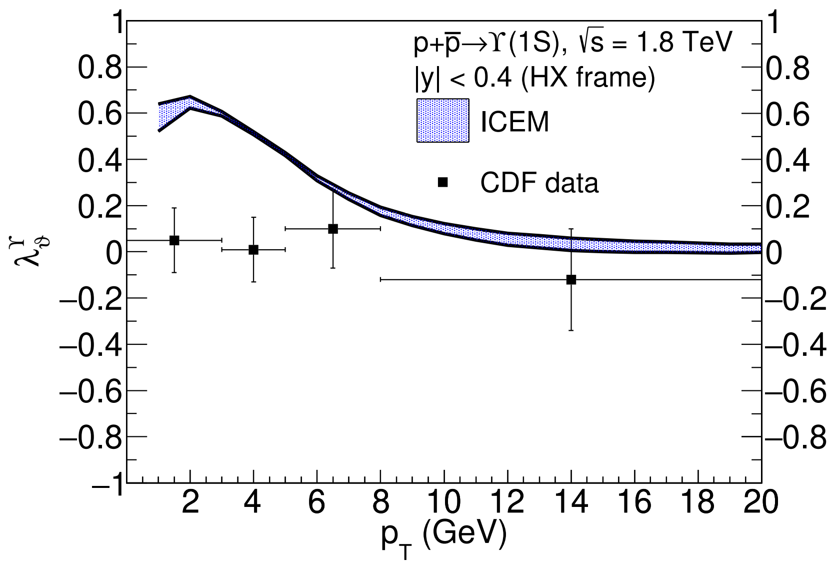

Figure 5.12. The p_T dependence of the polarization parameter λ_ϑ for prompt Υ(1S) production in the helicity frame at $\sqrt{s} = 1.8$ TeV with $|y| < 0.4$ in the ICEM using the "low p_T" c_Q's [101] with mass uncertainties are compared to the CDF data [129].

Therefore the polarization of $\Upsilon(n\mathrm{S})$ from χ_b feed down is similar to that for direct production $\Upsilon(n\mathrm{S})$ alone. Thus, varying the feed-down ratio, either by adopting the "high p_T" ratios from Ref. [101] used here or the p_T-independent ratios calculated in Ref. [84] and used in Ref. [58], changes the polarization by less than 0.05 over all p_T. Our results differ from an NLO NRQCD calculation finding that all $\Upsilon(n\mathrm{S})$ states are unpolarized: $(-0.2 < \lambda_\vartheta < 0.2)$ at low p_T [114]. In their approach, at low p_T, the direct $\Upsilon(n\mathrm{S})$ states are slightly longitudinally polarized while the contribution from χ_b feed down is slightly transverse, resulting in unpolarized prompt production.

5.4.2.2 prompt $\Upsilon(n\mathrm{S})$ polarization in $p + p(\bar{p})$ collisions at high p_T

We present the polarization parameters for prompt Υ(1S) in $p + p$ collisions at $\sqrt{s} =$ 7 TeV at central rapidity ($|y| < 0.6$) in the helicity frame respectively in Fig. 5.13. We compare our results with the data from the CMS Collaboration in the central rapidity region [130]. The ICEM polarization of prompt Υ in the helicity frame is near unpolarized at intermediate p_T ($p_T \sim M_\Upsilon$). We see that λ_ϑ becomes unpolarized for $p_T > M_\Upsilon$. The ICEM polarization agrees with the CMS data for Υ(1S) and only agrees with Υ(2S) and Υ(3S) data within 2σ. We do not find that the polarization has any significant rapidity

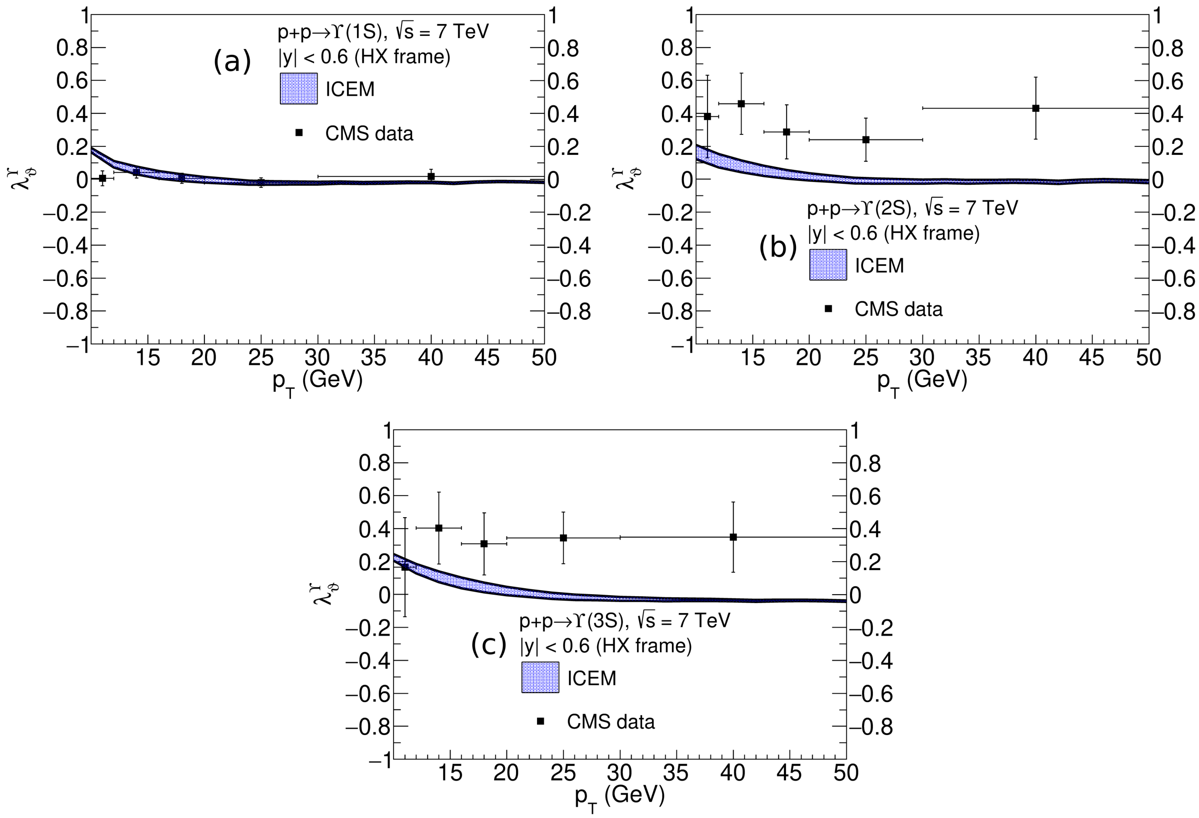

Figure 5.13. The p_T dependence of the polarization parameter λ_ϑ for prompt Υ(1S) (a), Υ(2S) (b), and Υ(3S) (c) production in the helicity frame at $\sqrt{s} = 7$ TeV in the ICEM using the "high p_T" $c_{\mathcal{Q}}$'s [101] with mass uncertainties are compared to the CMS data at midrapidity in the range $|y| < 0.6$ [130].

dependence.

We note that here we have used the "high p_T" set of feed-down ratios to consider the prompt $\Upsilon(n\mathrm{S})$ polarization. Although the contribution from direct Υ(1S) to prompt Υ(1S) drops from 71% to 45%, the polarization of the prompt production does not change significantly. This is because the polarization of all the bottomonium states below the $B\overline{B}$ threshold are very similar after feed down to prompt $\Upsilon(n\mathrm{S})$. We note that the polarization at intermediate p_T, $p_T \sim 15$ GeV, has no significant dependence on the choice of feed-down ratios, as shown in Figs. 5.11 and 5.13. The variation of the feed down fractions is negligible compared to the bottom quark mass variation.

Similar to our results at low p_T, we do not find significant differences in polarizations among the $\Upsilon(n\mathrm{S})$ states. Our results differ from an NLO NRQCD calculation finding that the polarization at $p_T \gtrsim 20$ GeV is more transverse for higher mass bound states, saturating at $\lambda_\vartheta \sim 0.2$, ~ 0.4, and ~ 0.9 for Υ(1S), Υ(2S), and Υ(3S) respectively [114]. The significant transverse polarization of Υ(3S) in their approach is due to the fact that the polarization is calculated without the contribution from χ_b feed-down production. In a subsequent update of Ref. [114], where $\chi_b(n\mathrm{P})$ feed-down production is considered, the polarization parameters saturate at $\lambda_\vartheta \sim 0.4$, ~ 0.6, and ~ 0.6 for Υ(1S), Υ(2S), and Υ(3S) respectively [131]. (See also Ref. [132].)

5.4.3 Frame dependence of λ_ϑ

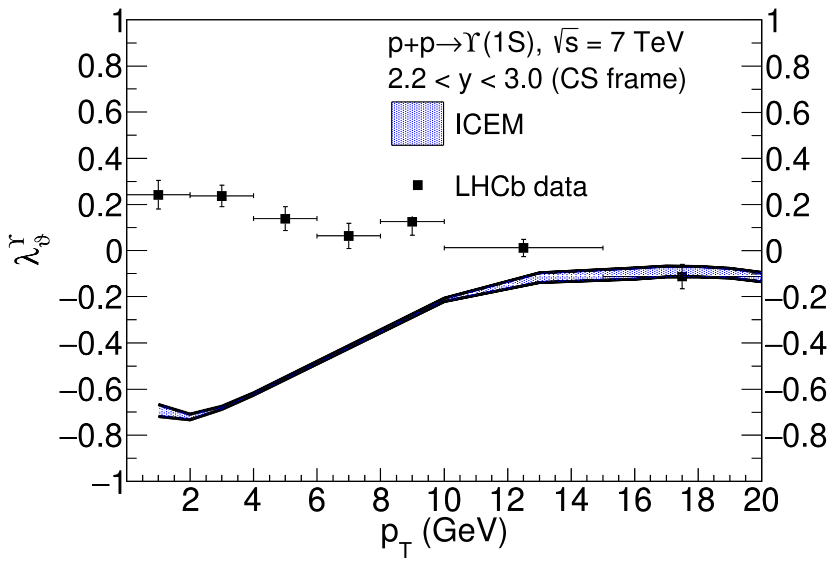

Figure 5.14. The p_T dependence of the polarization parameter λ_ϑ for prompt Υ(1S) production in the Collins-Soper frame at $\sqrt{s} = 7$ TeV and $2.2 < y < 3$ in the ICEM using the "low p_T" c_Q's [101] with mass uncertainties are compared to the LHCb data [128].

We now turn to the frame dependence of our 7 TeV results. We calculate the polarization parameter in $p + p$ collisions at $\sqrt{s} = 7$ TeV in the same kinematic region as presented in Fig. 5.11 in both the Collins-Soper and the Gottfried-Jackson frames, shown in Figs. 5.14 and 5.15 respectively. Since the polarization axes in the helicity frame and the Collins-Soper frame are always perpendicular to each other in $\mathcal{O}(\alpha_s^2)$ kinematics, the polarization in the Collins-Soper frame is opposite to that in the helicity frame in the ICEM. Therefore, at low p_T, where the Υ(1S) is predicted to be slightly transverse in the

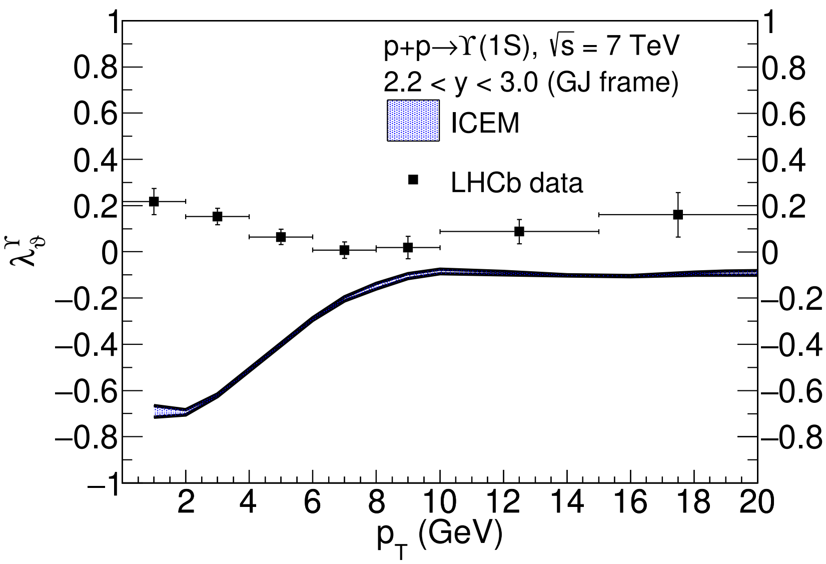

Figure 5.15. The p_T dependence of the polarization parameter λ_ϑ for prompt Υ(1S) production in the Gottfried-Jackson frame at $\sqrt{s}$ = 7 TeV and $2.2 < y < 3$ in the ICEM using the "low p_T" c_Q's [101] with mass uncertainties are compared to the LHCb data [128].

helicity frame, it is predicted to be slightly longitudinal in the Collins-Soper frame. For $p_T > M_\Upsilon$, λ_ϑ is predicted to be unpolarized in both frames. We only find agreement with the data in the Collins-Soper frame for the highest p_T bin. When $p_T \ll m_T$, the angle between the polarization axes in the Gottfried-Jackson frame and that in the Collins-Soper frame is small. As p_T increases, the polarization axis in the Gottfried-Jackson frame becomes collinear with that in the helicity frame. Therefore, the polarization calculated in the Gottfried-Jackson frame is opposite to that in the helicity frame at low p_T and thus similar to that in the Collins-Soper frame. However, as p_T increases, the polarization in the Gottfried-Jackson frame should asymptotically approach the polarization in the helicity frame. Since λ_ϑ is unpolarized in the helicity frame in the high p_T limit, the ICEM polarization becomes frame independent in this limit. We find the ICEM polarization agrees with the data in all frames at high p_T but does not agree with the low p_T data where the frame dependence is most significant.

5.5 Conclusions

We have presented the transverse momentum distributions of the prompt $\Upsilon(n\text{S})$ cross section as well as the the polarization of prompt $\Upsilon(n\text{S})$ production in $p+p$ and $p+\bar{p}$ collisions in the improved color evaporation model in the k_T-factorization approach. We compared the p_T dependence to data at collider energies. We also presented the ratio $\chi_{b2}(1\text{P})/\chi_{b1}(1\text{P})$ as a function of p_T at $\sqrt{s} = 8$ TeV. We find prompt $\Upsilon(n\text{S})$ production to be unpolarized at $p_T \gtrsim M_\Upsilon$, independent of frame. We do not observe any rapidity or energy dependence in the polarization in the ranges considered.

Since our calculation of the matrix elements is leading order in α_s, we expect improvements when we calculate the cross section to $\mathcal{O}(\alpha_s^3)$ in a future publication.

Chapter 6

Production and Polarization of Direct J/ψ in the Improved Color Evaporation Model using the Collinear Factorization Approach

Production and Polarization of Direct J/ψ in the Improved Color Evaporation Model using the Collinear Factorization Approach

V. Cheung[a] and R. Vogt[a,b,1]

[a]Department of Physics
University of California, Davis
Davis, CA 95616, USA
and
[b]Nuclear and Chemical Sciences Division
Lawrence Livermore National Laboratory
Livermore, CA 94551, USA

ABSTRACT

We calculate the production and polarization of direct J/ψ production in the improved color evaporation model at $\mathcal{O}(\alpha_s^3)$ in the collinear factorization approach. We present the production and the polarization parameters of direct J/ψ production in $p+p$ collisions as a function of transverse momentum. We include the p_T dependence of the polarization parameters λ_ϑ, λ_ϕ, $\lambda_{\vartheta\phi}$ in the helicty and the Collins-Soper frames, as well as the frame-invariant polarization parameter $\tilde{\lambda}$. This is the first p_T-dependent calculation of J/ψ production and polarization in the improved color evaporation model using the collinear factorization approach. We find agreement with both J/ψ cross sections and polarization measurements.

[1]This work was performed under the auspices of the U.S. Department of Energy by Lawrence Livermore National Laboratory under Contract DE-AC52-07NA27344 and supported by the U.S. Department of Energy, Office of Science, Office of Nuclear Physics (Nuclear Theory) under contract number DE-SC-0004014.

6.1 Introduction

Understanding quarkonium production is important to understand both the long and short distance aspects of QCD. Both the perturbative and non-perturbative natures of QCD are needed to model the production of quarkonium from heavy quark production in hard processes to the hadronization of the final state. Nonrelativistic QCD (NRQCD) [61], the most commonly employed model of quarkonium production cannot describe the J/ψ production and polarization while respecting the universality of the long distance matrix elements (LDMEs) for p_T cuts less than twice the mass of the quarkonium state [62, 63]. It also has difficulty describing the J/ψ polarization and the LHCb η_c production [92, 93] while using heavy quark spin symmetry [65–67]. On the other hand, the color evaporation model (CEM) [69–71] and the improved CEM [56] have only been employed extensively to hadroproduction on S-state quarkonia only. While polarization data is a strong test of models, precise data measured from the future electron-ion collider demand an expansion of the ICEM beyond hadroproduction.

Our previous charmonium and bottomonium polarization calculations performed in the k_T-factorization approach [58, 59] describes both the polarization and production at most p_T. However, the p_T-dependence of the production calculation has a strong dependence on the factorization scale chosen. Also, the frame-dependent discrepancies between the ICEM polarization calculation and the measured data are not visualized quantitatively. We address these issues in this paper by performing a polarized production calculation in the collinear factorization approach, and also computing a frame-invariant polarization parameter to compare with the data. In this calculation, only the production and polarization of direct J/ψ is presented. We will address the effects of feed-down production on J/ψ in a later publication.

In this paper, we present both the yield and the polarization parameters of direct J/ψ production as a function of p_T in the ICEM [56] using the collinear factorization approach. The ICEM assumes the J/ψ production cross section takes a constant fraction of the open $c\bar{c}$ cross section with invariant mass above the mass of the J/ψ but below the hadron threshold, which is the $D\overline{D}$ limit. A distinction is also made between the $c\bar{c}$

momentum and the J/ψ momentum in the ICEM compared to the traditional CEM. The direct J/ψ production cross section in $p+p$ collision in the ICEM is given by

$$\sigma = F_{J/\psi} \sum_{i,j} \int_{M_{J/\psi}}^{2m_D} dM dx_i dx_j f_i(x_i, \mu_F) f_j(x_j, \mu_F) \hat{\sigma}_{ij \to c\bar{c}+k}(p_{c\bar{c}}, \mu_R)|_{p_{c\bar{c}} = \frac{M}{M_{J/\psi}} p_\psi} , \quad (6.1)$$

where i and j are $q, \bar{q}$ and g such that $ij = q\bar{q}$ or gg, $F_{J/\psi}$ is a universal factor at fixed order for direct J/ψ production in the ICEM that is independent of projectile and energy, x is the momentum fraction of the parton, and $f(x, \mu_F)$ is the parton distribution function (PDF) for a parton of the proton as a function of x and the factorization scale μ_F. Finally, $\hat{\sigma}_{ij \to c\bar{c}+k}$ are the parton-level cross sections for $ij \to c\bar{c}$ with a light parton k. The invariant mass of the $c\bar{c}$ pair, M, is integrated from the physical mass of J/ψ ($M_{J/\psi} = 3.10$ GeV) to two times the mass of the D^0 hadron ($2m_{D^0} = 3.72$ GeV). In order to describe the p_T-distribution at low p_T, the initial state partons are each introduced to a small gaussian transverse momentum, k_T, kick of $\langle k_T^2 \rangle = 1 + (1/12)\ln(\sqrt{s}/20 \text{ GeV}) = 1.49 \text{ GeV}^2$ for $\sqrt{s} = 7$ TeV. The parton distribution functions are then multiplied by the gaussian function $g(k_T)$

$$g(k_T) = \frac{1}{\pi \langle k_T^2 \rangle} \exp(k_T^2 / \langle k_T^2 \rangle) , \quad (6.2)$$

assuming the x and k_T dependences completely factorize. The same gaussian smearing is applied in Refs. [56, 72, 133]. Note that in the traditional CEM, the lower invariant mass threshold for all charmonium states are all set to the production threshold, which makes the kinematic distributions of the charmonium states are almost identical except for a different $F_{\mathcal{Q}}$. The distinction between the J/ψ momentum and $c\bar{c}$ momentum also helps describe the p_T distributions at high p_T.

We consider diagrams with the projection operators applied to the $c\bar{c}$ [91, 134] to calculate the partonic cross sections. We denote the momenta of i, j, c, $\bar{c}$, and r in the partonic process $i+j \to c+\bar{c}+r$ are denoted as k_1, k_2, p_c, $p_{\bar{c}}$, and k_3 respectively, where r is the emitted parton, with $\epsilon(k_1)$, $\epsilon(k_2)$, and $\epsilon(k_3)$ denoting the polarization of the parton when applied. When calculating the $2 \to 3$ cross section, we transformed the momenta of the charm quark (p_c) and the anti-charm quark ($p_{\bar{c}}$) into the momentum of the proto-J/ψ

(p_ψ) and the relative momentum of the heavy quarks (k_r)

$$p_c = \frac{1}{2}p_\psi + k_r \ , \tag{6.3}$$

$$p_{\bar{c}} = \frac{1}{2}p_\psi - k_r \ , \tag{6.4}$$

and denote the polarization vector of the proto-J/ψ as $\epsilon(S_z)$ where S_z is the spin projection onto the polarization axis. Instead of taking the limit $k_r \to 0$, we note that since the mass of the proto-J/ψ is integrated from the physical mass of J/ψ to the hadronic threshold, the relative momentum k_r depends on the mass of the proto-J/ψ. We include 16 diagrams from $gg \to c\bar{c}g$, where the Feynman part of the amplitudes, $\mathcal{A}$, in $\mathcal{M} = C\mathcal{A}$, arranged by the number of three-gluon vertices, are

$$\begin{aligned}
\mathcal{A}_{gg0} &= ig_s^3 \,\mathrm{tr}\left[\not\epsilon_2(\not p_c - \not k_2 + m_c)\not\epsilon_3^*(-\not p_{\bar{c}} + \not k_1 + m_c)\not\epsilon_1 \not\epsilon(S_z)\frac{\not p_\psi + m_\psi}{2m_\psi}\right]\frac{1}{2p_c\cdot k_2}\frac{1}{2p_{\bar{c}}\cdot k_1} \\
&+ \text{permutations} \ , \qquad (6.5) \\
\mathcal{A}_{gg1} &= ig_s^3 \,\mathrm{tr}\left[\not\epsilon_3^*(\not p_c + \not k_3 + m_c)\gamma^\mu \not\epsilon(S_z)\frac{\not p_\psi + m_\psi}{2m_\psi}\right][(-k_1 - 2k_2)\cdot\epsilon_1\epsilon_{2\mu} \\
&+ (\epsilon_1\cdot\epsilon_2)(-k_1 + k_2)_\mu + (2k_1 + k_2)\cdot\epsilon_2\epsilon_{1\mu})]\frac{1}{2p_c\cdot k_3}\frac{1}{(k_1 + k_2)^2} \\
&+ \text{permutations} \ , \qquad (6.6) \\
\mathcal{A}_{gg2} &= ig_s^3 \,\mathrm{tr}\left[\gamma^\nu \not\epsilon(S_z)\frac{\not p_\psi + m_\psi}{2m_\psi}\right][(-k_1 - 2k_2)\cdot\epsilon_1\epsilon_2^\mu + (\epsilon_1\cdot\epsilon_2)(-k_1 + k_2)^\mu \\
&+ (2k_1 + k_2)\cdot\epsilon_2\epsilon_1^\mu)] \\
&\times [(-k_1 - k_2 - p_\psi)\cdot\epsilon_3^* g_{\mu\nu} + \epsilon_{3\mu}^*(k_3 + k_1 + k_2)_\nu + (p_\psi - k_3)_\mu\epsilon_{3\nu}^*]\frac{1}{(k_1 + k_2)^2}\frac{1}{m_\psi^2} \\
&+ \text{permutations} \ , \qquad (6.7)
\end{aligned}$$

and the diagram with a four-gluon vertex factorized in the form

$$\mathcal{M}_{gg4} = C_{gg4,1}\mathcal{A}_{gg4,1} + C_{gg4,2}\mathcal{A}_{gg4,2} + C_{4,3}\mathcal{A}_{gg4,3} \ , \tag{6.8}$$

with

$$\mathcal{A}_{gg4,1} = ig_s^3 \,\mathrm{tr}\left[\gamma^\nu \not\epsilon(S_z)\frac{\not p_\psi + m_\psi}{2m_\psi}\right](g_{\alpha\gamma}g_{\nu\beta} - g_{\alpha\beta}g_{\nu\gamma})\frac{1}{m_\psi^2}\epsilon^\alpha \epsilon_2^\beta \epsilon_3^{*\gamma} \,, \tag{6.9}$$

$$\mathcal{A}_{gg4,2} = ig_s^3 \,\mathrm{tr}\left[\gamma^\nu \not\epsilon(S_z)\frac{\not p_\psi + m_\psi}{2m_\psi}\right](g_{\alpha\nu}g_{\gamma\beta} - g_{\alpha\beta}g_{\gamma\nu})\frac{1}{m_\psi^2}\epsilon^\alpha \epsilon_2^\beta \epsilon_3^{*\gamma} \,, \tag{6.10}$$

$$\mathcal{A}_{gg4,3} = ig_s^3 \,\mathrm{tr}\left[\gamma^\nu \not\epsilon(S_z)\frac{\not p_\psi + m_\psi}{2m_\psi}\right](g_{\alpha\gamma}g_{\nu\beta} - g_{\alpha\nu}g_{\gamma\beta})\frac{1}{m_\psi^2}\epsilon^\alpha \epsilon_2^\beta \epsilon_3^{*\gamma} \,. \tag{6.11}$$

We include 5 diagrams from $gq \to c\bar{c}q$ which written in terms of Dirac spinors are,

$$\mathcal{A}_{gq,1} = -ig_s^3 \,\mathrm{tr}\left[\gamma^\nu \not\epsilon(S_z)\frac{\not p_\psi + m_\psi}{2m_\psi}\right][\bar{u}(k_3)\gamma_\nu(\not k_1 + \not k_2)\not\epsilon_1 u(k_2)]\frac{1}{m_\psi^2}\frac{1}{2k_1\cdot k_2} \,, \tag{6.12}$$

$$\begin{aligned}\mathcal{A}_{gq,2} &= -ig_s^3 \,\mathrm{tr}\left[\not\epsilon_1(\not p_c - \not k_1 + m_c)\gamma^\nu \not\epsilon(S_z)\frac{\not p_\psi + m_\psi}{2m_\psi}\right][\bar{u}(k_3)\gamma_\nu u(k_2)] \\ &\times \frac{1}{-2p_c\cdot k_1}\frac{1}{(-k_3+k_2)^2} \,,\end{aligned} \tag{6.13}$$

$$\begin{aligned}\mathcal{A}_{gq,3} &= -ig_s^3 \,\mathrm{tr}\left[\gamma^\nu(\not p_{\bar{c}} + \not k_1 + m_c)\not\epsilon_1 \not\epsilon(S_z)\frac{\not p_\psi + m_\psi}{2m_\psi}\right][\bar{u}(k_3)\gamma_\nu u(k_2)] \\ &\times \frac{1}{-2p_{\bar{c}}\cdot k_1}\frac{1}{(-k_3+k_2)^2} \,,\end{aligned} \tag{6.14}$$

$$\begin{aligned}\mathcal{A}_{gq,4} &= -ig_s^3 \,\mathrm{tr}\left[\gamma^\nu \not\epsilon(S_z)\frac{\not p_\psi + m_\psi}{2m_\psi}\right][(k_3 - k_2 - p_\psi)\cdot\epsilon_1 g_{\mu\nu} + \epsilon_{1\mu}(-k_1 - k_3 + k_2)_\nu \\ &+ (p_\psi + k_1)_\mu \epsilon_{1\nu}][\bar{u}(k_3)\gamma^\mu u(k_2)]\frac{1}{m_\psi^2}\frac{1}{(-k_3+k_2)^2} \,,\end{aligned} \tag{6.15}$$

$$\mathcal{A}_{gq,5} = -ig_s^3 \,\mathrm{tr}\left[\gamma^\nu \not\epsilon(S_z)\frac{\not p_\psi + m_\psi}{2m_\psi}\right][\bar{u}(k_3)\not\epsilon_1(\not k_3 - \not k_1)\gamma_\nu u(k_2)]\frac{1}{m_\psi^2}\frac{1}{-2k_1\cdot k_2} \,. \tag{6.16}$$

We include 5 diagrams from $g\bar{q} \to c\bar{c}\bar{q}$, which are,

$$\begin{aligned}
\mathcal{A}_{g\bar{q},1} &= -ig_s^3 \,\mathrm{tr}\left[\gamma^\nu \not\epsilon(S_z)\frac{\not p_\psi + m_\psi}{2m_\psi}\right][\bar{v}(k_2)\not\epsilon_1(-\not k_2 - \not k_1)\gamma_\nu v(k_3)]\frac{1}{m_\psi^2}\frac{1}{2k_1\cdot k_2}\ , &(6.17)\\
\mathcal{A}_{g\bar{q},2} &= -ig_s^3 \,\mathrm{tr}\left[\not\epsilon_1(\not p_c - \not k_1 + m_c)\gamma^\nu \not\epsilon(S_z)\frac{\not p_\psi + m_\psi}{2m_\psi}\right][\bar{v}(k_2)\gamma_\nu v(k_3)]\\
&\times \frac{1}{-2p_c\cdot k_1}\frac{1}{(-k_3+k_2)^2}\ , &(6.18)\\
\mathcal{A}_{g\bar{q},3} &= -ig_s^3 \,\mathrm{tr}\left[\gamma^\nu(-\not p_{\bar{c}} + \not k_1 + m_c)\not\epsilon_1 \not\epsilon(S_z)\frac{\not p_\psi + m_\psi}{2m_\psi}\right][\bar{v}(k_2)\gamma_\nu v(k_3)]\\
&\times \frac{1}{-2p_{\bar{c}}\cdot k_1}\frac{1}{(-k_3+k_2)^2}\ , &(6.19)\\
\mathcal{A}_{g\bar{q},4} &= -ig_s^3 \,\mathrm{tr}\left[\gamma^\nu \not\epsilon_1 \not\epsilon(S_z)\frac{\not p_\psi + m_\psi}{2m_\psi}\right][(k_3 - k_2 - p_\psi)\cdot\epsilon_1 g_{\mu\nu}\\
&+ \epsilon_{1\mu}(-k_1 - k_3 + k_2)_\nu + (p_\psi + k_1)_\mu \epsilon_{1\nu}][\bar{v}(k_2)\gamma^\mu v(k_3)]\frac{1}{m_\psi^2}\frac{1}{(-k_3+k_2)^2}\ , &(6.20)\\
\mathcal{A}_{g\bar{q},5} &= -ig_s^3 \,\mathrm{tr}\left[\gamma^\nu \not\epsilon_1 \not\epsilon(S_z)\frac{\not p_\psi + m_\psi}{2m_\psi}\right][\bar{v}(k_2)\gamma_\nu(-\not k_3 + \not k_1)\not\epsilon_1 v(k_3)]\\
&\times \frac{1}{m_\psi^2}\frac{1}{-2k_3\cdot k_1}\ . &(6.21)
\end{aligned}$$

Finally, we include 5 diagrams from $q\bar{q} \to c\bar{c}g$, which are

$$\begin{aligned}
\mathcal{A}_{q\bar{q},1} &= -ig_s^3 \,\mathrm{tr}\left[\gamma^\nu \not\epsilon(S_z)\frac{\not p_\psi + m_\psi}{2m_\psi}\right][(-k_1 - k_2 - p_\psi)\cdot\epsilon_3^* g_{\mu\nu} \\
&+ \epsilon_{3\mu}^*(k_3 + k_1 + k_2)_\nu + (p_\psi - k_3)_\mu \epsilon_{3\nu}^*][\bar{v}(k_2)\gamma^\mu u(k_1)]\frac{1}{m_\psi^2}\frac{1}{(k_1+k_2)^2}\ , \qquad (6.22) \\
\mathcal{A}_{q\bar{q},2} &= -ig_s^3 \,\mathrm{tr}\left[\not\epsilon_3^*(\not p_c + \not k_3 + m_c)\gamma^\nu \not\epsilon(S_z)\frac{\not p_\psi + m_\psi}{2m_\psi}\right][\bar{v}(k_2)\gamma_\nu u(k_1)] \\
&\times \frac{1}{2p_c\cdot k_3}\frac{1}{(k_1+k_2)^2}\ , \qquad (6.23) \\
\mathcal{A}_{q\bar{q},3} &= -ig_s^3 \,\mathrm{tr}\left[\gamma^\nu(-\not p_{\bar{c}} - \not k_3 + m_c)\not\epsilon_3^* \not\epsilon(S_z)\frac{\not p_\psi + m_\psi}{2m_\psi}\right][\bar{v}(k_2)\gamma_\nu u(k_1)] \\
&\times \frac{1}{2p_{\bar{c}}\cdot k_3}\frac{1}{(k_1+k_2)^2}\ , \qquad (6.24) \\
\mathcal{A}_{q\bar{q},4} &= -ig_s^3 \,\mathrm{tr}\left[\gamma^\nu \not\epsilon(S_z)\frac{\not p_\psi + m_\psi}{2m_\psi}\right][\bar{v}(k_2)\gamma_\nu(-\not k_3 + \not k_1)\not\epsilon_3^* u(k_1)] \\
&\times \frac{1}{m_\psi^2}\frac{1}{-2k_1\cdot k_3}\ . \qquad (6.25)
\end{aligned}$$

The color factors, C, in the squared amplitudes are calculated separately by summing over all colors and averaging over the initial state colors. We assume that the angular momentum of the proto-J/ψ is unchanged by the transition from the parton level to the hadron level. We then convolute the partonic cross sections with the CT14 PDFs [15] on the domain where $p_\psi \cdot k = 0$. We restrict the partonic cross section calculations within the perturbative domain by introducing a regularization parameter such that all propagators are at a minimum distance of $q^2_{reg} = M^2$ from their poles as used in Ref. [91]. We take the factorization and renormalizaton scale to be $\mu_F/m_T = 2.1^{+2.55}_{-0.85}$ and $\mu_F/m_T = 1.6^{+0.11}_{-0.12}$ respectively, where m_T is the transverse mass of the charm quark produced ($m_T = \sqrt{m_c^2 + p_T^2}$, where $p_T^2 = 0.5\sqrt{p_{Tc}^2 + p_{T\bar{c}}^2}$). We also vary the charm quark mass around 1.27 ± 0.09 GeV. These variations were determined in Ref. [72] where the uncertainty of total charm cross section were considered.

6.2 Polarized production of direct J/ψ

We factor the polarization vector, $\epsilon(S_z)$, from the unsquared ampltidues for all sub-processes, giving us the form

$$\mathcal{M}_n = \epsilon^\mu(S_z)\mathcal{M}_{n,\mu} \tag{6.26}$$

for each sub-process denoted by the initial states, $n = gg, gq, g\bar{q}, q\bar{q}$. The polarization vectors for $J_z = 0, \pm1$ in the rest frame of the proto-J/ψ are

$$\epsilon(0)^\mu = (1,0,0,0) \ , \tag{6.27}$$

$$\epsilon(\pm1)^\mu = \mp\frac{1}{\sqrt{2}}(0,1,\pm i,0) \ , \tag{6.28}$$

in the convention that the fourth component is the z-component. While the unpolarized cross section does not depend on the choice of z-axis, the polarized cross sections depend on the orientation of the z-axis. In this calculation, the y axis is chosen to be the normal vector of the plane formed by the two beams with momenta $\vec{P}_1$ and $\vec{P}_2$,

$$\hat{y} = \frac{-\vec{P}_1\times\vec{P}_2}{|\vec{P}_1\times\vec{P}_2|} \ . \tag{6.29}$$

In the helicity frame, the z_{HX}-axis is the flight direction of the $c\bar{c}$ pair in the center-of-mass of the colliding beams. In the Collins-Soper frame, the z_{CS}-axis is the angle bisector between one beam and the opposite direction of the other beam. The x-axis is then determined by the right-handed convention.

We compute the polarized cross sections matrix element, $\sigma_{i,j}$, in the rest frame of the $c\bar{c}$ pair by first taking the product of the unsquared amplitude with polarization vector of $J_z = i$ and the unsquared amplitude with polarization vector of $J_z = j$ in each sub-process (n), then adding them, and finally calculating the cross section according to Eq. (6.1)

$$\sigma_{i,j} = \int \sum_{n=gg,gq,g\bar{q},q\bar{q}} (\epsilon(i)\cdot\mathcal{M}_n)(\epsilon(j)\cdot\mathcal{M}_n)^* \ , \tag{6.30}$$

where $i,j = \{-1,0,+1\}$, and the integral integrates all variables explicitly shown in Eq. (6.1) as well as the Lorentz Invariant phase-spaces in $2\to3$ scatterings. The unpolarized cross section is the trace of the polarized cross sections matrix

$$\sigma_{\mathrm{unpol}} = \sum_i \sigma_{i,i} = \sigma_{-1,-1} + \sigma_{0,0} + \sigma_{+1,+1} \ . \tag{6.31}$$

The polarization parameters are calculated using the matrix elements of the polarized cross section. The polar anisotropy (λ_ϑ), the azimuthal anisotropy (λ_φ), polar-azimuthal correlation ($\lambda_{\vartheta\varphi}$) are given by [34],

$$\lambda_\vartheta = \frac{\sigma_{+1,+1} - \sigma_{0,0}}{\sigma_{+1,+1} + \sigma_{0,0}} , \tag{6.32}$$

$$\lambda_\varphi = \frac{\mathrm{Re}[\sigma_{+1,-1}]}{\sigma_{+1,+1} + \sigma_{0,0}} , \tag{6.33}$$

$$\lambda_{\vartheta\varphi} = \frac{\mathrm{Re}[\sigma_{+1,0} - \sigma_{-1,0}]}{\sqrt{2}(\sigma_{+1,+1} + \sigma_{0,0})} . \tag{6.34}$$

These parameters depend on the frame in which they are calcualted and measured. Since the angular distribution itself is rotationally invariant, there are ways to construct an invariant polarization parameter. One of the combinations to form a frame-invariant polarization parameter ($\tilde{\lambda}$) is [34]

$$\tilde{\lambda} = \frac{\lambda_\vartheta + 3\lambda_\varphi}{1 - \lambda_\varphi} . \tag{6.35}$$

The choice of $\tilde{\lambda}$ here will be the same as the polar anisotropy parameter (λ_ϑ) in a frame where the distribution is azimuthally isotropic ($\lambda_\varphi = 0$). We can remove the frame-induced kinematic dependencies when comparing theoretical predictions to data by considering also the frame-invariant polarization parameter, $\tilde{\lambda}$.

6.3 Results

We first present how our approach describes the transverse momentum distributions of J/ψ compared to LHCb [99] and ALICE [105] measurements at $\sqrt{s} = 7$ TeV, and compare our results with previous calculations in the ICEM. We then discuss the transverse momentum dependence of the frame-dependent polarization parameters λ_ϑ, λ_φ, and $\lambda_{\vartheta\varphi}$ as well as the frame-invariant polarization parameter $\tilde{\lambda}$ compared to the data measured by the LHCb Collaboration [113] and the ALICE Collaboration [112]. In our calculations, we construct the uncertainty bands by varying the charm quark mass, the renormalization scale, and the factorization scale as discussed in section 6.1. The total uncertainty band is constructed by adding the uncertainties in quadrature.

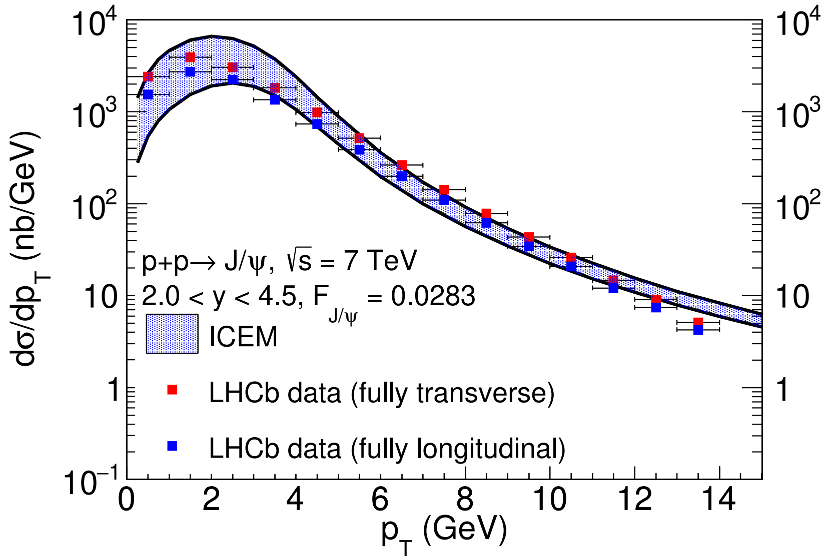

Figure 6.1. The p_T dependence of inclusive J/ψ production at $\sqrt{s} = 7$ TeV with rapidity within the range $2 < y < 4.5$ in the ICEM. The combined mass, renormalization scale, and factorization scale uncertainties are shown in the band and compared to the LHCb data [99]. The LHCb data [99] assuming the J/ψ polarization is totally transverse, $\lambda_\vartheta = +1$ (red square), and totally longitudinal, $\lambda_\vartheta = -1$ (blue square), are shown. The LHCb data assuming $\lambda_\vartheta = 0$ lie between the red and blue points and are not shown.

6.3.1 Unpolarized J/ψ p_T-distribution

We calculate the p_T-distribution of direct J/ψ production at $\sqrt{s} = 7$ TeV with rapidity within the range $2 < y < 4.5$. We assume direct production is a constant fraction of 0.62 of the inclusive production [84] to obtain the inclusive J/ψ p_T-distribution. We compare our ICEM inclusive J/ψ p_T-distribution with the data measured by the LHCb Collaboration [99]. The comparison is presented in Fig. 6.1. By comparing the total cross section for $p_T < 11$ GeV, we obtain the value of $F_{J/\psi}$ to be 0.0283, which is consistent with previous CEM [72] and ICEM calculations [59]. We note that since this calculation is done using collinear factorization, the variation in the factorization scale does not result in a large uncertainty band as seen in our previous calculation using the k_T-factorization approach. Overall, we have good agreement with the data over the p_T range measured.

We compare our ICEM p_T-distribution of inclusive J/ψ production at $\sqrt{s} = 7$ TeV with rapidity within the range $|y| < 0.9$ and $2.5 < y < 4$ with the data measured by the ALICE Collaboration [105]. The comparisons are presented in Fig. 6.2. The ALICE data

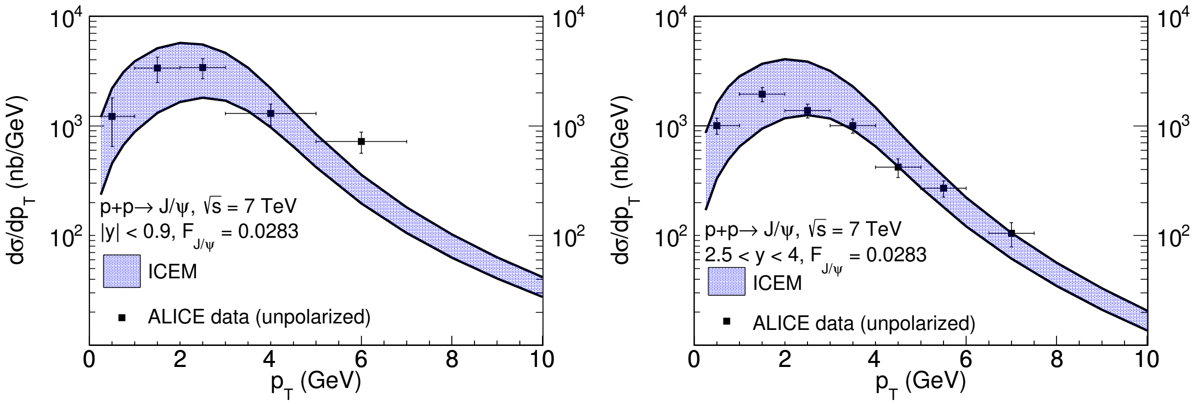

Figure 6.2. The p_T dependence of inclusive J/ψ production at $\sqrt{s} = 7$ TeV with rapidity within the range $|y| < 0.9$ (left) and $2.5 < y < 4$ (right) in the ICEM. The combined mass, renormalization scale, and factorization scale uncertainties are shown in the band and compared to the ALICE data [105]. The ALICE data are measured while assuming J/ψ production is unpolarized.

are measured assuming the J/ψ production is unpolarized. We find our ICEM results in good agreement with the data over the p_T range measured in both kinematic regions using the same $F_{J/\psi}$ by comparing with the LHCb data.

We compare the same p_T-distribution of inclusive J/ψ production at $\sqrt{s} = 7$ TeV shown in 6.1 with that from previous calculations in the ICEM. Although this distribution is for unpolarized J/ψ, the calculation selects only $c\bar{c}$ with the same spin as the J/ψ. We thus refer to this calculation as polarized collinear ICEM. We compare this distribution with the polarized ICEM in the k_T-factorization approach [59] and the unpolarized ICEM in the collinear factorization approach [56]. The former also selects $c\bar{c}$ with the same spin as the J/ψ but the latter is a spin-averaged calculation. The unpolarized collinear ICEM results are calculated in $2.5 < y < 4$ and the uncertainty band is constructed in the same way as the polarized collinear ICEM. The uncertainty band of the k_T-factorized ICEM is constructed by varying the renormalization scale in the interval $0.5 < \mu_R/m_T < 2$ and varying the charm mass in the interval $1.2 < m_c < 1.5$. We find our polarized collinear ICEM agrees with other calculations in the ICEM.

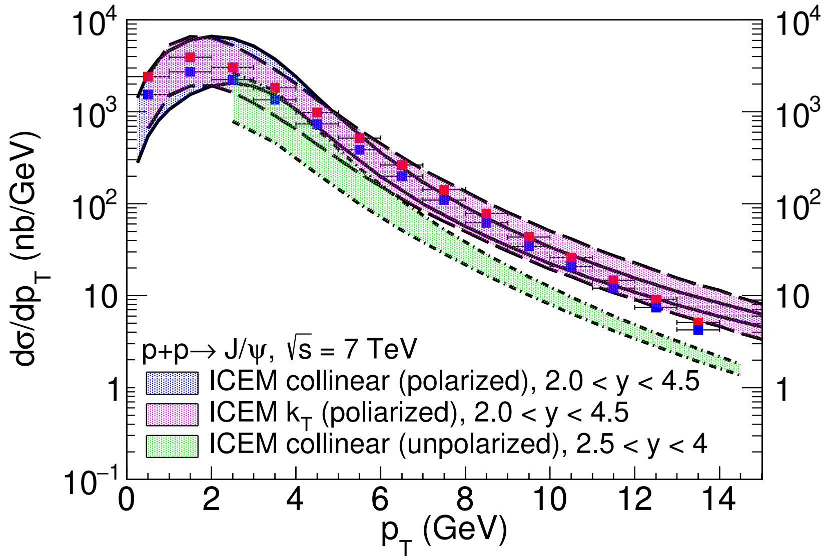

Figure 6.3. The p_T dependence of inclusive J/ψ production at $\sqrt{s}$ = 7 TeV in the polarized collinear ICEM (this calculation) (blue region), in the polarized ICEM using the k_T-factorization [59] (magenta region), in the unpolarized collinear ICEM [56] (green region). The LHCb data [99] are shown as in Fig. 6.1.

6.3.2 p_T dependence of λ_ϑ, λ_φ, and $\lambda_{\vartheta\varphi}$

We calculate the p_T-dependence of the frame-dependent polarization parameters λ_ϑ, λ_φ, and $\lambda_{\vartheta\varphi}$ at $\sqrt{s}$ = 7 TeV within the helicity frame and in the Collins-Soper frame. We do not observe any rapidity dependence in the polarization parameters. We compare these results with both the data measured by the LHCb Collaboration [113] and the data measured by the ALICE Collaboration [112] where the LHCb data are measured in $2 < y < 4.5$ and the ALICE data are measured in $2.4 < y < 4$. The comparisons in the helicity frame and in the Collins-Soper frame are presented in Figs. 6.4 and 6.5 respectively.

The polar anisotropy parameter (λ_ϑ) reflects the proportion of the J/ψ in each spin projection state, with $\lambda_\vartheta = 1$ refering to a completely transverse production of $J_z = \pm 1$, $\lambda_\vartheta = -1$ refering to a completely longitudinal production of $J_z = 0$. At low p_T, λ_ϑ is close to zero in both the helicity frame and the Collins-Soper frame, indicating equal amounts of J/ψ being produced in each spin projection state ($J_z = 0 \pm 1$). However, as p_T gets larger, the difference in λ_ϑ increases across the frames. In the helicity frame, λ_ϑ becomes more negative as p_T grows, showing that more J/ψ is produced with $J_z = 0$ than with

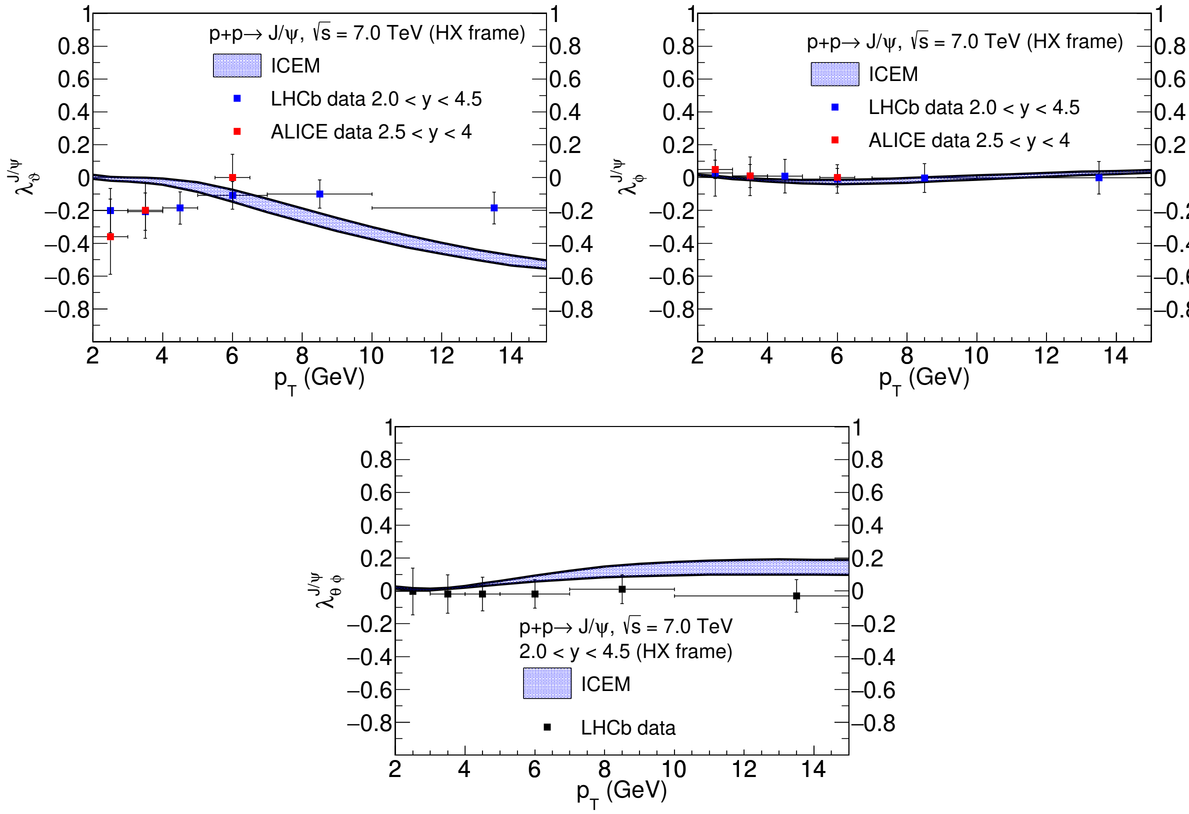

Figure 6.4. The polar anisotropy parameter (λ_ϑ), the azimuthal anisotropy parameter (λ_φ), and the polar-azimuthal correlation parameter ($\lambda_{\vartheta\varphi}$) in the helicity frame at $\sqrt{s} = 7$ TeV in the ICEM. The combined mass, renormalization scale, and factorization scale uncertainties are shown in the band and compared to the LHCb data [113] and the ALICE data [112].

$J_z = \pm 1$. This is consistent with the calculation in Ref. [91] where the calculation in k_T-factorized NRQCD is compared with the CDF data [135]. On the other hand, in the Collins-Soper frame, λ_ϑ becomes more positive as p_T grows, showing that more J/ψ is produced with $J_z = \pm 1$ than with $J_z = 0$. This relative behavior between λ_ϑ is expected because the polarization z-axes are parallel at $p_T = 0$ and become orthogonal in the limit $p_T \to \infty$.

The azimuthal anisotropy parameter (λ_φ) reflects the azimuthal symmetry of J/ψ production. When $\lambda_\varphi = 0$, the production is azimuthally symmetric. When $\lambda_\varphi = \pm 1$, the azimuthal distribution is maximally asymmetric. We note that this parameter strongly depends on the production mechanism as well as the frame the distribution is measured in. In the helicity frame, this parameter is close to zero over all p_T, which means that the

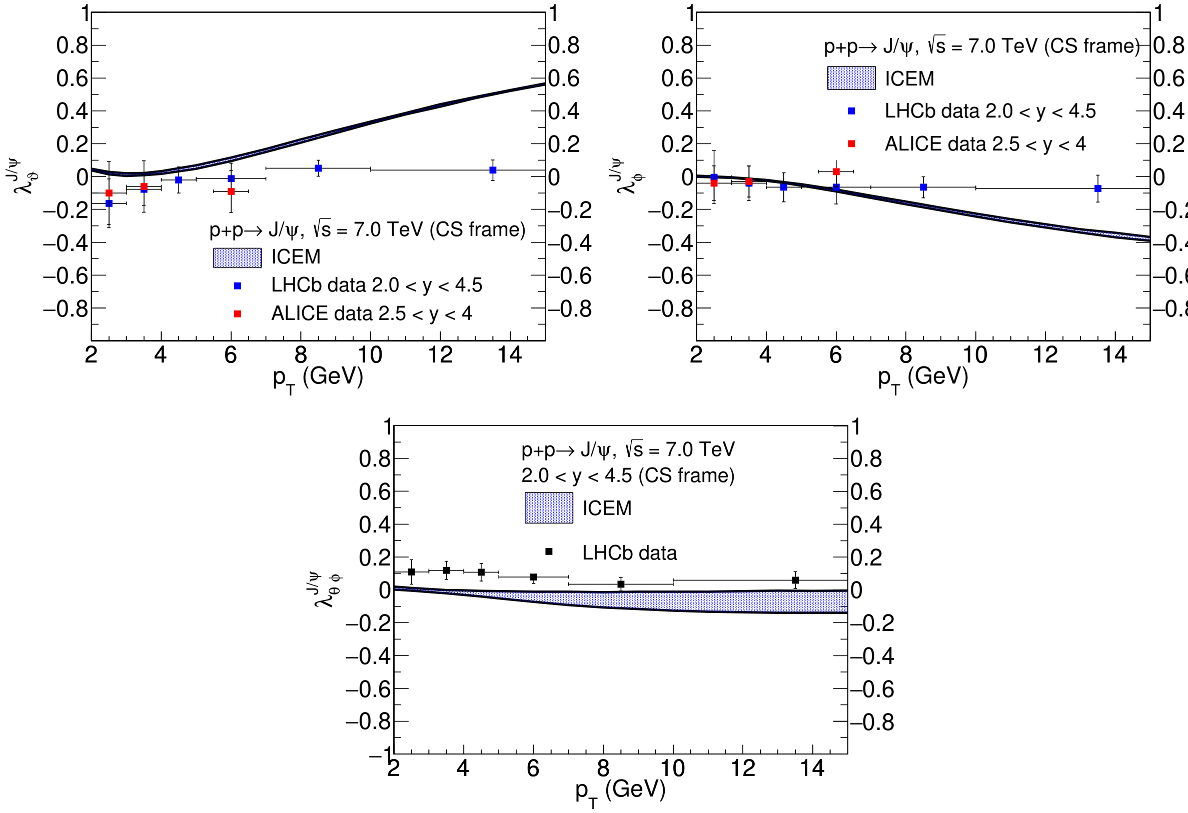

Figure 6.5. The polar anisotropy parameter (λ_ϑ), the azimuthal anisotropy parameter (λ_φ), and the polar-azimuthal correlation parameter ($\lambda_{\vartheta\varphi}$) in the Collins-Soper frame at $\sqrt{s} = 7$ TeV in the ICEM. The combined mass, renormalization scale, and factorization scale uncertainties are shown in the band and compared to the LHCb data [113] and the ALICE data [112].

z_{HX}-axis is approximately the azimuthal symmetry axis. In the Collins-Soper frame, this parameter is negative as p_T gets larger, which means the z_{HX}-axis is not the symmetry axis of the distribution. However, the distribution itself is rotationally invariant. The discrepancy between λ_φ in these two frames is a combination of two factors: z_{CS} and z_{HX} becomes approximately orthogonal as p_T increases, and production is not spherically symmetric.

The polar-azimuthal correlation parameter ($\lambda_{\vartheta\varphi}$) describes the angular correlation between 2ϑ and φ. When $\lambda_{\vartheta\varphi} = 0$, the two angles are uncorrelated and as $\lambda_{\vartheta\varphi}$ departs from 0, the behavior of the distribution becomes similar at locations where $2\vartheta = \varphi$. In both the helicity frame and the Collins-Soper frame, $\lambda_{\vartheta\varphi}$ is consistent with 0.

The angular distributions of the production in the helicity frame and in the Collins-

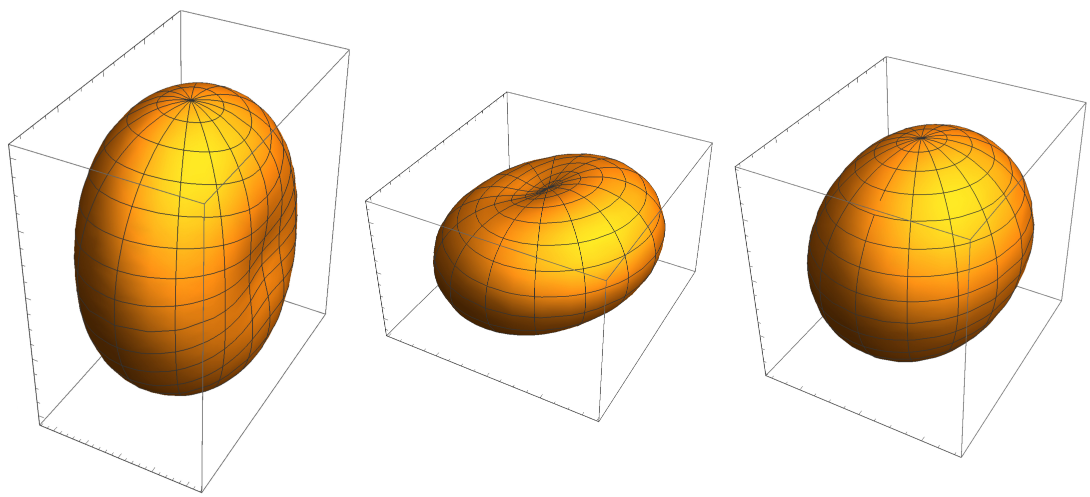

Figure 6.6. The angular distribution of the ICEM direct J/ψ production in the helicity frame (left) and in the Collins-Soper frame (middle) at $p_T = 12$ GeV. They represent the same angular distribution separated by one rotation. The angular distribution in the Collins-Soper frame based on the data collected in the $10 < p_T < 15$ GeV bin by the LHCb collaboration [113] is shown on the right for comparison.

Soper frame at $p_T = 12$ GeV are shown in Fig. 6.6. Note that two distributions are almost identical except they are rotationally approximately 90° apart. Thus the two distributions can be interpreted as a top view and a side view of the production distributions. The angular distribution in the Collins-Soper frame, based on the data collected in the $10 < p_T < 15$ GeV bin by the LHCb Collaboration, is also presented in the same figure.

We compare the polar anisotropy parameter, λ_ϑ, in this calculation with that calculated in the polarized ICEM using the k_T-factorization approach. Since the k_T-factorized ICEM considers only the contribution from off-shell Reggeized gluons at $\mathcal{O}(\alpha_s^2)$, we compare the p_T-dependence of λ_ϑ in the k_T-factorized ICEM with that in this calculation using the contribution from $gg \to c\bar{c}g$ at $\mathcal{O}(\alpha_s^3)$ only. Although the k_T-factorized ICEM considers a $2 \to 2$ process and this calculation considers a $2 \to 3$ process, when the emitted gluon is soft, most of the $2 \to 3$ diagrams resolve into the diagrams in the $2 \to 2$ process. This explains that the difference in λ_ϑ is comparatively small and within the uncertainty of the data at small and moderate p_T. However, at high p_T, the difference becomes larger as the diagrams considered in these calculations are distinct from each other.

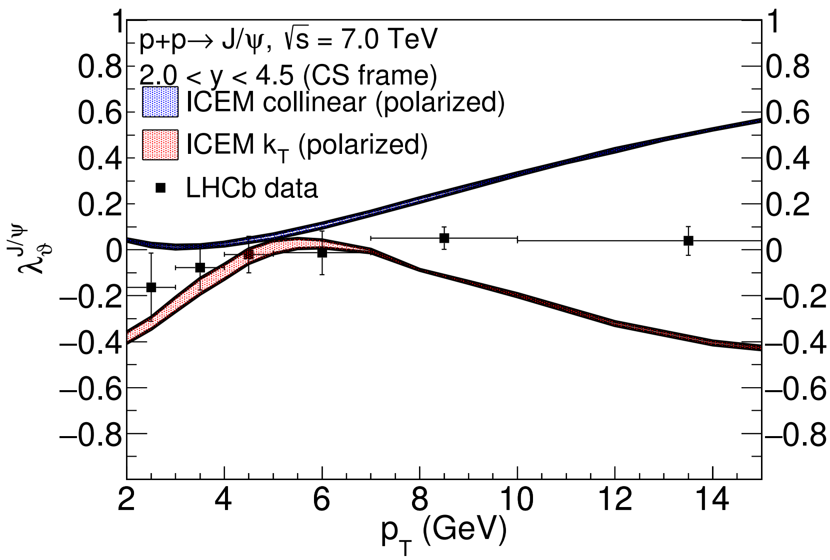

Figure 6.7. The polar anisotropy parameter (λ_ϑ) of direct J/ψ production at $\sqrt{s} =$ 7 TeV with rapidity within the range $2 < y < 4.5$ in the Collins-Soper frame calculated in the collinear ICEM (blue) and k_T-factorized ICEM. Both calculations include only the contribution from gg-channel production only and are compared to the LHCb data [113].

6.3.3 p_T dependence of $\tilde{\lambda}$

In Figs. 6.4 and 6.5, we observe that at high p_T, the ICEM shows better agreement with the measured data in the helicity frame than in the Collins-Soper frame. However, even though we are switching from one frame to another, we are still comparing the same angular distributions. The difference between the ICEM polarization results and the data is then best quantified by a frame-independent polarization parameter. Thus, we compute the frame-invariant polarization parameter $\tilde{\lambda}$ as a function of p_T using λ_ϑ and λ_φ. We compare $\tilde{\lambda}$ as a function of p_T with the LHCb data computed in the helicity and the Collins-Soper frames in Fig. 6.8. We find reasonable agreement with the measured data across all p_T.

6.4 Conclusions

We have presented the transverse momentum dependence of the direct J/ψ cross section as well as the polarization in $p + p$ collisions in the improved color evaporation model in the collinear factorization approach. We compare the p_T dependence to data

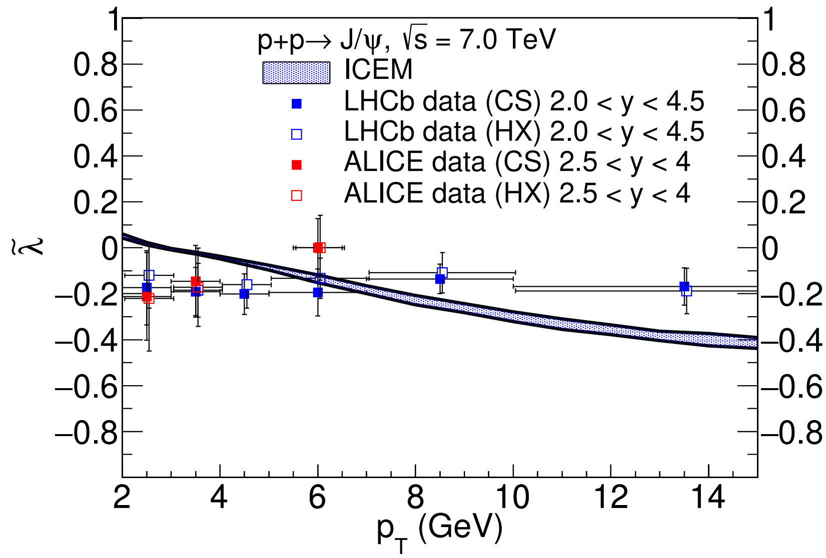

Figure 6.8. The p_T dependence of the frame-invariant polarization parameter, $\tilde{\lambda}$, in the ICEM compared to LHCb data [113] (blue) and the ALICE data [112] (red) measured in the Collins-Soper frame (solid box), and in the helicity frame (empty box). The LHCb in the helicity frame is displaced by 0.05 GeV for visualization purpose.

measured by LHCb. We also present the frame-invariant parameter, $\tilde{\lambda}$ as a function of p_T, and compare our results with the data. We find direct J/ψ production is consistent with the unpolarized data at small and moderate p_T and becomes slightly longitudinal in the high p_T limit. We will study the effects of feed-down production in this approach in a future publication.

Chapter 7

Closing Remarks

Our pioneering work on the CEM and ICEM polarization calculations has become successively more complex: first by providing separate polarization predictions for each quarkonium state and then adding the p_T dependence. Since quarkonium polarization remains a significant source of the systematic experimental uncertainties in quarkonium production measurements, expanding the ICEM to electro- and photoproduction is essential to reduce the experimental uncertainties in collider detectors including the later Electron-Ion Collider (EIC), and to make the ICEM competitive with NRQCD.

At this point, we can compare our polarization results in either the prompt production using the k_T-factorization approach or direct production using the collinear factorization approach with the p_T-dependent data in hadroproduction. The higher-order kinematics employed in the scattering matrix elements in the collinear factorization approach reduces the calculated uncertainty at high p_T arising from the factorization scale dependence of the unintegrated parton distribution functions in the k_T-factorization approach. To have a full comparison of both approaches, a calculation including the feed-down production from P states quarkonium at the same order is highly anticipated. In addition, the CEM and the ICEM have, so far, been applied to calculate the production and polarization of S and P state quarkonia only. The ICEM production of $J^{PC} = 0^{-+}$ states, which are the η_c and η_b states, should be considered in the future.

The current ICEM polarization predictions outperform the NRQCD calculations in hadroproduction where the initial states are quarks and gluons. To further compare with NRQCD, a calculation of quarkonium photoproduction and polarization in the ICEM should also be considered. These calculations can be compared to incoherent photoproduction at HERA, where data exist, and also in J/ψ and ψ' photoproduction in ultraperipheral collisions (UPCs). Production in ultraperipheral p+Pb and Pb+Pb collisions has been measured by the ALICE Collaboration [136]. Expanding the ICEM to electro- and photoproduction of quarkonium will also provide guidance for quarkonium production in the future EIC, the next big facility for high energy nuclear and hadronic physics in the US.

References

[1] S. L. Glashow, Nucl. Phys. **22**, 579-588 (1961).

[2] S. Weinberg, Phys. Rev. Lett. **19**, 1264-1266 (1967).

[3] A. Salam, Conf. Proc. C **680519**, 367-377 (1968).

[4] K. Riesselmann, *The Standard Model of particle physics*, Symmetry Magazine (2015). https://www.symmetrymagazine.org/article/july-2015/standard-model

[5] P. W. Higgs, Phys. Lett. **12**, 132-133 (1964).

[6] P. W. Higgs, Phys. Rev. Lett. **13**, 508-509 (1964).

[7] P. W. Higgs, Phys. Rev. **145**, 1156-1163 (1966).

[8] F. Englert and R. Brout, Phys. Rev. Lett. **13**, 321-323 (1964).

[9] G. S. Guralnik, C. R. Hagen and T. W. B. Kibble, Phys. Rev. Lett. **13**, 585-587 (1964).

[10] P. A. Zyla *et al.* (Particle Data Group), Prog. Theor. Exp. Phys. **2020**, 083C01 (2020).

[11] V. N. Gribov and L. N. Lipatov, Sov. J. Nucl. Phys. **15**, 438-450 (1972).

[12] L. N. Lipatov, Sov. J. Nucl. Phys. **20**, 94-102 (1975).

[13] G. Altarelli and G. Parisi, Nucl. Phys. B **126**, 298-318 (1977).

[14] Y. L. Dokshitzer, Sov. Phys. JETP **46**, 641-653 (1977).

[15] S. Dulat, T. J. Hou, J. Gao, M. Guzzi, J. Huston, P. Nadolsky, J. Pumplin, C. Schmidt, D. Stump and C. P. Yuan, Phys. Rev. D **93**, 033006 (2016).

[16] I. I. Balitsky and L. N. Lipatov, Sov. J. Nucl. Phys. **28**, 822-829 (1978).

[17] L. N. Lipatov, Sov. J. Nucl. Phys. **23**, 338-345 (1976).

[18] E. A. Kuraev, L. N. Lipatov and V. S. Fadin, Sov. Phys. JETP **45**, 199-204 (1977).

[19] F. Hautmann and H. Jung, Nucl. Phys. **B883**, 1 (2014).

[20] M. Hirai, S. Kumano and T. H. Nagai, Phys. Rev. C **76**, 065207 (2007).

[21] K. J. Eskola, P. Paakkinen, H. Paukkunen and C. A. Salgado, Eur. Phys. J. C **77**, 163 (2017).

[22] D. de Florian, R. Sassot, P. Zurita and M. Stratmann, Phys. Rev. D **85**, 074028 (2012).

[23] K. Kovarik *et al.*, Phys. Rev. D **93**, 085037 (2016).

[24] J. J. Aubert *et al.* (European Muon Collaboration) Phys. Lett. B **123**, 275-278 (1983)

[25] E. Eichten, K. Gottfried, T. Kinoshita, K. D. Lane and T. M. Yan, Phys. Rev. D **17**, 3090 (1978); **21**, 313(E) (1980).

[26] E. Eichten and F. L. Feinberg, Phys. Rev. Lett. **43**, 1205 (1979).

[27] R. Vogt, *Ultrarelativistic heavy-ion collisions* (Elsevier, New York, 2007).

[28] S. Okubo, Phys. Lett. **5**, 165 (1963).

[29] G. Zweig, CERN-TH-401 (1964).

[30] J. Iizuka, Prog. Theor. Phys. Suppl. **37**, 21 (1966).

[31] S. Chatrchyan *et al.* (The CMS Collaboration),JINST **7**, P10002 (2012).

[32] K. Gottfried and J. D. Jackson, Nuovo Cimento **33**, 309 (1964).

[33] J. C. Collins and D. E. Soper, Phys. Rev. D **16**, 2219 (1977).

[34] P. Faccioli, C. Lourenco, J. Seixas, and H. K. Wohri, Eur. Phys. J. C **69**, 657 (2010).

[35] G. Aad *et al.* (ATLAS Collaboration), Nucl. Phys. **B850**, 387 (2011).

[36] J. D. Bjorken and S. L. Glashow, Phys. Lett. **11**, 255-257 (1964).

[37] S. L. Glashow, J. Iliopoulos and L. Maiani, Phys. Rev. D **2**, 1285-1292 (1970).

[38] J. J. Aubert *et al.*, Phys. Rev. Lett. **33**, 1404 (1974).

[39] J. E. Augustin *et al.*, Phys. Rev. Lett. **33**, 1406 (1974).

[40] M. L. Perl *et al.*, Phys. Rev. Lett. **35**, 1489-1492 (1975).

[41] S. W. Herb *et al.*, Phys. Rev. Lett. **39**, 252-255 (1977).

[42] R. Baier and R. Ruckl, Z. Phys. C **19**, 251 (1983).

[43] C. H. Chang, Nucl. Phys. B **172**, 425-434 (1980).

[44] G. T. Bodwin, E. Braaten, and G. P. Lepage, Phys. Rev. D **51**, 1125 (1995); **55**, 5853(E) (1997).

[45] M. B. Einhorn and S. D. Ellis, Phys. Rev. D **12**, 2007 (1975).

[46] H. Fritzsch, Phys. Lett. **67B**, 217 (1977).

[47] M. Gluck, J. F. Owens and E. Reya, Phys. Rev. D **17**, 2324 (1978).

[48] J. Babcock, D. W. Sivers and S. Wolfram, Phys. Rev. D **18**, 162 (1978).

[49] J. P. Lansberg, Phys. Rep. (in press).

[50] J. P. Lansberg, Eur. Phys. J. C **61**, 693-703 (2009).

[51] M. Butenschoen and B. A. Kniehl, Phys. Rev. D **84**, 051501 (2011).

[52] M. Butenschoen and B. A. Kniehl, Phys. Rev. Lett. **108**, 172002 (2012).

[53] N. Brambilla *et al.*, Eur. Phys. J. C **74**, 2981 (2014).

[54] B. Gong, L. P. Wan, J. X. Wang, and H. F. Zhang, Phys. Rev. Lett. **110**, 042002 (2013).

[55] K. T. Chao, Y. Q. Ma, H. S. Shao, K. Wang, and Y. J. Zhang, Phys. Rev. Lett. **108**, 242004 (2012).

[56] Y. Q. Ma and R. Vogt, Phys. Rev. D **94**, 114029 (2016).

[57] V. Cheung and R. Vogt, Phys. Rev. D **95**, 074021 (2017).

[58] V. Cheung and R. Vogt, Phys. Rev. D **96**, 054014 (2017).

[59] V. Cheung and R. Vogt, Phys. Rev. D **98**, 114029 (2018).

[60] V. Cheung and R. Vogt, Phys. Rev. D **99**, 034007 (2019).

[61] W. Caswell and G. P. Lepage, Phys. Lett. B **167**, 437 (1986).

[62] G. T. Bodwin, H. S. Chung, U. R. Kim, and J. Lee, Phys. Rev. Lett. **113**, 022001 (2014).

[63] P. Faccioli, V. Knünz, C. Lourenco, J. Seixas, and H. K. Wöhri, Phys. Lett. B **736**, 98 (2014).

[64] Y. Feng, J. P. Lansberg, and J. X. Wang, Eur. Phys. J. C **75**, 313 (2015).

[65] M. Neubert, Phys. Rep. **245**, 259 (1994).

[66] F. De Fazio, in *At the Frontier of Particle Physics/Handbook of QCD*, edited by M. A. Shifman (Wolrd Scientific, Singapore, 2000) p.1671.

[67] R. Casalbuoni, A. Deandrea, N. Di Bartolomeo, R. Gatto, F. Feruglio, and G. Nardulli, Phys. Rep. **281**, 145 (1997).

[68] M. Butenschoen, Z. G. He, and B. A. Kniehl, Phys. Rev. Lett. **114**, 092004 (2015).

[69] V. D. Barger, W. Y. Keung, and R. J. N. Phillips, Phys. Lett. **91B**, 253 (1980).

[70] V. D. Barger, W. Y. Keung, and R. J. N. Phillips, Z. Phys. C **6**, 169 (1980).

[71] R. Gavai, D. Kharzeev, H. Satz, G. A. Schuler, K. Sridhar, and R. Vogt, Int. J. Mod. Phys. A **10**, 3043 (1995).

[72] R. E. Nelson, R. Vogt, and A. D. Frawley, Phys. Rev. C **87**, 014908 (2013).

[73] P. Cvitanović, Phys. Rev. D **14**, 1536 (1976).

[74] B. L. Combridge, Nucl. Phys. B **151**, 429 (1979).

[75] J. Pumplin, D. R. Stump, J. Huston, H. L. Lai, P. Nadolsky, and W. K. Tung, J. High Energy Phys. 07 (2002) 012.

[76] R. Vogt, Z. Phys. C **71**, 475 (1996).

[77] C. N. Brown *et al.* (NuSea Collaboration), Phys. Rev. Lett. **86**, 2529 (2001).

[78] M. Glück, E. Reya, and A. Vogt, Eur. Phys. J. C **5**, 461 (1998).

[79] Y. Q. Ma, K. Wang, and K. T. Chao, Phys. Rev. Lett. **106**, 042002 (2011).

[80] M. Butenschön and B. A. Kniehl, Phys. Rev. Lett. **106**, 022003 (2011).

[81] Y. J. Zhang, Y. Q. Ma, K. Wang, and K. T. Chao, Phys. Rev. D **81**, 034015 (2010).

[82] R. M. Godbole, A. Misra, A. Mukherjee, and V. S. Rawoot, Phys. Rev. D **85**, 094013 (2012).

[83] R. M. Godbole, A. Kaushik, A. Misra, and V. S. Rawoot, Phys. Rev. D **91**, 014005 (2015).

[84] S. Digal, P. Petreczky, and H. Satz, Phys. Rev. D **64**, 094015 (2001).

[85] P. Faccioli, M. Araújo, V. Knünz, I. Krätschmer, C. Lourenço, and J. Seixas, arXiv:1702.04208.

[86] T. H. Chang, Ph.D. Thesis, New Mexico State University, 1999.

[87] T. H. Chang *et al.* (NuSea Collaboration), Phys. Rev. Lett. **91**, 211801 (2003).

[88] C. Biino *et al.*, Phys. Rev. Lett. **58**, 2523 (1987).

[89] K. J. Eskola, H. Paukkunen, and C. A. Salgado, Nucl. Phys. **A855**, 150 (2011).

[90] M. Glück, E. Reya, and I. Schienbein, Eur. Phys. J. C **10**, 313 (1999).

[91] S. P. Baranov, Phys. Rev. D **66**, 114003 (2002).

[92] H. Han, Y. Q. Ma, C. Meng, H. S. Shao, and K. T. Chao, Phys. Rev. Lett. **114**, 092005 (2015).

[93] H. F. Zhang, Z. Sun, W. L. Sang, and R. Li, Phys. Rev. Lett. **114**, 092006 (2015).

[94] D. Kang, J. W. Lee, J. Lee, T. Kim, and P. Ko, Phys. Rev. D **71**, 094019 (2005).

[95] G. T. Bodwin, E. Braaten, and J. Lee, Phys. Rev. D **72**, 014004 (2005).

[96] E. A. Kuraev, L. N. Lipatov, and V. S. Fadin, Zh. Eksp. Teor. Fiz. **71**, 840 (1976) [Sov. Phys. JETP **44**, 443 (1976)]; I. I. Balitsky and L. N. Lipatov, Yad. Fiz. **28**, 1597 (1978) [Sov. J. Nucl. Phys. **28**, 822 (1978)].

[97] J. C. Collins and R. K. Ellis, Nucl. Phys. **B360**, 3 (1991).

[98] B. A. Kniehl, D. V. Vasin, and V. A. Saleev, Phys. Rev. D **73**, 074022 (2006).

[99] R. Aaij *et al.* (LHCb Collaboration), Eur. Phys. J. C **71**, 1645 (2011).

[100] D. Acosta *et al.* (CDF Collaboration), Phys. Rev. D **71**, 032001 (2005).

[101] A. Andronic *et al.*, Eur. Phys. J. C **76**, 107 (2016).

[102] T. Aaltonen *et al.* (CDF Collaboration), Phys. Rev. D **80**, 031103 (2009).

[103] G. Aad *et al.* (ATLAS Collaboration), J. High Energy Phys. 07 (2014) 154.

[104] A. Cisek and A. Szczurek, Phys. Rev. D **97**, 034035 (2018).

[105] K. Aamodt *et al.* (ALICE Collaboration), Phys. Lett. B **704**, 442 (2011); **718**, 692(E) (2012).

[106] B. B. Abelev *et al.* (ALICE Collaboration), Eur. Phys. J. C **74**, 2974 (2014).

[107] I. Abt *et al.* (HERA-B Collaboration), Eur. Phys. J. C **60**, 517 (2009).

[108] R. R. Ma (STAR Collaboration) (private communication).

[109] A. Abulencia *et al.* (CDF Collaboration), Phys. Rev. Lett. **99**, 132001 (2007).

[110] E. Braaten, B. A. Kniehl, and J. Lee, Phys. Rev. D **62**, 094005 (2000).

[111] S. Chatrchyan *et al.* (CMS Collaboration), Phys. Lett. B **727**, 381 (2013).

[112] B. Abelev *et al.* (ALICE Collaboration), Phys. Rev. Lett. **108**, 082001 (2012).

[113] R. Aaij *et al.* (LHCb Collaboration), Eur. Phys. J. C **73**, 2631 (2013).

[114] B. Gong, L. P. Wan, J. X. Wang, and H. F. Zhang, Phys. Rev. Lett. **112**, 032001 (2014).

[115] G. Aad *et al.* (ATLAS Collaboration), Phys. Rev. D **87**, 052004 (2013).

[116] R. Aaij *et al.* (LHCb Collaboration), Eur. Phys. J. C **74**, 3092 (2014).

[117] G. Aad *et al.* (ATLAS Collaboration), Phys. Lett. B **705**, 9 (2011).

[118] V. Khachatryan *et al.* (CMS Collaboration), Phys. Rev. D **83**, 112004 (2011).

[119] R. Aaij *et al.* (LHCb Collaboration), J. High Energy Phys. 06 (2013) 064.

[120] R. Aaij *et al.* (LHCb Collaboration), J. High Energy Phys. 11 (2012) 031.

[121] R. Aaij *et al.* (LHCb Collaboration), Eur. Phys. J. C **72**, 2025 (2012).

[122] S. Chatrchyan *et al.* (CMS Collaboration), Phys. Lett. B **727**, 101 (2013).

[123] G. A. Schuler and R. Vogt, Phys. Lett. B **387**, 181 (1996).

[124] R. Aaij *et al.* (LHCb Collaboration), J. High Energy Phys. 11 (2015) 103.

[125] S. Abachi *et al.* (D0 Collaboration), DOI:10.2172/102428.

[126] V. Khachatryan *et al.* (CMS Collaboration), Phys. Lett. B **743**, 383 (2015).

[127] R. Aaij *et al.* (LHCb Collaboration), J. High Energy Phys. 10 (2014) 088.

[128] R. Aaij *et al.* (LHCb Collaboration), J. High Energy Phys. 12 (2017) 110.

[129] D. Acosta *et al.* (CDF Collaboration), Phys. Rev. Lett. **88**, 161802 (2002).

[130] S. Chatrchyan *et al.* (CMS Collaboration), Phys. Rev. Lett. **110**, 081802 (2013).

[131] Y. Feng, B. Gong, L. P. Wan, and J. X. Wang, Chin. Phys. C **39**, 123102 (2015).

[132] H. Han, Y. Q. Ma, C. Meng, H. S. Shao, Y. J. Zhang, and K. T. Chao, Phys. Rev. D **94**, 014028 (2016).

[133] M. L. Mangano, P. Nason and G. Ridolfi, Nucl. Phys. B **373**, 295-345 (1992).

[134] E. L. Berger and D. L. Jones, Phys. Rev. D **23**, 1521-1530 (1981).

[135] T. Affolder *et al.* (CDF Collaboration),Phys. Rev. Lett. **85**, 2886 (2000).

[136] D. De Gruttola (ALICE Collaboration) Nucl. Phys. **A926**, 136 (2014).